Investigating the Tribological Behaviours of a Jet Engine's Abrasive Rotor and Stator Vane Contact

Julián Alberto García Panizo

Department of Mechanical Engineering
The University of Sheffield

This dissertation is submitted for the degree of
Doctor of Philosophy

April 2022

This thesis is dedicated to my dad, Julian Garcia Bono, without whose constant love and support I would never have reached this point in life; and to Lidya Gimenez, who I cared for as my mom and cancer took away mid pandemic without making it possible to say goodbye. I will always carry you in my heart.

Acknowledgements

I would like to thank Rolls-Royce for giving me the opportunity to undertake this project, and I particularly want to acknowledge the invaluable help of Glen Pattinson, Mike Keenan, Lloyd Pallett, and James Provins, whose expertise considerably added to this research.

I am deeply grateful to my supervisor Matt Marshall. As an international student, I've faced moments of deep loneliness and insecurity, and I can't stress enough the key role that Matt has played in my emotional and mental development, and also personal growth. He has embraced me with warmth and constant positivity and has picked me up every time I've felt defeated by the PhD or life itself, with the outbreak of the COVID-19 pandemic and the loss of a family member. He has not only been an exemplar supervisor sharing his expertise but he's been the one who has given Sheffield a sense of home to me. I also thank Andrés Rovira wholeheartedly for giving me Matt's contact and leading me into this life-changing journey, along with Dr Charles Lord for his helpful feedback on my work.

The contribution of university technicians cannot be emphasised enough, as producing this work would have been particularly difficult without their help. Especially Christopher Todd, Dave Butcher, Richard Kay, and Bez Khan who offered me their assistance during critical stages of this research work, and whose help went above and beyond what was required of them. These people make work in the labs possible and their unending kindness makes it a pleasure. I am also deeply indebted to my colleges and friends – Eldar, Boxiu, Andreas, and Alvaro – for a cherished time spent together and for creating a friendly environment to work in.

Lastly, my completion of this project could not have been accomplished without the constant encouragement of my dad, Julián García Bono, and without my flatmates, Emilios Leonidas and Daniel Jones, whose kind attitude provided comfort and relief at home. My appreciation also goes out to my international friends, Andrea Guajardo and Michael Caampued, who opened my eyes and showed me the beauty of their cultures, to Cindy To, who supported me unconditionally through my second year and I owe her a lot, and also to Cindy Cosset, whose love and support helped me go through stressful times during the COVID-19 pandemic and has marked my life. A special mention also to Spanish speaking friends–Jose, Samantha and Ian–for their moral and emotional support; and to Lova Chechik for showing me how to enjoy running in British weather, helping me stay sane from early in the PhD.

Abstract

Plasma-Sprayed ceramic coatings are an appealing alternative to shrouded vane interstage labyrinth seals, as they offer a simpler architecture and a significant drop in aero-engine's weight. Historically, aero-engine sizes have not allowed manufacturers to mount vanes in cantilever. Due to their length, stresses have had to be diminish by securing their inner ends to a shroud; then using an abradable lining to limit gas recirculation around the stator. Currently, engine sizes have decreased, allowing to improve the weight penalties introduced by this design by removing the shroud and directly applying an abrasive lining on the rotating drum, with sealing achieved by the liner on the drum wearing the stator blades. Whilst abradable based sealing systems where the blade cuts the liner are well researched, little work has been undertaken on abrasive systems where the static blade is now worn.

The initial focus of this research has been to develop a high-speed rig and a monitoring system that allows the evaluation of different contact scenarios under more representative in-service conditions. The gathered data, during and post-test, has served to identify metrics that describe the tribological system and holds the opportunity to link aero-engine conditions with the ceramic lining performance. Cutting speed, incursion rate, ceramic material, abrasive surface finish, and coatings' porosity have been identified as system variables, and a statistically planned test matrix has allowed to identify the significance and dependencies of each, along with building the required knowledge to optimise the tribological system.

The wear mechanism was defined as rubbing, with it exhibiting a progressive and thermally driven adhesion. Zirconia's outcome was dragged down by its low conductivity, whilst alumina was found to delaminate. Extending the arc of contact and triggering surface renewal were seen to delay the progressive process. Further investigation with added porosity (e.g. through polyester) showed that the coating's microstructure can be tuned for the applied stresses, and when self-renew the outcome does not depend on coatings' conductivity.

Table of contents

List of figures

List of tables

Nomenclature

Greek Symbols

α Thermal expansion coefficient

η_B Ideal Brayton Efficiency

γ Ratio of specific heats (c_p/c_v)

λ Thermal conductivity

ν Poisson's ratio

Acronyms / Abbreviations

c_p Specific heat at constant pressure

c_v Specific heat at constant volume

p Pressure

Q Heat

R Gas Constant

s Entropy

T Temperature

V Volume

W Work

AHR   Adhesion plus heavy rubbing

APS   Atmosphere Plasma Spray

AR   Adhesion plus rubbing

CMC   Ceramic Matrix Composite

CPSP   Critical Plasma Spray Parameter

DoE   Design of Experiment

E   Young's modulus

EBPVD Electron beam physical vapour deposited

EDX   Energy Dispersive X-Ray Analysis

Ex   Exposure to wear

g   Grams or the force of the earth's gravitational pull, depending on the context

hBN   hexagonal boron nitrate

HVOF High Velocity Oxy-Fuel

Hz   Hertz

K   Kelvin

MPa   Megapascal

N   Newtons

PAR   Plowing plus adhesion and rubbing

PCA   Principal Component Analysis

PE   Polyester

RMS   Root Mean Squared

SEM   Scanning electron microscope

SGE   Specific Grinding Energy

SPS   Suspension Plasma Spray

TBC   Thermal Barrier Coating

TGO   Thermally Grown Oxide

V   Volt

Wr   Measure of wear

XRD   X-Ray Diffraction

YSZ   Yttria-Stabilised Zirconia

Zr   Zirconia

ºC   Degrees Celsius

Chapter 1

Introduction

1.1 Labyrinth seals

Labyrinth seals' non-contact properties make them very attractive. While sustaining pressure gradients, their design minimises power loss due to friction. For these reasons, labyrinth seals are particularly appropriate when connecting machine elements with high relative speeds. For instance, labyrinth seals are used in bearings to sustain lubrication, or in water pumps to prevent water leakage. In essence, this mechanical seal provides an elegant low-friction/long-life connection between static and rotary components.

Labyrinth seals strongly depend on tolerances to sustain pressure gradients; Fig. 1.1 shows their design idea. Notwithstanding that leakage is unavoidable because they are a non-contact seal, leakage across the boundary is minimised with intricate/interlocking paths and carefully designed geometries. Their architecture changes the fluid dynamics [1] and increases the fluid's difficulty to flow.
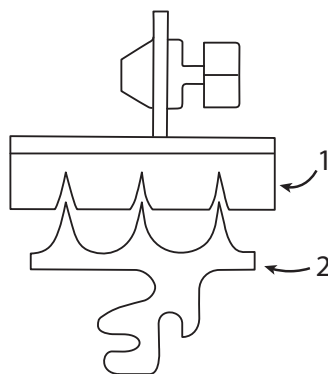
Fig. 1.1 Schematic diagram showing a side view of a labyrinth seal arrangement. Labels: (1) Stator with grooves; (2) Rotor with teeth like cutting geometries. Figure adapted from Raper [2]

The benefits of labyrinth seals are highlighted in Fig.1.2. Clearance reduction restrains the fluid flow, and applying carefully designed geometries introduces vortices. Maximising pressure loss across the intricate path allows a higher pressure gradient to be sustained. Therefore, the arrangement in Fig. 1.2b is more desirable than that in Fig. 1.2a.

(a) Fluid flow without labyrinth seal   (b) Example of fluid flow with labyrinth seal
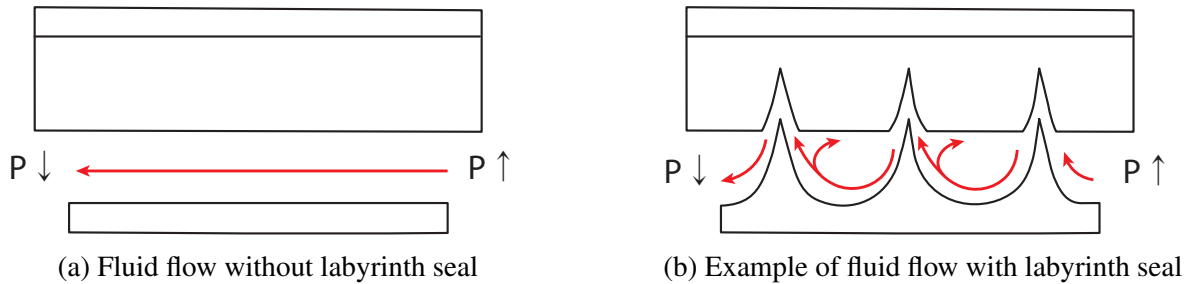
Fig. 1.2 Schematic diagrams displaying side views of two hypothetical arrangements with fluid flow across them.

For an experimental example, Denecke *et al.* [3] investigated groves' influence on labyrinth seal leakage. Their water-channel experiment showed vortices' generation on a configuration comprising steps and rub-grooves (displayed in Fig. 1.3). Their work focused on the turbine seals where pressure gradients are opposite to those found in the compressor. Thus, the fluid flow is reversed from the ones shown in Fig. 1.2b. Nevertheless, the behaviours are equivalent, and the experimental results are suitable for illustrating the importance that geometries and tolerances have on leakage across labyrinth seals.
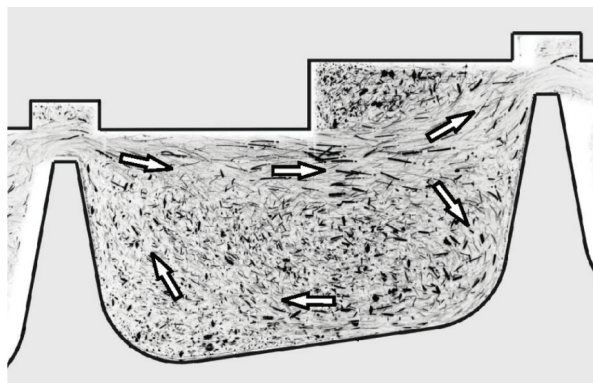
Fig. 1.3 Side view of a stepped labyrinth seal, experimental example of vortices generation. Source: Denecke *et al.* [3]

1.2 Use of labyrinth seals in turbomachinery

Civil aviation engines (hereafter referred to as "aero-engines") are embraced under the tur-bomachines' family name and use many types of seals between rotating and non-rotating elements. Among these, some engines use labyrinth seals to minimise pressure losses between stages[1]. This thesis addresses precisely those located in the high-pressure compressor section (*label 1* in Fig. 1.4). Additional aero-engine sealing systems can be found in the extensive overview of Chupp *et al.* [4] or those disclosed by Webster *et al.* [5].
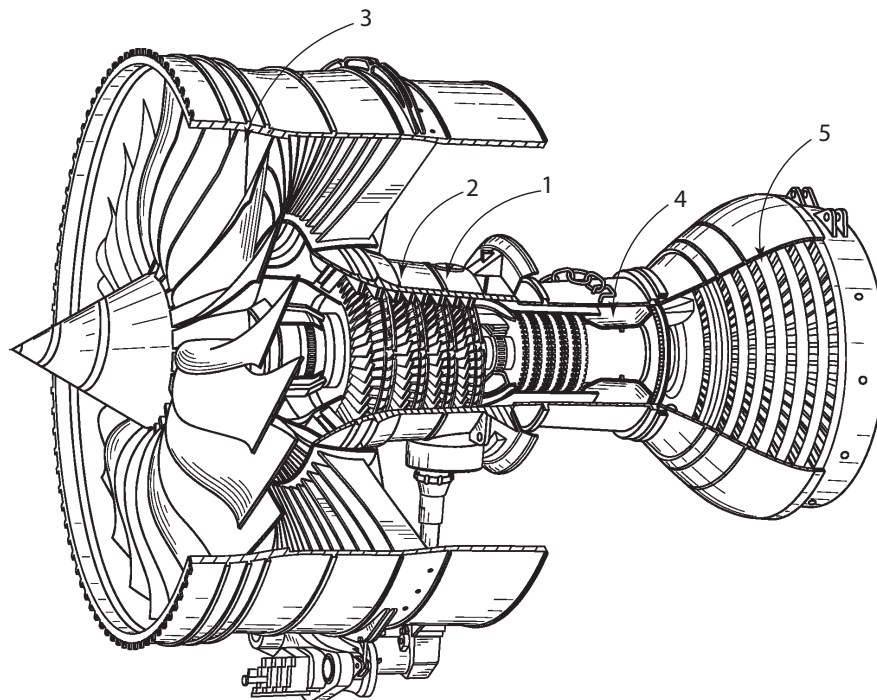
Fig. 1.4 A cross section of a gas turbine engine. Labels: (1) Compressor section; (2) Static/Stator Vane assembly; (3) Fan assembly; (4) Combustion chamber; (5) Turbine section. Figure extracted and adapted from Becker *et al.* [6]

1.2.1 Fundamental background and importance of labyrinth seals

To introduce why sealing is crucial in aero-engines and the importance of tolerances, it feels necessary to mention the Brayton cycle; the ideal thermodynamic cycle happening inside aero-engines [7, p. 463]. A simplified aero-engine is sketched in Fig. 1.5 with the airflow separated in four different processes, numbered from the compressor's inlet (**1**) to the turbine's outlet (**4**). This sketch joined with Fig. 1.6a (a "Pressure-Volume" graph) and Fig. 1.6b (a "Temperature-Entropy" graph), will help explain the ideal Bryton cycle, the significance of sealing, and the importance of tolerances in an engine's efficiency.

---

[1]A stage is composed of a rotating blade and a static vane or stator blade.
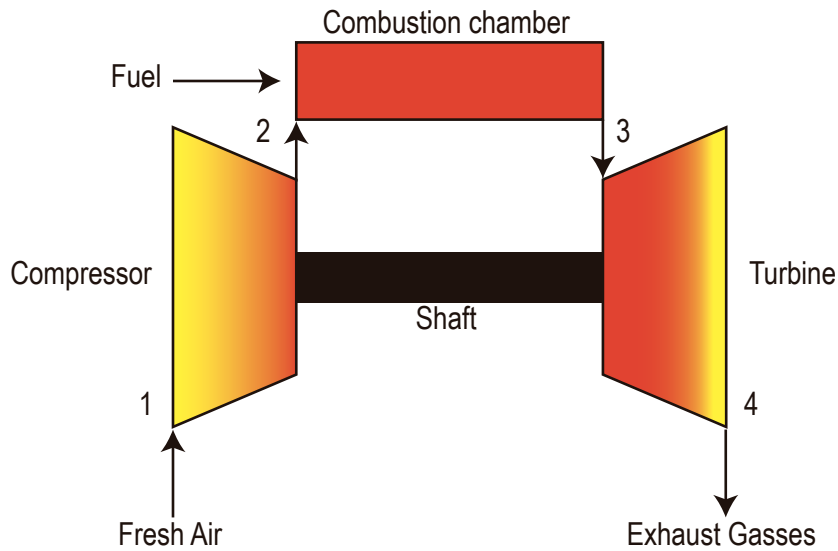
Fig. 1.5 Aero-Engine Simplification

Considering the ideal scenario, fresh air first enters the compressor and undergoes an isentropic compression (process **1** to **2s**). That is a compression process that is assumed 100% efficient, disregarding, e.g. frictional effects, fluid leakage, or heat transferred to the surroundings. Despite these assumptions being far simplistic, they are valid for an ideal Brayton cycle. An "efficiency coefficient" [8] then permits estimating the actual efficiency. Implementation of this correction is illustrated in Fig. 1.6 with points **2** and **4**, where P is used for pressure, V for volume, S for entropy, and T for temperature.

(a) P-V Graph   (b) T-S Graph
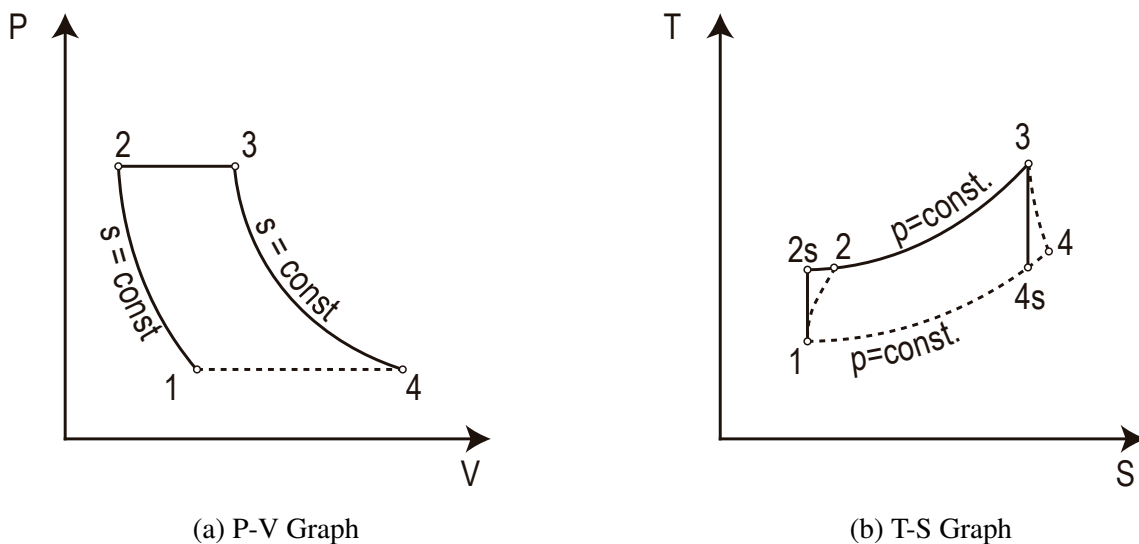
Fig. 1.6 Pressure-Volume (a) and Temperature-Entropy (b) Graphs

The assumption of a 100% efficient process is based on considering that the fluid flow is fast and that losses are small relative to the gross amount of fluid flow. In process **1** to **2s** of Fig. 1.6, in essence what is assumed is that all work is done to compress a specific volume differential [9]. Sealing methods such as those employed for the interstage seal will aim for this optimum working condition with constant entropy, pressure and temperature increase, and volume decrease. The resulting thermodynamic equations governing the isentropic compression process are shown below [10]; where c_p represents specific heat at constant pressure, and γ the ratio of specific heats.

$$Equation\ of\ state \longrightarrow \qquad pV = RT \tag{1.1}$$

$$Entropy\ of\ gas \longrightarrow \qquad s_{2s} - s_1 = c_p\ ln\left(\frac{T_{2s}}{T_1}\right) - R\,ln\left(\frac{p_{2s}}{p_1}\right) \tag{1.2}$$

Since the process is considered isentropic:

$$s_{2s} - s_1 = 0 \tag{1.3}$$

$$Final\ State\ equation \longrightarrow \quad c_p\,ln\left(\frac{T_{2s}}{T_1}\right) = R\,ln\left(\frac{p_{2s}}{p_1}\right) \tag{1.4}$$

With $R/c_p = 1 - 1/\gamma$ the pressure and temperature will therefore be given by:

$$Pressure's\ effect\ on\ Temperature \longrightarrow \qquad \frac{T_{2s}}{T_1} = \left(\frac{p_{2s}}{p_1}\right)^{1-1/\gamma} \tag{1.5}$$

$$Volume's\ effect\ on\ Pressure \longrightarrow \qquad \frac{p_{2s}}{p_1} = \left(\frac{v_1}{v_{2s}}\right)^{\gamma} \tag{1.6}$$

After the compressor, the compressed air proceeds into the combustion chamber where fuel is added and burned. Considering that the combustion chamber has open ends to both compressor and turbine, the fluid's pressure is assumed constant as entropy, temperature, and volume increases. This process is an isobaric addition of heat, and is illustrated with process **2s** to **3** from Fig. 1.6.

The resulting products from the combustion then continue into the turbine and ideally experience the direct opposite to what happens in the compressor; an isentropic expansion (state **4s**). Here, since the compressor and turbine share the same shaft (for engines with one shaft), the work transferred from the fluid to the turbine's rotor is precisely consumed in the compressor.

Finally, the Brayton's cycle is completed when the exhaust reaches atmospheric conditions outside the engine (process **4s** to **1** from Fig. 1.6), and the engine's efficiency (η_B) can be calculated. It is defined as the work done with the energy used (or heat input), and as provided by Borgnakke and Sonntag [7], it equates to:

$$\eta_B = \frac{Net\ Work}{Heat\ Input} = \frac{W_{Turbine} - W_{Compressor}}{Q_{in}} = \frac{c_p((T3 - T4s) - (T2s - T1))}{c_p(T3 - T2s)}$$

$$\eta_B = 1 - \frac{(T4s - T1)}{(T3 - T2s)} \tag{1.7}$$

Notice how an engine's efficiency (η_B) can equivalently be calculated from pressures, and how sustaining high temperatures is equivalent to sustaining high pressures because they are directly related. To further show this relation, first consider that compression and expansion are isentropic:

$$Compressor \longrightarrow \frac{T_{2s}}{T_1} = \left(\frac{p_{2s}}{p_1}\right)^{1-1/\gamma} \qquad Turbine \longrightarrow \frac{T_3}{T_{4s}} = \left(\frac{p_3}{p_{4s}}\right)^{1-1/\gamma} \tag{1.8}$$

Then, knowing that the pressure at the compressor's output and the turbine's input are equal ($P2s = P3$), and that the pressure at compressor's input and turbine's output are also equal ($P1 = P4s$). From Equation (1.8):

$$\left(\frac{p_{2s}}{p_1}\right)^{1-1/\gamma} = \left(\frac{p_3}{p_{4s}}\right)^{1-1/\gamma} \qquad \longrightarrow \qquad \frac{T_{2s}}{T_1} = \frac{T_3}{T_{4s}} \tag{1.9}$$

Finally, an engine's efficiency can be expressed in terms of temperature ratios ("$T2s/T1$") by rearranging Equation (1.9) and simplifying Equation (1.7). Equivalently, it can be expressed in terms of pressure ratios ("$p2s/p1$") by substituting Equation (1.9) in Equation (1.10):

$$\eta_B = 1 - \frac{T1\left(\frac{T4s}{T1} - 1\right)}{T2s\left(\frac{T3}{T2s} - 1\right)} = 1 - \frac{T1}{T2s} = 1 - \frac{1}{T2s/T1} \tag{1.10}$$

$$\eta_B = 1 - \frac{1}{(p_{2s}/p_1)^{1-1/\gamma}} \tag{1.11}$$

Since the engine's efficiency is defined indifferently with either temperature or pressure ratios (Equation (1.11) and Equation (1.10)), their importance is evident, and the behaviour of aero-engine manufacturers is expected. Fig. 1.7 shows the increase of engine pressure ratios with time.
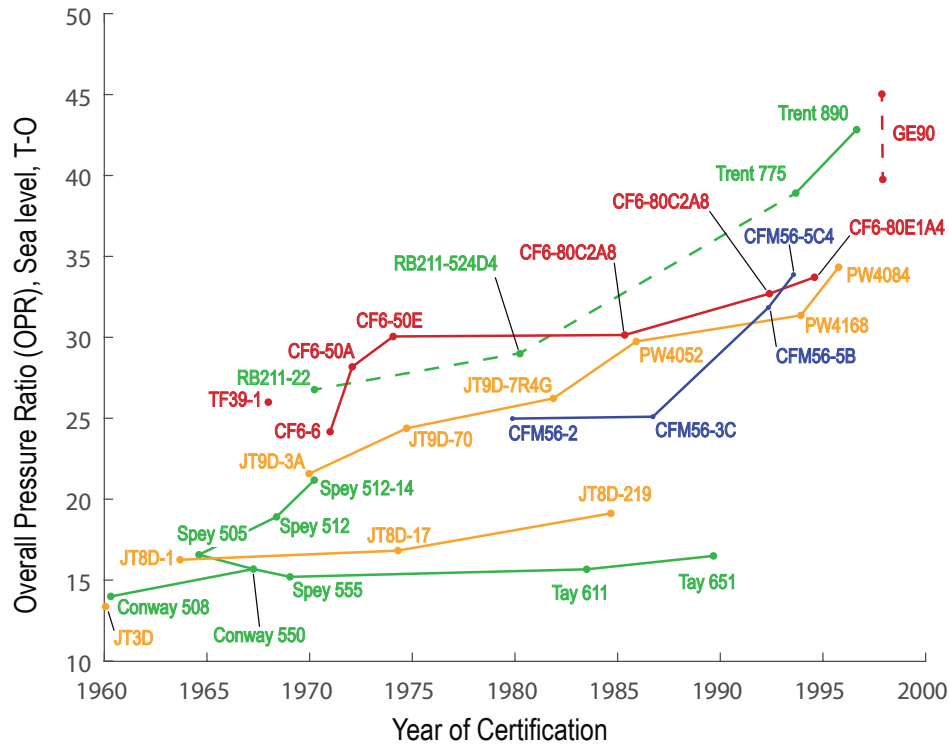
Fig. 1.7 Time history graph showing pressure ratio trends in gas turbine engines. Adapted from Jane's Aeroengines [11]

In conclusion, sealing in aero-engines has a substantial economic implication. This section has shown that the engine's efficiency is tied to the compressor's pressure/temperature ratios. Furthermore, given that an efficiency increase decreases the specific fuel consumption, and that tight tolerances attain higher pressure/temperature rations, the importance of tolerances is implicit. Wilson cites many significant figures [12]. For example, Melcher and Kypuros [13] estimated that a decrease of 0.25 mm in tip clearances reduces 1 % the specific fuel consumption and yields a yearly saving of over $160 M.

1.3   How is sealing achieved

During an aero-engine's life, components suffer complex displacements and deformations that cannot be accounted for during the design period. Even if this was possible, the labyrinth seal's tight tolerances would restrain the manufacturing process.

The alternative that Rolls-Royce has been using is not to machine labyrinth seals but to use the engine to create them by the engine itself during the running-in period (when the engine is first turned on) [14]. During this period, the engine undergoes meticulously planned manoeuvres (e.g. controlled centrifugal loadings and thermal expansion) that force components into contact. Tolerances are, thus, created when one of these components is worn. Since the achieved tolerances mark the engine's efficiency, the running-in period is critical in an engine's life.
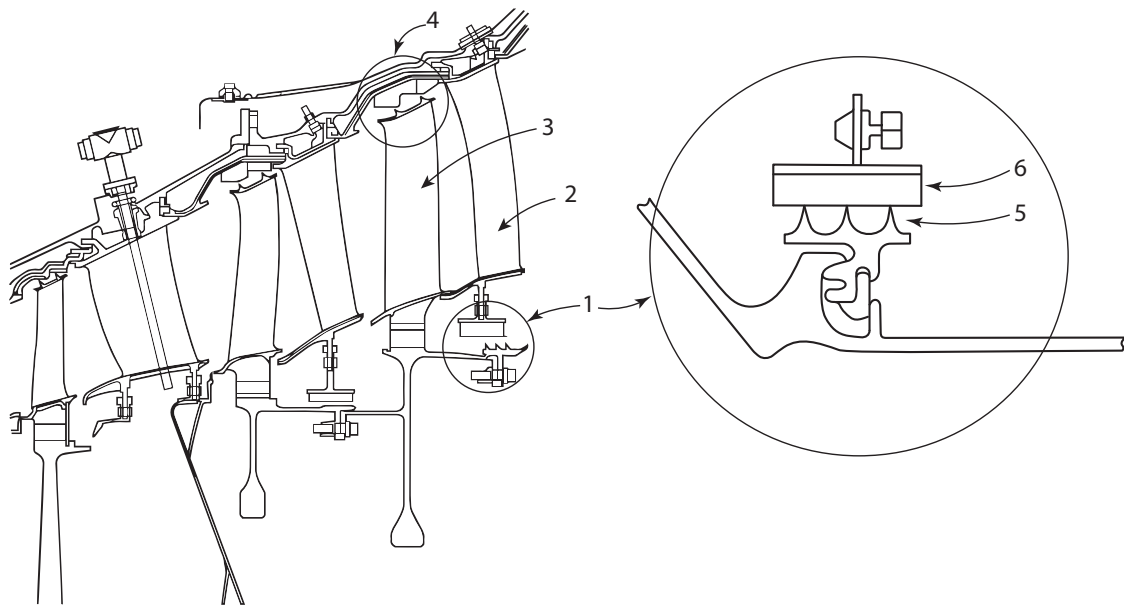
Fig. 1.8 Side cross-section of a gas turbine engine. Labels: (1) Interstage seal arrangement; (2) Static/Stator Vane; (3) Rotor Blade; (4) Seal arrangement on rotating blade;(5) Fin on rotating component; (6) Abradable lining on stator. Extracted and adapted from Piggott *et al.* [15] (left) and Raper [2] (right)

Abradable linings are applied between moving and stationary components to ensure that when components interact, one is worn in preference; easing grove generation, and ensuring that no unexpected tolerances are opened. Fig. 1.8 locates the interstage seal between the rotating drum and the static blade (*label 1*), and also includes a version of Rolls Royce's patented seal [15]. Notice the similarity in architecture between the interstage seal (rotating drum/static blade) and the one used between the rotating blade/static casing (*label 4*). Also, note that although Fig. 1.8 shows a turbine section, the high-pressure compressor's arrangement is very similar, only designed to hold the opposite pressure gradient.

To illustrate how an abradable coating works and to show the benefits of applying one, an example chain of running-in manoeuvres is presented in Fig. 1.9. In this example, the engine starts cold with as-machined tolerances (x_0) and then undergoes a series of slam manoeuvres.

These manoeuvres develop an expansion rate mismatch between rotating and static components that minimise tolerances and make seals experience heavy contact (x_1). (The rate in which this happens is named incursion rate for experimental matters.) Under these conditions, an abradable lining protects the seal's teeth from wearing (Fig. 1.9b); conversely, damaged teeth result when no abradable lining is used (Fig. 1.9a). The benefits of using abradable coatings become evident when the engine returns to regular operating conditions: non-damaged teeth fit in the pre-cut groove and minimise leakage, while the contrary is observed with worn teeth. As displayed in Fig. 1.9, not using abradable linings results in like-for-like material contact, and the labyrinth seal fails. The undesired alternative is to avoid contact by leaving bigger tolerances. Notice the difference in tolerances x_2.

(a) Performance of labyrinth seal without abradable lining

(b) Performance of labyrinth seal with abradable lining
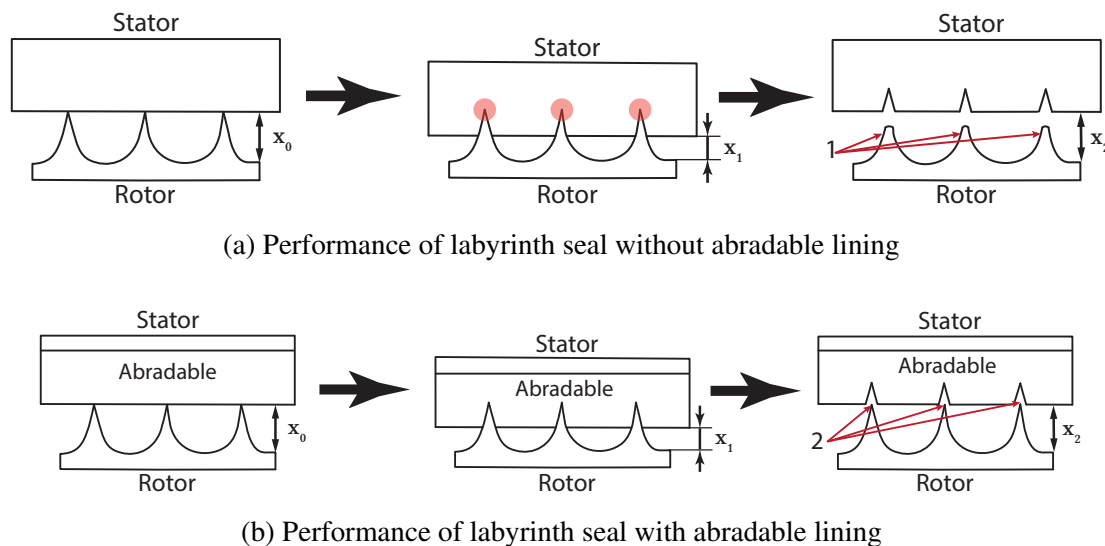
Fig. 1.9 Comparison of labyrinth seal performance during an exemplary chain of events: before, during, and after. (1) Fins are damaged during contact; (2) Fins are not damage.

Further benefits of using abradable linings include more flexibility against uncertain dynamic effects like bearing crossover, rapid engine shut down, or forced excitation of natural frequency modes. Abradable linings also reduce the effect of manufacturing problems like out-of-roundness of components as they allow the engine to rotate on its mass centre without this having to be its geometric centre [12, 16]. The employment of a sacrificial lining is highly justified since the engine can suffer from many dynamic events that cannot be accounted for.

Refer to Keenan's patent application for additional information on the related art [14] (circumferential seals). For explanations about events that lead to tolerances opening or for additional clearance control methods, refer to Lattime [17].

1.4   Current status: the main subject of interest

The principal theme for this thesis is the contact happening between the rotating drum and the static blade (Fig. 1.10). As explained in Section 1.3 (on the creation of labyrinth seals), sacrificing one of the component's surface during the first contact is the key that grants minimum tolerances and pressure losses. Either wearing the stator or the rotor could be adopted when applying this technique. However, abradable coatings are generally not used on rotating (i.e. centrifugally loaded) components; stationary components are preferred instead. The reason is that sacrificing a highly stressed surface as that of the rotor carries considerable risks; any surface deterioration could initiate cracks that lead to severe engine damage with their growth.
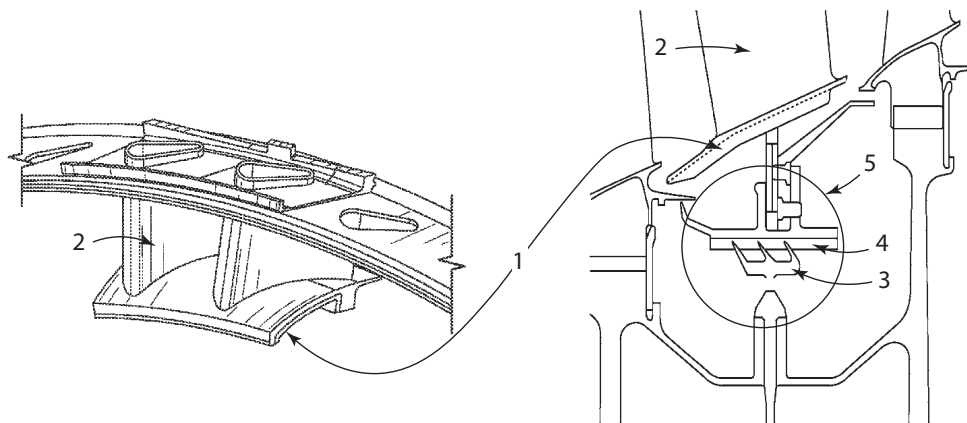
Fig. 1.10 Schematic diagram of the vane assembly and a side view of an interstage seal. The figure identifies with labels: (1) Inner ring; (2) Stator vane; (3) Labyrinth seal member, sometimes referred as fin; (4) Abradable lining; (5) Interstage seal assembly. Extracted and adapted from Freeman *et al.* [18] (left) and Piggott *et al.* [15](right)

Considering that wearing static components is favoured and that long stator cantilever vanes are susceptible to bending, the seal is achieved with slight complexity by first mounting the vanes between two concentric rings and then attaching a secondary assembly to the inner surface of the smaller ring (*label 1* and *label 5* from Fig. 1.10). This architecture stiffens the vanes by mounting them in a fixed-end beam arrangement and presents a design that aligns with ideals; seals can be generated by wearing a static component.

Currently, stator vanes can be mounted in cantilever because their length has decreased and they are stiff enough to manage operational stresses. Accordingly, the stiffening inner ring (*label 1* from Fig. 1.10) is unnecessary and can be removed to reduce weight. As illustrated in Fig. 1.11 and in patents of Lewis [19] or Alvanos [20], instead of employing a sub-assembly with an abradable, additional weight reduction can be achieved by using the rotor to wear the stator vanes.
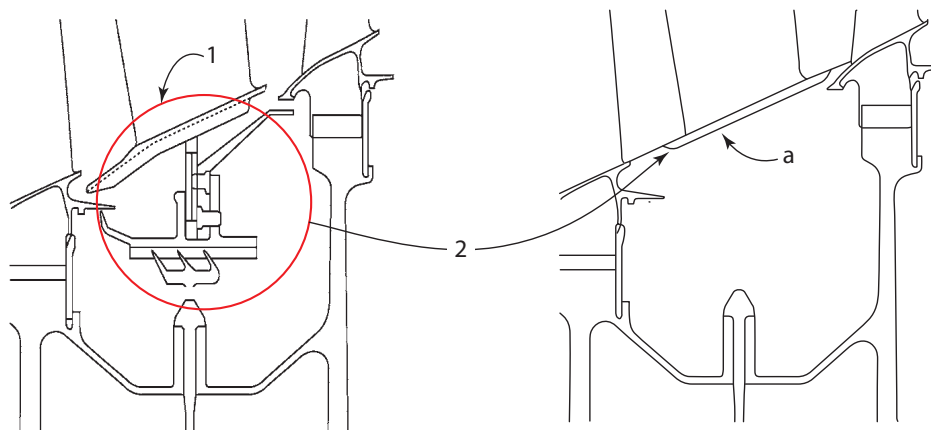
Fig. 1.11 Introducing the simplification process of the interstage sealing arrangement with a side view of the seal. Labels: (1) Current arrangement with secondary assembly and abradable lining; (2) Simplified arrangement showing no secondary assembly and a continuous rotor; (a) Abrasive liner applied directly on the rotor and immediately beneath stator blades. Figure extracted from Piggott *et al.* [15] and adapted to show the abrasive lining.

Notwithstanding that the rotor wears the stator vanes instead of an abradable, the seal is produced equivalently to the one previously described in Section 1.3. Likewise, tolerances are an important factor for avoiding tip leakage [21, 22], and the design criterion is to protect the rotating component (the rotor in this case). The rotor is coated with a hard ceramic coating for such purposes (*label a* from Fig. 1.11), which enhances the rotor's cutting behaviour during the rotor/stator vane interaction and minimises clearances.

The proposed changes produce an economic benefit; thus, the industrial interest. As weight is reduced by removing sub-assemblies and simplifying the interstage seal, the Specific Fuel Consumption of engines is enhanced. These changes also allow to scale down the engines and especially facilitate the design of those sections where space is a constraint, e.g. sections with small stator vanes. Hence, allowing for further improvements in Specific Fuel Consumption and causing an increase of industrial interest.

1.5 Knowledge gap

Conversely to where abradable linings stand today, far less attention has been drawn to abrasive linings. The main drawback of their infant state seems to be that stator-vane/rotor tolerances have been kept bigger than desired to avoid high-force contact scenarios (e.g. during unexpected engine manoeuvres or runaway events); events that historically have caused coating spallation or blade bending, and imply unscheduled engine removals for off-wing maintenance.

Rolls Royce is considering hard ceramic composites for their use as abrasive linings on their rotors, particularly 7%Yttria-Stabilised Zirconia (7YSZ), Alumina or Alumina-3%Titania. However, issues with these linings still seem to persist; several of which can be identified from the patented technology [23] and from the following confidential information that Rolls-Royce has provided (G. Pattinson, Rolls-Royce, private communication, March, 2020).

Deposits (accumulation of aerofoil material) seem to occur during the stator vane/rotor interaction (Fig. 1.12). This mechanism has been related to rubbing events and seem to be more common in linings with abrasive rather than abradable characteristics.
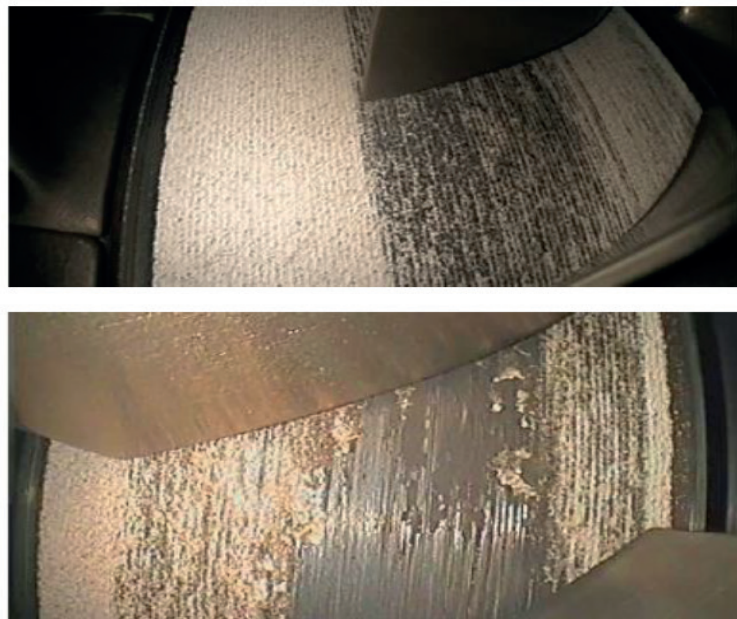
Fig. 1.12 Ceramic liner showing aerofoil deposition/material transfer

Spallation and chipping are also expected failure mechanisms. Based on fleet experience, spallation (localised broken areas in the coating's surface) appear to predominate at rotor sections with heavy accumulation/deposition of aerofoil material. Fig. 1.13 shown a spallation example of the rotor's coating. On the other hand, chipping (indentation), is rare. However, it has been observed changing in size and position and affects in those cases almost the coating's full depth. This condition has been related to rubbing effects or foreign object damage and is possible to occur in areas where the aerofoil has not contacted the ceramic liner. Since the drum design has no exposed edges, chipping is a fairly uncommon observation and consequently is a condition that needs further examination whenever observed.

Fig. 1.13 Ceramic liner showing spallation

Delamination is a highly undesirable loss of material that has also been observed (Fig. 1.14). It has been related to a flawed manufacturing process, such as an inappropriate selection of material, inadequate deposition parameters, poor surface preparation before coating; or unsatisfactory bond coat selection, coverage, or quality.

Fig. 1.14 Failure of the coating due to their inappropriate manufacturing/processing

These materials have been selected by Rolls-Royce not only because they have been extensively studied but also because they are employed as wear-resistant coatings or Thermal Barrier Coatings (TBCs). Hence, most have been engineered to withstand the high-pressure compressor's harsh environmental conditions and already hold most of the required characteristics.

On examination of similar patented coatings (Table 1.1), these are thermally sprayed hard ceramic matrix composites (CMC) and generally show an analogous design criterion to Rolls Royce's. However, the ceramic matrix of the patented coatings has been seen to include hard particles/grits of either alumina, hBN, CBN, diamond, silicon carbide, YSZ, gadolinia-zirconate, hafnia, mullite, or a mixture thereof [23–25]. Other materials have also been used as the ceramic matrix, like gadolinia-zirconate, hafnia, mullite, cubic zirconia or any material with a hardness of at least 7 Mohs [26] (e.g. diamond, quartz). A summary table of these patents and properties of the coatings has been included in Table 1.1.

Table 1.1 Summary of patents

Description	Matrix mat.								Grits					
	Al	*D*	*cZr*	*gZr*	*H*	*M*	*YSZ*	*Q*	*Al*	*hBN*	*CBN*	*D*	*S.C*	*Zr*
Method: Seal formation w/t abrasive rotor. Airfoil mat. more abradable than rotor. *Date: 26/04/2012* [27]	—— Abrasive rotor ——													
Self dressing mild abrasive MMC w/t grits. *Date: 26/04/2012* [28]	-	-	-	-	-	-	-	-	Y	-	Y	Y	Y	-
Method: texturing (laser engraved). Uses ceramics>7 Mohs hardness. *Date: 08/07/2014* [26]	Y	Y	Y	-	-	-	-	Y	-	-	-	-	-	-
Method: crush grinding/grit blasting – increased surface roughness/abradability. *Date: 08/07/2014* [29]	-	-	-	-	-	-	Y	-	-	-	-	-	-	-
Low strength CMC w/t coated grits. *Date: 29/07/2014* [24]	Y	-	-	Y	Y	Y	Y	-	Y	-	Y	Y	Y	Y
Spall resistant CMC; gradual increased proportion of low density filler. *Date: 04/11/2014* [25]	Y	-	-	Y	Y	Y	Y	-	-	Y	-	-	-	-
Low strength CMC w/t hBN+CBN mix. CBN grits are coated. *Date: 27/10/2015* [23]	Y	-	-	Y	Y	Y	Y	-	-	Y	Y	-	-	-

The abbreviations in Table 1.1 mean: *Al* alumina; *D* diamond; *cZr* cubic zirconia; *gZr* gadolinia-zirconate; *H* hafnia; *M* mullite; *YSZ* yttria-stabilised zirconia; *Q* quartz; *hBN* hexagonal boron nitrate; *CBN* cubic boron nitride; *S.C* silicon carbide; *Zr* zirconia

What seems confusing is that despite having the same purpose, these coatings show distinct architectures and have been patented in a short period of three years. Some coatings possess friable [24], hard [27], or graded density matrices [25]; some contain grits [25, 27], and some

not; others possess renewable cutting edges like a self-dressing grinding wheel [28], or a textured surface (laser engraved, sand blasted, or crush ground) [26, 29].

Notwithstanding the coatings' differences, all patents seem to look for abradability improvements. First, at a surface level with laser engraving, crush grinding, or grit blasting [26, 28, 29]. Then, changing architecture by either tuning the spraying process to generate a friable matrix, adding hard particles [24], low-density fillers [25], or using all thereof (a friable matrix with low strength fillers and hard particles) [23].

Given that all the patented coatings show distinct architectures, it seems that companies are uncertain about the design path to take. Furthermore, to the best of the writer's knowledge, there also appears to be no academic study on this matter. The uncertainty about the performance of different coating materials and architectures during the stator-vanes/rotor wear process has been the knowledge gap that has driven Rolls Royce to explore three different coatings. These have been YSZ, Aluminium Oxide, and Alumina-3wt.%Titania, which are thermal barrier coatings (TBCs).

1.6   Aim and objectives of this research

The study of abrasive linings for the rotor has grown in importance to minimise the stator-vanes/rotor gap and it is believed that this research is the first academic research concerned about simulating the service conditions of aero-engines to assess the interstage cantilever beams/rotor contact. Moreover, whilst previously studied to resist abrasion, it is also believed that this research is the first academic research aiming to enhance the abrasive properties of thermal barrier coatings.

The aim of this thesis is to provide a clear development direction, and the objectives for achieving this aim are:

- To position this research into context, collecting previous knowledge that allows to formulate a hypothesis about the system under consideration. Likewise, building the backbone for experimentation.

- To develop a testing platform that recreates the in-service failure mechanisms under a more controlled environment, without being less representative, and providing the means for characterizing the contact. The critique of this will set the basis for further development.

- To discriminate between observations, establishing a collection of tools that describe the contact and the coatings under examination.

- To identify the main variables that drive this tribological system.

- To understand the fundamental properties of this coatings in order to enhance their abrasive characteristics.

1.7   Thesis layout

Proceeding this introductory chapter, a review of literature related to the abrasive rotor/stator blade contact will be presented in Chapter 2. The literature review covers the thermal spraying process used for conforming these coatings, and how the process influences their final microstructure. The properties of the powders are also reviewed, as well as their relationship with the coating's end properties. A review on wear studies and how these have studied the coatings' performance is also included.

Chapter 3 sets the needs for a testing platform that studies these abrasive coatings, and joined with the previous literature defines the set of variables that are important for this study (i.e., cutting speed, incursion rate, coatings' material, coatings' surface, and coatings' spraying parameters). The chapter then focuses on recreating the contact, maintaining pertinent aspects of the rig that is currently used for testing abradables at the University of Sheffield, but designing and manufacturing other components. The following Chapter 4 then covers the instrumentation and signal processing performed, and the acquisition process.

Given the novelty of the rig and the number of factors, an experimental investigation is carried out to evaluate the rig and the strength of each factor. Chapter 5 includes the screening experiment and results. Speed is evaluated first, and dropped from the investigation. The other four factors are statistically investigated in terms of material removed, contact forces and temperatures, as well as force ration and specific grinding energy. A general view of the results is achieved through a principal components analysis (PCA), which in the next chapter (Chapter 6) is interpreted as a wear map. Therein, a deeper understanding on the wear mechanism is reached from examining the surfaces through SEM, and investigating the time-domain data. Alumina is shown to delaminate, and the effect of microstructure was emphasised as an opportunity to enhance the performance of zirconia coatings instead.

Chapter 7 further explores the impact of spraying parameters on the coating's microstructure, and also the option of a filler (in this case polyester) for producing an extra effect in the microstructure. The role of spraying on microstructure is understood and the option of influencing the microstructure with a filler is reinforced with the results as zirconia's performance is improved ut to levels of alumina.

A final discussion is carried out in Chapter 8 bringing the research together and into context, as well as how this work can be taken forward. Chapter 9 are the final conclusions.

Chapter 2

Literature review

A complete tribological study on this matter finishes when the externalised mechanisms are linked with the microstructures of the materials in contact. Only at this point, a hypothesis can be drawn, and materials can be modified or changed to enhance the tribological system.
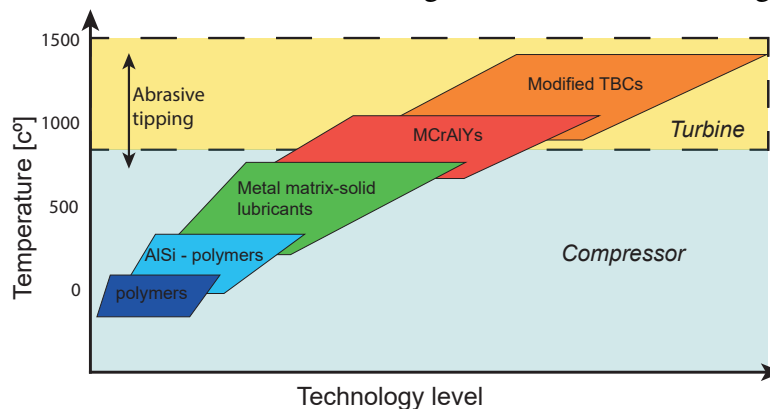
Fig. 2.1 Technology level of abradables. Adapted from Sporer and Giannozzi [30]

Abradable & indeed abrasive linings used for sealing in hot sections of aero-engines tend to be ceramic-based, and those used under extreme conditions essentially derive from TBCs (Fig. 2.1). Given the widespread application of these materials as TBCs, reference will be made to material science studies that optimise properties adequate for this application. Despite that this thesis's focus is their use as abrasive liners, given shared environmental/operational conditions, much of the research on TBCs is highly relevant from a materials science perspective.

This literature will address materials without entering into less relevant aspects of TBCs (e.g. thermal, erosive or chemical properties). Furthermore, it will cover their manufacturing process and different powder compositions, highlighting common failure mechanisms of the coatings and promising alternatives in the manufacturing process. Finally, wear studies and alternative sources of information will be reviewed, identifying wear mechanisms and inferring coating properties under representative conditions.

2.1   Thermal spraying technique

The ISO Standard 14917:2017 [31] defines thermal spraying as: "process in which surfacing materials are heated to the plastic or molten state, inside or outside of the spraying gun/torch, and propelled onto a prepared surface". The ceramic linings' data sheets [32–34] show that these can be applied through two different thermal spraying processes, either Atmosphere Plasma Spray (APS) or Combustion Powder Thermospray. Without being restricted to it, the industrial sponsor has selected the APS process because it is relatively cheap, versatile, has high deposition rates, and achieves higher temperatures (which is advantageous when working with refractory ceramics). Herman *et al.* [35] provide a review on different spraying processes and agree with this statement, further adding that combustion powder spraying yields low-performance coatings that are not applicable when well bonded and dense coatings are required. The resulting coatings are friable; thereby, combustion powder spraying is a process more commonly seen in the manufacture of abradable linings [36].

Table 2.1 includes features of the two recommended spraying processes and High Velocity Oxy-Fuel (HVOF), which is a variation of combustion spraying that yields dense coatings. Furthermore, the table shows that distinct microstructural features result from the different spraying processes; hence, each is suitable for different industrial applications.

Table 2.1 Summary table of the spraying processes. Adapted from Herman *et al.* [35]

Spray Process	Flame temp. [°C]	Particle velocity [m/s]	Micostructural features	Applications
Combustion	∼ 3000	∼ 40-100	Relatively high porosity & oxidation	Reclamation, corrosion protection
APS	∼ 5000-25.000	∼ 80-300	Porosity in ceramic deposits	Thermal barrier, insulators
HVOF	∼ 3000	∼ 400-800	High density, excellent adhesion, compressive stresses	Wear protection

The APS deposition process is illustrated in Fig. 2.2. The spraying tool includes two electrodes (a cathode and a water-cooled anode) to generate a strong electric arc. A plasma jet is created when gas (commonly argon, hydrogen, nitrogen, helium, or a mixture thereof) is injected and ionised. When feedstock powder is introduced into this jet (usually with a carrier gas), particles are melted to some extent and propelled into the substrate. Consequently, producing the coating. Among many authors, Pawlowski [37, p. 74–79] or Herman [38], further describe the spraying process.
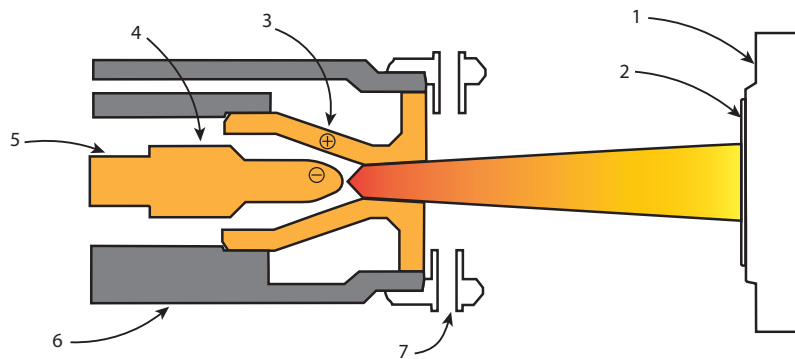
Fig. 2.2 Schematic diagram of an APS process. Labels: (1) Workpiece; (2) Coating; (3) Water-cooled anode; (4) Cathode; (5) Plasma gas+current; (6) Insulator; (7) Powder port. Source: adapted from O.Metco [39]

2.2   The importance of the spraying process

Numerous microdefects are present in the microstructure of a typical coating [38] (Fig. 2.3). Pores and inter-lamellar or intra-lamellar cracks are examples and result from imperfect splat contact or as a stress relaxation mechanism during the cooling down process, namely a quenching process. Both the cooling down of individual splats and the bulk material have been found to have an implication on the latter [40, 41]. Oxides and foreign particles can also be found as imperfections and have been related to the degree of melting achieved or if particles react with the spraying atmosphere [38]. Oxide content, porosity, and bond strength are some of the metrics used to assess the integrity and quality of coatings [35], and as will be addressed later, are factors that have an effect on wear and the failure mechanisms.
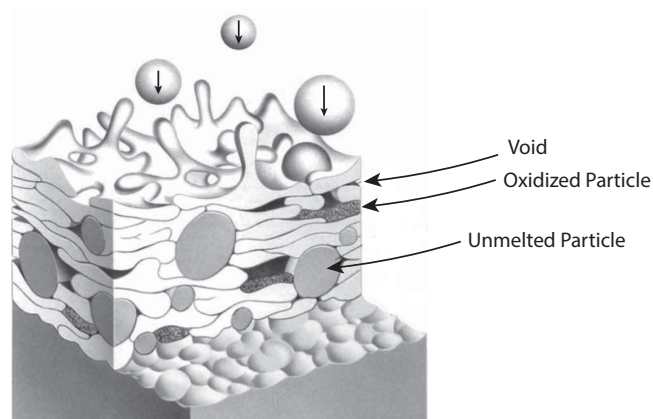
Fig. 2.3 Schematic cross section of an APS coating build-up. Adapted from Herman [38]

Literature concerning the spraying process is extensive [35, 42–51]. Spraying parameters control the coating formation and the cooling rates, therefore governing the coating's macrostructure, the crystallographic arrangement within each splat, and the defect architecture. Accordingly, the effect of the spraying process on the coatings' properties is high, being possible to engineer coatings of opposite characteristics such as abrasive and abradable [52] by tuning the process. Sensing techniques and computer-aided methods have improved the understanding and control of the spraying process [50, 53]; however, the relation between variables is complex and the spraying process remains a very active field of study [54].

Concerning the spraying process of abrasive linings used for aero-engine sealing applications, no research has been found. Abradable linings, however, do seem to have drawn some attention [55, 56], although still uncommon. It is known that there is a need to tailor the spraying process to suit the coating's purpose. Thus, it would not be unreasonable to believe that for this specific topic the interest has shifted from understanding the spraying process to improving specific coating behaviours for such industrial applications. In other words, tribological systems are complex and understanding the coatings' requirements are needed before optimising their manufacturing process.

Similarly, it is beyond the scope of this thesis to examine the in-depth relation of coating properties with spraying parameters. Yet, it seems necessary to consider the spraying process for any tribological study, due to its influence on coatings properties, and some relationships will be treated to illustrate the influence of some powder characteristics (Section 2.6) and to explain general wear mechanisms and the results of tribological studies (Section 2.7).

2.3 Design constrains of high temperature ceramic coatings

The structure of TBCs is illustrated in Fig. 2.4, which essentially consists of 4 sections: the substrate, the bond coat, the thermally grown oxide (TGO), and the coating.
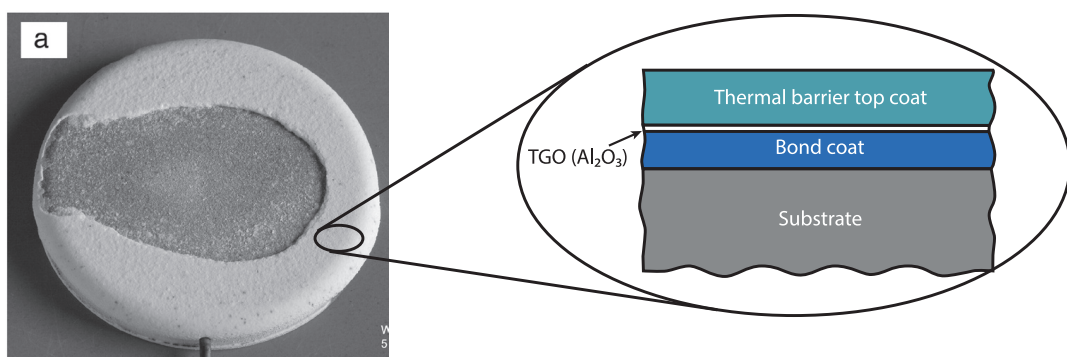
Fig. 2.4 Schematic of a TBC structure and example of delamination after been subjected to thermal cycling. Left photo adapted from Karger *et al.* [57].

From a structural point of view, the challenges to overcome with ceramic coatings seem to be founded on the classical problems of layered composite systems; their rather bad behaviour with inter-lamellar shear stresses and limited strain compliance. Layered coatings are thermomechanically limited. The different layers of coatings have a clear mismatch in thermal expansion coefficients and expand at uneven rates when temperature increases during operational conditions. Consequently, a stress gradient is developed, leading to crack growth, spallation or delamination [58]; thermal cycles and defects in the coating aggravate this state. In aero-engines, this scenario would mean that the components are exposed to temperatures capable of melting and exposed to the rapid attack of hot corrosive gases. Thereby, coating delamination is a highly undesirable scenario.

As described by Evans *et al.* [59], several mechanisms can make coatings fail, but the ones of greatest concern are those that cause large scale buckling or spalling of the coatings. In many cases these processes have been related to the continuous and irregular growth of the TGO, that result from the prolonged exposure to the oxidizing gases that diffuse through TBC's top layer. The TGO thickens irregularly due to surface imperfections in the substrate, developing uneven stresses that initiate cracks, which then propagate along the surface interface [60]. An illustration of the cracking mechanisms is included in Fig. 2.5. Clarke *et al.* [61] and Padture *et al.* [62] produced highly cited reviews on TBCs for gas-turbine engines, further covering the structure, properties and failure mechanisms.

(a) SEM of cross section. (b) Schematic
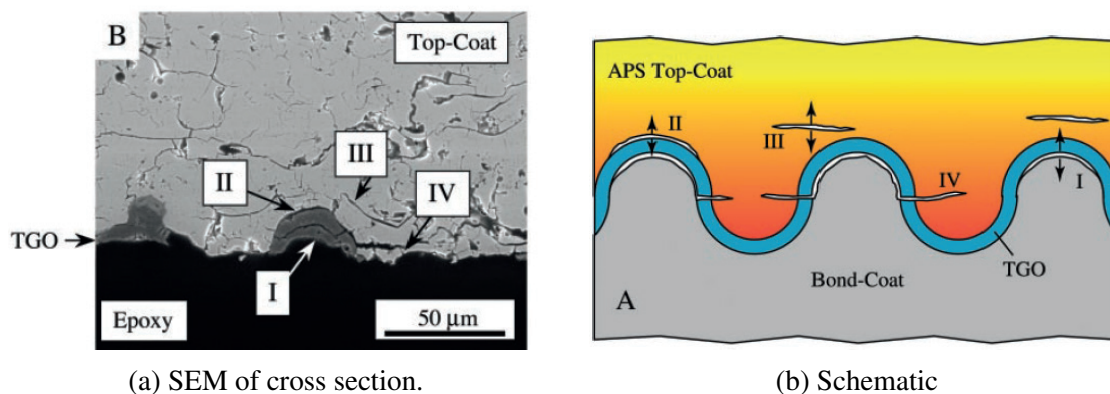
Fig. 2.5 Illustration of cracking mechanisms in APS coatings. Adapted from Padture *et al.* [62]

All things considered, the stresses related to the growth of the TGO seems to be of arguable relevance to recreate the contact conditions. The wear process studied herein happens mainly during the initial running-in period while the growth of the TGO happens through a significantly longer period (due to inter-diffusion of oxidising gases and prolonged exposure to these). However, interlamellar shear stresses do seem to have a clear importance on the large scale failure of coatings and should be taken into account in any type of experimental design.

2.4   Assessment of alternative spraying techniques

The spraying process has received particular interest to improve the permissible deformations and life of TBCs, given its influence on coatings' properties [49]. It appears that adjustments to the process have focused on increasing porosity, leading to coatings with lower thermal conductivity [63] and higher strain compliances. For some scenarios, the required porosity can be introduced by optimizing spraying parameters. Among many methods [64], functionally graded [65] or multilayered coatings [66] are examples of implementing this idea. However, these techniques do not seem to yield the expected results on highly stressed components, and other techniques are required. Deliberately introducing vertical cracks has been studied [67–70] and patented [71] since this has shown to improve the coatings' strain tolerance.

With a similar idea of introducing vertical defect, spraying methods that form columnar microstructures like EBPVD or SPS have also been the focus of many studies and recent development [68, 72–74]. However, extreme care must be taken not to run into other failure mechanisms. These architectures can leave the TGO more exposed to the oxidising atmosphere and lead to delamination of the coating due to its continuous growth [75–77]. Fig. 2.6 from Bernard *et al.* [63] illustrates the different microstructures and provides a comparison of their thermal conductivity.
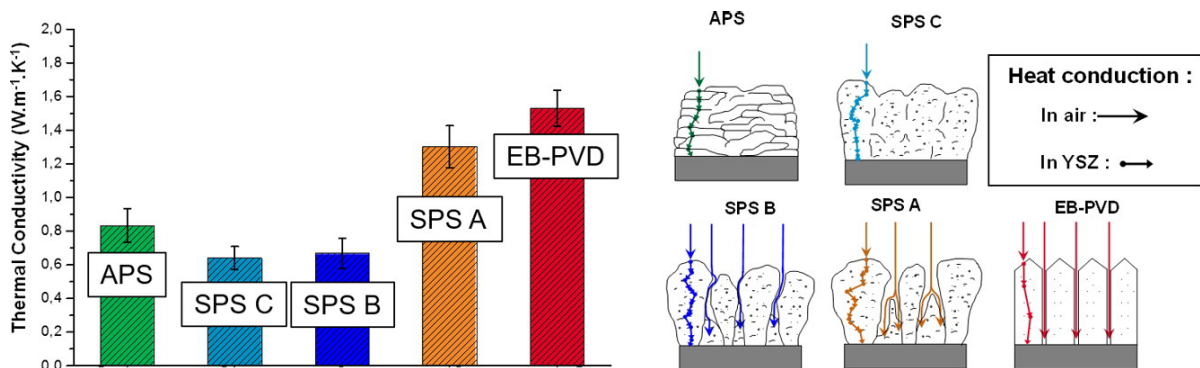
Fig. 2.6 Different microstructures and their thermal conductivity. Source: Bernard *et al.* [63]

The manufacturing processes previously mentioned find many applications in aero-engines due to the enhanced thermomechanical properties and lifetimes of the coatings they produce. However, they do not seem appropriate for a highly stressed rotor. Surface defects (columnar or cracked coatings) can be the origin of cracks that quickly propagate into the rotor's main body, causing rapid or unexpected failures. Accordingly, the only apparent options are the dense coatings manufactured with APS or HVOF processes, which despite having a relatively bad cyclic behaviour, seem to be the preferred choice for coatings that are wear resistant [35].

2.5 Nanostructured powders for APS ceramics coatings

Later research has shown that manufacturing coatings with smaller particle powders enhance thermal shock resistance [78], wear resistance, adhesion, toughness, and spallation resistance [79, 80]. Nano-sized coatings possess a bimodal microstructure if correctly manufactured (Fig. 2.7), which have zones of the initial nano-sized feedstock that act as crack arresters (Fig. 2.8) [52, 81]. Lima and Marple [52] covered the above and describe how the coatings could be manufactured as tough for anti-wear applications or as friable as metallic-based abradables by controlling the distribution of nano-zones. However, researchers report that if nano-sized powders are completely melted, the bimodal microstructure is lost, and the resulting coatings are comparable to those obtained from conventional powders [52, 82]. Thereby, the importance of the spraying process is highlighted once again.
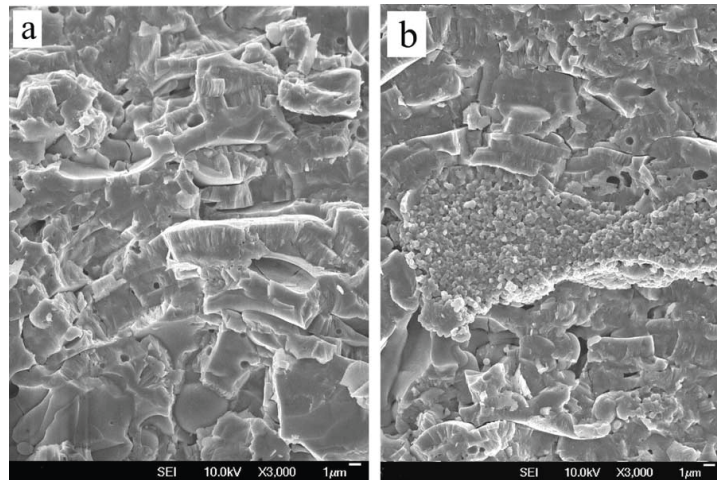
Fig. 2.7 SEM micrographies comparing Al_2O_3-3wt.% TiO_2 coatings manufactured through (a) conventional and (b) nanostructured powders. Source: Lin *et al.* [83]
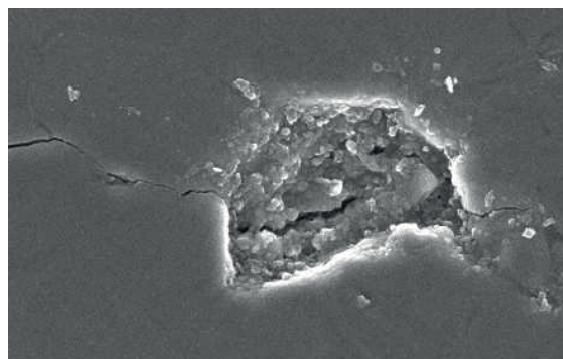
Fig. 2.8 Crack arrestment mechanism on nanozone section. Source: Lima and Marple [52]

2.6   Powders, impurities, and coating properties

The three proposed powders for abrasive liners are commercially available by Oerlikon Metco and are known as Metco 105NS, Metco 101NS, and Metco 204B-NS. These correspond respectively to Aluminium Oxide, Aluminium Oxide-3wt.% Titanium Dioxide, and 7%Yttria-Stabilised Zirconia.

2.6.1   Alumina and alumina/titania coatings

The composition of Metco 105NS and Metco 101NS powders are shown in Table 2.2. These powders are manufactured through a fusing and crashing process; a processing method that can be used for fragile materials and creates dense powders of an angular or blocky morphology (Fig. 2.9). Different powders possess distinct thermal and aerodynamic properties depending on their morphologies, densities, sizes, and size distributions [49]. It follows that inconsistencies in coatings' structure have been related to angular or blocky powder morphologies; their small irregularities mean variable in-flight behaviours and different interactions with the plasma jet, therefore, a variable deposition process.

Table 2.2 Summary of Aluminium Oxide-Titanium Dioxide(-0wt.%&-3wt.%) [32, 33]

	Alumina (Metco 105NS)	Alumina-3%Titania (Metco 101NS)
Chemical formula:	Al_2O_3	$Al_2O_3TiO_2$
Manufacture:	——— Fused and crushed ———	
Powder composition:	Al_2O_3 98.0+ wt.%	Al_2O_3 94.0 wt.%
	-	TiO_2 2.5 wt.%
	$Na_2O \leq 0.75$ wt.%	-
	$SiO_2 \leq 2.0$ wt.%	SiO_2 2.0 wt.%
	-	Fe_2O_3 1.0 wt.%
Nom. part. size dist.:	$-45\mu m \leq x \leq 15\mu m$	$-45\mu m \leq x \leq 11\mu m$
Morphology:	——— Angular/Blocky ———	
Colour:	White	Grey
Service Temperature:	≤ 1650ºC	≤ 1100ºC
Process:	—— Atmospheric Plasma Spray Combustion Powder Thermospray	——
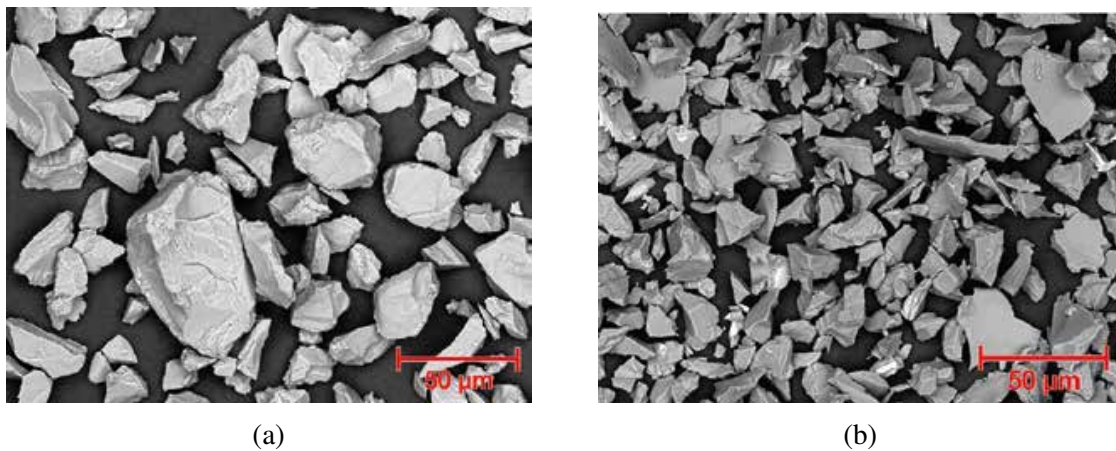
Fig. 2.9 Scanning Electron Microscopy (SEM) Photomicrography: (a) Metco 105NS, (b) Metco 101SF (similar to Metco 101NS). Source: Product Data Sheet [32, 33] respectively.

The product data sheet of Metco 105NS [32] describes alumina (Al_2O_3) as a widely used material that is hard, wear-resistant, chemically inert, and stable at high temperatures. An XRD analysis of this powder identified the composition as α-Al_2O_3 [84], which is the most desirable phase because of its high hardness and corrosion resistance. However, as-sprayed coatings contain other forms of alumina such as γ- or δ-Al_2O_3, resulting from process-dependent factors such as cooling rates. These other phases are said to be metastable and, unlike the stable α-phase, endure phase transformation during thermal cycling. This is a well-known material behaviour [42, 43] that comes with a volume change and leads to coating cracking.

Table 2.2 shows that Metco 105NS does not only include pure α-alumina phase (corundum), but also includes small impurities of Sodium Oxide (Na_2O), and Silicon Dioxide (SiO_2). Despite there being extensive research on Aluminium Oxide, little seems to be known about the effect that these impurities have on the plasma spraying process and the coating's properties. It might be possible that impurity contents under 1-2% have no significant effect on the mechanical properties of plasma-sprayed coatings. However, the addition of small impurity amounts has been studied during the sintering processes of alumina, relating these to a phenomenon called abnormal grain growth; a process associated with a detrimental effect on the mechanical properties of sintered ceramics (e.g. creep) [85]. The impurities present in Metco 105NS have been

be the current focus of many studies [86, 87]. Furthermore, the data sheet does recommend using higher purity powders for electronic or biomedical applications, which acknowledges some influence on the plasma sprayed coating.

Referring to Table 2.2, Metco 101NS [33] appears to be a variation of Metco 105NS that does not include Sodium Oxide (Na_2O) but includes small quantities of titania (TiO_2) and Iron Oxide (Fe_2O_3). Researches have related the addition of TiO_2 and Fe_2O_3 with a stabilization improvement of the α-alumina phase in the sprayed coatings [88–90]. The datasheet also states that adding a small quantity of TiO_2 to Al_2O_3 powders increases the toughness of the wear and erosion resistant coating. An increase in toughness comes with a decrease in hardness because these are related, and although the chemical resistance of the coatings is also reduced, the data sheet states that these can still be used in most acid and alkali environments. This statement seems to be generally accepted and is in agreement with other studies within the field [91].

Researchers like Fevel *et al.* [92] concluded that the wear resistance of plasma-sprayed Al_2O_3 increase with TiO_2 contents. Although this conclusion seems accepted, other researchers like Ramachandran *et al.* [93] obtained contradicting results; Al_2O_3 coatings had a better performance than those of Al_2O_3 mixed with TiO_2. The variability that spraying parameters introduce can be a possible explanation for this contradiction. While a material change affects coatings' wear behaviour, to some extent, it appears that its influence can be overrun by spraying parameters. In terms of wear, the relative importance of spraying power and material composition can be inferred from the results provided by Ramachandran *et al.* [93] (Fig.2.10).
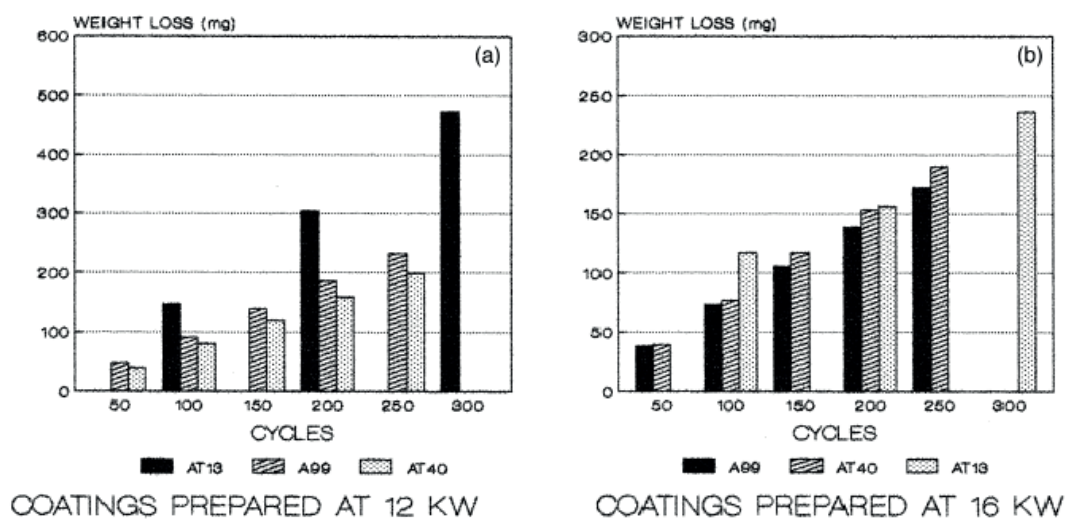
Fig. 2.10 Abrasive wear test for coatings engineered using two different torch powers and different compositions. Key:Al_2O_3 (A99), Al_2O_3-13wt.% TiO_2 (AT13), Al_2O_3-40wt.% TiO_2 (AT40); adapted from Ramachandran *et al.* [93]

Further research has been carried out about the impact of spraying parameters on alumina-titania coatings by researchers like Sahab *et al.* [94], Bounazeff *et al.* [95], or Wang and Shaw [96]. The latter showing that simple parameters like the mix distribution of feed powder affect crack growth, hardness, or abrasive wear resistance. In conclusion, the spraying process

appears to introduce an important variability that must be considered. Furthermore, since a change in powder composition may alter the optimum parameters to spray a coating with, it does not seem appropriate to reach conclusions about wear properties by direct comparison of coatings engineered with different compositions and the same spraying process.

Nano-sized powders appear to benefit plasma-sprayed coatings (as previously mentioned in Section 2.5). Metco 105NS and Metco 101NS powders, which are conventional powders of micrometre size, are no different. Researchers like Lin *et al.* [83], who specifically compared Al_2O_3-3wt.% TiO_2 coatings manufactured from conventional and nano-sized powders, attributes the enhanced behaviour to several factors. With nano-powders, there is an increase in coatings' homogeneity and in α- to γ-Al_2O_3 proportion. Furthermore, the fine powders seem to make TiO_2 almost completely react with Al_2O_2 during the spraying process to form a metastable solid solution (mechanism described by Kear *et al.* [97]). Lin *et al.* [83] reports that when comparing conventional with nanostructured coatings of similar hardnesses, the latter exhibit a higher adhesion strength and crack extension force. Therefore, as suggested by Lima and Marple [52], general knowledge associating hardness and wear might not be applicable for nanostructured coating; Section 2.7, will extend on this belief.

2.6.2 Yttria-stabilised Zirconia

Alumina and zirconia were both considered in the early development of TBCs. Later, Al_2O_3 was disapproved because it suffered significant drawbacks; in essence, the relatively high thermal conductivity and the coating cracking resulting from alumina's phase change (Section 2.6.1). As industry demanded higher operational temperatures and extended life for components, the attention then shifted to YSZ, and currently, YSZ claims to be the state-of-the-art material for TBCs [68]. Refer to Miller [98, 99] or Grisaffe [100] for further reading on the history and development of these thermal barrier coatings.

Despite their differences, both coatings are still suitable for some applications, are widely studied, and show complementary properties. For instance, adding 35 wt.%Al_2O_3 to YSZ has prevented the excessive growth of the TGO on the bond coat, increasing the coatings' thermal cycle life [101]. It appears that Al_2O_3 has very low solubility in ZrO_2 [102] and acts as a diffusion barrier. Addition of Al_2O_3 has also shown benefits in bonding strength [101], Young's modulus, hardness, and fracture toughness [103]. Moreover, experimental results have shown that in combination with TiO_2, it successfully decreased the effect of CMAS attack (glass deposits developed from airborne sand particles that attack the coatings) [104]. The drawback is that, since Al_2O_3 has a higher conductivity than ZrO_2, and both have distinct thermal expansion coefficients, addition of Al_2O_3 decreases the thermal shock resistance and increases the conductivity of coatings [105].

Concerning YSZ, Table 2.3 shows the composition of Metco 204B-NS (one of its commercial names). This powder includes 7-8wt.% Y_2O_3 and ZrO_2 to balance, which stabilises the tetragonal-prime (t') phase of ZrO_2. Many authors have claimed that this phase is the most desired, among other reasons because it is stable within the operation temperatures of aero-engines (up to about 1400ºC). However, as with Al_2O_3, the thermal cycling lifetime of coatings manufactured from YSZ also appear to diminish because of phase transformations. As explained by Tsipas [106] or Langjahr [107], the stability of the t' phase decreases during prolonged exposure to temperatures over 1200 ºC, decomposing into a cubic (c) and a tetragonal (t) phase. Then, during cooling, the tetragonal phase further transforms into monoclinic (m), which conveys a 4% volume change.

Table 2.3 Summary of 7-8%wt. Yttria-Stabilised Zirconia [34]

7-8%wt. Yttria-Stabilised Zirconia (Metco 204B-NS)	
Chemistry:	$ZrO_2\, 8Y_2O_3$
Manufacture:	Agglomerated & HOSP
Powder composition:	ZrO_2 Balance Y_2O_3 7-8 wt.% $SiO_2 \leq 0.7$ wt.% $TiO_2 \leq 0.2$ wt.% Al_2O_3 0.2 wt.% Fe_2O_3 0.2 wt.% Other Oxides ≤ 1.0 wt.% Monoclinic Phase $\leq \sim 10$ wt.% $Na_2O \leq 0.75$ wt.%
Nom. part. size dist.:	$-75\mu m \leq x \leq 45\mu m$
Morphology:	Spheroidal
Service Temperature:	≤ 1250ºC
Process:	APS or ChamPro^{TM} (LVPS, LPPS,VPS)

There are many options to stabilise the t' phase, but compared to other elements, using Yttria provides additional benefits [62]. For example, thermal cycling lifetime, low conductivity at high temperatures, unusual toughness at high temperature, and resistance to foreign object impact, erosion and corrosion [61]. Clarke *et al.* [61] explains that despite the t' phase not being the toughest of the Zirconia's phases, its toughness remains at high temperatures. In contrast, other phases sustain their properties only up to low to medium temperature. Refer to Clarke *et al.* [61] for further reference; Smialek and Miller [108] or Bakan and Vaßen [68] cover historical development of 7YSZ.

The proportions of impurities in Metco 204B-NS are small, below 1wt. %. As for Metco 105NS and Metco 101NS, little attention seems to have been paid to the implication of this impurity level on low temperature mechanical properties of coatings. At high temperatures, however, these small proportions do seem to influence the phase stability, affecting the coating's

sintering resistance and lifetime. SiO_2 has gathered special interest among impurities, while Al_2O_3 [106, 109, 110] and Fe_2O_3 have also been considered [111]; the latter showing lower detrimental influence than the former [112]. High purity YSZ does seem to show more sintering resistance than low purity YSZ [113]; however, the impact of impurity influence still seems to be under debate.

The powder size of Metco 204B-NS are conventional size, like those of Metco 105NS and Metco 101NS; however, their morphology is different. Metco 204B-NS powders are HOSPs (homogeneous oven spherical powders) [37, p. 18], which are powders that are spherical and porous or even hollow inside (Fig. 2.11). Authors reviewing the spraying process have identified that the structure of coatings sprayed with HOSPs is more consistent than when sprayed with fused and crushed powders [49]. This has been attributed to their geometric homogeneity, as it results in better flowability of the powders (a critical property in thermal spraying processes) and more regular feedstock feed rates [49]. Furthermore, coatings manufactured from HOSP powders seem to possess a higher splat interface density than coatings manufactured through other methods like fusing & crushing, agglomerated/sintered, or Sol-Gel [49]. This results in coatings with lower conductivities [114, 115], lower elastic modulus, and lower resistance to thermal shock [115]. Fused and crushed powders like Metco 105NS and Metco 101NS would result in coatings with higher densities.
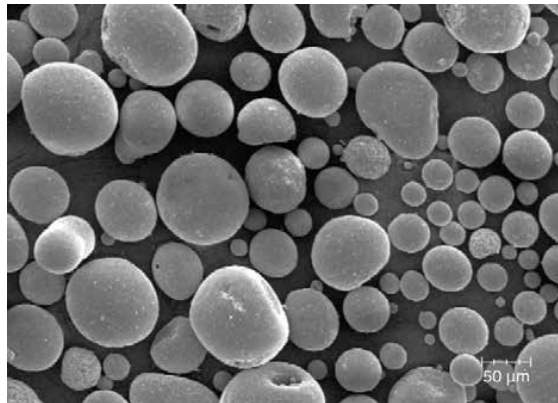
Fig. 2.11 Photomicrography representing a typical Yttria-Stabilised Zirconia powder manufactured through Metco's HOSP process. Source: Metco 204B-NS Data Sheet [34]

As for alumina and titania coatings, using nanosized powders enhances aspects of YSZ coatings. For example, Li *et al.* [116] compared the wear performance of nanostructured and conventional YSZ APS coatings (deposition process was first optimally designed by Li *et al.* [117]) and observed that while having similar friction coefficients, coatings using nanosized powders had a significantly lower wear rate than those using conventional powders. Since conventional knowledge does not seem to apply, authors warn about making conclusions

from recorded forces or any single variable; an individual variable might not make justice to the wear process. Therefore, authors recommend monitoring several variables simultaneously for a more reliable understanding of the process. Regarding the improvement in wear resistance shown by nanostructured coatings, it is generally attributed to the increase in difficulty for cracks to generate and propagate [52, 68, 118, 119], i.e., the enhancement in fracture toughness. Yet, equivalently to what has been discussed previously for nanostructured alumina and titania coatings, there still seems to be some debate about the causes. Wear studies and mechanisms will be further described in Section 2.7.

2.7   Wear studies and general wear mechanisms

So far, this review lacks an in-depth discussion on the wear properties of these APS coatings. To gain a clear insight into their material properties, given the absence of research into their use as abrasives, the review has focused instead on material properties and their use as TBC's. Whilst some wear studies exist, these fall under the field of materials' research and are performed in carefully controlled experimental conditions that might lie far from how the materials are typically used. A collection of conventional wear tests is provided in Table 2.4 to illustrate the disparity in testing conditions.

Table 2.4 Selection of conventional tests, methods and maximum testing speeds

Author	Method	Max Speed ms^{-1} (2 d.p.)
Wang *et al.*[120](1989)	block-on-ring	3.80
Chen *et al.*[121](2002)	block-on-ring	0.42
Tao *et al.*[118](2005)	pin-on-disc	1.08
Chen *et al.*[119](2006)	ball-on-plate (reciprocative)	0.16
Song *et al.*[122](2006)	pin-on-disc	0.13
Song *et al.*[123](2008)	pin-on-disc	0.13
Rico *et al.*[124](2009)	pin-on-disc	0.10
Aruna *et al.*[125](2011)	ball-on-plate (reciprocative)	0.09
Singh *et al.*[126](2011)	pin-on-disc	0.50

Table 2.4 shows aero-engine speeds are far beyond those achieved in conventional wear tests (100 times bigger if engine tip speeds around 400 ms^{-1} are considered). Consequently, experimental results do not seem representative and cannot be faithfully believed. Researchers such as Stringer and Marshall [127] use an equivalent argument to express the need for testing abradable linings under more typical aero-engine conditions. Yet, the wear mechanisms identified in these controlled studies might explain experimental results observed in more severe environments. Hence, a brief review of these wear studies will follow in Section 2.7.1.

2.7.1   Wear studies under materials' research

Wear studies under material's research seem to have addressed several issues: the influence of different molar proportions [125], the effect of powder size [118, 119, 121, 124, 126], and the impact of varying spraying parameters, e.g. critical plasma spray parameter (CPSP) or spraying distance [122, 123]. All these studies appear to follow a similar workflow. These generally evaluate the friction coefficient and the wear rate, and characterise the latter as the volume change over rub length (units: mm^3/m) or over rub length and applied load (units: mm^3/Nm) when the load applied is also a variable. SEM imaging and elemental analysis follows to identify wear mechanisms or phase transformations whenever these are thought relevant. Finally, wear properties are broadly explained through microstructure, material properties, or both.

Considering wear mechanisms, many authors have identified materials with similar friction coefficients but different wear rates. An explanation is provided by Tao *et al.* [118], who (using SEM and x-ray diffraction) identified a lubricating film composed of counterpart material and wear debris. This film appeared more integrated into the nanostructured coatings; hence, appearing more effective at reducing wear. It seems that the debris size is also a critical factor in coating's wear, with an effect comparable to that of three-body abrasive wear [119, 128]. Since it is widely recognised that nanostructured coatings have smaller grains and size defects (e.g. microcracks and pores), Chen *et al.* [119] attributed the wear resistance enhancement to their finer debris. Although abrasive wear dominated, an increase in brittle fracture was reported with load increase. Specially at high loads, conventional coatings showed worse behaviour than nanostructured ones (Fig. 2.12), and it was associated with their inferior cohesion and toughness. Note from the results provided by Chen *et al.* [119] (included in Fig. 2.12) how conventional

(a) Coatings' wear rate   (b) Counterpart's wear rate
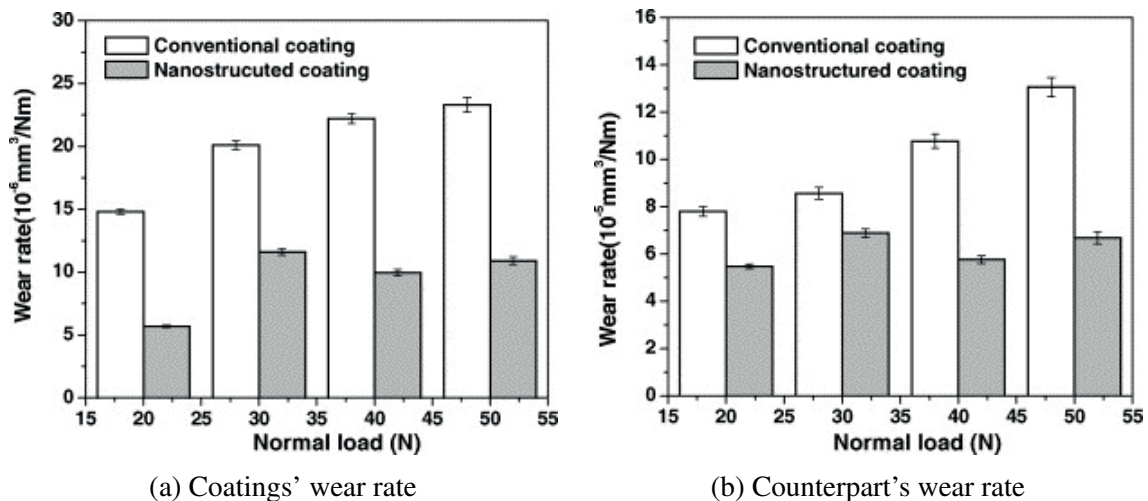
Fig. 2.12 Wear rates variation with load. Source: Chen *et al.* [119]

coatings exhibit higher wear rates, and these correlate with those of the counterpart. Fig. 2.13 is an SEM image of the wear scars and has been included as a visual representation of the wear behaviours. Differences between coating types are clear.

(a) Nanostrucutured coating

(b) Conventional coating
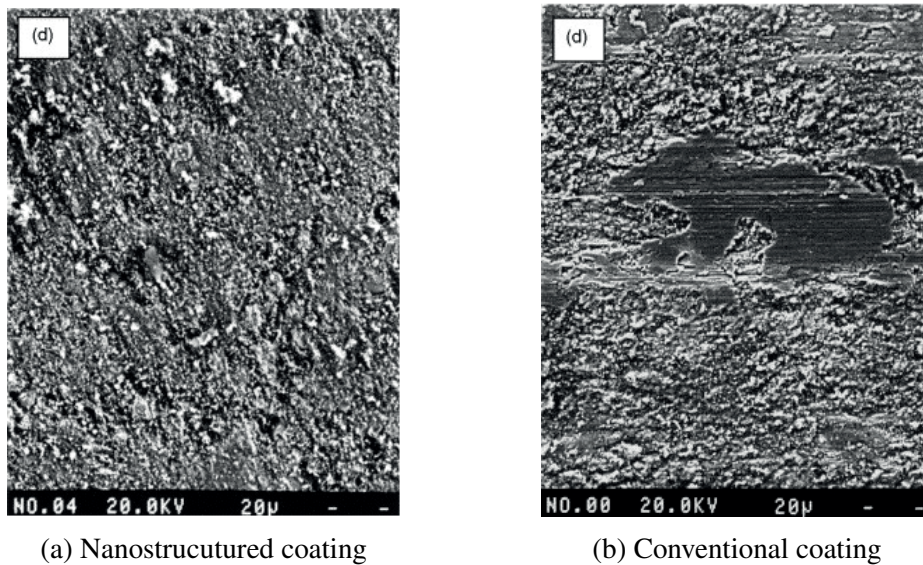
Fig. 2.13 SEM image of wear scars on coatings at 50N load. Adapted from Chen *et al.* [119]

Studies varying load have also reported a transition in wear mechanism from mild to severe [124]. It appears that cracks in coatings do not always propagate parallel to the surface. At lower loads (Fig. 2.14a), cracks generally initiate and propagate parallel to the surface, across splat boundaries, with final delamination of splats. Whereas above a threshold load (Fig. 2.14b), transverse cracks appear starting from the surface that can go into the bond layer, crossing splats and causing complete spallations.

(a)

(b)
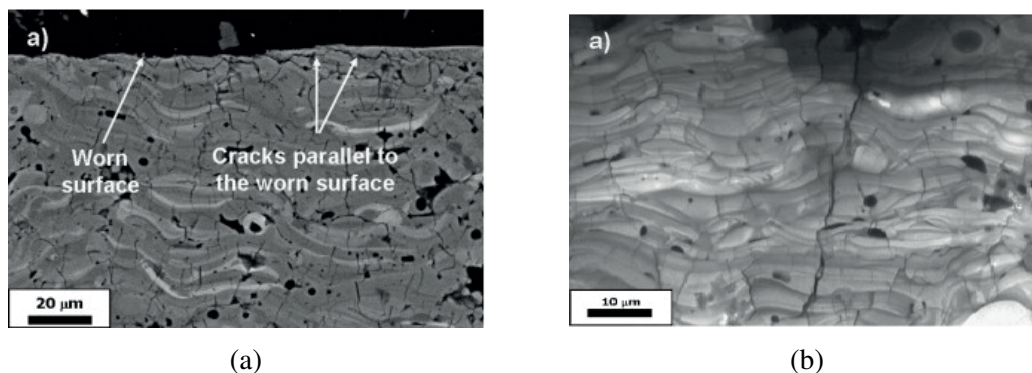
Fig. 2.14 Crack propagation change when transitioning from mild (a) to severe (b) wear. Adapted from Rico *et al.* [124]

It is rare to see papers that do not mention the spraying process within material's research, and it is because it profoundly affects the coatings' properties (Section 2.2), especially if nanostructured powders are used (Section 2.5). The wear of the coatings is not an exception. It is generally acknowledged (e.g. studies cited in Table 2.4 and those in Section 2.5) that if the spraying process is carefully tuned, coatings possess a bi-modal microstructure comprised of soft, partially melted sections within the hard matrix. This structure increases the energy needed for cracks to propagate, namely the material fracture toughness, and it is the apparent cause of the coatings' wear resistance enhancement.

Many authors suggest that conventional knowledge does not always apply to these kinds of coatings. For instance, Song *et al.* [122] showed that hardness and wear resistance generally increases with CPSP (Fig. 2.15). However, the best wear resistance was shown at the lowers hardness. Essentially, the bi-modal structure is lost if the feedstock is completely melted, and cohesion (bond strength) decreases excessively if not melted enough. Wear mechanisms transition from what Song describes as abrasive wear at low CPSP to delamination at high CPSP. Hence, an equilibrium is needed, conventional knowledge does not always apply, and it is essential to use metrics such as CPSP to control the powders' temperatures inside the plasma [122, 123].

(a) Hardness   (b) Wear rate
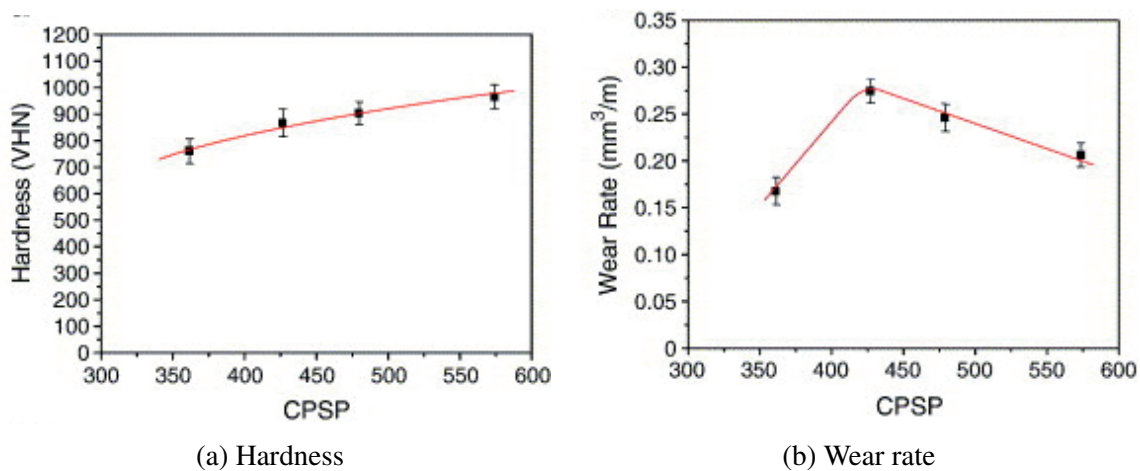
Fig. 2.15 Adapted from Song *et al.* [122]

Similarly, the same process can be understood in terms of the bond strength within the coatings' structure. As discussed earlier in Section 2.2, the coating's structure and mechanical properties are related to the defects on the coatings (e.g. pores and cracks), and the spraying process heavily influences these. Coatings with a lower porosity are generally achieved with a higher ratio of melted particles and are associated with lower roughness, lower friction coefficients, and lower wear rates [129]. Thereby, the opposite is also generally true and introducing some porosity might be an opportunity for abrasive linings.

Whilst not desirable for wear resistance in coatings, these mechanisms might be an opportunity for abrasive ones. Note the similarity with the grinding process where cutting edges are renewed when these become blunt and forces increase above a threshold [130]. The more efficient cutting process happening in a grinding is partly because cutting edges are renewed. This wear mechanism happening in APS coatings thus presents an opportunity for making these coatings more abrasive, and the applied load might be key for inducing different mechanisms. Furthermore, since higher porosity and conventional coatings are generally associated with a higher wear rate, coatings manufactured from conventional powders might be the most desirable; the slight wear of the coatings might mean that the surface is renewed, enhancing abrasive behaviour and removal mechanism.

2.7.2 Alternative sources of information

These materials are currently used in aero-engines as TBCs or wear resistant coatings [4, 62, 68, 72, 131, 132], which implies that they already possess exceptional properties. Consequently, some information can be extracted from these studies. As an example, Cao *et al.* [88] provides a very useful summary to compare between materials based on application, some of which are included in Table 2.5.

Table 2.5 Indicative material properties. Adapted from Cao *et al.* [88]

Property	7-8YSZ	Al_2O_3	$Al_2O_3 + TiO_2$
λ [W m^{-1} K^{-1}]	0.8-1.6 (298-773K) [133]	5.8 (1400 K)	n/a
E [GPa]	40 (293K)	30 (293K)	n/a
α [$\times 10^{-6} K^{-1}$]	10.7 (297-1273K)	9.6 (1273K)	5.56 (1073K)
ν [-]	0.22	0.26	n/a

Meaning of symbols in Table 2.5: λ, Thermal Conductivity; E, Young's modulus; α, Thermal expansion coefficient; ν, Poisson's ratio.

Since TBCs have influenced the development of some abradable linings, studies on these that are conducted under representative conditions can be used as an alternative source of information. Whilst highly limited in number, these studies report that the ceramics' behaviours are not abradable as intended but abrasive instead. Sporer *et al.* [134], for instance, expressed difficulties in manufacturing YSZ abradable linings, and outline their tendency to be abrasive to the metal alloy blades. Accordingly, for YSZ abradable, there is a need to tip the blades with a harder material capable of cutting through. Others like Aussavy *et al.* [56] reached very similar conclusions, also expressing the need to add materials like polyester to enhance the abradability characteristics.

2.8   Summary

This section of the literature review has covered the APS thermal spraying process, recognising the spraying parameters as a critical factor in the manufacturing process. The overall coatings' characteristics seem to rely on the spraying process since it heavily influences the coatings' structure. As for common layered composites, the inter-lamellar shear stresses seem to be a limiting factor that has to be considered in any kind of design. Alternative spraying processes were considered, and the APS seems to be the most appropriate technique mainly because of the defect structure and the flexibility of the process. Considering the APS process, reducing the powder size seems to enhance coatings' properties regardless of the material.

Each ceramic powder was then individually reviewed, showing a morphology difference (apart from the evident chemical difference), which affects the flowability and, thus, the deposition rate's regularity. Chemical impurities within the coating appear to influence chemical stability at high temperatures, although studies do not seem to have considered them for mechanical properties. In terms of spraying parameters and chemical composition, the former seems to dominate on wear. Materials' research on wear seemed to be far from representative; however, these were reviewed, and several wear mechanisms were identified. It appears that at low loads, there is a mechanism of initiation and propagation of cracks along splat boundaries, with final delamination of the splat. Whereas at high loads, cracks propagate through the coating starting from the surface across splats. Wear debris also seemed to have an influence, and again, the spraying process was a highlight.

Opportunities for abrasive linings arrived from the wear mechanisms and porosity introduction, given the similarity with the renewing process of cutting edges in grinding. Finally, abradable linings were sought for alternative observations, which characterised the ceramic materials as abrasive rather than abradable.

Chapter 3

Test arrangements for abrasive contact

Studies on abradable coatings have focused on thermal blade wear, heat partition in the contact, or material rupture [135–137]. Given that abradable materials are far softer and have been designed to be removed, it is unsurprising that the removal mechanisms are fundamentally different to the ones studied herein. However, the research on abradable linings has had meaningful progress (e.g. [138–140]) that is well suited to be also used for improving abrasives mostly given to the fact that historically, these abrasives share the same engine application.

Given the historical background and the similarities that abradable and abrasive linings share, this section will use the more extensive research on abradables to lay the foundation to experiment on abrasives. With this aim, several aspects will be examined. It will first identify a systematic approach for the experimentation on abradables that holds the potential to be transferred to abrasives. This section will then compare the requirements for both types of linings to understand what can be adapted. Subsequently, to gather information on how representative data is produced, general studies on tribology will be reviewed; and to identify how aero-engine conditions have been experimentally recreated, closely related researchers will be examined. The collected information illustrates how to develop and instrument, in other words an experimental test platform, which will be the final topic of this section.

3.1   Current abradable linings and applications

3.1.1   Transferable requirements

The design characteristics that abradable linings need are generally accepted, as can be found from authors such as Novinski [141], Wilson [12] and Borel *et al*. [138]. In essence, these requirements are set by the harsh environmental conditions the linings must support; hence, lining requirements vary depending on the engine section where they are applied.

Notwithstanding the differences within engine sections, abradable linings are directly exposed to the fast-moving airstream that carries particles and other fluids; thus, they are require to have sufficient erosive and corrosive resistance. Furthermore, they require good thermal shock and thermal cycling resistance since they will face changing temperature through the engine's operation. Also, they should be abradable enough to be cut efficiently by a blade without damaging it and leaving a good surface finish on the surface to minimise the aerodynamic losses.

Given that abrasive linings are used in a very similar application, it seems reasonable transferring some of the requirements from abradable linings and adapting others. The requirements for abrasive lining should therefore be:

- **Properties of abradable linings.** Withstand erosion and corrosion, need to cope with oxidation in the presence of high-temperature gasses, and must have good thermal shock behaviour and resist thermal cycling.

- **Properties opposite to abradable linings.** Have to be abrasive enough to efficiently cut through the blade without damaging either the coating or the blade, leaving a good finish on the blade's surface to minimise the aerodynamic losses.

3.1.2   The experimental research process for abradable linings

In terms of experimental research, Borel *et al.* [138] studied the wear mechanisms occurring in abradable seals and, as part of their research, they defined a four-step systematic approach for studying and developing abradable linings. A flowchart summarising the proposed steps is included in Fig. 3.1. It is worth noting that it is an iterative process developed for abradables.
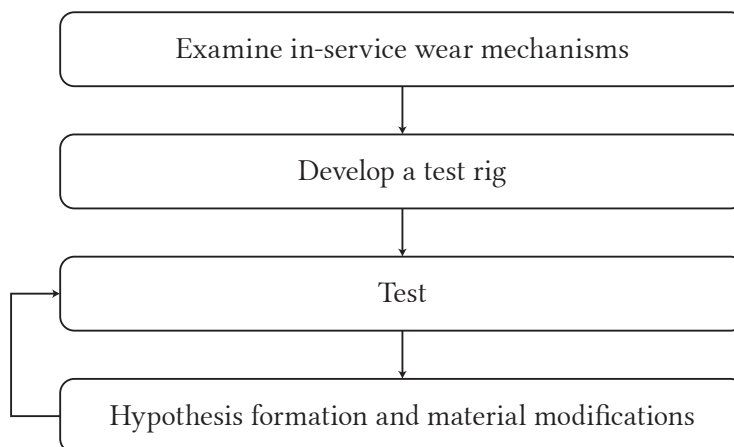
Fig. 3.1 Four-step systematic approach suggested by Borel *et al.* [138] for the study and development of abradables.

Borel *et al*. [138] describes that engine components are commonly analysed during the early stages of research to identify the different in-service wear mechanisms. Usually, a rig is then developed to test the coatings in a more controlled laboratory environment. In this setup, experimental variables are widely varied to simulate the service conditions. As a result, wear maps are created, and the experimental wear mechanisms are linked with the materials' properties, microstructure, and in-service behaviours, thereby creating a hypothesis that explains the results. Finally, findings are placed into practice to design new materials, and the process of testing and designing is repeated iteratively.

Many other experimental researchers studying abradable linings seem to follow this four-step approach. For instance, see Stringer and Marshall [127], Bounazef *et al.* [142], Gao *et al.* [143], Xue *et al.* [144], or Taylor *et al.* [145]. Notwithstanding that the research on abradable linings is less relevant, this four-step systematic approach seems generic for investigating high-speed contacts under representative conditions; hence, it does not seem unreasonable to apply it for developing abrasive linings.

3.1.3   General requirements for a testing platform studying wear

Hutchings and Shipway [146, p. 109] present general features to consider when carrying a laboratory investigation on wear. On this matter, they report several things that must be considered: the materials in contact, component's shape and dimensions (i.e. shape and general dimensions), the test loads and induced contact stresses, the relative contact speeds, and the testing environment. Note that these variables are very similar to those presented earlier in Section 2.7.1 when addressing wear studies under materials' research studying TBCs.

They further provide a generalised definition for wear rate in terms of a *measure of wear* (*Wr*) and *exposure to wear* (*Ex*), defining *wear rate* as *dWr/dEx* [146, p. 369]. They propose volume and mass as typical wear measures, warning that densities should be considered if using mass for comparing the wear rate among different materials. Experimentally this translates into interrupting the test at different stages to record the variation in a specimen's variable (e.g. mass or volume change) or, alternatively, inferring specimens' wear from a dimensional change that is constantly monitored (e.g. with a displacement sensor) [146, p. 113]. Regarding the term *exposure to wear*, they define it as any form of quantifying the duration of the wear conditions to which the materials are exposed [146, p. 369]. They highlight some variables that not only characterise the exposure to wear but also describe the wear severity. These are, for instance: sliding distance, the mass of abrasive particles impinged (probably a variable only used for erosive wear), time, and frictional energy dissipated.

The requirements for building a rig that studies wear can be inferred from these variables, and a conceptual map has been designed to summarise them (Fig. 3.2).
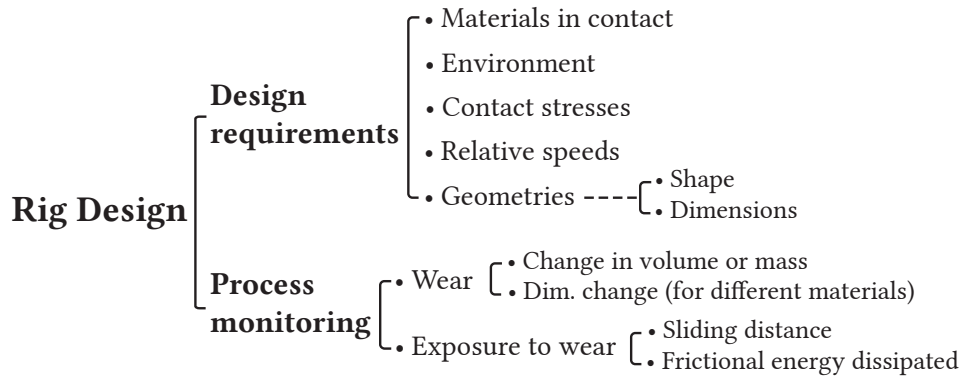
Fig. 3.2 Conceptual map of rig requirements

3.1.4   Review of testing platforms studying abradable linings

Several experimental rigs designed to study abradable linings have been collected in Table 3.1. From these, insight into how aero-engine conditions have been accomplished and which variables are more significant can be obtained.

Table 3.1 Several experimental rigs studying abradable linings with their monitored variables

Experimental rig	Measured Variables				Controlled Variables			
	F	T	D	O	V_t	T	I.R	Atm
Pratt and Whitney (1982) [135]	X	X		X	300	600	4.00	No
Washington (1983) [147]	X	X	–	–	100	–	0.15	No
Sulzer (1989) [134, 138]	X	X	–	–	500	1200	10	No
Ohio State (2005) [148–150]	X	–	–	–	400	–	406	No
Praxair (2007) [145]	X	X	X	–	152	–	10	No
IAR (2008) [151, 152]	X	X		X	425	–	1.14	No
CAS (2012) [143, 144, 153–155]	X	X	X	–	350	1200	5	No
Sheffield (2012) [127, 139, 140, 156]	X	X	X	X	200	–	5.70	No
FAL (2013) [157]	X	–	–	X	100	–	500	No
Snecma (2015) [136, 158]	X	X	–	X	400	–	n/a	Yes
Zheang (2016) [159, 160]	X	X	–	–	520	1200	6.70	No
Karlsruhe (2016) [161, 162]	X	X	–	–	165	–	n/a	No

The abbreviations in Table 3.1 mean: *F* Force; *T* Temperature (C°); *D* Debris collection; *O* Optical assessment of wear; V_t Maximum tangential speed (m/s); *I.R* Maximum incursion rate (μm/rev); *Atm* Atmosphere conditions

Based on the general rig requirements discussed earlier (Section 3.1.3), it seems that replicating the actual contact conditions is essential for a test rig to be representative. Test platforms take a variety of arrangements but the one designed by Stringer and Marshall [127] shows what seems to be the most common arrangement for studying abradable linings; a rotating blade and static abradable (Fig. 3.3).
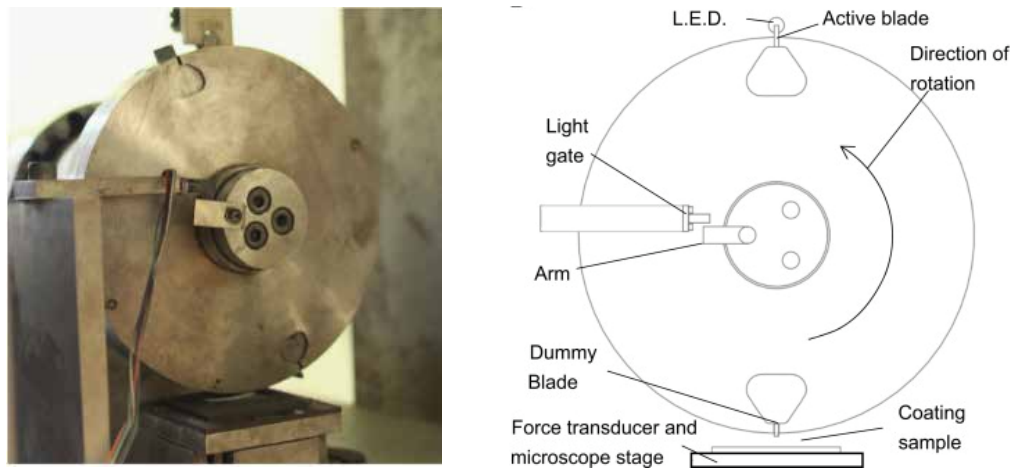
Fig. 3.3 Simplified test platform showing a rotating blade and a static abradable [140]

From Table 3.1 and from what is commented by Stringer and Marshall [127], the most representative conditions reside among full-scale rigs manufactured from aero-engine parts or out of service components. These rigs are inherently complex, which increase the difficulty of understanding the tribological system. The learning process is further constrained as installing the appropriate instrumentation also becomes a challenge [127]. Thus why researcher report that full-scale rigs compromise speed and depth of research for gaining representativity [127].

Simplified test platforms are an alternative to full-scale rigs that yield benefits from not fully recreate aero-engine conditions. Relaxing constraints allow them to be highly instrumented and gather high amounts of data. Furthermore, permitting to explore aspects that cannot be easily done with complex experimental arrangements (e.g. the isolation of variables for investigating their independent response). Thus, simplified test platforms build knowledge faster. The drawback, they produce data with a lower level of veracity [127].

Base on the experimental rigs, it seems that some environmental conditions in aero-engines can be neglected due to the relatively high speeds of the experiment. Laverty [135], for example, justifies the use of ambient testing conditions, arguing that the contact temperature rapidly outweighs it. From the aforementioned test rigs (Table 3.1), none fully replicate the aero-engine environmental conditions, although some can introduce a temperature change or vacuum conditions [135, 143, 158].

It follows that from simplified and full-scale test platforms, the former seems to be sufficiently representative. For instance, that produced by Stringer and Marshall [127] manages to achieve the broad spectrum of wear mechanisms observed in both aero-engines and the more representative full-scale rigs without simulating temperature or atmospheric conditions and only reaching 200 m/s. The use of simplified testing platforms is founded on what many researchers have historically argued, namely that in wear, the effects of incursion rate (Fig. 3.4) and rub length dominate over the effect of speed and other parameters like atmospheric conditions [127, 135]. The widespread tribological mechanisms achieved in simplified test platforms strengthen these conclusions. Hence, some researchers first decide to undertake fast and in-depth research at the expense of some representativity and then use full-scale test platforms to validate conclusions.
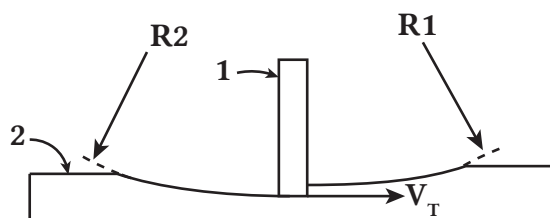
Fig. 3.4 Schematic diagram showing the side view a blade contacting an abradable to illustrate incursion. Labels: (1) Blade/cutting tool; (2) Abradable; (R2-R1) Incursion, radius difference, or step size; (Vt) Tangential speed.

Experimental researchers on abradable linings generally vary incursion and rub length, given their influence. In essence, these variables appear to be the *exposure* and *severity of wear* previously mentioned in Section 3.1.3, and it is not uncommon to see researchers using them to compare the performance among systems (e.g. different materials, contact geometries, or contact speeds).

Concerning the procedures that researchers in the field carry out, these do not differ from the generalizations made by Hutchings and Shipway (Section 3.1.3). The wear process is generally assessed by monitoring the contact forces and temperatures in a continuous manner without interrupting the test. Some more instrumented rigs also include optical measurement techniques such as thermal [161], video [135], or optical cameras [127, 139, 140, 156, 163]. These are normally used to validate a hypothesis but have also led to groundbreaking research [127]. Qualitative data is typically achieved post-test (postmortem) to support the observations and link the tribological behaviour with the microstructure. Among many postmortem techniques, SEM and XRD microscopy techniques seem to be very common to investigate material transfer and wear mechanisms. For instance, see Fig. 3.5.
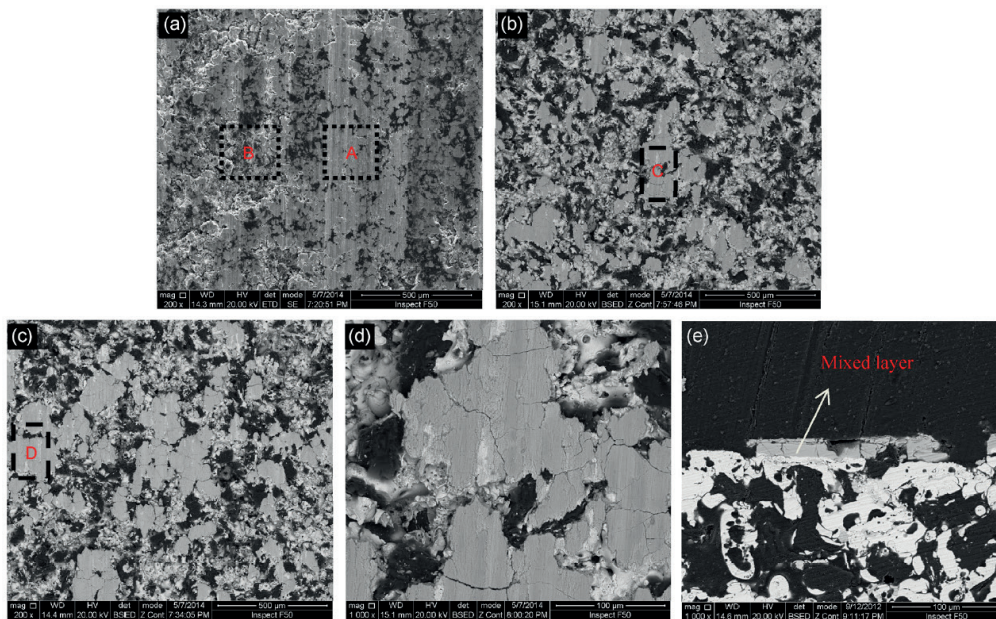
Fig. 3.5 Identification of different rub mechanisms with SEM. Extracted from Gao *et al.* [153]

3.1.5 Conclusions

This section intended to cover methods and requirements for the experimentation of abrasives; instead, it has gathered relevant information on abradable linings, given the absence of such studies. In addition, general tribological studies have also proven to be very valuable in the absence of specific research concerning abrasive linings.

The requirements for abradable linings were first discussed and adapted to those that an abrasive coating would need. The differences being that an abrasive would need to cut efficiently through a blade rather than an abradable. The review then identified a systematic approach for studying abradables, which is generally followed by experimental researchers and appears applicable for researching abrasive linings. This process is a four-step iterative procedure and entails examining in-service wear mechanisms, developing a testing platform, testing, and creating a hypothesis. Materials can then be modified and re-tested iteratively.

A slight departure from abradables identified the general requirements for developing a testing platform that studies wear. These highlighted the need for recreating contact conditions and identified several variables commonly employed for evaluating wear and exposure to wear. In addition, differences in approaches were noted as some allow to acquire data during the test and others require interruptions.

From general needs, the focus was then narrowed by investigating the testing platforms that study abradable linings. These revealed that adopting fully representative aero-engine conditions embrace many issues and researchers generally reach a compromise. The devel-

opment of simplified test platforms are the result and have successfully recreated a broad range of wear mechanisms. Among many strengths, these platforms are more flexible for installing appropriate instrumentation, allowing for fast and in-depth studies while still being representative.

Reviewing abradable linings revealed that the systems are complex, and many variables are required to recreate the contact. For abradable linings, these may be summarised in four groups: the study of the materials in contact with their material properties, the contact stresses, the geometries in contact, and the relative speeds. It appears that a fifth variable, environmental conditions, can be dropped from consideration because of the relatively high-speed contact. All these variables form part of recreating the contact conditions and should therefore be considered when designing an experiment.

Concerning the variables, it does not sound unreasonable to evaluate abrasive linings with the methods used for abradables, i.e., through changing incursion rate, rub length, and contact speeds, for different materials and geometries. However, evidence suggests that the arrangement used for abradable linings should be reversed to replicate the abrasive contact; the general rotating blade and static abradable should therefore be a rotating abrasive and a static blade.

Finally, it was found that researchers in the field frequently evaluate wear through contact forces and temperature and its severity from the recording of time and other variables that, after being post-processed, allow to obtain identifiers like rub-length or rub-energy (or a newly defined one). Conclusions will be commonly drawn at this stage, which will be supported by observations in the macrostructure and microstructure of the materials, helping understand the contact's mechanical and chemical nature and the relation between both. The value of assessing wear continuously during a test rather than only post-test was also revealed. Hence, a testing platform that allows the implementation of such experimental methods is highly desirable.

All things considered, one might support the use of simplified test platforms, the reverse contact used for abradable linings, and the same variables. In addition, more representative rigs can be reserved for validating conclusions, an approach that proves high industrial confidence and reduces development time and costs.

3.2   Recreating the contact

The previous Section 3.1.3 has highlighted the importance of recreating the contact conditions for any type of wear study. Hence, this is the first task that this work has undertaken. To do so, the current rig (which the group has been using for studying abradable linings [127]) has been examined and evaluated, and aspects have been changed to essentially reproduce the more

continuous contact that the abrasive-rotor/stator blade assembly experiences compared to the more well-known discontinuous contact of the conventional rotor-blade/abradable lining.

More specifically, the changes undertaken to reconfigure the rig are summarised in Fig. 3.6, where the static abradable is now abrasive and is sprayed on a rotating substrate (*label 3* of Fig. 3.6), and the blade which was held by the rotor now is static and held by a load cell (respectively *labels 2* and *1* from Fig. 3.6). The following subsections will cover these changes where Section 3.2.1 will describe the design of the substrate, Section 3.2.2 the design of tooling for spraying the ceramic coating, Section 3.2.3 the design of the mandrel (i.e., the clamping tool now used to transfer the rotating movement to the substrate and ceramic), and Section 3.2.4 the design of the blade sample; the use of a conventional load cell instead of piezoelectric force sensor will be covered in the next chapter which addresses the rig instrumentation.
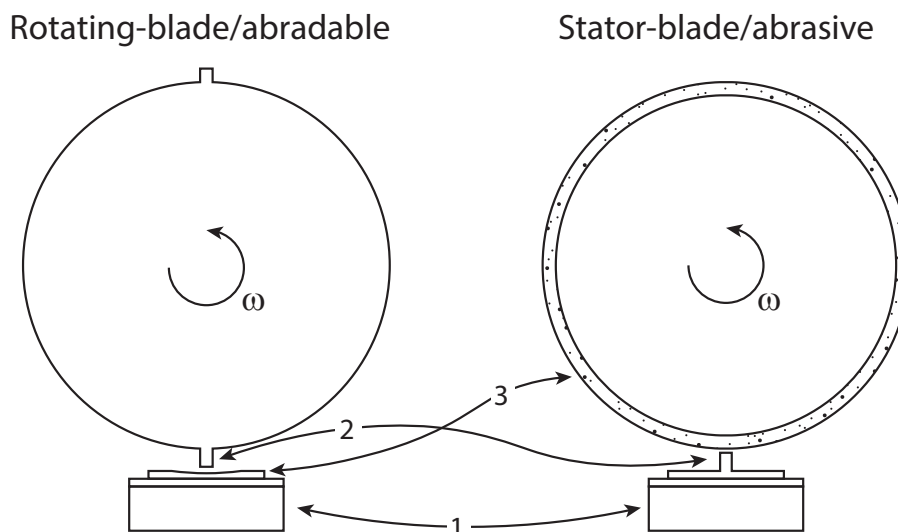
Fig. 3.6 Rig re-design from rotating-blade/abradable to stator-blade/abrasive. Labels: (1) Force sensor; (2) Blade sample; (3) Lining sample.

Other aspects like the electrical spindle (GMN Paul Müller Industrie GmbH & Co. KG, type HSP 120g - 21000/9) and the vertical micrometer (Sigma Koki, type OSMS80-20ZF-0B) complete the rig and have remained unchanged between configurations. This is because despite the abradable contact being fundamentally different to the one addressed herein, the concept of closure rates (i.e., the rate by which a lining approaches a blade or what is experimentally named incursion rate [2]) remain fundamentally equal for both abradable and abrasive contacts and hence the equipment can still be used. In essence neither the stage nor the spindle have been change with respect to the abradable setup described by Stringer and Marshall [127].

---

[2]The vertical displacement of the micrometrical stage per revolution of the spindle

However, changes in the coding of the stage and its controller have been introduced and a brief description is therefore included in Section 3.2.5. The full outline of the rig is then given in Section 3.2.6.

3.2.1 Design of the rotating substrate for ceramic linings

Stresses generated in the contact was highlighted as one of the factors that had to be considered. Unevenly distributed stresses are especially undesirable from a design point of view (Section 2.3) as these can lead to major failure mechanisms such as delamination. Furthermore, stresses generated on the ceramic coatings have a fundamental role in the tribological system and their overall failure mechanisms (Section 2.7.1). Thus, nonuniform stresses are also undesirable from a research point of view and must be accounted for, otherwise they can lead to misleading conclusions. Any design must therefore induce a uniform stress distribution along the coating's entire surface and should sustain them within the envelope of running conditions.

The substrates were required: to be economically accessible (probably disposable or reusable); to have an easy but safe clamping that provided uniform stresses; that the outer diameter reaches at least 200 m/s at 20 000 rpm; and that stresses do not exceed the yield point of the base material at maximum speed. After many considerations, as outlined in the following section, the design of the rotating samples is as displayed in Fig. 3.7; a ring with an outer diameter of 195 mm, an inner diameter of 173 mm, and a width of 22 mm.
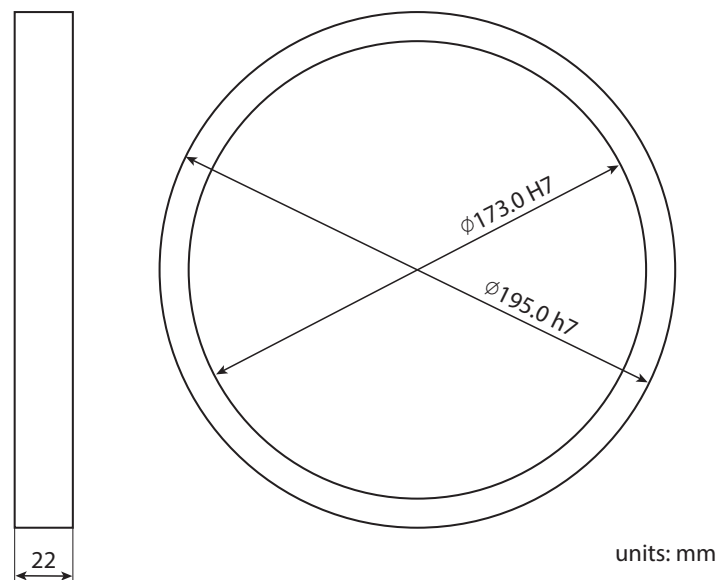
Fig. 3.7 Sample design. Sample fabrication: Kannect Precision Services Ltd.

Two additional restrictions were set on the design. The plasma spraying process introduces internal stresses that make the samples buckle; thus, at least a 4 mm wall thickness was needed.

The precision machining company then defined the actual 11 mm shown in Fig. 3.7 to ease the manufacturing process and minimise the production costs. The outer diameter had to achieve a tangential speed of 200 m/s at the maximum speed of the spindle (20 000 rpm). Any diameter larger than 191.08 mm (Equation (3.1)) would fulfil this requirement.

$$v = \omega \times r \tag{3.1}$$

The final dimension of 195 mm was chosen from the closest available tubing, minimising expenses and waste material. Given the dimensions, the manufacturing process starts with a long tube as raw material, turns the outer and inner diameter, and finally slices the tube into 22 mm thick rings (i.e., the samples). The manufacturing procedure requires careful consideration as it has a direct effect on the resulting tolerances, meaning manufacturing errors like out-of-roundness and concentricity. Aside from being a safety hazard as it contributes to unbalance and vibrations, these will affect the recorded forces, which will be cyclical and will peak when a high spot of the sample coincides with the side of the unbalance, and will reach a minimum when a low spot in the sample is opposite to the unbalance. With the selected manufacturing procedure, an entire batch of samples can be manufactured with a single clamping operation to the lathe, reducing manufacturing operations and errors.

In considering manufacturing materials for experimentation, it is important that these withstand operational stresses. With the defined running conditions and sample geometries, Lamé's equations can be used to explain the resulting stresses on a rotating body. From Shigley [164], the stresses developed along the wall of a rotating ring are calculated as follows:

$$\sigma_t = \rho\, \omega^2 \left(\frac{3+\nu}{8}\right) \left(r_i^2 + r_o^2 + \frac{r_i^2\, r_o^2}{r^2} - \frac{1+3\nu}{3+\nu} r^2\right) \tag{3.2}$$

$$\sigma_r = \rho\, \omega^2 \left(\frac{3+\nu}{8}\right) \left(r_i^2 + r_o^2 - \frac{r_i^2\, r_o^2}{r^2} - r^2\right) \tag{3.3}$$

where r is the radius to the stress element under consideration, σ_r and σ_t are respectively the radial and tangential stresses, r_i and r_o are the internal and external radius, ρ is density, ω is angular velocity, and ν is poisson coefficient.

From Equations (3.2) and (3.3), the resulting stresses are proportional to the materials' density (ρ), and there is no radial stress at the internal and external surfaces (at $r = r_o$ and $r = r_i$, $\sigma_r = 0$). Consequently, at these locations, von Mises yield stress is equivalent to tangential stresses (Equation (3.4)) [165], and the highest stresses arise at the internal surface.

$$\sigma_t^2 - \sigma_t\, \sigma_r + \sigma_r^2 = \sigma_{VM}^2 \xrightarrow{r=[r_i,r_o]} \sigma_{VM} = \sigma_t \tag{3.4}$$

Initially, *Mild Steel 4140* and *Aluminium 6082 T6* were considered as, being widely used for piping, they have a suitable raw geometry. Moreover, as shown by substituting in Equation (3.2) the density and the Poisson Coefficient of Aluminium and Steel, neither reach yield conditions under experimental situations (Equation (3.5)). Yet, these results show that not all aluminium and steel alloys are suitable, highlighting the importance of checking the stresses at the inner surface of the samples before using a certain material as substrate.

$$\rho_{Al} = 2700 \text{ kg/m}^3 \; ; \; \nu_{Al} = 0.35 \quad \longrightarrow \quad \sigma_{VM} = 132.5 \text{ MPa}$$
$$\rho_S = 7900 \text{ kg/m}^3 \; ; \; \nu_S = 0.3 \quad \longrightarrow \quad \sigma_{VM} = 386.5 \text{ MPa}$$

(3.5)

A major issue has been considered before selecting a material, namely the unbalance of the samples. A defective process in either the manufacturing of the substrate or the deposition of the coating can lead to an unbalanced sample, which is a hazard, especially at high rotational speeds. Before batch manufacturing (that reduces costs), a small experiment is therefore desirable. Twelve samples were manufactured to carry out a two-level full factorial design with three repeats. This was inclusive of two abrasive materials and two substrates, i.e., Alumina and Yttria-Stabilised Zirconia, Aluminium and Steel. The experimentation process was carried out in two steps: first, tolerances were evaluated and then overall vibrations in the rig.

Concerning tolerances, each sample's internal diameter was measured in 12 different places with a micrometre. A summary is included in Table 3.2, where the categorical variables are the sample material (aluminium or steel) and the coating material (alumina or YSZ). Table 3.2 showed that the internal diameter was very close to the one stated in the drawings (173 mm). Furthermore, the standard deviation of aluminium samples appeared higher than that manufactured from steel, showing that higher tolerance consistency is achieved with the latter.

Table 3.2 Descriptive statistics for the inner diameter (ID) of the rings

Substrate	Coating	Mean ID[mm]	Std. Deviation	N. samples
Steel	105-NS	172.983	0.006	3
	204B-NS	172.977	0.003	3
	Total	172.980	**0.005**	6
Aluminium	105-NS	173.008	0.014	3
	204B-NS	173.006	0.020	3
	Total	173.007	**0.015**	6
Total	105-NS	172.995	0.017	6
	204B-NS	172.992	0.021	6
	Total	172.993	0.018	12

The levels of each variable (coatings and substrates) was then plotted (Fig. 3.8) to illustrate their effect on the end tolerances. As can already be seen, samples with different substrates hold bigger differences, regardless of the applied coating. A Least Significant Difference (LSD) test was then performed to evidence this observation. Given the variables, this test compares the difference between all possible pairs and, by rejecting or accepting the null hypothesis, concludes if the change is significant.
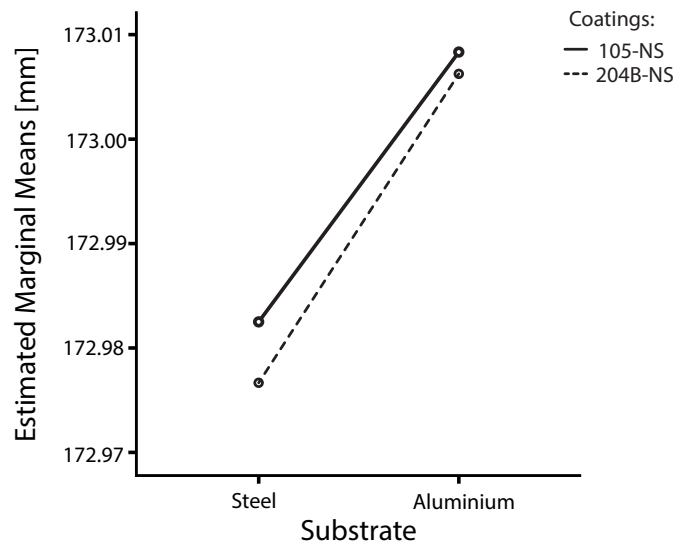
Fig. 3.8 Interaction plot between coatings and substrates

Table 3.4 and Table 3.3 show that changing substrates has a significant effect, whereas changing coating material has not. Furthermore, the standard deviation (Table 3.2) of aluminium is higher than that of steel, suggesting that the effects are different. As a result, the manufacturer was asked to verify tolerances after each operation for both materials, identifying differences only upon segmenting the tubes into rings (the last operation). This observation presents evidence for internal stresses in the raw material (due to the cold rolling process that yields it) and can explain why aluminium samples are more affected than steel ones.

Table 3.3 Pairwise comparison of coatings

(I) Coating	(J) Coating	Mean Diff. (I-J)	Std. Error	Sig.[a]	95% Confidence Interval for Difference[a]	
					Lower Bound	Upper Bound
105-NS	204B-NS	0.004	0.007	**0.6**	-0.13	0.012
204B-NS	105-NS	-0.004	0.007	**0.6**	-0.021	0.013

Based on estimated marginal means
a.Adjustment multiple comparisons: Bonferroni

Table 3.4 Pairwise comparison of substrates

(I) Substrate	(J) Substrate	Mean Diff. (I-J)	Std. Error	Sig.[b]	95% Confidence Interval for Difference[b]	
					Lower Bound	Upper Bound
Steel	Aluminium	-0.028*	0.007	**0.005**	-0.044	-0.011
Aluminium	Steel	0.028*	0.007	**0.005**	0.011	0.044

Based on estimated marginal means

*. The mean difference is significant at the 0.05 level.

b. Adjustment multiple comparisons: Bonferroni

It might not be unreasonable to select steel samples, given the higher consistency of tolerances. However, it was concluded that sample tolerances were not enough for discriminating between materials; the vibration level was the deciding factor. Whilst aluminium samples could run safely, the vibration levels for steel samples presented a safety hazard, not being even possible to collect data. This behaviour is likely due to how heavier loads displace the natural frequency towards lower frequencies (i.e., $\omega_0 = (k/m)^{1/2}$, with k and m referring respectively to the mass and stiffness of the full rig), hence, why aluminium samples are more benevolent to unbalance. An alternate explanation is that a manufacturing error in steel samples represents a higher unbalance than for aluminium (given the density differences). All in all, aluminium samples presented more benefits and steel samples were dropped from consideration.

Concerning the samples' cross-sectional area, it required to generate a uniform stress state. Accordingly, a rectangular cross-section was selected. The importance of selecting geometry will be illustrated by examining the stresses in a profile with a slight taper of 5º (Fig. 3.9). This example has been chosen because tapers are widely used in the manufacturing industry for their auto-centering properties. Nevertheless, it will be shown how a taper introduces non-uniform stresses and is not the most suitable profile for the samples.

As presented earlier, the stresses on the profile can be investigated with Equations (3.2) and (3.3). These equations show that radial stresses on the surface would equal zero ($\sigma_{rA'} = \sigma_{rA} = \sigma_{rB'} = \sigma_{rB} = 0$), and tangential stresses would be lower at point A' since the ring is thicker in that location. Substituting now the radius ($r = r_o = 195/2$ mm) and, e.g., the properties of steel ($v = 0.3 \,; \rho = 7900$ kg/m^3), the von Misses stresses can be calculated at point A' and A. Fig. 3.9 illustrates the non-uniform stress distribution along the cross-sectional area, and Equation (3.6) shows the numerical results specifically at points A' and A.

$$\sigma_{tA} = 330.96 \text{ MPa} \quad | \quad \sigma_{tA'} = 319.51 \text{ MPa}$$
$$\sigma_{tA} = 1.0358 \, \sigma_{tA'}$$

(3.6)
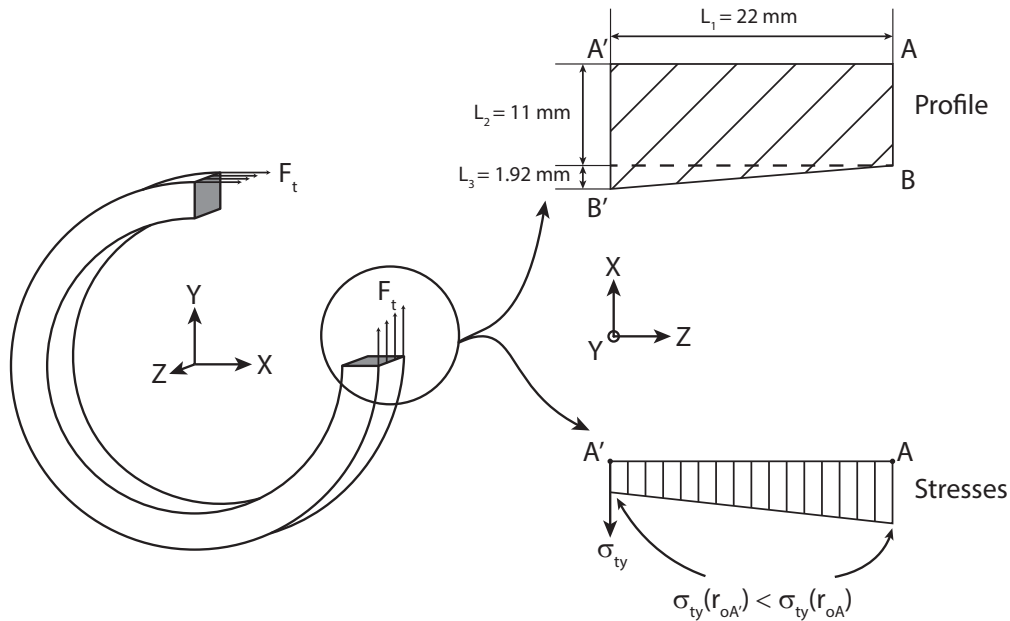
Fig. 3.9 Maximum stresses on a tapered sample

Based on these results, a tapered sample equates to an uneven stress distribution and radial deformations along the axial direction; thus, different contact conditions along the same surface and possibly non-representative or difficult-to-differentiate wear mechanisms. Thereby, the importance of selecting an appropriate geometry for the profile. As such, the aforementioned aluminium samples design was selected.

3.2.2   Design of thermal spraying tooling

An uncomplicated way to coat circular components is by rotating them while displacing the spraying gun axially. Such a process can be used for the ring samples used herein (Section 3.2.1) by mounting them on a turntable. Accordingly, spraying tooling was designed hand in hand with Rolls-Royce's technical experts to ease spraying, enhance productivity, and ensure consistency between different specimens.

The resulting product, a reusable mould (Gerard Poly Mouldings), has a modular design that allows samples to be sprayed in stacks rather than individually (Fig 3.10). The moulds were required to provide a separation of 2-5 mm between samples and leave a free-standing outer surface. Such separation between samples is required to ensure that coatings are applied uniformly, else material accumulates at the edges. The stack is secured to the top of the turntable using a shaft that goes through. The thermal spraying parameters are included as experimental variables; these will be addressed in the coming experimental chapters.
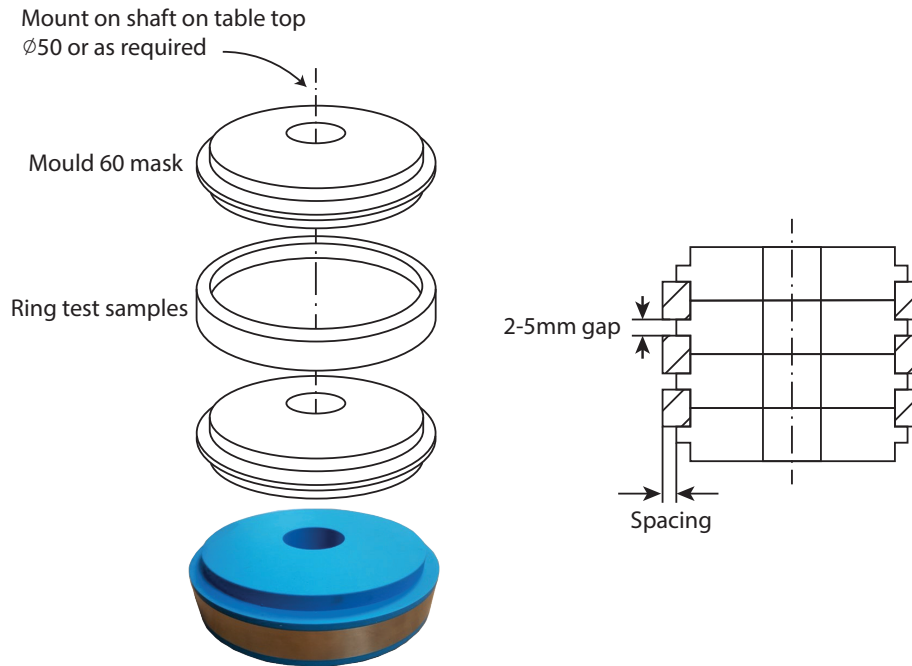
Fig. 3.10 Spraying tooling designed for fitting a 173 mm ID samples. Figure includes a individual unit and its assembly. Manufacturer: Gerard Poly Mouldings

3.2.3   Design of clamping tool

It is worth noting that the samples have been jointly designed with their clamping system, although explained separately to ease the narrative. It is because of the clamping system that the samples' design can be simple, allowing a straightforward and thus economic manufacturing process with consistent tolerances and no unexpected unbalances. Furthermore, the substrates and their clamping system work as an assembly (they are interdependent). Thus, both must be jointly designed because they affect the coating's stresses.

An expandable mandrel has been the chosen solution for clamping the samples. Equivalently to the disc used when testing abradables, the mandrel will be driven by the spindle. The mandrel's design is presented in Fig. 3.11, which is the design of Craftsman Tools Ltd with in-house modifications. The design comprises a shaft (HSK-C40), a hardened steel (SAE-8620) base component with a 5º taper, and an anodised aluminium sub-assembly that carries an expandable steel (EN47) sleeve with a tolerance of 173c8 (172.77-172.71 mm).

The base component is constrained to the shaft with six M5 high tensile screws (Grade 12.9, 1200 MPa max tensile strength, socket cap) and stainless steel wedge-locking washers (Nord-Lock Ltd, series NL5ss-254) that prevent these from untightening with vibrations. The sleeve sub-assembly is located on the same shaft and only has axial freedom of movement; rotation has been restrained with three dowels that fit into the base component. Finally, the

assembly is complete with an M10 nut that screws at the end of the shaft. This nut controls the axial position of the sleeve and prevents the components from disassembling. The thread direction has been chosen so that the nut locks against the direction of rotation. In this way, it would not untighten due to inertial forces. Note that the nut's helix would prevent the sleeve from being square in the assembly, and it is a slight overhang of the shaft that enforces the correct position regardless of the force introduced by the nut. These three main components are displayed in Fig. 3.11.
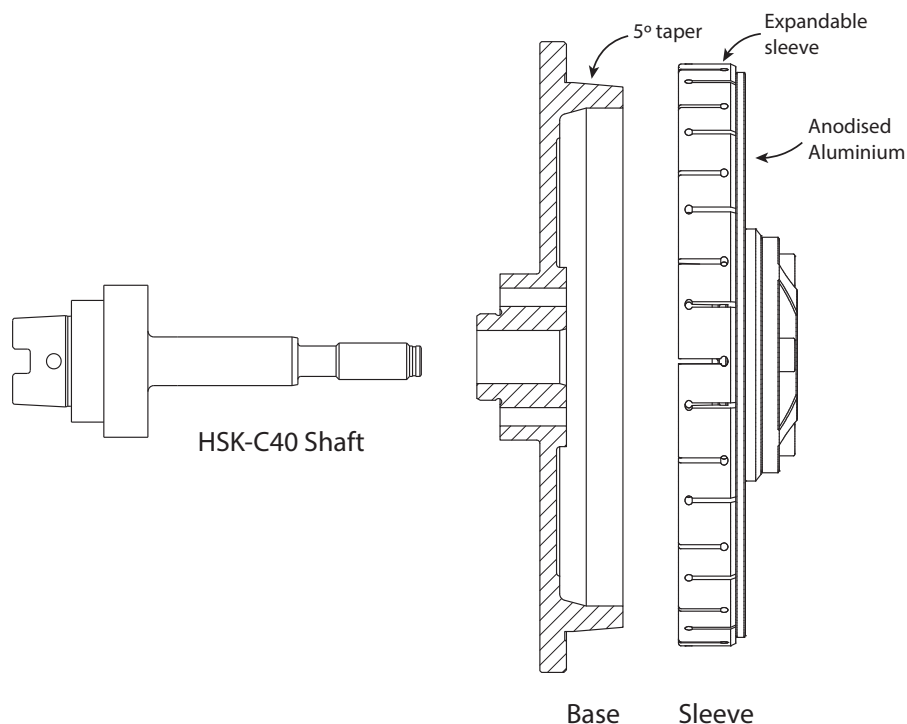
Fig. 3.11 Expandable mandrel main components

The process of clamping a sample then becomes simple: when a torque is applied to the nut, the sleeve sub-assembly slides along the shaft and the sleeve expands because of the 5° taper on the base component. A key aspect of this design was using the same shaft to connect all the components since it granted the complete assembly to always remain square.

The unbalance of samples has been an unknown during the design period and has influenced this design since unbalanced rotors carry a well-known risk. Accordingly, the clamping system was conceived with a modular design that could accommodate an active auto-balancing system (Hofmann Mess- und Auswuchttechnik GmbH & Co. KG, system AB9000, type 51). Notice the difference in shaft length between the latest version of the mandrel (Fig. 3.11) and the initial design displayed in Fig. 3.12.
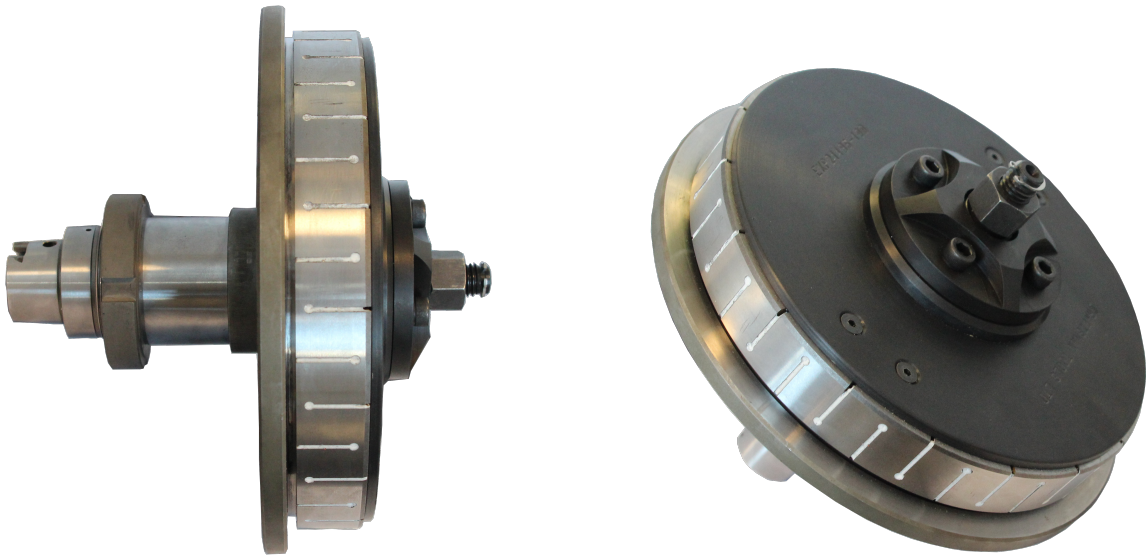
Fig. 3.12 Expandable mandrel for clamping the rotating samples

Eventually, the balancing system was neither needed nor tested because a shorter shaft (Fig. 3.11) was sufficient to keep vibrations within an acceptable level. Nevertheless, the active auto-balancing system is still a feasible option if the samples were to have a higher unbalance (that go beyond safe limits) or if a more precise contact was wanted. Refer to Appendix B for the explanation of the system and design. Aside from risks, it is also worth highlighting the impact of a tool like an auto-balancing system on the recorded forces. These would show a reduction in fluctuations related to the unbalance and also reduce the impact of manufacturing errors such as out-of-roundness and concentricity; as mentioned earlier, the results of a more precise contact.

3.2.4   Design of blade

The blade samples' design (included in included in Fig. 3.13) is a simplification of what colleagues are using in abradable experiments; see Stringer and Marshall [127]. These are 2 mm thick 10x19 mm rectangular plates that are manufactured through laser cutting. With this manufacturing process and the chosen geometries, specimens can be arranged side by side without extra spacing, minimising waste material and hence costs. Alternatively, a guillotine could be used, which is cheaper; however, it cuts by shear and distorts the edges. Either way, manufacturing is completed with a thru-hole and countersink. These features are created with a pedestal drill and are later used for securing the specimen with an M3 screw.

The material for the specimens is Inconel 718, which is readily available as 2 mm thick sheets (Huntington Alloys Corporation, Inconel alloy 718, vacuum induction melted-electroslag remelted, sheet in coil, cold-rolled, annealed .0800 x 36 inch, thickness tolerance +/- 0.003). The full report (RA tracer 0551086, Certificate No. 87442-01) includes tensile testing at high & room temperature, stress to rupture, heat treatment, creep testing, bending test, grain size measurements, intergranular attack test, and microstructure.
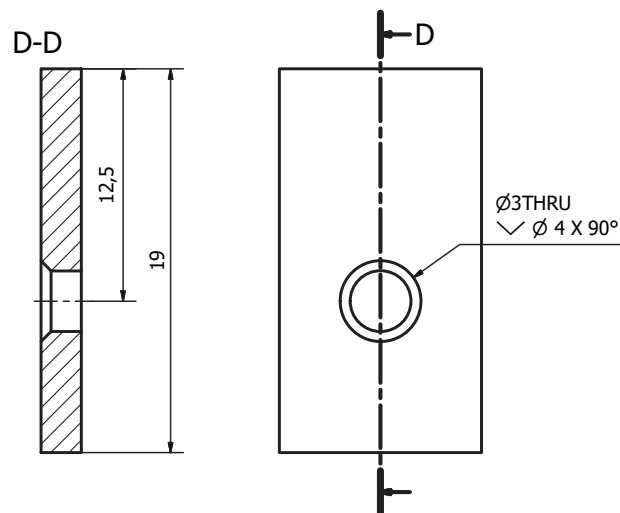
Fig. 3.13 Inconel 718 blade sample. General dimension 19 x 10 x 2 mm; drawing not to scale. Sample fabrication: T. Jones Fabrications (Ridings) Ltd

3.2.5   Stage & stage controller

The rate at which the blade displaces vertically towards the rotating sample is the incursion rate, and it is equivalent to what is done in the research of abradables. For the research of abrasives, however, an incursion rate does not necessarily equate to a material removal rate; this depends on the coating's abrasive capabilities. In this case, the incursion rate could also be considered a way of controlling the load rate and be significant for extrapolating the experimental results to more representative conditions.

To achieve a vertical displacement at a specific rate, a micrometer motorised stage (SIGMA KOKI, model OSMS80-20ZF) is used in combination with its controller (SIGMA KOKI, model shot-202). Table 3.5 presents a summary of their properties. It should be noted that this is the same stage and controller already in existence on the rig [127].

Table 3.5 Summary table of the stage's characteristics

Travel [mm]	20
Stage Size [mm]	80x80
Resolution (Full/Half) [um/pulse]	0.2/0.1
Minimum Incremental Motion [um]	0.05
MAX speed [mm/s]	1
Position Repeatability [um]	5
Load Capacity [N]	147

Concerning the controller's control, the RS232C interface is used to establish serial communication with the computer. LabVIEW is then used for commanding the desired speed and displacements. For this purpose, the manufacturer's LabVIEW program has been adapted to gain extended control, the main instructions of which are shown in Table 3.6.

Table 3.6 Implemented instructions for driving the stage. Table adapted from the manual.

Command	String	Details	Response
Set number of pulses for relative movement	M	Inputs taken: axis of movement, direction, number of pulses	When MAIN is used: "OK" response when command received normally or "NG" when problem
Simultaneous linear travel for two axis	K	Linear interpolation	
Confirmation Commands			
Drive command	G	Start	No response
Status 1	Q	Returns position etc.	
Status 2	!	Returns B/R (READY)	The manual refers to Page 25
Internal information	?	Internal information	
Control Commands			
Speed setting	D	Set S, F, and R	When MAIN is used: "OK" response when command received normally or "NG" when problem
Switch number of steps	S	Switch number of steps	
Stop	L:E	Emergency stop	

Concerning the stage's movement, this is driven in pulses per second (pulses/s). Every pulse is predefined as 0.1 microns per pulse (um/pulse), which means that the stage's speed can be calculated in microns per second (um/s). Finally, given the desired incursion rate in microns per revolution (um/rev) and the rig's running rotational speed in Hz, the inverse process can be followed to find the stages' speed in pulses per second. This calculation is performed automatically with LabVIEW, see Equation (3.7):

$$Stage\ speed[\text{pulses/s}] = \frac{Incursion\ rate[\mu\text{m/rev}] \times Wheel\ rotational\ frequency[Hz]}{Pulse\ resolution[\mu\text{m/pulse}]} \quad (3.7)$$

It is worth mentioning that parameters for communication are set as per documentation. From Table 3.6, the communication protocol establishes an "OK" response when the command is received correctly and an "NG" when it does not. An exception occurs when the command expects some data on return, e.g. "Q" or "?". In this case, data will be returned instead of an "OK". Furthermore, as the manufacturer recommends, no command is sent without previously checking the controller's status. The code is available electronically in Appendix C.

3.2.6 Outline of the rig

The preceding components form the experimental rig that intends to recreate the stator-blade/rotor abrasive contact. The overall arrangement is displayed in Fig. 3.14, which can be contrasted with Fig. 3.3, highlighting the outlined modifications made to consider the contact in question. Instrumentation will be addressed in the next chapter.
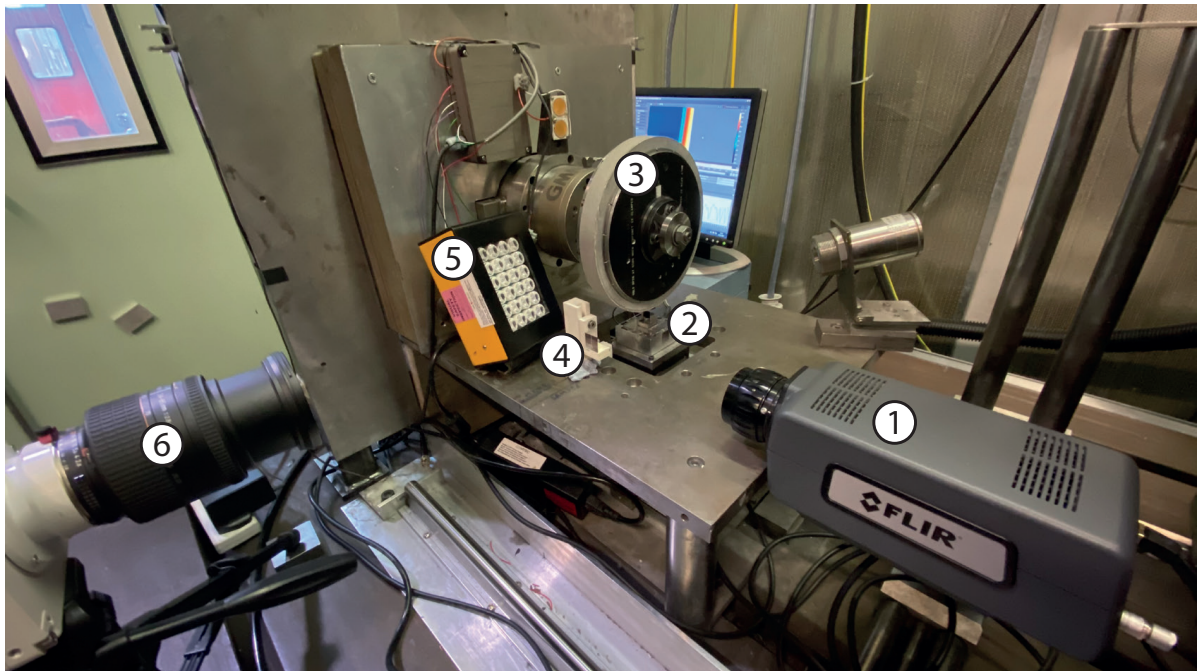
Fig. 3.14 Rig configuration. Labels: (1) Thermal camera; (2) Load cell with static Inconel blade sample on micrometric stage; (3) Expandable mandrel with substrate and abrasive ceramic coating; (4) 90º Gold mirror; (5) LED; (6) High speed camera.

3.3   Summary

This chapter has focused on recreating the contact conditions for experimenting with abrasive linings. For this purpose, a brief literature review was conducted for establishing the needs of studies such as this one. Then, the current rig (employed for abradable studies) was evaluated and modified.

The rotating sample (used as the substrate for the ceramic coating) has been the first component considered, whose design was constrained with the need of null tangential forces. A sample with simple ring-like geometry with rectangular cross-section fulfilled the requirements and was thus selected. Aluminium and steel were initially considered, and the former was selected because it resulted in lower vibrations after the manufacturing process. Finally, an expandable mandrel that could accommodate an active balancing system was chosen for clamping the samples to the electrical spindle; the samples were designed hand in hand with the mandrel because of their interdependency.

Additionally, tooling was designed (with the engineering support of Rolls-Royce) to deposit the samples with the ceramic coatings. The static sample (the blade) was then designed using Inconel 718 (which is the material used for the aero-engine section considered in this study) and a 2x20mm cross-sectional area (to simplify what is currently used for an economical manufacturing process). The stage and its controller are reused from the abradable setup and will be used equivalently (to produce a vertical displacement, i.e. an incursion rate).

Chapter 4

Instrumentation and signal processing

The literature review identified the need for a representative contact, and thus recreating the contact has been addressed in the previous chapter. Additionally, the need for more than postmortem measurements was identified, and that the measured variables should intend to explain wear and the exposure to wear. Instruments are responsible for providing these measurements and consequently are also of vital importance in experimental research.

The role of instrumentation is evidenced, for instance, in the rig of Stringer and Marshall [127]. Historically, studies in the field had only focused on postmortem data to identify wear mechanisms. Then, Stringer and Marshall monitoring the process during the test and identified a time and position dependency of the wear mechanisms, thereby exposing the inadequacy of measuring the bulk change in variables (e.g. length or weight change) and changing the route for experimenting with abradables after that. The use of a stroboscopic technique during testing on a simplified test platform was an essential contribution to this discovery, highlighting both: the benefits of using an optical approach for monitoring the tribological process and the advantages of simplified test platforms for performing the research on abradable linings. Fig. 4.1 is an example of their data that shows how the wear mechanisms vary over time.
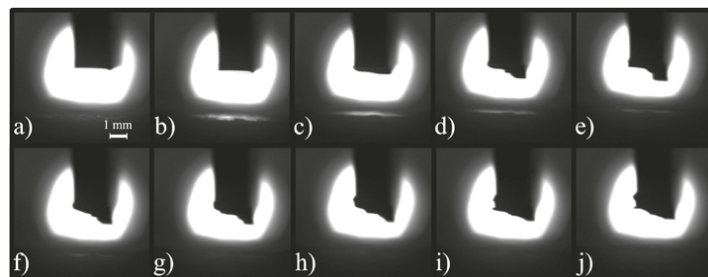
Fig. 4.1 Succession of images performed with the stroboscopic technique showing inconsistencies of the debris build-up on a blade. Source: Stringer and Marshall [127]

Based on the acquired knowledge, it was decided that an in-situ measurement technique was the best method to adopt. Additionally, it seemed adequate to sense contact forces, temperatures, vibrations, and build-up of adhered material on the coating. The selected instruments are a conventional 3-axis load cell, a thermal camera, an accelerometer, and a high-speed camera. The following sections will describe these instruments with the acquisition and processing of their data.

4.1 Load cell

For the research of abradable linings, forces have been generally measured with 3-axis piezoelectric load cells (e.i. Kistler Instruments Ltd., Type 9347 C). However, conventional piezoelectric force transducers are no longer ideal for a system like the one herein considered given that it involves a continuous contact and the presence of moments. The reason is that 3-axis piezoelectric force sensors are very vulnerable to moments because they measure force directly. Additionally, their signal drifts with a continuous excitation because they need an amplifier. If the continuous nature of the force was the only source of drift (which is normally not), drift follows a linear trend and can be corrected. The issue of having moments is solved by choosing an overdesigned sensor or simply choosing one that allows moments. Still, neither of the latter would solve the problems as it would mean that the sensor range is far greater than the measured forces (bringing the signal to the noise level), and a sensor that allows moments would be expensive and would probably not solve the drift issue. In summary, conventional load cells (based on strain gauges) have been the most suitable force transducer from those considered.

4.1.1 Load cell properties

The load cell (Interface Force Measurements Ltd., model 3A60A, stainless steel version) measures forces indirectly through strain gauges. Calibration is subsequently needed to relate the measured voltage with the applied force. The model 3A60A (Fig 4.2a) is a 3-axis load cell with bulk size 60x60x25 mm comprising for each axis a 375 $\pm$5 Ohm (nominal resistance) strain gauge full-bridge configuration. These are installed on a bridge-like component (Fig 4.2b) and grant measurements to be temperature compensated within a range (-10 to +70 ºC); the influence of temperature change within this range is low ($\pm$ 0.02 %/ºC). The rated capacity is 500 N (FS), accepting 750 N (150 % of FS) as safe overload and 1500 N (300 % of FS) as ultimate overload. Within the rated capacity, the forces show small nonlinearity of $\pm$ 1 N ($\pm$ 0.2 % of FS) and crosstalk error of $\pm$ 2 % on each axis. The sensor also allows a maximum

moment of 10 Nm, which means a maximum tangential force of 526 N with the current blade length. The electrical rated output (nominal) is $\pm$ 0.5 mV/V meaning $\pm$ 5 V output with the maximum excitation of 10 V. The enclosure of the sensor achieves a sealing with protection level IP54: protection against water spray from any direction and limited protection against dust ingress. These characteristics make it adequate for a grinding process where dust is expected. Table 4.1 summarises this data.

(a) Interface 3A60A load cell. Top view with break out section to show the "live end" component.

(b) Live end component (top and side view)
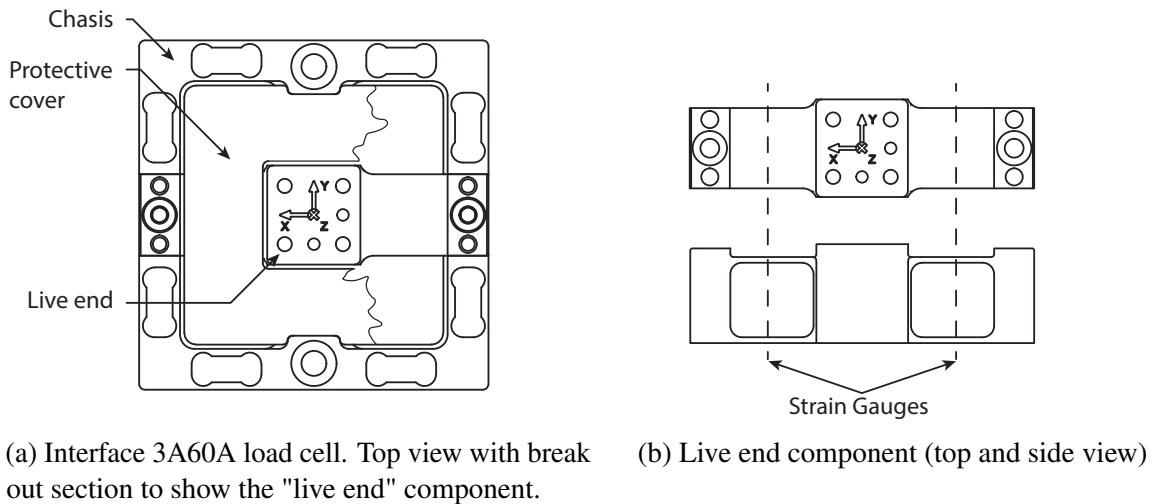
Fig. 4.2 Load cell illustration

Table 4.1 Summary table of load cell attributes; additional data with serial nº 18104112

Mechanical			Eccentricity and moment	
Rated Capacity (FS) -[N]	500		Allowable moment [Nm]	10
Material	Stainless steel		Crosstalk: x:y/y:x [%]	$\pm$2
Deflection - Fx, Fy [mm]	0.20		Crosstalk: z:x/y [%]	$\pm$2
Deflection - Fz [mm]	0.15		Crosstalk: x/y:z [%]	$\pm$2
Total weight [kg]	0.2		Eccentric Load Sensitivity [%FS] @ 20mm	$\pm$1
Safe Overload [%RO]	150			
Ultimate Overload [%RO]	300			
Protected Level	IP54		Temperature	
			Effect on Output [%/ºC]	$\pm$0.02
Electric (calibration)			Compensated range [ºC]	-10 to +70
			Operating range [ºC]	-10 to +85
Max. Excitation Voltage [V]	10			
Rated Output X-axis [mV/V]	0.519469		Accuracy - (Max error)	
Rated Output Y-axis [mV/V]	0.606484			
Rated Output Z-axis [mV/V]	0.739599		Nonlinearity [%FS]	$\pm$0.2
Resistance X-axis [Ω]	372.98			
Resistance Y-axis [Ω]	373.78			
Resistance Z-axis [Ω]	373.72			

4.1.2   Load cell assembly

The load cell is mounted as per manufacturer requirements. The setup uses a combination of fasteners and dowels to secure the load cell to a base plate (in-house manufactured ground GFS O1 tool steel), Fig. 4.3a. A reason for such a securing combination could be that dowels provide more tolerance restraints than a thread, ensuring that screws do not suffer from shear stresses and provides repeatable measurements by allowing precise positioning every time the sensor is mounted. The manufacturer recommends, for sensors of rated capacity 500 N and above, to prevent slippage with the use of a high strength retaining compound, particularly Loctite 638. Instead, a thread sealant liquid (Loctite 243) with slightly lower properties has been used for threads, dowels, and connection surfaces. In this case, fasteners with a higher grade than recommended (grade 12.9, M4 x 16 mm) have been selected, providing the torque by hand; only 1 Nm is recommended at the live end and 3 Nm at the dead end.

(a) Top view of load cell's mounting plate   (b) Bottom view of load cell (dead end)
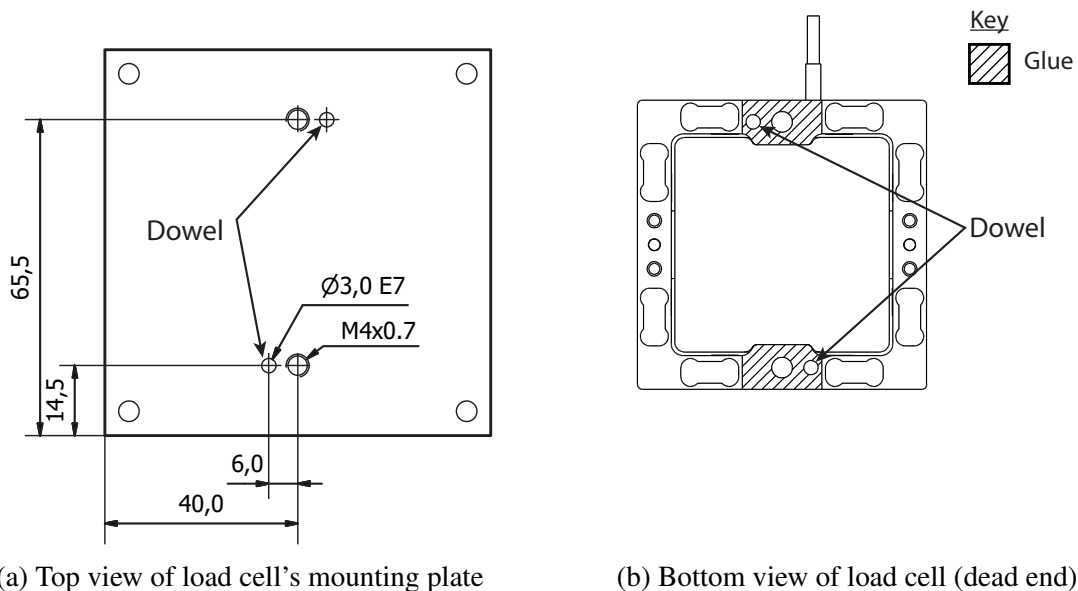
Fig. 4.3 Load cell mounting on base plate: positioning of dowels and glue.

The blade holder is positioned on the live end (top side) of the load cell, and its installation is almost identical to the previously described for the base plate. It uses one dowel (1 x Ø2 mm) and screws (4 x M3); however, without any sealant. It would be desirable to use 2 dowels instead, but the geometry of the blade with the features on the live end do not allow for it. Nevertheless, the dowel used is located on the direction of the main tangential force (the cutting direction), and should be enough to restrain any possible movement; F_T in Fig. 4.4.
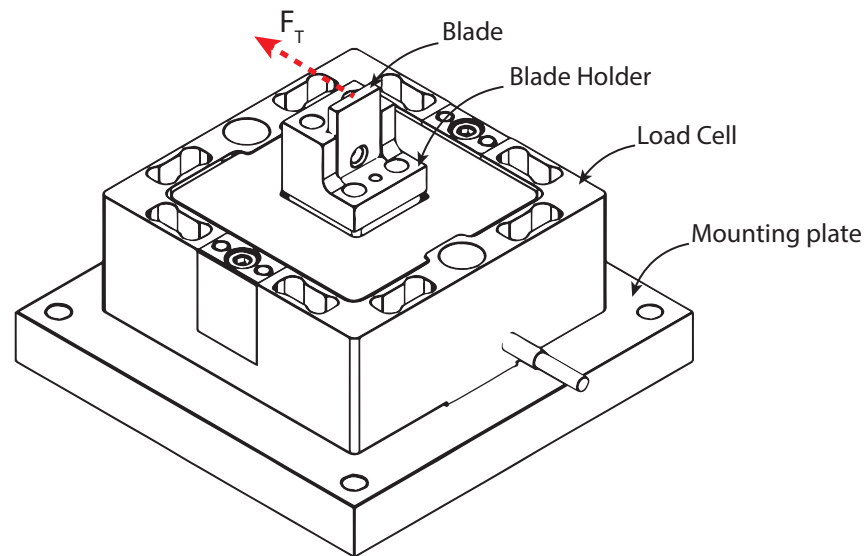
Fig. 4.4 Load cell assembly: blade, blade holder, load cell, base mounting plate

The material is tool steel (GFS O1) and the connecting surface is ground. The holder's design has a low profile to minimise the moments (induced from the tangential forces at the tip of the blade) and accommodates the specimen in the middle of the load cell to reduce the eccentricity error. Note that these also bring benefits in terms of vibrations as it reduces the mass on the load cell. Fig. 4.4 displays the full assembly of the load cell, including the base plate and holder.

4.1.3 Electronic hardware for load cell data

The electronic hardware for data collection involves a NI 9237 card connected to a NI cDAQ-9174 chassis. This module is specific for load cells; accordingly, it includes all the required signal conditioning and powering to acquire data simultaneously from four bridge-based sensors. The sampling rate is 50 kS/s at 24 bits resolution which equates to a minimum measurable load of 5.96e-5 N (minimum bit level) with the 10V excitation of the card and the 0.5mV/V (nominal) sensitivity of the load bridge. The connection is provided through 3 x NI 9949 modules and RJ-50 connections (one for each full bridge of the load cell). The diagram showing the electronic hardware and the connections is included in Fig. 4.5, note the connection of the insulating metal sleeve to both the load cell and to the ground of the NI cDAQ-9174 chassis.

After a trial test, a frequency analysis of force data identified forces at 50 Hz and 3 kHz intervals, which are frequencies related to electromagnetic noise introduced from the power lines and the inverter. Accordingly, a braided cable sleeve manufactured from tin-plated copper
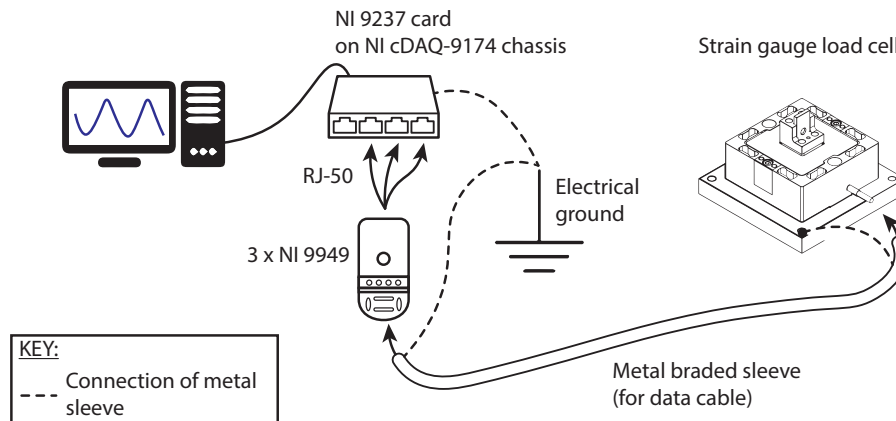
Fig. 4.5 Schematic showing the load cell connection and electronic hardware

(Typco Electronics UK Ltd, RAY-101-3.0) was used to insulate the data cable from electrical noise. Alternatively, a different procedure (e.g. a software procedure using low pass or bandpass filters) could have been used to remove the noise from the signal. However, a hardware approach was preferred because it operates over the whole signal before its acquisition, rather than being limited to specific user-defined frequencies selected during post-processing.

Two signals of 0.1 s length that have been recorded during testing conditions are included in Fig. 4.6 to illustrate the performance of shielding. These correspond to signals without and with shielding and have a calculated variance of 48.952 N^2 and 0.801 N^2, respectively; a 98% variance reduction. Considering that the standard deviation with shielding is $\pm$ 0.895 N and that the 50 Hz and 3 kHz peaks could no longer be distinguished from the background noise after frequency analysis, the quality of the data seems sufficient for this experimental setup.
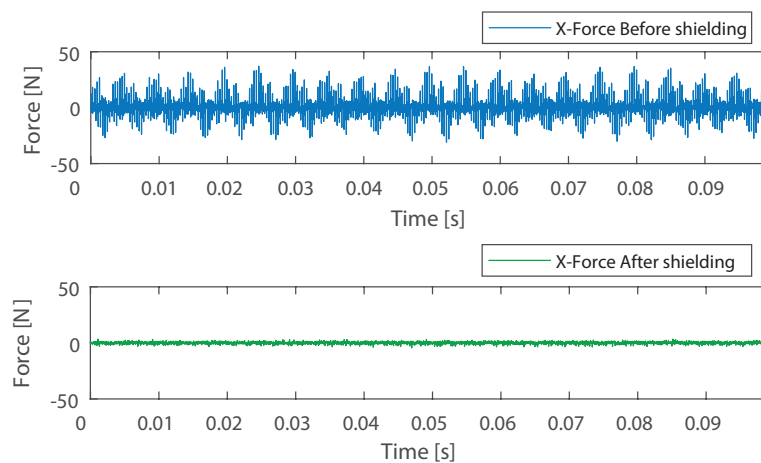
Fig. 4.6 Load cell signal without and with shield data cable

4.1.4   Force correction and processing

Generally, force sensors based on strain gauges do not provide accurate measurements of dynamic forces [166]. Their stiffness is lower than that of other sensors making them have an inappropriate frequency response, e.g. having longer oscillatory responses that vary in duration and magnitude depending on the frequency of the applied force. Consequently, corrections are needed when treating a dynamic force like that of a cutting process.

The correction of the dynamic effect is done through the Fourier transform [166]. In principle, for a linear system like that illustrated in Fig. 4.7, the force input to the system can be related to the output through a frequency-dependent transfer function *H(f)* [166].
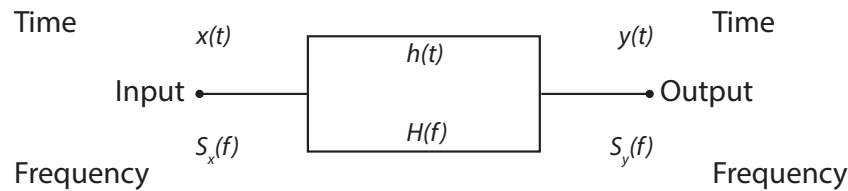
Fig. 4.7 Block diagram showing the relationship between input and output of a linear system. Adapted from Miyazawa and Usui [166]

This relationship is expressed mathematically in Equation (4.1), where $S_x(f)$ and $S_y(f)$ are respectively the Fourier transform of the input signal $x(t)$ and output signal $y(t)$, and $H(f)$ is the elementwise quotient between them.

$$H(f) = \frac{S_y(f)}{S_x(f)} \tag{4.1}$$

The input to the system can thus be calculated from the output if the transfer function is known, i.e. the Fourier transform of the output divided by the transfer function yields the input. The inverse Fourier transform provides the time domain data, as in Equation (4.2) (IFFT denotes the Inverse Fast Fourier Transform).

$$x(t) = IFFT \left[\frac{S_y(f)}{H(f)} \right] \tag{4.2}$$

Experimentally, the transfer function has been estimated through the impulse method, which is applied with an instrumented hammer (Dytran Instruments, Inc., model 5800B4, sensitivity 103.4 mV/lbf). The forces produced by the instrumented hammer are set as reference, given that its resonance frequency is high and forces are expected to be close to the actual input. The hammer and load cell are connected respectively to NI 9234 and NI 9237 cards on a NI cDAQ-9174 chassis. LabVIEW is used for recording the data, and the Matlab function

"tfestimate" [167] is used on both signals (input and output) to estimate the transfer function $H(f)$. For this procedure, no windowing or extra parameters are used as these introduce distortions in the signal and require additional corrections that are subjective (to a degree) and open to interpretation. Signals are recorded at 51.2 kHz and contain roughly 100 impacts per measuring direction. Three different tip hardnesses were tested, and those signals performed with hard metal tip were the ones used for estimating $H(f)$, as they showed better coherence (estimated with the function "mscohere" [168]). The process yields two $H(f)$ functions (one for each load cell axis), which are saved until needed for correcting the forces during tests. These are provided below in Fig. 4.8 and Fig. 4.9, which respectively show $H(f)$ in normal (z) and tangential (y) direction.
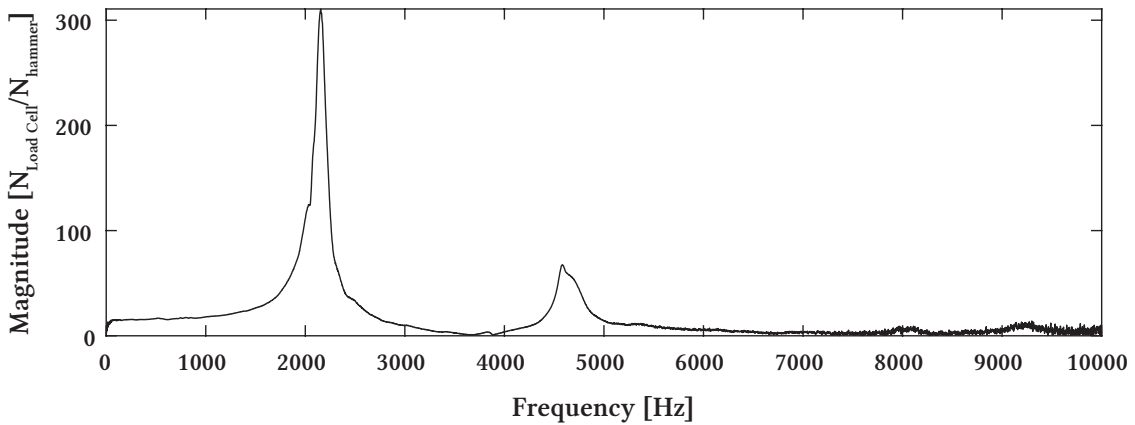
Fig. 4.8 The $H_1(f)$ estimate of the transfer function in the normal direction (z) between impact hammer and load cell. Zoomed view of frequencies between 0-10 kHz
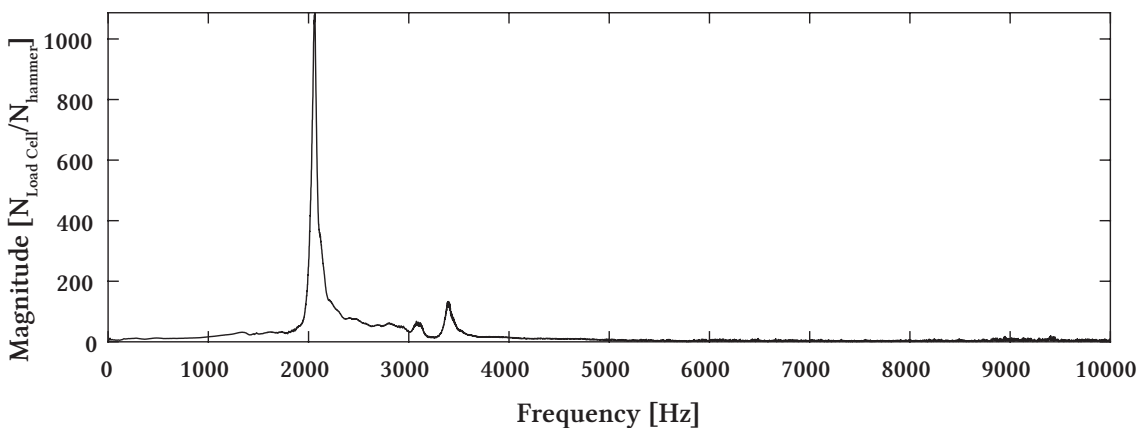
Fig. 4.9 The $H_1(f)$ estimate of the transfer function in the tangential direction (y) between impact hammer and load cell. Zoomed view of frequencies between 0-10 kHz

For applying the dynamic correction to the force signals from tests, the load cell forces are converted into the frequency domain through the Fast Fourier Transform. Since the frequency resolution depends on the length and the recording speed of the force signal, and most certainly differ from those of the transfer function $H(f)$, the values of $H(f)$ in the frequency points of the recorded force $S_y(f)$ are achieved through interpolation. After the process, $H(f)$ and $S_y(f)$ will have the same length and Equation (4.2) can be computed to achieve $x(t)$, i.e. the Inverse Fourier Transform of the elementwise quotient between $S_y(f)$ and $H(f)$. The application of this technique on the impact hammer tests (which do not need interpolation because signals are recorded at the same speed and are of equal lengths) yield Fig. 4.10; an example of the time domain forces with and without correction. An uncertainty estimate can be acquired by comparing the load cell's corrected signal with that of the hammer (if the latter is considered as 'real'). Comparing peak values yields a mean difference of 0.23$\pm$0.19 N in the normal direction and 0.10$\pm$0.09 N in the tangential direction, which translate into an accuracy error of 2.60% and 1.71% when considering the magnitude of the forces. Thus not being unreasonable to consider these values acceptable for experimental matters.
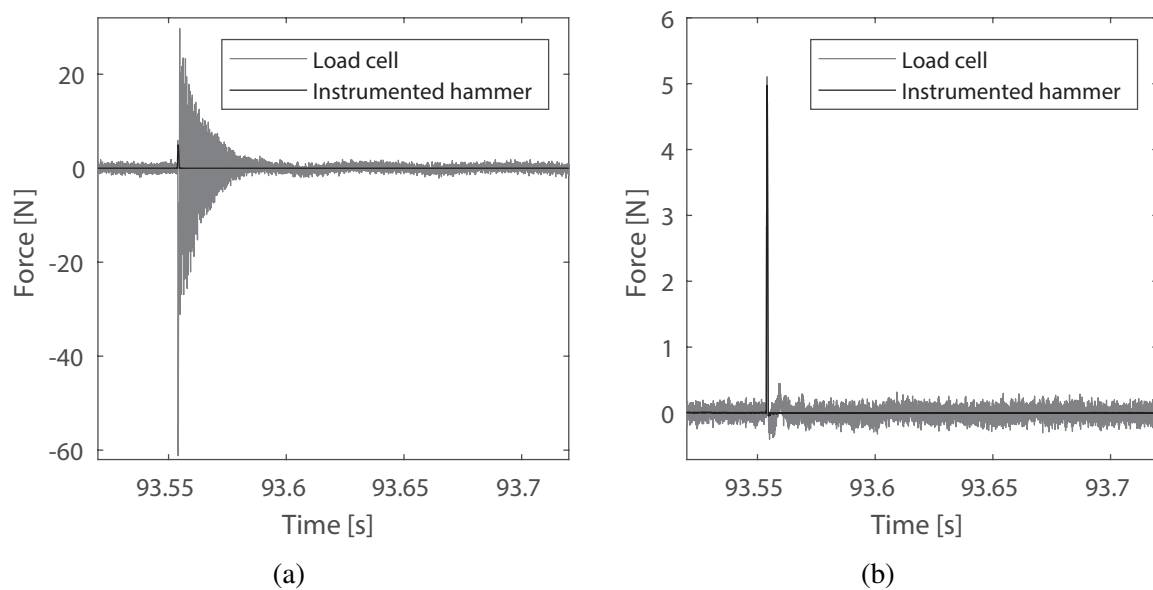
Fig. 4.10 Comparison of time domain forces between instrumented hammer (reference) and load cell. (a) Non-corrected forces, (b) Corrected forces.

Given the dynamic behaviour of the force signals, the root mean squared (RMS) value is computed after they are dynamically corrected. This procedure captures the energy of the signal and is more commonly applied in vibrations. In this work, RMS values are acquired by squaring the signal's values and performing a moving average with the "movmean" [169]

function, then doing the square root of the values. The length of the sliding window (in points) over which the local average is performed is selected to equal the period of a revolution, i.e., force sampling rate/rig running frequency (Fig. 4.11). Thereby removing the cyclic behaviour that appears in the force waveform related to the unbalance of the disc and manufacturing errors such as out-of-roundness or concentricity of the rotating assembly; issues previously exposed in Section 3.2.1 that have require averaging over a full rotation. Since a moving average introduces a phase shift in the signal (a delay), the same operation is performed again backwards to correct for it. Thus, for a given force signal that has been dynamically corrected, the root mean squared (RMS) is computed in the forward and reverse direction, creating a zero phase difference. Fig. 4.11 shows an example of the three processing steps that a force signal goes through. As shown, the method effectively averages the signal maintaining the overall trend.
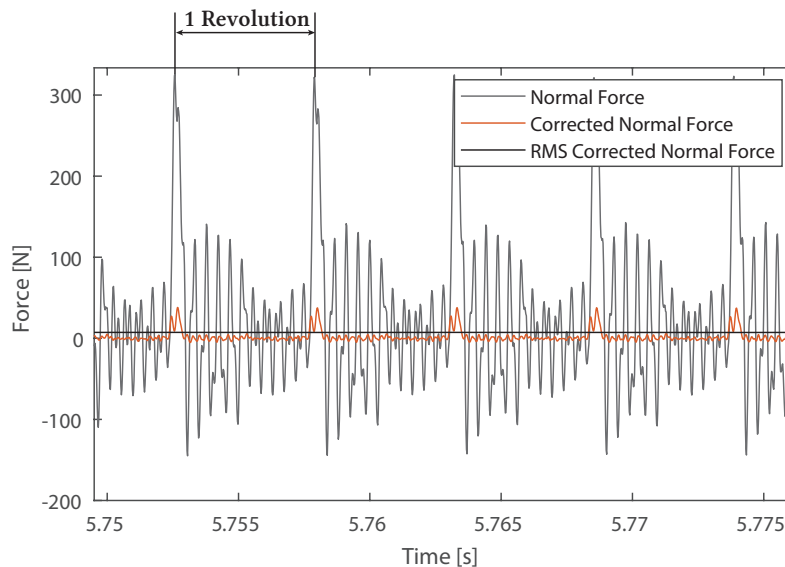
Fig. 4.11 Processed force signal during contact of the blade from a basic trial at 115m/s and 0.31μm/pass

4.2   Thermal camera

Temperature is a common metric that is used for understanding the underlying physical mechanisms of damage and wear. Almost every rig included in the literature review records temperature when studying abradable linings, and other manufacturing fields like grinding and metal cutting also follow very similar procedures [170]. Therefore, given the likely thermal aspects aspects to wear in this study, it does not feel unreasonable to use temperature as a metric and implement a method that senses it.

Thermocouples are very common for taking the aforementioned temperature readings. Whilst simple to use and relatively inexpensive, they are relatively slow compared to other methods and are invasive, which change the thermal behaviour of bodies and can yield inaccurate results. Non-invasive and high-speed methods such as Pyrometers and thermal cameras are thus highly desirable. Both systems are optical, with the difference being that thermal cameras provide two-dimensional information while pyrometers provide an average measurement of a surface spot. Accordingly, although both work with the same principles, thermal cameras provide a superior understanding of the tribological system because they allow observing the entire contact area instead of being constrained to a single spot. In other words, thermal cameras present an advantage because they allow for spatial discrimination. Due to the attractive characteristics of thermal cameras (i.e. non-contact, non-intrusive, fast recording speeds, and spatial discrimination), such a instrument is the chosen measurement tool for this research.

4.2.1   Thermal camera general properties

The camera used (Flir Systems, model A6751 SLS) senses in the long wave infrared (LWIR) band, particularly in the 7.5-9.5 μm range, with a strained-layer superlattice (SLS) detector. The achieved resolution is 640x512 and manages to capture all pixels simultaneously in under 190 μs with a frame rate of 125 Hz. Integration time of up to 480 ns and frame rates of above 4175 Hz can then be achieved by windowing down at focal plane array (FPA) level that decreases the size in steps of 16 columns and 4 rows of pixels. The camera focal ratio (f number) is f/2.5 and has been purchased with a 50 mm lens. A $\pm1\%$ of the reading is a typical accuracy error attributed to the camera for temperatures above 100 ℃. A custom calibration has been performed by Flir Systems, Inc. using NIST (National Institute of Standards and Technology) traceable equipment to achieve a temperature measuring range that is appropriate for testing (200 ℃ to 1400 ℃). The use of this pre-set requires the installation of an internal bandpass filter in the 9100-9455 nm wavelength range. Three other factory calibrations are present in the camera with temperature pre-sets of -10-50 ℃, 55-350 ℃, and 150-650 ℃. These do not require the use of an internal filter and the temperature overlap allows for a superframing measuring technique; however, the custom calibration provides additional benefits for this research as the following sections will show.

4.2.2   Stabilisation of temperature measurements

A general misconception is that such optical methods measure temperature and it is worth commenting that this is not entirely true. In fact, these sensors use detectors (focal plane arrays) that respond to electromagnetic radiation in the infrared range. It is only after applying physical

laws (e.g. Planck's law) and corrections that temperature can be related to the signal perceived by the sensor. Consequently, temperature estimations are only as accurate as the considerations made for the system under observation and generally carry a considerable error. Due to this, contact methods like thermocouples normally outperform those of optical measurements and are therefore more adequate for providing absolute temperature values. All this considered, the aim of this research is not to measure temperature on an absolute scale but to use it as a comparative metric. The difficulty of this then relies on the ability to achieve a stable system where uncertainty remains constant thought time.

To develop a stable system, it is first adequate to identify the different sources of error that measurements from the thermal camera carry. The ASTM International standard (ASTM E2847-14) [171] discusses the calibration and accuracy verification of optical thermometers and identifies eleven sources of uncertainty. As shown in Table 4.2, these can be divided into two groups: those concerning the source and those of the infrared thermometer.

Table 4.2 Uncertainty component. Adapted from (ASTM E2847-14) [171]

Source Uncertainties		Infrared Termometer Uncertainties	
U_1	Calibration Temperature	U_7	Size-of-Source Effect
U_2	Source Emissivity	U_8	Ambient Temperature
U_3	Reflected Ambient Radiation	U_9	Atmospheric Absorption
U_4	Source Heat Exchange	U_{10}	Noise
U_5	Ambient Conditions	U_{11}	Display Resolution
U_6	Source Uniformity		

Authors like Lane *et al.* [172] discuss some of these uncertainties and their experimental implementation for temperature measurements of a metal cutting process. Given a calibrated device, most sources of error seem to have a negligible effect if the camera optic is temperature compensated and remains at a temperature significantly below ambient. Further uncertainty reduction is attained if the distance from the camera to the target (the measuring distance) can be considered small, and the camera is exposed to small heat sources during short periods. Meeting these conditions allows, amongst others, to assume negligible the emission of the optics, that the atmosphere does not cause a significant signal attenuation (transmissivity of the atmosphere is unity), and that the temperature of the optics and atmosphere remains constant during the recording time. The implementation of these simplifications leads to the standard measuring scenario illustrated in Fig. 4.12.

Some of the manufacturer's implementations already bring the system very close to that displayed in Fig. 4.12. For example, the uncertainty sources related to the optics have been significantly reduced with the employment of a Strained Layer Superlatice (SLS) cooled
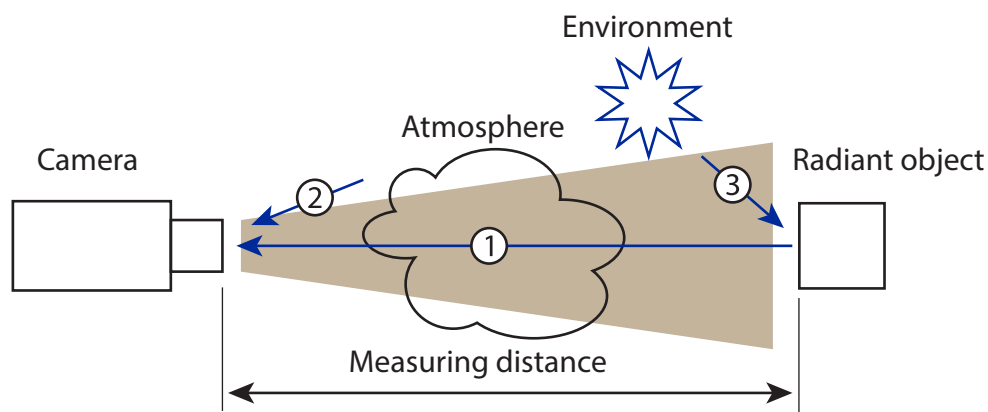
Fig. 4.12 Standard measuring situation. Labels: (1) Contribution of radiant body; (2) Environmental contribution - other radiant sources reflected on the radiant object; (3) Direct contribution of the atmosphere.

detector that works at <80 K, or the use of FLIR's thermal imaging software (ResearchIR) that, by default, uses an internal flag as a reference to correct for measurement offsets every 30 minutes, or alternatively, when the detector's temperature varies in one degree.

Moreover, ResearchIR can correct the atmosphere's effect on uncertainty by estimating the atmospheric transmissivity. The correction is based on the environment's humidity, its temperature, and the measuring distance. These variables have been recorded for the testing site: measuring distance is about 0.4 m, temperature varies between 20 ºC to 30 ºC after much testing, and humidity is generally under 20 %. These values yield an almost constant atmospheric transmissivity of over 99 %; thereby, why environmental absorption is usually considered negligible [172] for comparative measurements taken at small distances (<3 m in midwave and <8 m longwave). Nevertheless, according to the ASTM International standard (ASTM E2847-14) [171], the correction should still be performed. Hence, temperature and humidity measurements are taken before testing, and the automatic correction is performed.

Environmental reflections have also been contemplated since tests are performed inside a safety container with highly reflective aluminium inner walls, and reflections are a potential issue. As shown in Fig. 4.13, the container walls have been painted with an all-purpose high emissivity matt black paint, which has effectively minimised reflections. Environmental and atmospheric effects have been further reduced by taking measurements for temperature ranges way above the atmospheric temperature (150-1400 ºC) and using the bandpass filter (9100-9455 nm) mentioned earlier. These three implementations, namely painting the container walls, measuring in the 150-1400 ºC range, and using an internal filter, have been sufficient to prevent the camera from detecting any signal except the one produced by the contact.

4.2.3   Source emissivity uncertainty

The effect of the target's emissivity is known to be the main uncertainty contributor [171, 172]; hence, it is worth treating it individually. One of the sources of error is that emissivity must be assumed constant during the recording time, which is a serious assumption that does not acknowledge its variability. Emissivity can vary, for instance, with surface changes in the material such as oxidation or deformations; or simply with a change in temperature or change in observing angle (to mention a few). Since these behaviours indeed happen in the abrasive contact studied herein, the target's emissivity must be carefully considered.

Lane *et al.* [172] mentions three conditions for a system to resemble the standard system illustrated previously in Fig. 4.12. These conditions are: that there is a function relating the camera's response to the signal perceived, that emissivity is constant through the camera's measuring wavelength range, that emissivity and temperature are independent. The existence of the function is usually only of the manufacturer's concerns, and by using the aforementioned narrow bandpass internal filter, the assumption of constant emissivity through the camera's wavelength measuring range can be made. Thus, only the last requirement (emissivity being independent of temperature) has not been treated yet.

A stable emissivity has been attained by first selecting the blade as the target and then painting it with a high emissivity and high-temperature paint (LabIR, type HERP-HT-MWIR-BK-11, temperature resistance up to 1000 ºC, emissivity above 0.9 between 7.5-13 μm). Noting that the rotating abrasive samples could be an alternative target, selecting the blades provide several benefits. For instance, the system can be considered quasi-static, which makes factors related to the integration time of the camera less important. Furthermore, emissivity can be considered high (0.92 is used for these experiments), known, and constant, given that paint can be used on the reflective Inconel samples to effectively increase the emissivity. The bandpass filter further eases the latter consideration, as variations in emissivity become almost negligible when reducing the recording wavelengths from 7500-9500 nm to 9100-9455 nm.

It must be noted that the implemented procedures in this study attain a consistent uncertainty for temperature measurements. Thus, it is possible to treat measurements as comparative values, and an uncertainty estimate is not required. Nevertheless, determining absolute temperatures is desirable, and further work on uncertainty estimation has been carried out in Appendix E. On a side note, an alternative technique has been recently developed that minimises uncertainty due to emissivity variations. For this technique, the temperature is estimated from measurements at two distinct wavelengths, which has benefits because emissivity cancels out from the measurement equations and become irrelevant for temperature estimations. Thus being appealing for studies like this one, where emissivity varies. Refer to Hooper [173] or manufacturers such as Williamson Corporation [174] for further reading about this dual-wavelength technique.

4.2.4   Experimental configuration of the thermal camera

The camera configuration has been performed to minimise sources of uncertainty. Although not purpose-specific, the ASTME [171] and ISO [175, 176] standards on uncertainty estimation have been followed as guidelines; a schematic of the measuring system is provided in Fig. 4.13.
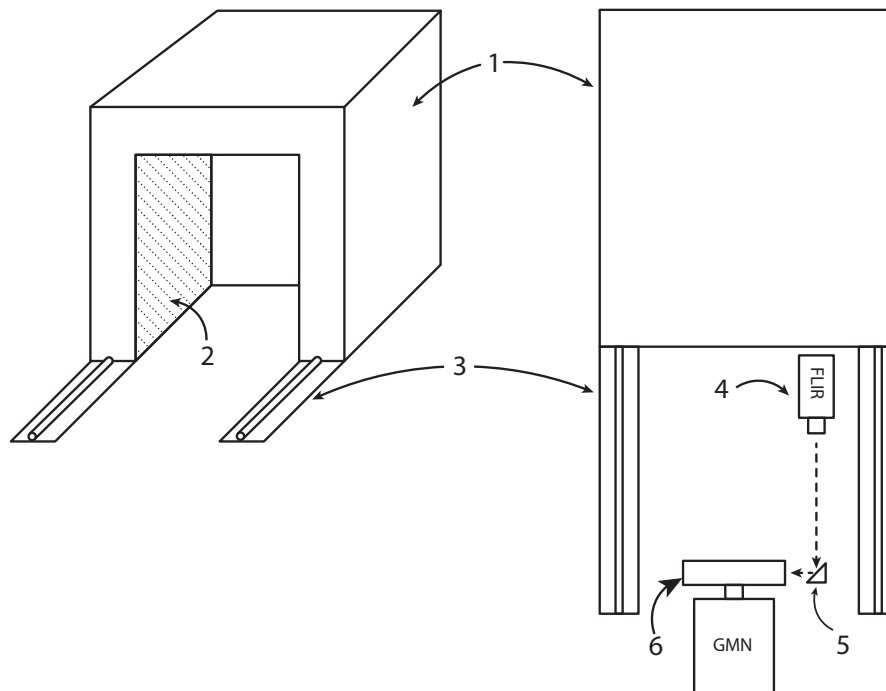
Fig. 4.13 Isometric and top view schematic of the safety container and thermal camera positioning. Labels: (1) safety containment; (2) painted inner wall; (3) rails for positioning of containment; (4) Flir thermal camera; (5) 45° gold plated mirror; (6) ceramic sample mounted on GMN electrical spindle

To protect the camera from debris, and because of space constraints in the safety casing, the camera's point of view is rotated by 90° with a gold plated mirror (Thorlabs LTD), 20 mm Protected Gold Right Angle Mirror, average reflectance >96 %). The schematic in Fig. 4.13 also shows the painted inner walls of the container and the camera's position relative to the ceramic sample. The thermal camera, blade sample, and golden mirror are located on the same horizontal plane, which is the horizontal plane where the camera fully views the blade and a small section of the disk.

The proposed set-up exceeds the ISO specifications for condition monitoring and diagnostics of machine systems and is believed to provide comparative measurements. "Apparent temperature" is a term frequently used in the literature that acknowledges the uncertainty in temperature readings and, consequently, is the term that will be used.

4.2.5   Thermal data acquisition and processing

FLIR's ResearchIR software is used for acquiring the thermal camera data. It generates ".ats" files that are optimised for saving data from FLIR devices. These file formats are more compact than others; thus, they facilitate storage and transfer. Furthermore, they include all the recording information, which is very useful for the user during postprocessing. These allow, for instance, to change between units (i.e. temperature, radiometric, or counts) or to perform corrections (e.g. emissivity or transmissivity). Other third-party software such as LabVIEW do not allow for this, meaning that corrections must be performed during the data acquisition. After that, the backward procedure cannot be performed without the calibration curves (which are not accessible to the user). Hence, raw data is lost, and corrections (e.g. applying a different emissivity) cannot be made after acquiring the data.

The chosen approach for this study is to use ResearchIR together with its Matlab SDK. Such a combination provides all the described benefits as it allows for corrections to be made after testing. Accordingly, it enables the user to operate the thermal camera without previous knowledge of the system. Note that the camera calibration curves have been found as part of the uncertainty work mentioned previously in Section 4.2.3. These can be used if a third-party software was to be used, and can be found in Appendix E.

With the setup mentioned earlier in Section 4.2.3 and 4.2.4, frames of size 256x320 pixels are captured at 398 Hz continuously during a test. An example frame is provided in Fig. 4.14.
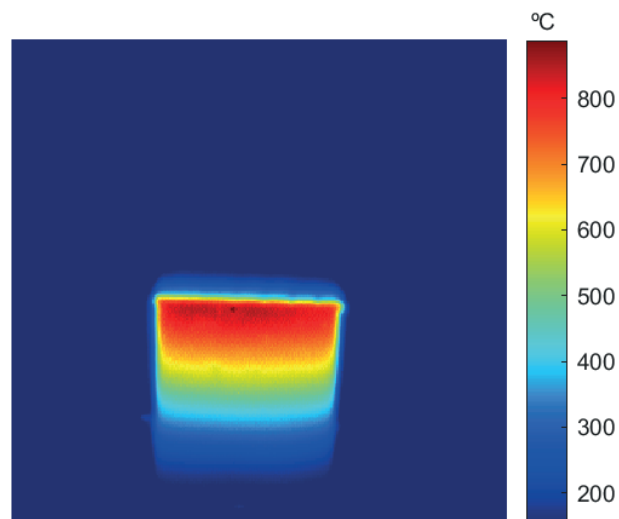
Fig. 4.14 Example frame of the blade captured with the thermal camera

Considering the temperature distribution shown in Fig. 4.14 and that the blade is thin compared to the rest of its dimensions, the heat conduction problem is a transient 2D heat conduction problem. Moreover, since the tests are short (<8.59 s), one can assume the boundary

conditions to be constant and known, e.i., test cell temperatures. With this interpretation, only the temperature at the contact edge is required to calculate the entire temperature distribution of the blade at each point in time. Fourier's law in 2D describes the process:

$$\rho c \frac{\partial T}{\partial t} = \frac{\partial}{\partial x}\left(k\frac{\partial T}{\partial x}\right) + \frac{\partial}{\partial y}\left(k\frac{\partial T}{\partial y}\right) \tag{4.3}$$

where ρ is density, k is the material's conductivity, t is time, T is temperature, and c is specific heat capacity.

However, several reasons, such as the presence of a 'lip' conformed of molten material (Fig. 4.14) or the absence of high emissivity paint in the contact interface, obscures the direct acquisition of the contact temperature. A solution is to apply the inverse 2D boundary heat conduction problem, that is, to estimate the contact temperature based on the known internal measurements [177–179]. Notwithstanding that this approach is suitable, acquiring data in the vicinity of the contact has been sufficient to discriminate between testing conditions.

The image processing process to acquire temperature data is performed with Matlab and starts by identifying the contact edge. For this purpose, the edges are first accentuated with a range filter and a Laplacian of the Gaussian Filter (respectively 'rangefilt' [180] and 'imfilter' [181] Matlab functions). Then, the Hough transform [182] is used to identify the contact edge, and a line is fitted and translated vertically with the same gradient approximately 5 pixels below the contact line (the precise displacement will depend on the magnification of the image and the gradient/tilting of the camera so varies within setups). Finally, the maximum temperature is selected among the pixels covered by the line.

(a)   (b)
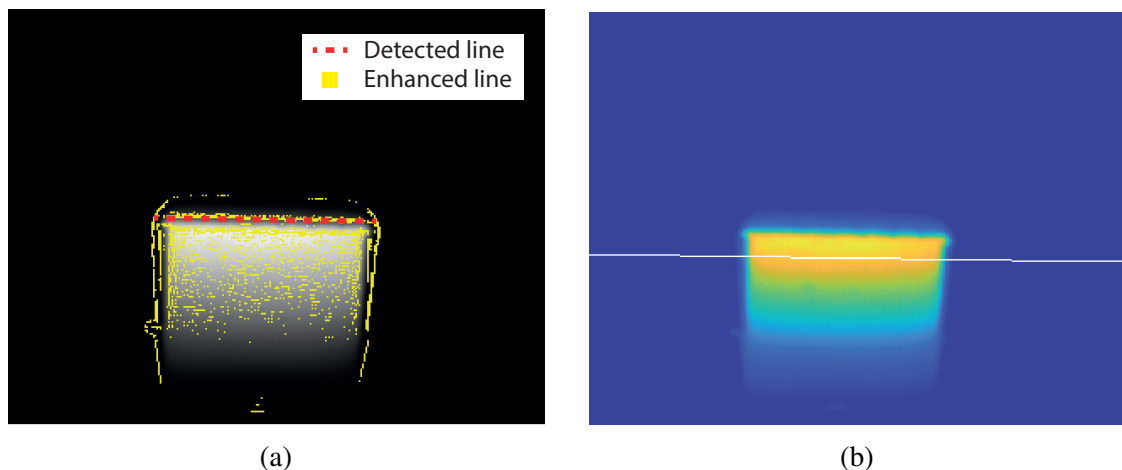
Fig. 4.15 Intermediate images extracted from the processing process. (a) Detected edge and fitted line, (b) Translated line (line of measuring points).

The aforementioned processing process is illustrated in Fig. 4.15. It should be noted that since there is a distance between the selected point and the contact edge, the estimated temperatures will have a delay and also will be damped in magnitude [177, Fig. 2.2]. Thus the importance of selecting a measuring point close to the contact edge is apparent. Furthermore, it should be noted that the inverse heat conduction problem is a continuation of the work presented, and if required, continuing with the analysis can lead to an estimate of the contact temperature.

4.3   High speed camera – Surface monitoring

In situ monitoring of the contact has been critical for the development of many tribological systems. Based on the literature review, optical devices have proven to be effective in identifying and discriminating distinct wear mechanisms happening during the contact period. Thus, it has been decided to monitor the ceramic's surface during the test with a high-speed camera (Vision Reseach ltd., Phantom VEO710 model, 18GB RAM). The setup also includes a zoom lens (Nikon UK Ltd, 24-85mm f/2.8-4D IF AF NIKKOR) and an LED (GS Vitec GmbH, model Multiled LT-V9-15, 24 high power LEDs, 84 W, 7700 Lumen total, 160*117*80 mm dimension).

4.3.1   Data acquisition and processing

The selected resolution is set to a frame size of 320x240 pixels, which corresponds to a field of view (FOV) of approximately 20 mm at the experimental setup (Fig. 4.16). The criterion followed to select the frame rate has been to achieve at least 20% overlap between frames at the particular running speed of the rig. That means that 39 frames are needed considering the circumference of the samples ($\pi d = \pi 195$ mm); see Equation (4.4). The selection of a 20 % overlap is adequate for creating panoramic images (or image stitching) that aid when tests are visually inspected during post-processing. The required frame rate can be calculated with the running speed of the rig (in hertz) as in Equation (4.5). Exemplar images captured in this way and post-processed are presented in Fig. 4.16.

$$n^o \, Frames = \left\lceil \frac{Sample \; circunference}{FOV \times (1 - \frac{\% \; overlap}{100})} \right\rceil \tag{4.4}$$

$$FPS = n^o \, frames \times rig \; runing \; speed \; [Hz] \tag{4.5}$$
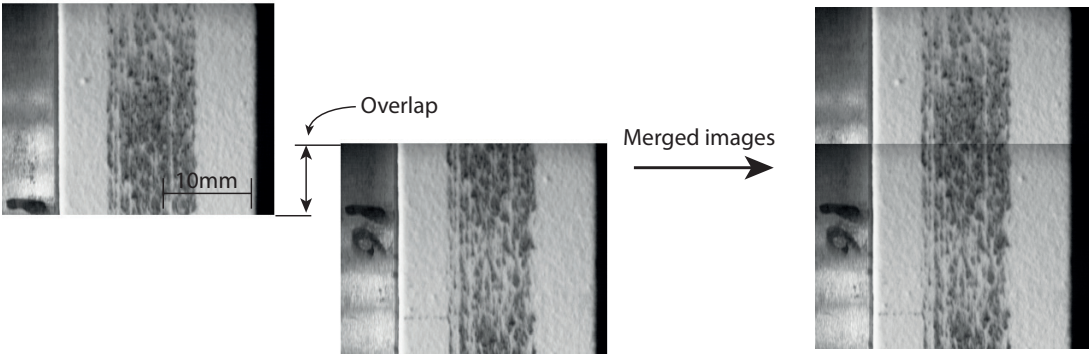
Fig. 4.16 Exemplar images captured with the high-speed camera during testing conditions at 115m/s, illustrating the overlap between images and the merging process.

Exposure time is minimised to achieving the least possible motion blur in the images, which is why a natural illumination is insufficient and the LED mentioned earlier is employed. Note that the high power of the LED results in heating energy, which might affect the thermal camera readings. However, the LED mainly emits in the visible spectrum, and its temperature does not reach the thermal camera's measuring range (150-1400ºC). Thus the thermal camera perceives no signal and suffers no influence from the LED, even when it is placed directly in front of the thermal camera during prolonged exposures. Concerning the LED's colour, the standard white has been selected, although different alternatives, such as microscopy's filtering techniques could be used if feature enhancing is required.
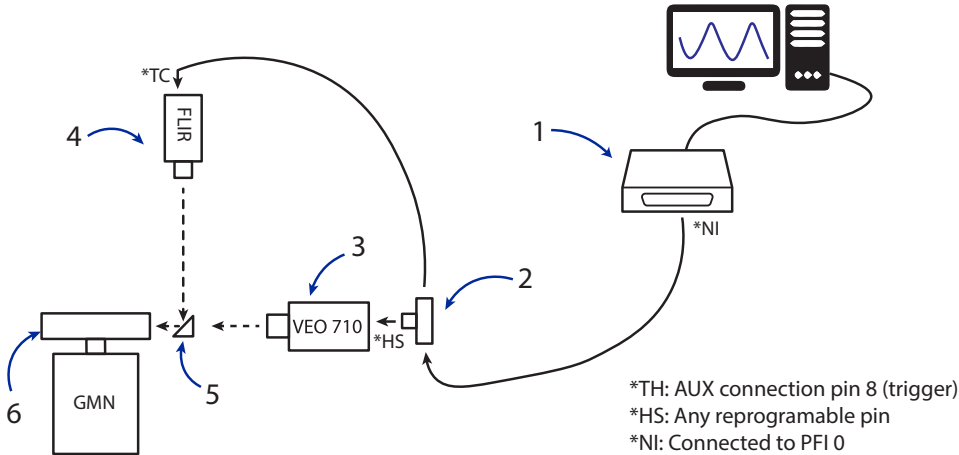
Fig. 4.17 Schematic of High speed camera and thermal camera connection. Labels: (1) NI 9401; (2) BNC-T connector; (3) Phantom VEO710; (4) Flir A6751 SLS; (5) 45º Golden mirror; (6) Ceramic sample under test

The recording parameters described before (i.e., frame rate, exposure time, and frame size) are selected in the Phantom Camera Control (PCC) software. Additionally, the 'memory gate' recording method is selected, which is an option that allows controlling the recording process externally. This option uses a TTL signal (a +5 V or 0 V signal) to identify which frames to record, and in this study is used to synchronise devices. Fig. 4.17 illustrates how the high-speed camera and thermal camera connect to the same TTL signal for their simultaneous operation.

As shown in Fig. 4.17, the arrangement employs BNC cables and a BNC-T connector to connect both cameras to a NI C-series digital module (National Instruments, module NI 9401, 8 Channels, 100 NS, TTL Digital I/O Module). This module is programmed through LabVIEW, and delivers a high TTL signal to start recording and a low to terminate it (the user can decide the signal's polarity). With the recording speed and frame size, it is essential to verify that the available recording time is no longer than the test time. Otherwise, the camera's memory is overwritten, and data is lost. In this study, the verification has been coded in LabVIEW; refer to Appendix A and C for further details on the LabVIEW code.

The processing is straightforward. For each acquired frame, the sum of its pixel intensity is performed for the contact region, e.g., the rub section of images previously presented in Fig. 4.16. Then, a moving average is computed with the 'movmean' Matlab function [169] to smooth the time domain data. Employing the length of a revolution for this purpose (i.e., 39 frames) removes the fluctuations related to non-uniformities in the contact effectively and highlights the overall trend in material adhesion. Exemplar results are shown in Fig. 4.18. This technique is suitable for comparing force, temperatures, and intensity signals (related to surface changes) in a cause-effect manner for a single test without the need for interrupting the test. A different approach would however be needed for comparing adhesion progression for separate tests, as the scales are not generally comparable. Some alternatives could be those suggested by Gwidon and Batchelor [183, Ch. 10], who review some recently developed optical methods for the characterisation of tribological surfaces.
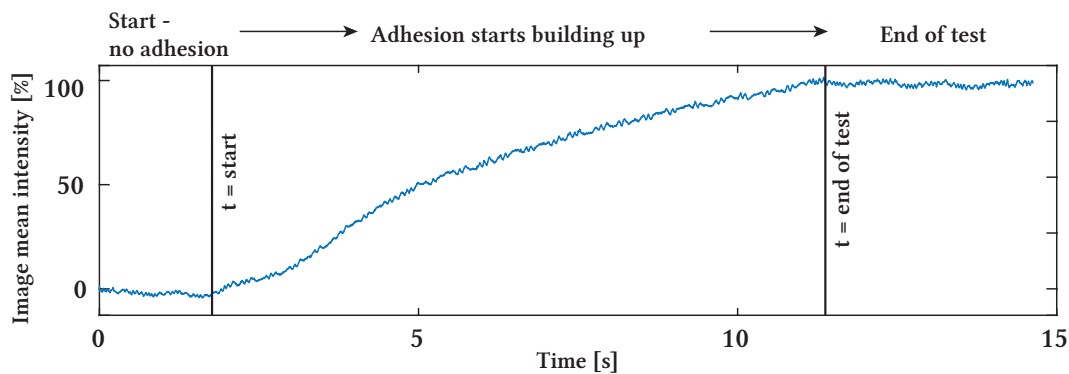
Fig. 4.18 Exemplar results of the high-speed camera, showing the progression of adhesion.

4.4   Accelerometer

An accelerometer is installed mainly for safety reasons, yet data is recorded from the time that the rig starts running and can be used for vibration analysis. The accelerometer (Kistler, IEPE single axis accelerometer, PiezoBeam type 8640A, range $\pm$ 50g, sensitivity 95.5 mV/g) is mounted onto the top part of the spindle with a ground isolated adhesive mounting base (Kistler, type 800M158); earlier electrical noise was identified when employing a magnetic mount. The guidelines marked by the ISO standards ISO 5384:1998 [184] on "Mechanical mounting of accelerometers" and ISO 20816-1:2016 [185] on general guidance for "measurement and evaluation of machine vibrations" were followed. The mounting is illustrated in Fig. 4.19.
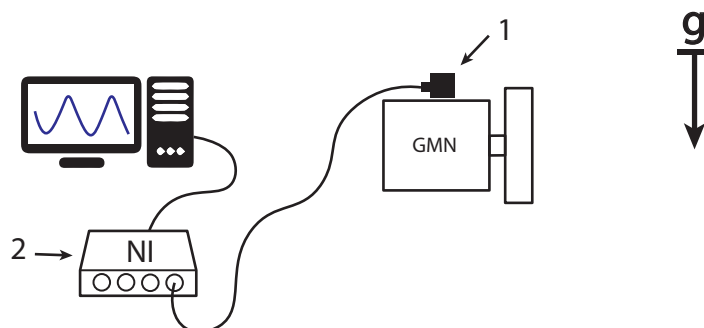
Fig. 4.19 Side view of the spindle with the accelerometer and its data acquisition. Labels: (1) Kistler's PiezoBeam 8640A with ground isolated 800M158 stud on GMN's spindle; (2) NI 9234 module

Fig. 4.19 also shows the connection of the accelerometer to a National Instrument's acquisition module (NI 9234, 4 analog input channels, $\pm$ 5 V, 24 bit resolution, 2 mA IEPE software selected excitation, 51.2 kS/s max sampling rate), which is connected to a chassis (NI cDAQ-9174 chassis); the same used by the rest of the devices.

4.4.1   Data acquisition and processing

Data from the accelerometer is acquired through LabVIEW at the maximum recording speed (51.2 kS/s) and is treated in-situ in vectors of length 2.56 kS (i.e. arrays are acquired every 0.5 s). Based on the general guidelines of ISO standards [185–191], then accelerometric data (in g units) is transformed into velocity (in units mm/s RMS). This process is accomplished by first transforming the accelerometric data into frequency domain through the Fast Fourier Transforms. Then, as shown in Equation (4.6) from ISO 2372-1974 [192], each entry in the spectrum is divided by its frequency, which yields velocity units.

$$v(n) = \frac{a(n)}{2 * \pi * \Delta f * n} \times 9807 \quad [\text{mm/s}] \tag{4.6}$$

Values of RMS velocity (mm/s RMS) are finally achieved with Equation (4.7), i.e. the root mean square value of the velocities divided by root two. The overall equation as stated in ISO 2372-1974 [192]:

$$v_{rms} = \sqrt{\left(\frac{1}{2}\right)\left[\left(\frac{a_1}{\omega_1}\right)^2 + \left(\frac{a_2}{\omega_2}\right)^2 + \ldots + \left(\frac{a_n}{\omega_n}\right)^2\right]} \quad [\text{mm/s}] \tag{4.7}$$

The process is performed in-situ on the collected signal without considering the first 10 Hz (commonly attributed to noise and static signal) and without applying any filters. Values of v_{rms} will be used later for balancing the samples, as will be explained after in the experimental method's section (Section 5.1.3). As mentioned, these procedure is undertaken in-situ primarily for safety reasons; however, the vibration data is recorded and can also provide valuable insight into the mechanics of the contact (if needed). Exemplar data of a full test prior processing is presented in Fig. 4.20, showing the different stages of the contact.
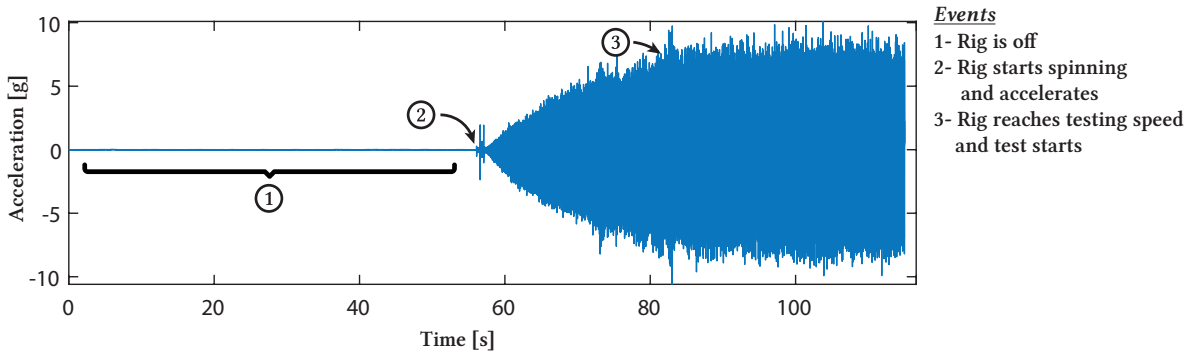
Fig. 4.20 Exemplar data captured with the accelerometer during a test.

4.5 Data acquisition

Data is acquired through LabVIEW with a program that has been annexed in Appendix C. A brief explanation of its main characteristics is provided herein and continued in Appendix A.

The program's operation is divided into three steps that can be followed from the Main VI's front panel (Fig. 4.21). The first step is to select the required instruments from the "boolean panel", joined with their expected computer port. Each device has been identified with a boolean ("On" or "Off") indicator, which on selection will remain "On" if the device is connected;

else, it will display a warning, and the indicator will be turned "Off". Each device also allows the input of specific settings that will be saved for later use. The selection of the "Initialise" button terminates the first step and initiates the second: an automatic process that disables the front panel, opens a connection to all verified devices (each is coded in separate VIs), and implements all the user parameters. Subsequently, devices start outputting data and awaits for the user to press the "Start" button. This action marks the beginning of a test (the third step), where data is finally recorded, and other devices such as the micrometric stage also start.
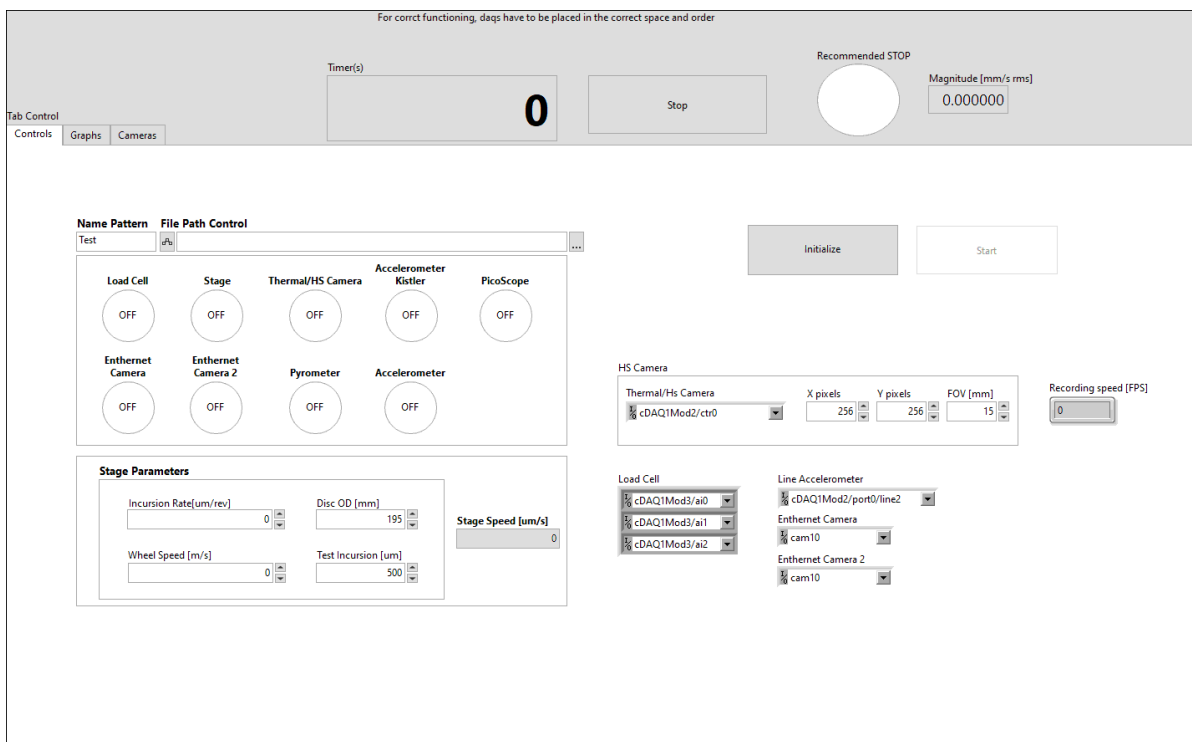
Fig. 4.21 LabVIEW User interface

Coding has been accomplished with the JKI state machine, which operates in essence like a more commonly known macro code. More precisely, the user interaction with the front panel is recognised as an event that triggers a particular task (coded previously as a string instruction). The program uses shared variables to communicate between the Main program and the VIs that this one controls. Such variables are used, for instance, to send the "start" and the "stop" command to the VIs, or in reverse, for answering back to terminate the Main program. Shared variables are also used to visualise live data on the main program, although this option is normally disabled for computing efficiency. Saving data is conducted in each VI independently with a producer-consumer loop architecture and is triggered when the Record (or Start button) is pressed; TDMS files are used for this purpose.

As briefly mentioned, the code is composed of a master VI and VIs for each instrument. In essence, the code is a Master-Slave architecture, where the master program controls in the background the different instrument VIs. This architecture offers some benefits. For instance, it allows using pre-existent VIs (that manufacturers commonly provide) without having in-depth knowledge of the device's functionality or the code itself. It also enables the user to implement simple instructions at first while still maintaining the full functionality of the manufacturer's program; hence, allowing to later extend the capabilities of the master program (if required) without extra time or effort. Furthermore, coding errors are also reduced as additional coding (e.g. adding an extra device) becomes an iterative process that the conventional user can accomplish by following a pre-established series of instructions. Thus, also not requiring proficient knowledge of a device (otherwise needed).

Aside from coding benefits, LabVIEW's behaviour fundamentally changes when instruments are coded in separate VIs (in contrast to a conventional implementation with Sub-VIs). The conventional implementation is a typical multi-tasking implementation, which provides the false appearance of simultaneity by alternating very quickly between tasks. Conversely, a multi-threaded application is created when separate VIs are called from a master VI, which means that applications (instruments) can be run simultaneously rather than in a queue of fastly alternating instructions. Coding instruments in separate VIs thus change LabVIEW's behaviour from multi-tasking to multi-threading and provide the benefits thereof.

4.6   Summary

This section concerned the installation of instrumentation and implementation of measuring techniques. The literature review identified forces, temperature, and loading as the important variables; thus, instrumentation was chosen to provide these readings.

Monitoring of contact forces was provided with a conventional strain-gauge load cell, for which an adaptor was designed and manufactured for securing the blade sample. Furthermore, the signal was insulated to clear the data from electrical noise. Contact temperature was provided by a thermal camera that is focused on the blade. Measuring conditions were improved by applying a high (known and constant) emissivity paint. Initial work on error estimation was produced, and measurement error is believed to be constant, thus providing comparative results. A high-speed camera was selected to achieve a visual inspection of sample loading during the contact time. Additionally, an accelerometer has been installed to monitor vibrations during a test.

Finally, the appropriate electronic hardware was chosen, namely NI modules, and the design of the testing platform terminated with the development of a LabVIEW program for operating the devices while acquiring data.

Chapter 5

Screening Experiment

Following Montgomery's guidelines [193, p. 13], recognising and formulating the problem is the first element to consider when designing experiments. As recommended, this process was performed in a team setting with Rolls-Royce and yielded the central question that this thesis wants to answer: *what are the wear mechanics of abrasive coatings and can performance be improved?*

The literature review revealed no clear answer, given that no research was found about this particular subject. However, it did provide a direction to follow, highlighting variables and possible answers. On sharing these findings with Rolls-Royce, five different controlled variables were identified: spraying parameters, rotor speed, closure rates, ceramic's surface finish, and ceramic material. The selection of these variables was supported by other studies on abradables and thermally sprayed materials in the literature review.

Not all the variables mentioned above are expected to be important; thus, this chapter aims to determine the dominant ones for the abrasive process. A large part of this research has involved developing the experimental method used for this chapter. The aim now moves towards analysing the data to ultimately develop an understanding of the linings' abrasive properties and the tribological process itself. This chapter will cover the procedure followed to reach these goals.

5.1 Materials and Methods

5.1.1 Materials

Samples are manufactured of two different materials, two different spraying levels, and two different surface finishes. The selected materials are Alumina and Yttria-Stabilised Zirconia, although any of the three coatings described earlier in Section 2.6 could have been chosen.

Furthermore, each coating is sprayed at two different conditions, chosen as extreme values within Rolls-Royce's engine operational envelope. These are summarised in Table 5.1 and consist of a change in deposition rate and spraying distance; in essence, properties that change the cohesion/density of the coatings. It must be noted that the spraying process is undertaken with the tooling described earlier in Section 3.2.2, designed explicitly for the samples.

Table 5.1 Spraying parameters as provided by Rolls-Royce.

Coat n°	Top Coat	T/C Thickness	Bond Coat	B/C thickness	Feed	Stand off
1	M 105 NS	750 μm	M 450	150-200 μm	20 g/min	150 mm
2	M 105 NS	750 μm	M 450	150-200 μm	40 g/min	100 mm
3	M 204 B-NS	750 μm	M 450	150-200 μm	20 g/min	150 mm
4	M 204 B-NS	750 μm	M 450	150-200 μm	40 g/min	100 mm

Gun Type 9MB with GH nozzle
Cooling jets
Surface Speed 1000mm/s
Traverse at 10mm step height

Strategy: Every 20 passes, measure, calculate, then top up to reduce the number of interrupts.

Table 5.1 abbreviations: *M* Metco.

In aero-engines, these coatings are sometimes machined for the abrasive rotor/stator-blade contact, and thus such an operation should be considered as a variable. Accordingly, the samples have two different finishes. Some are left as-sprayed (untouched after the spraying process), as it allows to study the pure effects of the spraying process and the coatings itself without any other manufacturing processes. Others undergo a truing process, representing a manufacturing operation. A dressing tool is used for the latter (as will be explained next), which yields a smooth surface that does not feel unreasonable to use as a reference. It is noteworthy that as-sprayed coatings present benefits from an aero-engine manufacturing point of view since sources of errors are reduced, fewer operations must be researched and optimised.

As previously mentioned, a smooth surface is achieved with a dressing tool (Tyrolit Ltd., type 50AP-Dressing plate 10x33x5 mm). The process undertaken is illustrated in Fig. 5.1 and is similar to what is conventionally done on grinding wheels. The tool is placed beneath the wheel with an overlap of 2 micrometres and then displaced in the wheel's axial direction (i.e. across the wheel). A 50% overlap is chosen between every pass of the wheel, which at a surface speed of roughly 10m/s (16.4 Hz) equates to an axial speed of 12293.3 micrometres/second (considering that the diamond tips are 3 mm thick). The process is repeated until vibrations reach a consistent point and marks on the ceramic (created previously with a ballpoint pen) are no longer visible.
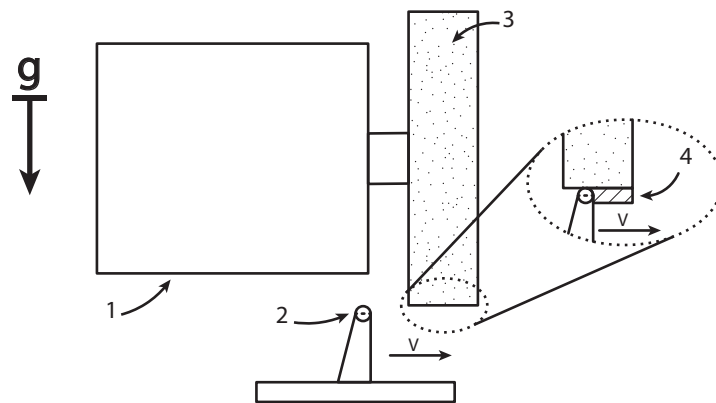
Fig. 5.1 Schematic diagram of the truing process. Labels: (1) GMN Spindle; (2) Dressing tool with diamond tip; (3) Ceramic coating; (4) Removed material per pass.

Fig. 5.2 and 5.3 are images of the resulting surfaces that were acquired during testing conditions (i.e., consecutive images have a 20% overlap, and 39 images constitute a full circumference). It can be seen that as-sprayed surfaces for both alumina and zirconia (samples *A* and *C*) have a very similar appearance, with no visible difference between samples sprayed at different conditions. However, zirconia samples do have a darker tone than alumina samples and are slightly rougher ($R_a = 4.35\ \mu$m, $R_q = 5.34\ \mu$m for zirconia; $R_a = 2.06\ \mu$m, $R_q = 2.60\ \mu$m for alumina). As for the trued samples (*B* and *D*), alumina samples result in smooth matt white ($R_a = 2.69\ \mu$m, $R_q = 3.49\ \mu$m) and zirconia ones show a smooth glossy, almost vitrified dark grey colour ($R_a = 2.93\ \mu$m, $R_q = 3.82\ \mu$m). Alicona is used for roughness measurements.
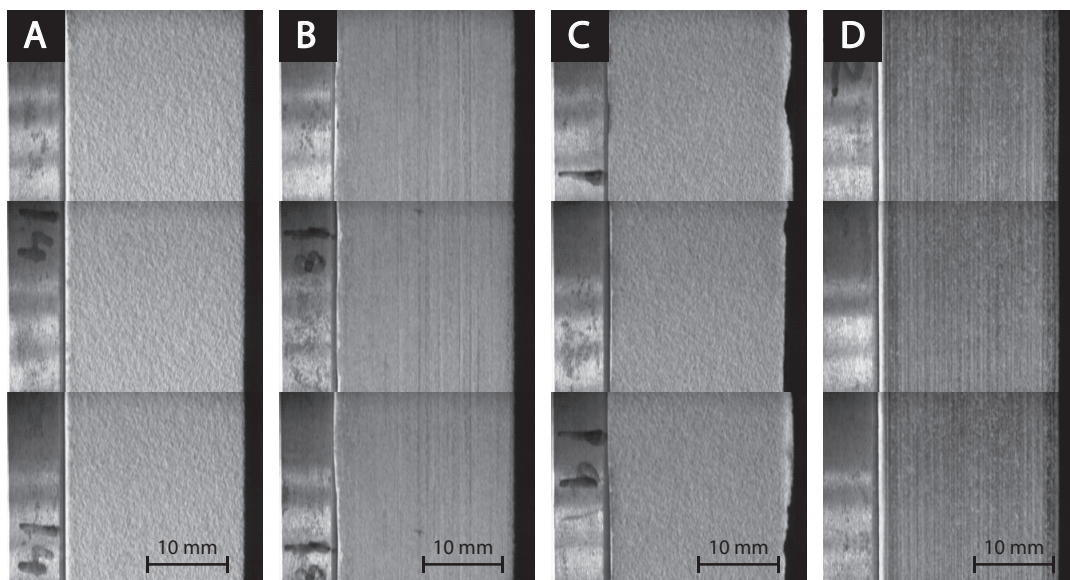
Fig. 5.3 Three consecutive images for each of Zirconia's samples. Labels correspond to surface, feed, and stand off and are: (a) AS-20-150; (b) True-40-100; (c) AS-40-100; (d) True-20-150.
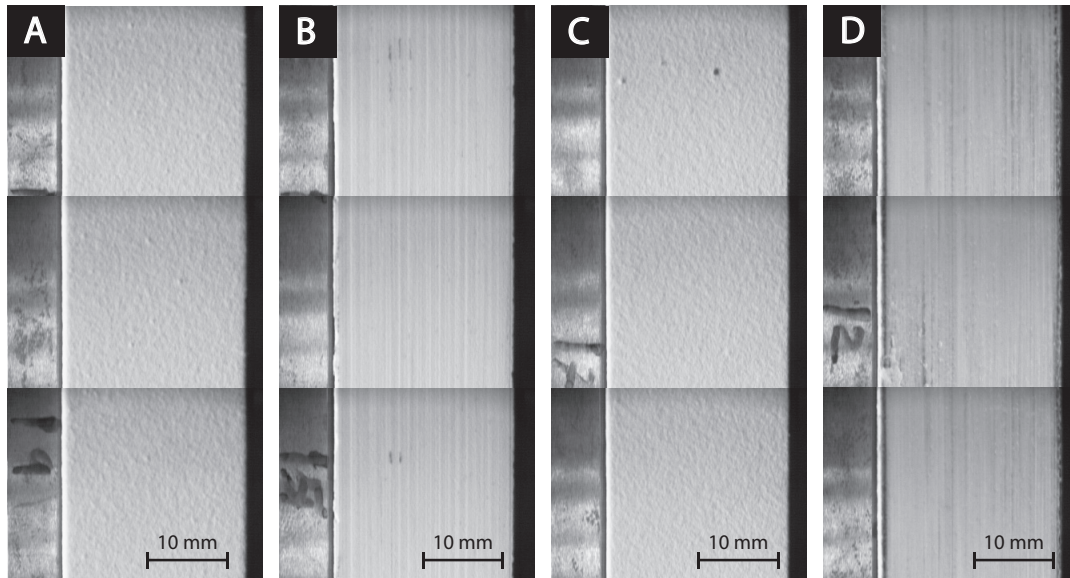
Fig. 5.2 Three consecutive images for each of Alumina's samples. Labels correspond to surface, feed, and stand off and are: (a) AS-40-100; (b) True-20-150; (c) AS-20-150; (d) True-40-100.

5.1.2 Statistical design of experiment (DoE)

Process factors of the high speed abrasive contact

The literature review identified that the material's wear properties vary with spraying parameters and the applied load. Furthermore, in typical engineering applications, contact speed and roughness (or surface topography) are generally acknowledged as factors that affect wear behaviours. Hence this research has addressed five factors: the material, the spraying parameters, the surface finish, the contact speed, and the incursion rate (a variation of the applied load that is more appropriate for aero-engine applications). A model of the process is included below in Fig. 5.4, and each input and controlled variable is understood as follows:

- **Material:** Understood as a change in the chemical composition of the samples.

- **Surface:** A surface change is understood as a macroscopic topography change that is achieved via post-spraying procedures.

- **Spraying parameters:** A spraying change is understood as the changes that can be introduced during the spraying of the ceramic coatings.

- **Incursion rate:** Understood as the displacement of the blade per revolution of the coating. It is similar to the closure rates in aero-engines.

- **Speed:** The surface speed achieved by the ceramic coating during testing conditions.
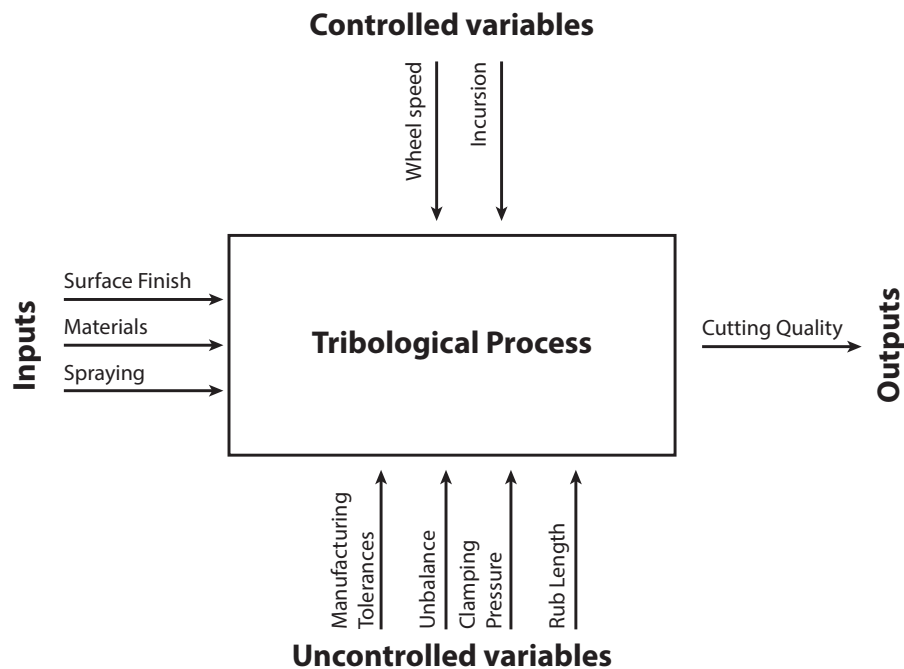
Fig. 5.4 General model of the tribologycal process

Note that a distinction has been made between spraying, surface, and material, albeit changing spraying conditions involves a surface change and a material change. This differentiation is made because surface and spraying can be understood as two different levels of changing topology, whilst a material change implies a change in chemical composition. Also, notice that only the main uncontrolled factors have been included in Fig. 5.4 (there are many more).

The half-factorial experimental design

The experiment was designed with one aim in mind: to identify the influence of controllable factors in cutting quality. Given the early stages of experimentation where many variables are considered, and only some are likely to affect the response, the half-factorial design (a typical design for screening experiments) was chosen. The factors and levels of which are included in Table 5.2. No repeats are carried out thus being an un-replicated half-factorial design with 5 factors, or 2^{5-1} (16 runs). A pictorial representation of the design is included in Fig. 5.5.

Table 5.2 Coded variables

Variable	Name	-1 Level	+1 Level
A	Speed	115m/s	165m/s
B	Material	Alumina	Zirconia
C	Incursion	0.31um/pass	1.71um/pass
D	Surface	Trued (smooth)	As sprayed
E	Spraying	20	40
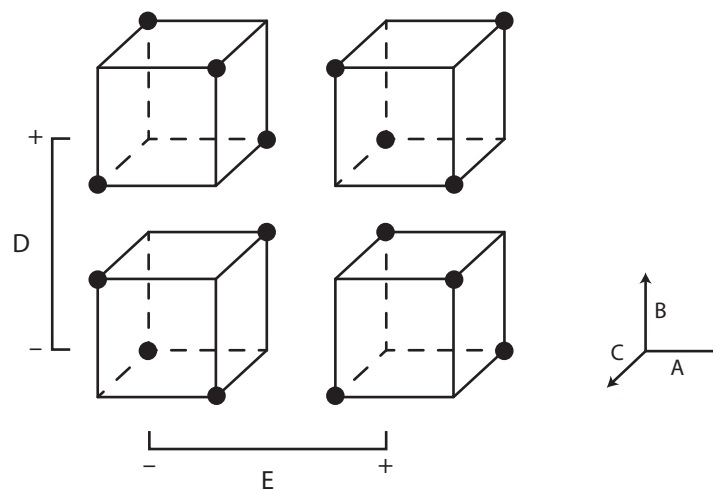
Fig. 5.5 Pictorial representation of the 2^{5-1} half-factorial design. "●" represents runs.

The levels of speed and incursion rates have been chosen based on Rolls-Royce's running and handling operations. Incursion rates and running speeds are commonly in the range of 0 to 2μm/pass and 300 to 400 m/s (refer to Section 3.1.4 in the literature review). While the latter speeds are currently not achievable (rig max. speed is 200 m/s), the magnitude and direction of the effect when varying speed is the only interest at this research stage. Thus, speeds were chosen within the operational capabilities of the electrical spindle, leaving a margin for future augmentation within limits (e.g. expanded into a response surface design). The incursion rates were selected similarly, with levels of 0.31μm/pass and 1.71μm/pass; the levels for materials, spraying, and surface have been described earlier in Section 5.1.1.

It is worth noting some of the many attractive qualities of the half-factorial design, such as their sparse design, the projective property, and the possibility for sequential experimentation [193, p. 329]. More precisely, the half-factorial design requires a reduced number of runs (a fraction of that needed in a full-factorial design) and will project into a higher level if factors are dropped from consideration (e.g., if a factor is found to have no notable effect).

Furthermore, subsequent experimentation allows combining several fractional factorials into a bigger design or extending the design into a different one (such as a response surface design). Thus, it grants opportunities for further development, which might happen if more runs are needed, different regions want to be explored, or additional variables are to be studied.

5.1.3 Experimental method

The type of contact addressed herein has been discussed previously in Sectionn 3.2; it is relatively fast, continuous, and differs from the conventional contact in abradables. An experimental method has been developed due to not finding any prior studies that help understand this type of contact. Chapters 3 and 4 have already covered the design and instrumentation; this section will address the testing procedure. Specifically, setting up the samples, the stage, and performing a test.

Sample setup

For testing, the samples are first selected and installed as in Fig. 5.6. The procedure involves fixing the blade sample to the load cell and the specific ceramic sample to the mandrel (for which a 30Nm torque is sufficient). It is worth noting that the latter samples are inherently unbalanced. They thus present a safety hazard and require balancing before an experiment.
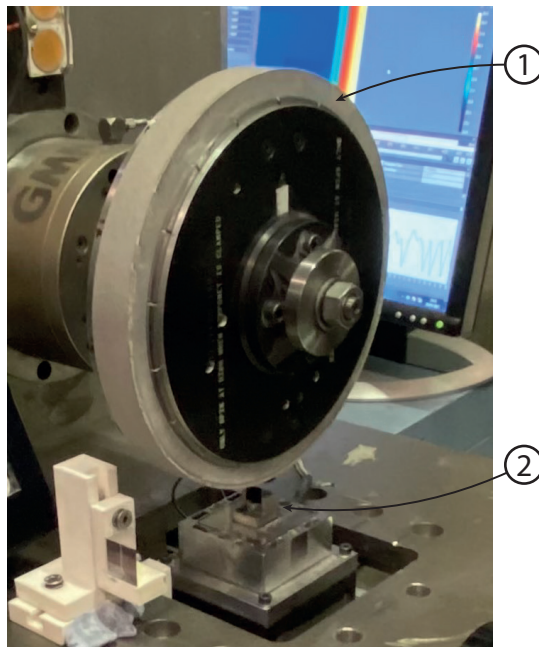
Fig. 5.6 Image showing the positioning of the ceramic sample on the mandrel and the blade sample on the load cell. Labels: (1) Ceramic sample; (2) Blade.

Fig. 5.7 illustrates a 3 step process that has been followed to achieve acceptable vibration limits, namely running the spindle (with the mandrel and sample) just below the first natural frequency (e.g., at ≈70 Hz) and recording the vibration level as described earlier in Section 4.4. Then, the samples are rotated 90 degrees anticlockwise (for sign convention), and the whole process is repeated two more times. Subsequently, Equation (5.1) is fitted through the three collected readings.
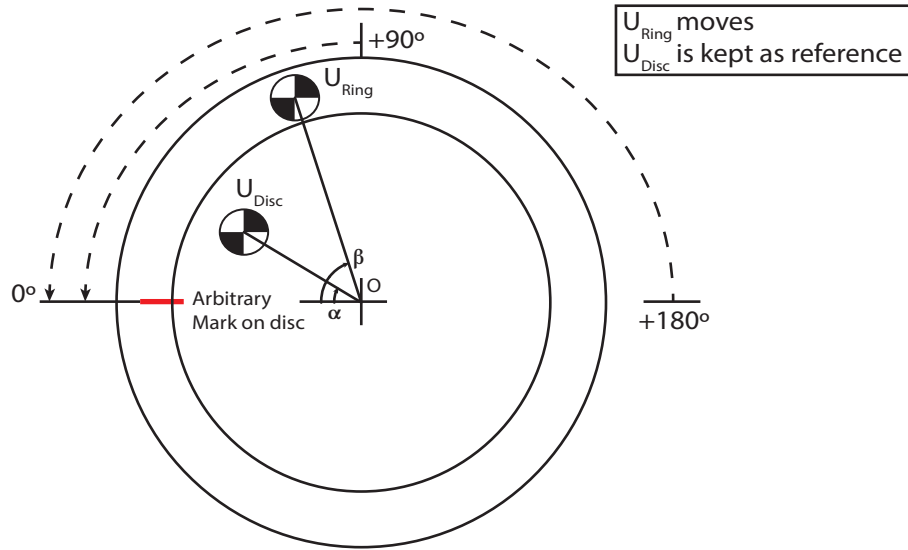
Fig. 5.7 Illustration of balancing procedure showing how the sample can be rotated to change the relative position of the unbalances and identify when these are in opposition

$$U = \sqrt{(A\cos(\alpha) + B\cos(\beta))^2 + (A\sin(\alpha) + B\sin(\beta))^2} \qquad (5.1)$$

Equation (5.1) is Newton's law assuming that the ring and disc both have a single mass imbalance (A and B respectively, and α and β their angles with respect to the initial run). The equation's minimum is the most favourable angle to position the sample on the disc. In other words, the position where the unbalance of the ring is opposite to that of the disc. Appendix B includes the code for fitting this equation and finding the optimum angle.

Fig. 5.8 shows an H1 Frequency Response Function (FRF) estimate of the spindle that has been used for identifying the adequate running conditions. Experimentally the excitation was provided with an instrumented hammer (Dytran Instruments, Inc., model 5800B4, sensitivity 103.4 mV/lbf) fitted with a metallic head; the response was measured with the accelerometer and setup described earlier in Section 4.4. The FRF H1 estimate was computed through Matlab's 'tfestimate' function [167] using a signal that consisted of 55 impacts. The FRF results are consistent with what is experimentally observed. That is, an increase in response is witnessed after ≈70 Hz, and a maximum is reached at ≈115 Hz.
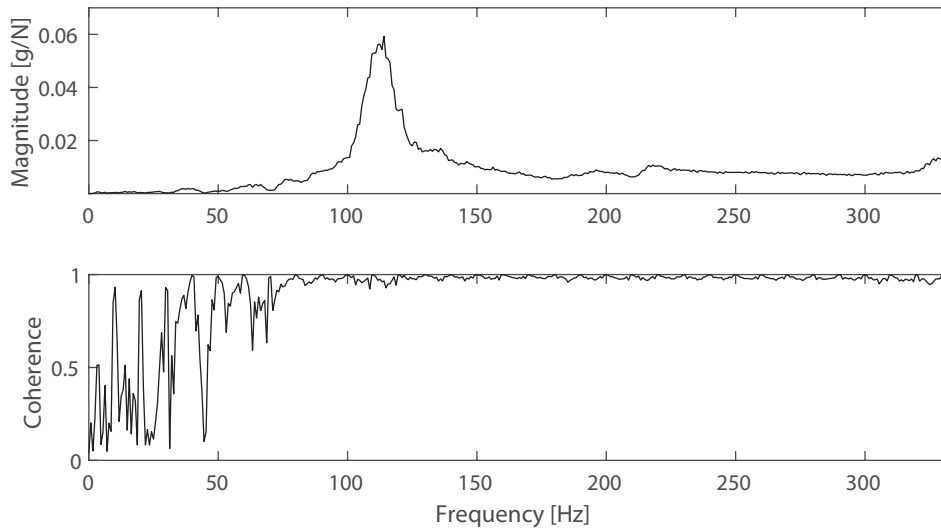
Fig. 5.8 The spindle's H1 estimated FRF.

The vibration safety limit is set to 7 mm/s (taken for ISO Standard 20816-1 [185]) while it is allowed to slightly overcome it during transient states of spin up or down. It must be noted that this vibration level is less conservative than what the manufacturer of the spindle has established, who sets a warning level at 3.5 mm/s rms for tools with an HSK attachment and strongly discourages overcoming 6mm/s rms. The consideration made is that tests are short and discontinuous as opposed to a conventional manufacturing process, which is continuous.

Acceptable running conditions are those within safety limits (i.e., below 7 mm/s rms). The FRF shows that running at 70 Hz is acceptable for acquiring balancing data (and balancing), given that any irregularity will be detected before reaching the natural frequency. Experience has shown that vibration levels remain safe, even at the natural frequency, if samples do not exceed 0.5 mm/s RMS at 70 Hz. Nevertheless, it is advisable to cross the natural frequency at high accelerations, which is common practice with unbalanced rotors.

Stage setup and testing

After the samples are safely placed, the stage is set to a distance of 500 μm from the ceramic sample. Then, the test parameters (speed and incursion rate) are entered in LabVIEW, and the spindle is powered (monitoring vibrations for safety reasons). The test is performed once the testing speed is reached.

The only process the program performs is to move the stage while recording data. The coded movements are three and can be distinguished from Fig. 5.9, displaying data collected with a laser displacement sensor (Micro-Epsilon UK Ltd., Laseroptical displacement sensor ILD 1320-10, range 10 mm, measuring rate up to 2 kHz). There is an initial approach at high speed that moves 500 μm at 0.5 mm/s. Recalling that the stage's position is initially

-500 μm; thus, the contact is expected after this movement. Subsequently, the test incursion starts, undergoing another 500 μm movement but this time at the test incursion rate (0.31 or 1.71 μm/pass). Finally, the stage returns to the initial position with a fast retract of 1 mm at 0.5 mm/s. As shown in the figure there are short interruptions between movements. These are approximately 73ms in length and have been related to the processing time of LabVIEW and the stage. The total incursion of 500 μm was chosen with Rolls-Royce as being representative within aero-engines.
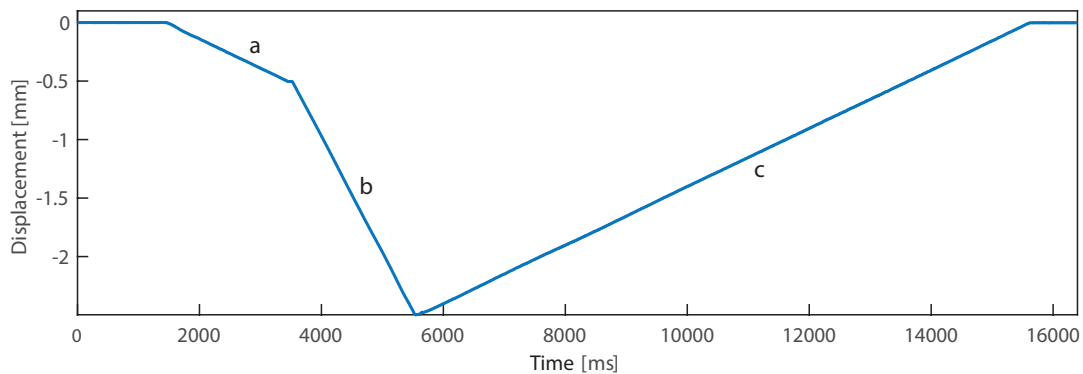
Fig. 5.9 Example incursion profile recorded with a laser displacement sensor. Negative displacement denotes stage approaching the sensor (and the ceramic sample). In this case showing a test incursion of 2 mm at $\approx$1 mm/s. Labels: (a) Approach at 0.5 mm/s; (b) Incursion period; (c) Retreat at 0.5 mm/s.

It must be noted that samples expand because of centrifugal loading, and with this approach, contact happens slightly before the end of the approaching period. The method has been changed for later experiments so that the first contact happens at the test incursion rate, i.e., the initial approach is changed to 300 μm and the test incursion to 700 μm while maintaining the initial position of the stage (500 μm below the coating). Thus, the full incursion remains close to 500 μm, and the initial contact is now ensured to happen at the test incursion rate.

5.1.4   Measurements

The chosen measurements are numerical and optical descriptors of the tribological process. Forces and temperatures are in-situ numerical measurements for which data acquisition and processing has been described in depth previously in Sections 4.1 and 4.2, and will thus not be covered again. This section will extend the explanation of the high-speed camera images as in-situ optical descriptors of the rub and will cover the acquisition of second-level numeric descriptors such as force ratio and specific grinding energy (SGE). Furthermore, postmortem techniques such as weight measurements of the blades and sample preparation for SEM images will also be included herein.

High-speed camera rub images

Section 4.3 described how the camera was set up and how images are acquired and processed to sense the evolution of the surface through time, e.g. to observe how pickup progresses through time. In addition, images are acquired during tests with a 20% overlap so that they can be stitched together and visualise the surface at any point in time. This process is achieved with Photoshop's 'Photomerge' tool with no correction applied; images are only repositioned. The stitching process is most useful when there are contrasts/features in the images; thus, consecutive images will be presented in the absence of evident patterns to match (e.g. in the presence of smooth surfaces with constant tone).

Although a panoramic image serves the same purpose, stitching images has been favoured as it does not correct for light non-uniformities between images, i.e., it does not correct the colour between image borders.

Force ratio

The force ratio is calculated from the normal and tangential forces. For each point in time, the quotient between tangential force and normal force is computed, and if a mean is required, then the average force ratio is calculated over the contact time. Mathematically expressed, the equation followed is:

$$F_{rat}(t) = \frac{F_t(t)}{F_n(t)} \tag{5.2}$$

where $F_t(t)$ and $F_n(t)$ respectively corresponds to tangential and normal force at the same instant in time, and $F_{rat}(t)$ denotes to the time dependent force ratio.

Specific Grinding Energy (SGE)

SGE is a metric commonly used for evaluating the efficiency of grinding processes (efficiency is the inverse of the energy). In this research, the definition of work has been used to calculate the energy of the contact. First, normal and tangential forces are integrated over time and then each force is multiplied by the relative moving speeds in their direction. This operation assumes that speed is constant during the incursion and is mathematically expressed as:

$$W_z = \int F_z \cdot v_z \, dt = v_z \int F_z \, dt \qquad | \qquad W_y = \int F_y \cdot v_y \, dt = v_y \int F_y \, dt \tag{5.3}$$

where v_z and v_y are respectively the velocities in the normal and tangential direction, namely, the incursion speed and the ceramic surface's speed.

Finally, work is divided by volume removed to yield SGE:

$$SGE = \frac{W_z + W_y}{V} \qquad [\text{J/mm}^3] \tag{5.4}$$

The volume removed is estimated from the measured weight and taking the density of Inconel as 8.192 g/cm^3. An experimental incursion of 500 μm does not necessarily mean that an equivalent amount of material is removed; it will depend on the tribological process. Thus, the more empirical approach of measuring the weight and calculating the volume, as it is felt this gives a better estimate of the SGE than using input process parameters.

Weight

The weight of each blade is taken before and after testing with a scale (Fisher Scientific, Analytical series, 0.1 mg precision). For both cases, three weight measurements are performed and the average is calculated.

SEM: Sample preparation and imaging

The rub track of each sample was divided into four different sections as illustrated in Fig. 5.10. Sections labeled as '1' and '4' are left untouched for visualising the nature of the adhesion, whilst sections '2' and '3' are then impregnated with A8 resin and mounted in conductive Bakelite. The purpose of the latter two is to visualise the coatings in the longitudinal and transverse directions of the rub track. Hence, these samples are also prepared for SEM. It must be noted that Rolls-Royce provided material preparation support given that there were access issues due to the Covid-19 pandemic at the University. Thus, the directions given are the ones that have been discussed. SEM images are taken with the backscattered and EDX options.
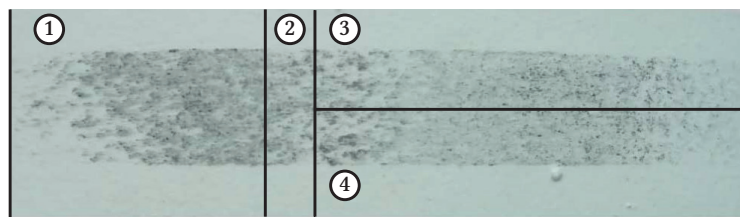
Fig. 5.10 Typical alumina sample after testing, illustrating with lines where cuts are performed.

5.2 Results

A preliminary analysis of the data identified speed and material as the dominant variables by far; see factors *A* and *B* from the half-normal plots in Fig. 5.11. Whilst this is possible, it is actually the premise that speed is not the main factor upon which the use of simplified test platforms is supported (Section 3.1.4). Additionally, it is also not consistent with the literature on grinding [194, p. 172], and samples were also observed to fail in a particular way. Upon further investigation and as shown in the proceeding paragraphs, evidence was found that these results are not entirely a consequence of the coatings but also include the effects from the spraying process annealing the aluminium substrate and the sample–mandrel assembly introducing uneven stresses.

(a) Half-normal plot of normal forces

(b) Half-normal plot of tangential forces

Labels	
A (Speed)	
C (Incursion Rate)	
B (Material)	
D (Surface)	
E (Spraying)	

(c) Half-normal plot of apparent temperature
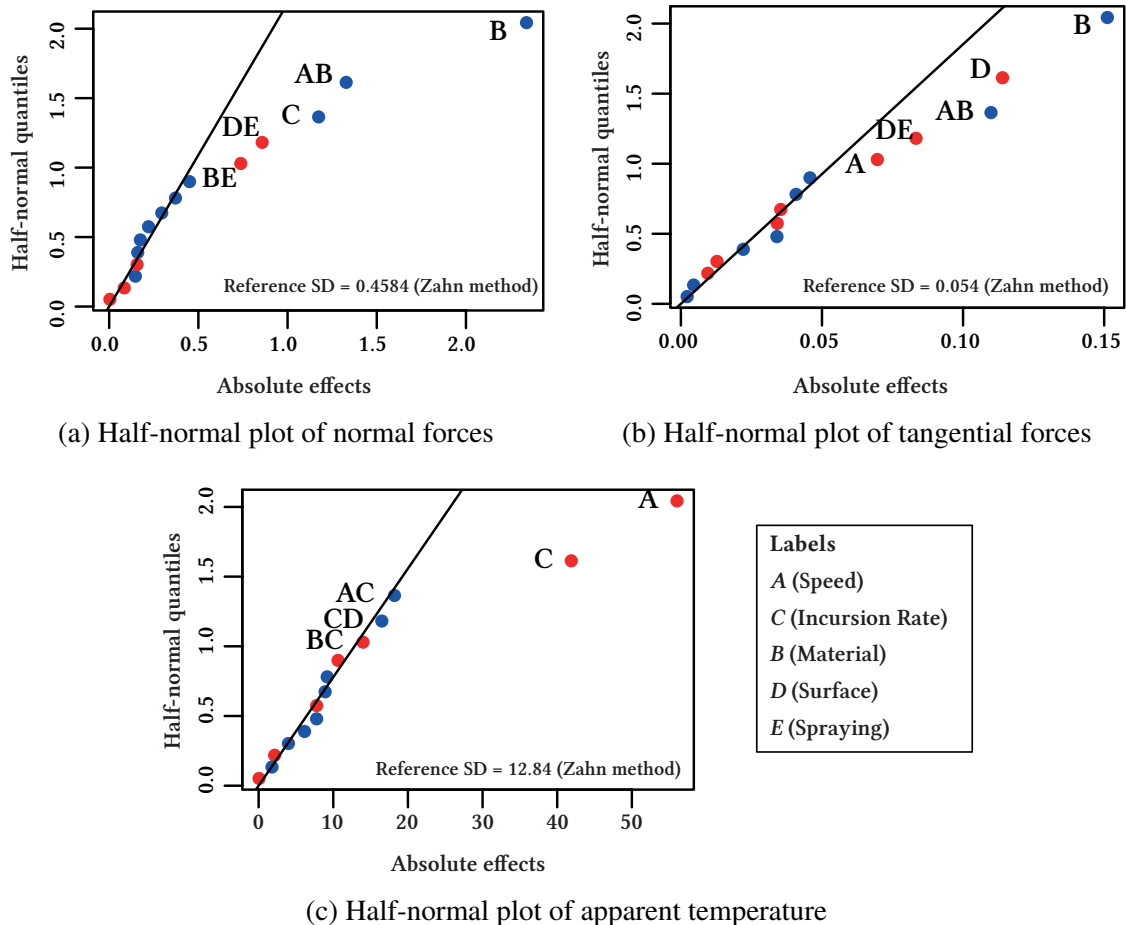
Fig. 5.11 Half-normal plots of forces and apparent temperature for the 16 tests performed. Red has been used to represents negative values and blue for positive.

It was observed that coatings, particularly alumina ones, would generally burst before achieving 185 m/s, and substrates would exhibit plastic deformations after dismounting. As this should not happen based on the stress calculation in Section 3.2.1, Vickers hardness of

substrates was taken as a proxy to tensile strength (Fig. 5.12), and a one-way ANOVA test revealed a highly statistically significant difference between coatings (p-value <0.0056). It coincides that the high heat resistance polymer moulds had been noted to burn during the thermal spraying process of alumina, and in turn, the alumina samples yielded the lowest hardnesses. It is thus concluded that indeed there is a difference between coatings, and this is due to the spraying process annealing the aluminium substrate when spraying alumina, as opposed to any effect due to the coating itself.
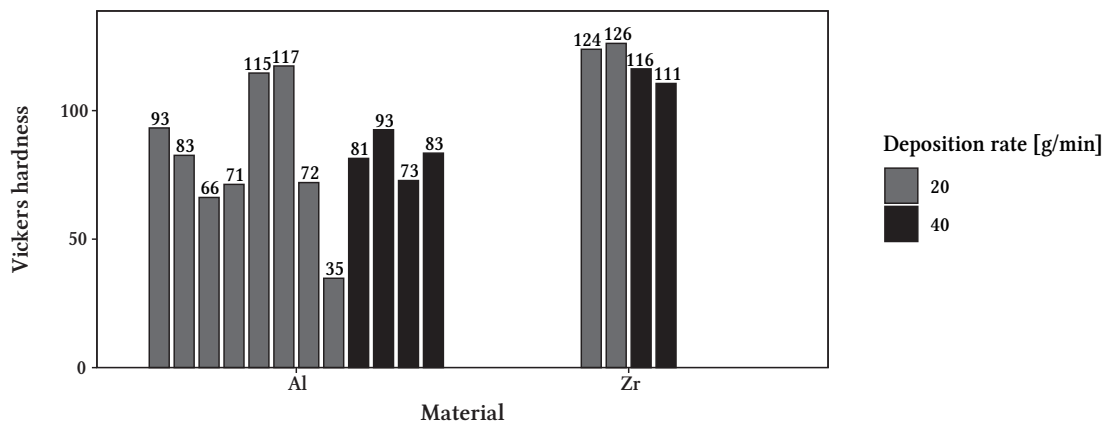
Fig. 5.12 Plot showing the Vieckers Hardness of alumina and zirconia samples sprayed at two different conditions. Each value is the average of 3 measurements taken different positions around the aluminium ring.

Going back to the more general large effect of speed, this is likely due to the mandrel. Fig. 5.13 shows an image of a typical sample after failure of the coating. As shown in the figure, large scale delamination occurs at the bond coat level, predominately at the inner side of the sample. In addition, samples are plastically deformed showing a taper.
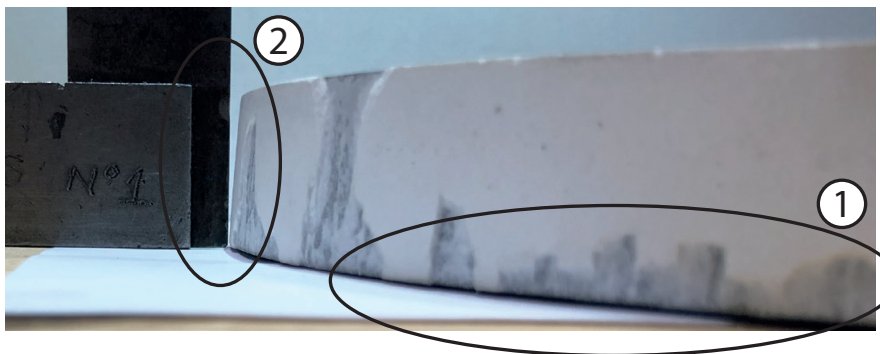
Fig. 5.13 Sample of Alumina after failure at 185 m/s without testing. Label (1) indicates delamination occurring at the inner side of the mandrel (axially), label (2) shows that the sample has plastically deformed with the inner side showing larger deformation than the outer. These coincide with labels in Fig. 5.14: inner is "A2", outer is "A1".

These characteristics can be related to features on the expandable sleeve provided in Fig. 5.14. The "L" shaped profile (e.g. seen in section A) means that uneven stresses are introduced into the samples (and intralaminar in the coatings) when these are centrifugally loaded. It can be seen from segment "A" that higher hoop stresses result in section "A2" than in section "A1", explaining why samples display a taper when plastically deformed and coatings delaminate.
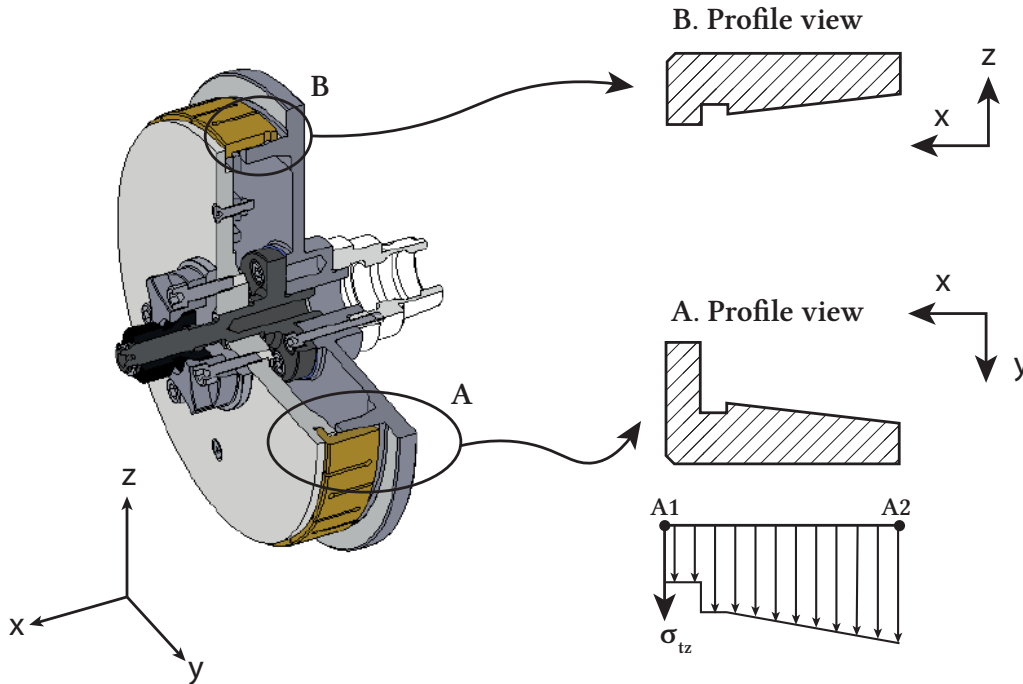
Fig. 5.14 Image displaying a section of the mandrel in isometric view, and illustrating the stresses in the profile of the expandable sleeve (not to scale), which are identified with labels "A" and "B".

It is also clear from Fig. 5.14 that sections "A" and "B" are different. Precisely at point "B" (and symmetric about the axis of rotation), the profile shows a reduction in size so that it can be held in place by two inserts. In addition to the deformations explained in the previous paragraph, these two regions will accumulate hoop stresses and consequently show higher absolute deformations when centrifugally loaded, yielding an oval shape. This would explain why samples consistently show one or two symmetric contacts in the same positions regardless of how the samples were placed on the mandrel.

As such, it is clear that whilst a relationship with speed does indeed exist, this is a consequence of the test set up, and indeed sample preparation in some cases and is therefore not appropriate for considering when assessing the variables influencing the tribological response of the contact. It is interesting to note, however, that large scale delamination was already

identified in Section 1.5 when discussing how these coatings typically fail in aero-engines. In such a case, large scale delamination is usually related to an inappropriate manufacturing process or selection of the coating. The equivalent happens here with the result that a ceramic coating is subjected to interlamellar stresses.

In conclusion, since experimental design cannot purposely control the deformation of the substrate when changing speed, the latter is chosen for the remainder of this research and speed is dropped from consideration. In addition, since annealing effects are aggravated at higher speeds, the decision was taken to continue the analysis only considering samples running at 115 m/s (there is no evidence that annealing has an effect at this speed). The resulting experimental design is reduced to a half-factorial 2_{IV}^{4-1} design with factors B, C, D, and E (i.e., material, incursion rate, surface finish, and spraying).

5.2.1 Processed results

The proceeding section will present the results of the screening experiment only examining samples tested at 115 m/s. The aim is to identify the most influential factors, and thus, only mean values are considered; time-dependent mechanisms will be studied in the next chapter. As for the structure, the first part of this section will present images of the eight tests being considered, providing a visual description of the tests and general behaviours of the samples. The second part will present first level numerical descriptors (material loss, forces, and apparent temperature) and secondary level descriptors (force ratio and specific grinding energy).

Fig. 5.15 shows that as-sprayed surfaces tested at a low incursion rate result in a single contact with a very light secondary one. Adhesion in the leading side is relatively square to the back-plate of the mandrel, and both sides of the rub track having a similar length (indicating that deformations in the samples are fairly uniform). The adhesion itself can be described as a series of two regions that alternate: a region where local initiation with propagation occurs and another showing a more uniform appearance. The labels L for "localised" and U for "uniform" have been used to identify these regions. It can be seen that the alternating frequency of these patterns is higher on image B (corresponding to zirconia), and the surface exhibits a more uniform overall appearance of the rub track. A possible explanation for this might be the better flowability of zirconia's HOSP powders compared to alumina's (of angular/blocky morphology). As mentioned in the literature review (Section 2.6.2), an enhancement in flowability translates into more regular deposition rates and thus coatings of higher consistency. Although further research would be needed to confirm this relation, a more even topology and uniform contact for the zirconia coatings would explain the observations. Regarding the blade samples, both show an equivalent level of thermal discolouring (label T) and show a lip-like formation that extends out of the trailing edge of the blades.
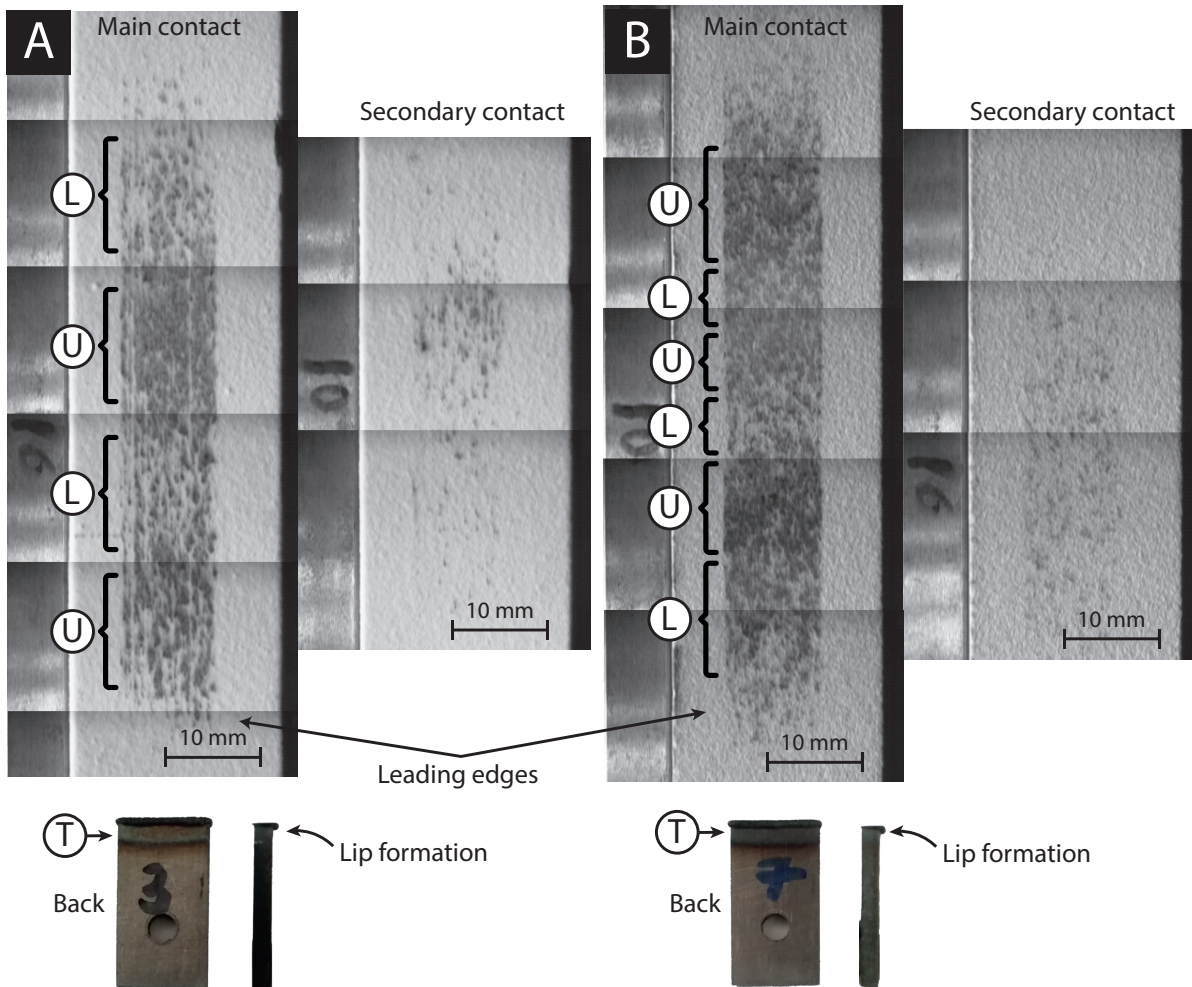
Fig. 5.15 Stitched images of alumina and zirconia coatings in their as-sprayed condition after being tested at 115 m/s and 0.31 um/pass. The tests names are Al-0.31-AS-40-100 and Zr-0.31-AS-20-150, which correspond respectively to images "A" and "B". The images also include a side view of the blade and a back view (front side is covered in high emissivity paint). The labels denote: (L) Region of coma-like localised adhesion; (U) Region with a more uniform adhesion; (T) Region corresponding to thermal discolouring of the blade samples.

When comparing as-sprayed samples for both materials tested at a higher incursion rate (see Fig. 5.16), these tests show a more evident secondary contact that also increases in length; the main contact does not show any evident difference in length. However, the appearance of the adhesion does seem different to that previously seen at lower incursion rates. The same labels *U* for "uniform" and *L* for "localised" adhesion have been used, and it can be observed that the proportion of uniform adhesion has incresead with respect to what is seen at low incursion rates. The number of transitions between regions has also reduced: the alumina sample's main contact now shows a single transition (previously two), whilst the secondary contact

shows two transitions; for the zirconia sample, its main contact also shows a single transition (previously three), and the secondary contact remains fairly uniform. Furthermore, zirconia (in image *B*) now shows signs of a more severe form of adhesion, which could be described as the beginning of galling. This has been labeled *S* for "severe". Concerning the blades, their thermal decolouring (label *T*) is again equivalent between both samples but arguably smaller to that previously shown when addressing as-sprayed surfaces tested at a lower incursion rate. In addition, whilst the blades tested against as-sprayed zirconia still forms a lip, the blades tested against as-sprayed alumina do not.
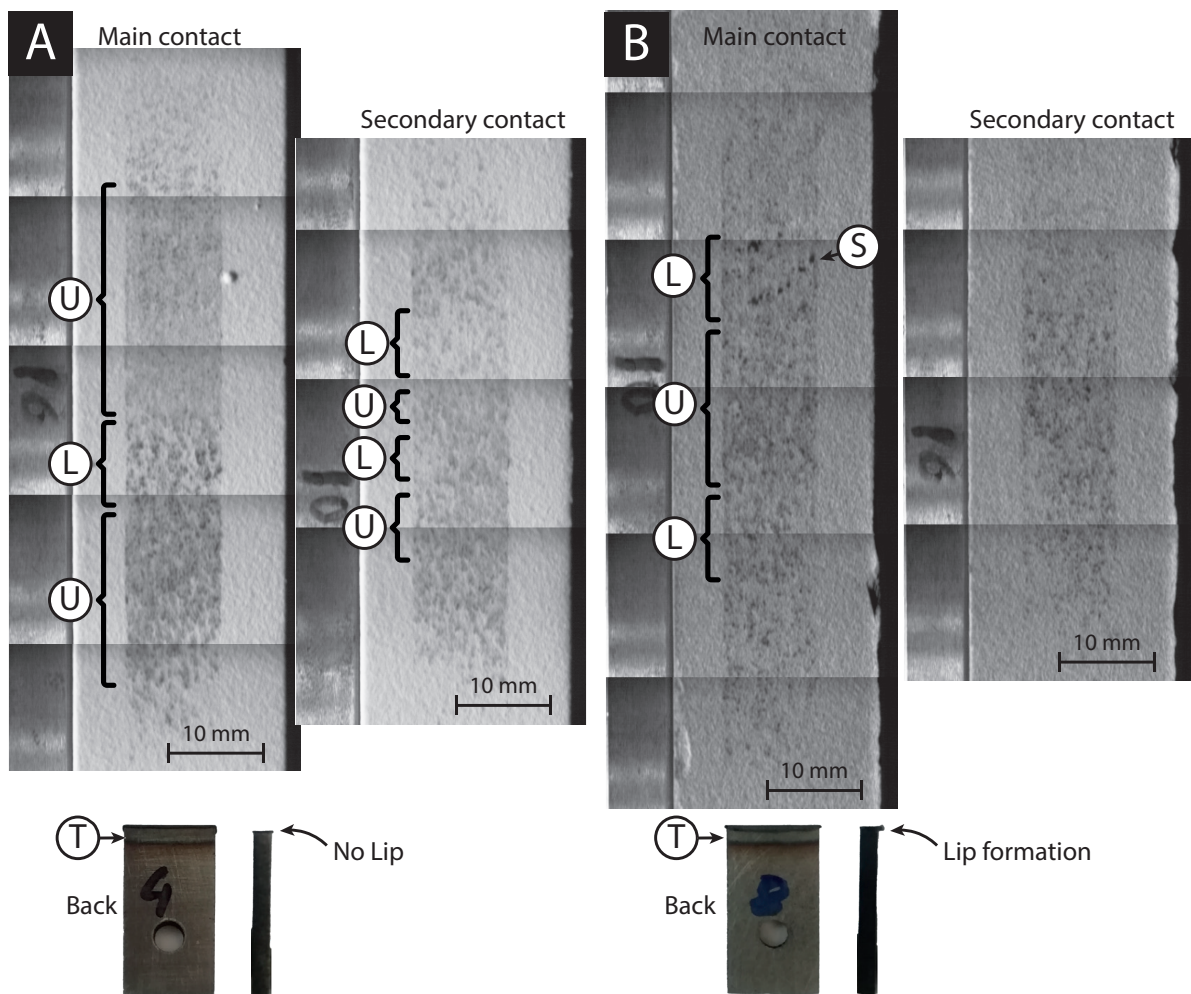
Fig. 5.16 Stitched images of alumina and zirconia coatings in their as-sprayed condition after being tested at 115 m/s and 1.71 um/pass. The tests names are Al-1.71-AS-20-150 and Zr-1.71-AS-40-100, which correspond respectively to images "A" and "B". The images also include a side view of the blade and a back view (front side is covered in high emissivity paint). The labels denote: (L) Region of coma-like localised adhesion; (U) Region with a more uniform adhesion; (T) Region corresponding to thermal discolouring of the blade samples; (S) Severe form of adhesion.

Considering now samples with a trued surface (see Fig. 5.17 and Fig. 5.18), these show distinctively longer arc of contact than those attained with as-sprayed surfaces. The trued alumina sample tested at 0.31 um/pass shows two contacts and the longest arc of contact amongst all (including as-sprayed coatings). At this condition, adhesion increases rapidly at the leading side (label *LS*) and decreases more gradually with a longer tail at the trailing side (label *Tr*). This similarly happens with the trued zirconia sample, albeit with a significantly shorter arc of contact. In both cases, adhesion has a more uniform appearance than that shown with as-sprayed samples. However, whilst alumina shows a continuous adhesion, zirconia is divided into two areas and shows signs of more severe adhesion (label *S*).

The appearance of trued coatings at higher incursion rates is significantly different (see Fig. 5.18). Trued alumina shows a single contact and shows a scar. On the other hand, zirconia shows a double contact, and the rub track appears lighter than the initial trued surface. When considering the thermal discolouring of the blades, these show the same pattern as previously described: affected areas are distinct between incursion rates whilst being very similar at the same incursion rate. Furthermore, the affected areas seem to be indistinct from those happening when testing against as-sprayed coatings. However, the lip-like material formation does seem to have been reduced when testing trued coatings at high incursion rates.
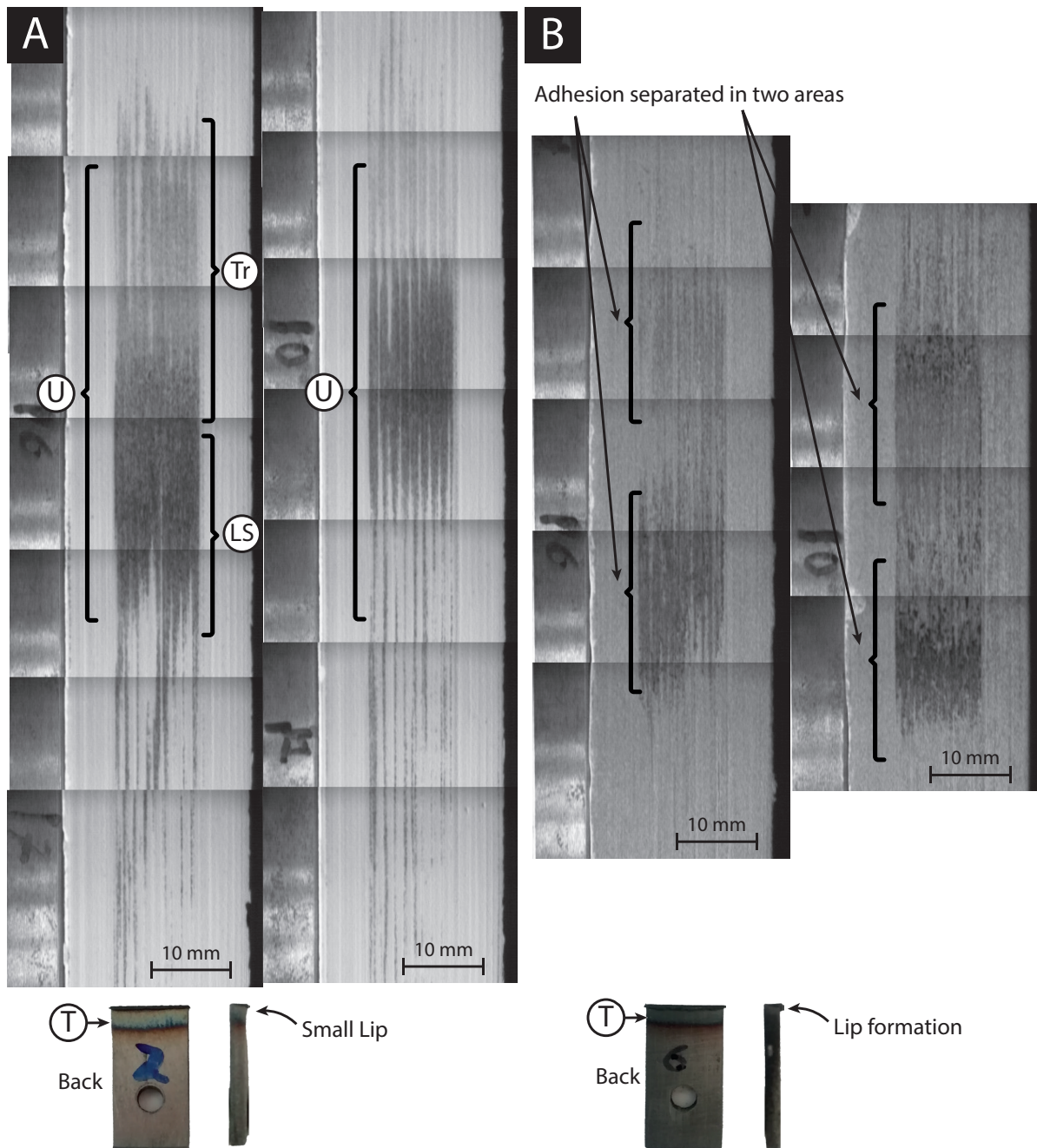
Fig. 5.17 Stitched images of alumina and zirconia coatings in their trued condition after being tested at 115 m/s and 0.31 um/pass. The tests names are Al-0.31-True-20-150 and Zr-0.31-True-40-100, which correspond respectively to images "A" and "B". The images also include a side view of the blade and a back view (front side is covered in high emissivity paint). The labels denote: (U) Region with a more uniform adhesion; (T) Region corresponding to thermal discolouring of the blade samples; (S) Severe form of adhesion.
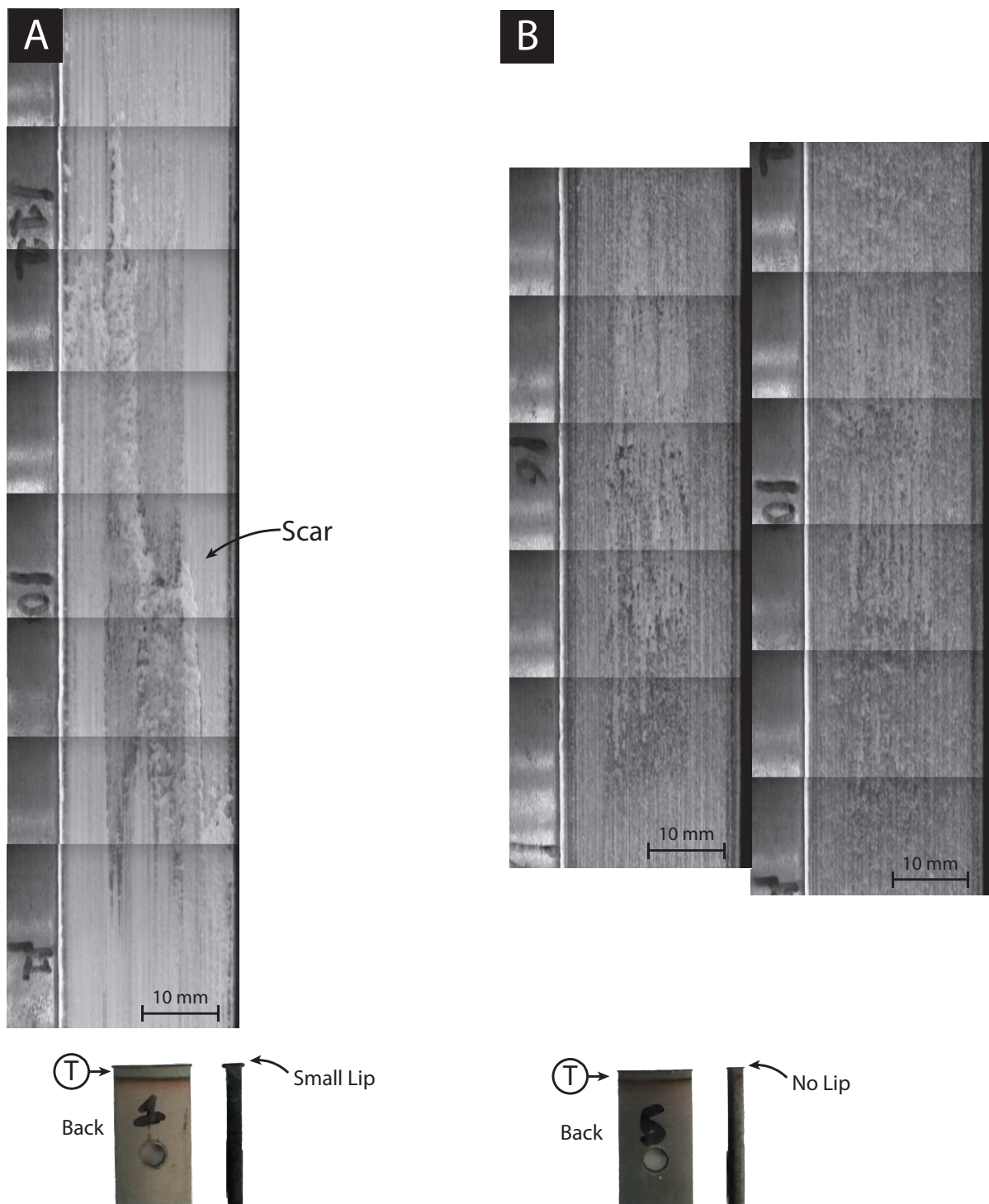
Fig. 5.18 Stitched images of alumina and zirconia coatings in their trued condition after being tested at 115 m/s and 1.71 um/pass. The tests names are Al-1.71-True-40-100 and Zr-1.71-True-20-150, which correspond respectively to images "A" and "B". The images also include a side view of the blade and a back view (front side is covered in high emissivity paint). The labels denote: (T) Region corresponding to thermal discolouring of the blade samples.

Inspecting the wear scars has highlighted differences in appearance between samples tested at different conditions. Below, the relationship between samples will be further investigated using the numerical descriptors of the contact. Table 5.3 summarises the time domain data and assigns the numerical response to the samples' treatment combination. The resulting relationships can be visualised in Fig. 5.19, a cube plot illustrating the 2^{4-1}_{IV} statistical design. The factors being considered are material (B), incursion rate (C), surface (D), and spraying (E); speed (A) has been dropped from consideration. As such, the numerical descriptors will be examined in the order presented in Table 5.3.

Table 5.3 Table collecting time-domain average data of tests at 115m/s. The model is reduced to 2^{4-1}_{IV} after dropping speed (A) from consideration and has a defining relation $I = ABCDE$

	Basic design											
Run	*A*	*B*	*C*	*D*	*E = ABCD*	**T.C.**	**M**	**NF**	**TF**	**T**	**F.ratio**	**SGE**
1★	−	−	−	−	−	(1)	-0.1067	4.68	1.40	813.81	0.31	116.73
2★	−	+	−	−	+	be	-0.0816	8.73	1.45	811.54	0.17	156.46
3	−	−	+	−	+	ce	-0.0718	9.61	1.68	702.18	0.18	53.97
4★	−	+	+	−	−	bc	-0.0570	9.06	1.65	617.08	0.20	61.19
5	−	−	−	+	+	de	-0.0565	6.85	1.13	789.57	0.17	168.58
6	−	+	−	+	−	bd	-0.0779	9.64	1.49	825.65	0.16	169.27
7★	−	−	+	+	−	cd	-0.0979	7.61	1.40	709.65	0.19	30.65
8★	−	+	+	+	+	bcde	-0.0858	9.41	1.35	731.01	0.15	37.26

Table 5.3 abbreviations: *T.C.* Treatment combination; *M* Matrial loss [g]; *NF* Normal force [N rms]; *TF* Tangential force [N rms]; *T* Apparent temperature [ºC]; *F.ratio* Force ratio [-]; *SGE* Specific grinding energy [J/mm^3] ; ★ Denotes double contact.
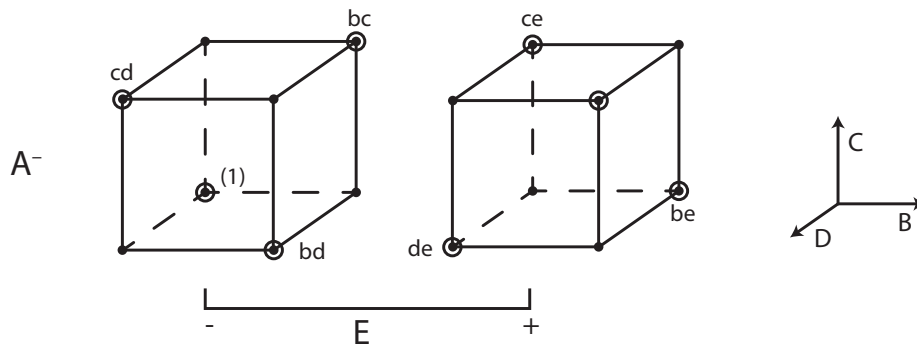
Fig. 5.19 Pictorial representation of the 2^{4-1}_{IV} design after dropping speed (A) from consideration.

Material loss

Given the nature of the experimental design, direct comparisons between tests are not possible, and relationships are only revealed by subsequent statistical analysis of the data. However, some clear trends are visible from inspecting the mass loss measurements presented in Fig. 5.20. Therein, tests are grouped by material and colour coded in pairs to distinguish incursion rates and surface type. Further, the character '*' is used to identify those samples showing a double contact instead of a single one.
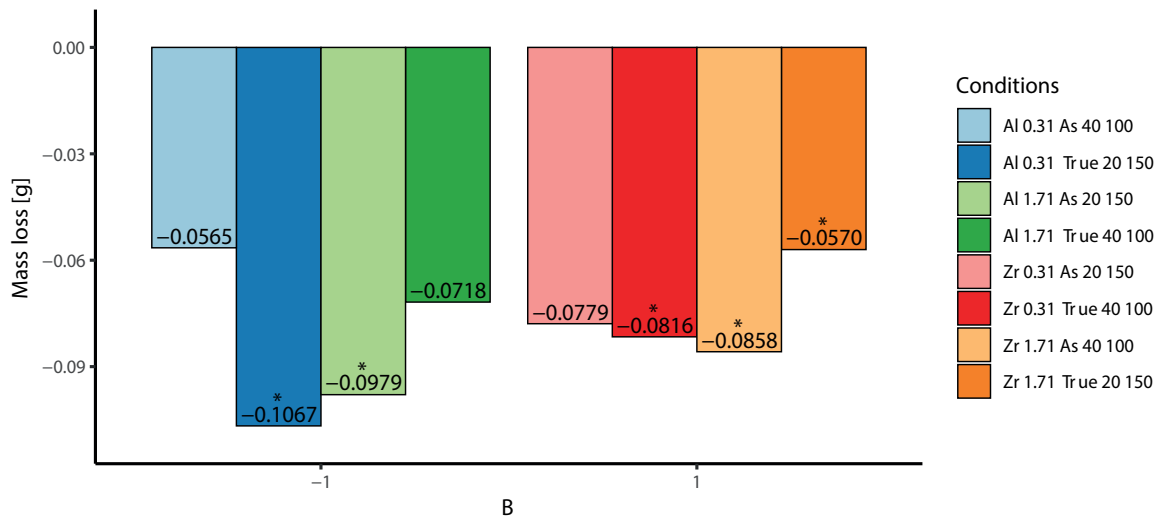
Fig. 5.20 Bar chart of blade material loss. (*) Denotes double contact.

The latter figure shows that as-sprayed and trued surfaces behave distinctively depending on the incursion rate and the material. At the lower incursion rate of 0.31um/pass, differences between surfaces are sharp for the case of alumina, with the trued case removing significantly more material. Conversely, weight differences for zirconia remain fairly constant. It is worth noting that due to the DoE, spraying could equally be the dominant factor since it has also changed. Moving to the higher incursion rate (1.71 um/pass), the material removed is now reduced with truing for both materials, where spraying is again a variable. It is interesting to note in this latter case that material loss is consistently reduced whilst spraying is varied in the opposite sense with respect to as-sprayed vs trued samples for each material.

In order to explore these relationships further and decouple variables, the data presented earlier in Table 5.3 has been statistically analysed. Table 5.4 contain a summary of the results, which have been calculated by fitting a linear model with the R function 'lm' [195]. It should be noted that effects are aliased due to the DoE.

Table 5.4 Estimate of effects and alias structure for weight loss.

Results		Legend		
Estimated effect	**Aliasing structure**	**Factor**	**-1 Level**	**+1 Level**
$[B] = \quad 0.0038$	$[B] \rightarrow B + CDE$	B: Material	Alumina	Zirconia
$[C] = \quad 0.0013$	$[C] \rightarrow C + BDE$	C: Incursion	0.31 um/pass	1.71 um/pass
$[D] = -0.0001$	$[D] \rightarrow D + BCE$	D: Surface	Trued (smooth)	As sprayed
$[E] = \quad 0.0055$	$[E] \rightarrow E + BCD$	E: Spraying	20	40
$[BC] = \quad 0.0029$	$[BC] \rightarrow BC + DE$			
$[BD] = -0.0062$	$[BD] \rightarrow BD + CE$			
$[BE] = -0.0136$	$[BE] \rightarrow BE + CD$			

The effects shown in Table 5.4 can also be visualised with a half-normal and Lenth's plot (Fig. 5.21), with these two figures used in combination to identify significant factors influencing material loss. The functions 'parplot' and 'hnplot' from the R package 'unrepx' [196] have been used in this case.
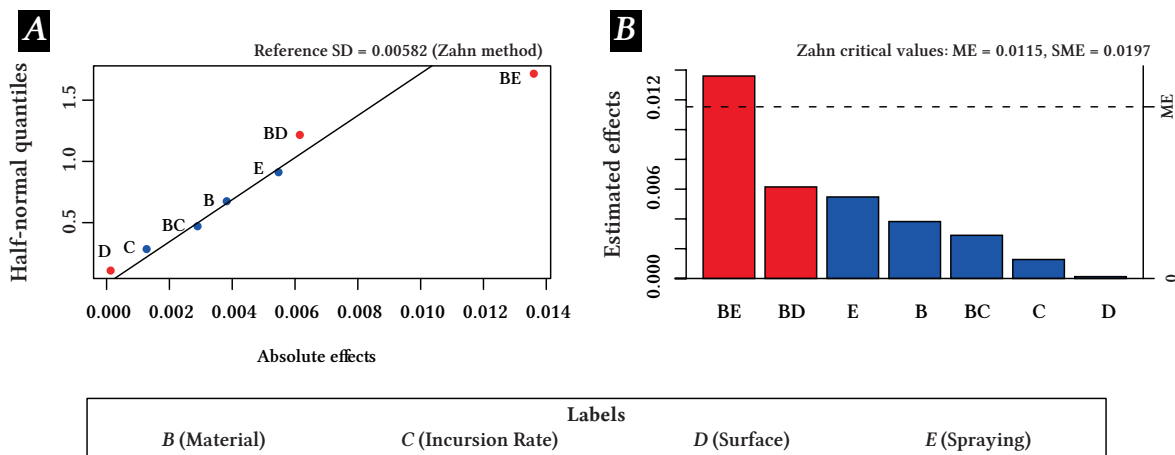
Fig. 5.21 Half-normal (*A*) and Lenth's plot (*B*) for weight change. Red has been used to represents negative values and blue for positive.

Table 5.4 and Fig. 5.21 show that material and spraying are the strongest variables; incursion rate and surface finish follow, with the latter having a minimal impact. These results are in line with the observations previously made regarding Fig. 5.20 and provide further insight. When the results were first inspected, the influence of surface (as-sprayed vs trued) was difficult to determine, and it is now clear, based on the limited influence of surface finish (*D*), that the changes observed were due to a combination of material (*B*) and spraying (*E*). This outcome highlights the importance of material in general in the observed wear mechanic for the stator-blade/rotor system, particularly when the strength of its interactions is also considered (*BE*).

Further, as shown in Fig. 5.21, higher incursion rates also lead to a slight increase in material loss, with this effect masked in the initial results given the strength of the variables related to material and their interaction. Table 5.5 summarises these relationships after dropping the surface finish (*D*) from consideration, where strength, direction, and relative importance of both variables and interactions are shown.

Table 5.5 Summary of estimate effects for material loss

Factor	Effect estimate	Sum of Squares	Percentage Contribution*
B (Material)	0.0038	0.000117	5.27
C (Incursion rate)	0.0013	0.000013	0.59
E (Straying)	0.0055	0.000240	10.80
BC	0.0029	0.000067	3.03
BE	-0.0136	0.001480	66.67
CE	-0.0062	0.000303	13.63

* % Contribution = factor's sum of squares/Total sum of squares

Further work on the model is commonly carried out to validate the predicted values and the quality of the model. It is worth noting that it would be unrealistic to expect an accurate estimate for mass loss from these results, given the complexity of the blade/rotor system and the small number of observations. Hence, such work is not included. An ANOVA test is carried out notwithstanding, and the results are included in Table F.1 from Appendix F.

Normal force, tangential force and temperature

Equivalently to what has been done previously with material removal, a bar plot has been included herein (Fig. 5.22). In this case the plot presents the measurements of normal and tangential force, as well as apparent temperature. The same colour code has been employed to distinguish between materials, surfaces, and incursion rates; the character '*' identifies those samples that show a double contact instead of a single one.
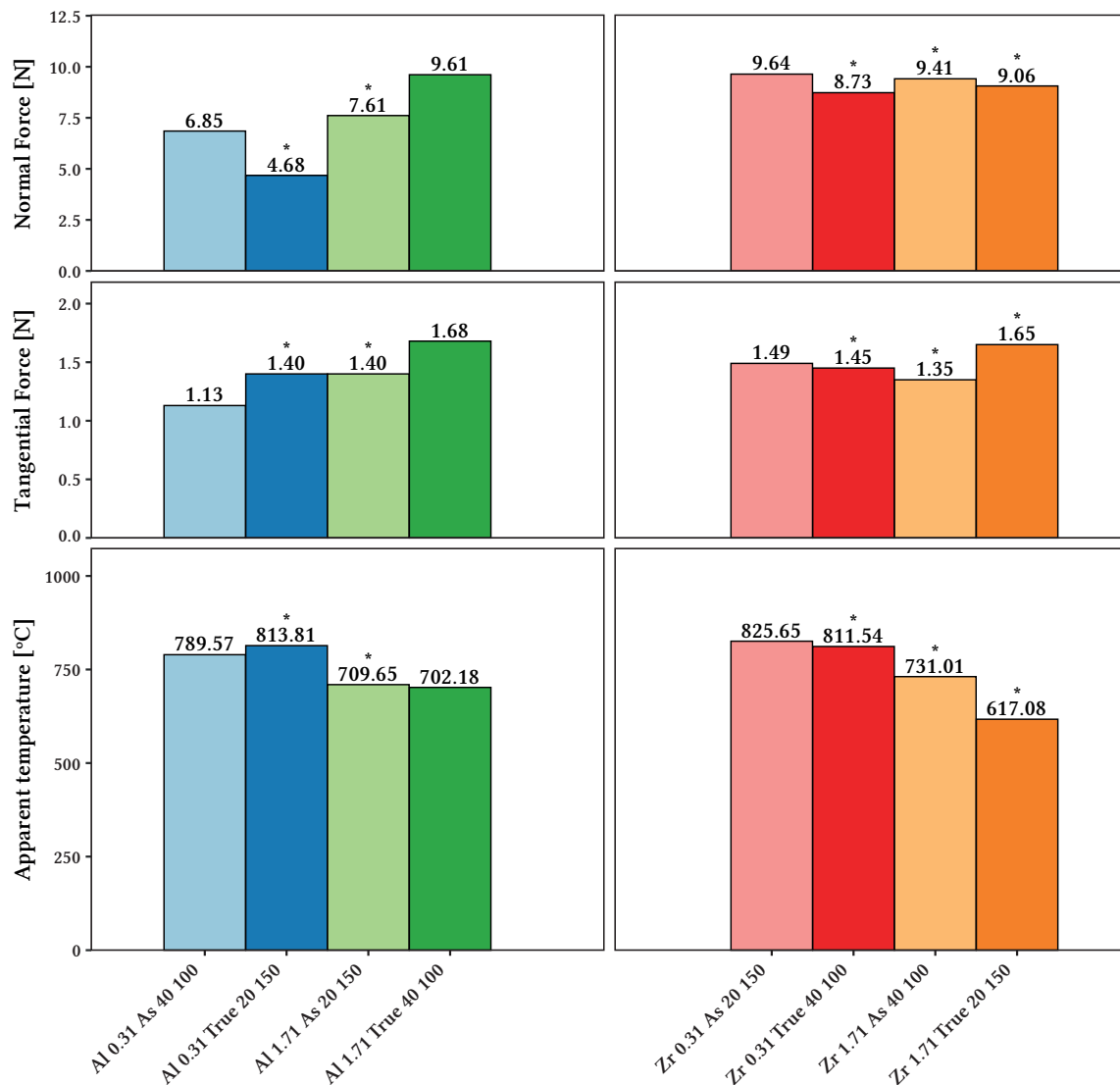
Fig. 5.22 Bar chart of forces and apparent temperature. (*) Denotes double contact.

Inspecting the results once again, trends in forces and temperatures are evident when comparing materials. Zirconia shows almost constant normal and tangential forces regardless of changing spraying condition, surface, or incursion rate. In contrast, alumina displays more significant variations, showing that normal and tangential forces increase when moving from 0.31 um/pass to 1.71 um/pass. Further, trued surfaces generally yield higher normal and tangential forces, except at 0.31 um/pass, where the as-sprayed surfaces yield higher normal forces. Shifting from 0.31 um/pass to 1.71 um/pass is also accompanied by a drop in temperature, with very slight differences happening between materials and surface finish; zirconia at 1.71 um/pass showing the most significant variations when comparing the as-sprayed

and the trued condition. However, the latter relationship could also be due to a shift in the spraying condition given the DoE factors are aliased, and this will now be explored.

As before, a linear model is fitted to each of the measurements for investigating the results statistically. The estimated effects are included in Table 5.6, which are visualised through a half-normal and Lenth's plot (Fig. 5.23, 5.24, 5.25).

Table 5.6 Estimate of effects and aliase structure for normal force, tangential force, and apparent temperature.

Factor	Estimated effect*			Aliasing structure
	Nor.	Tan.	Tem.	
B (Material)	1.01	0.04	-3.74	$B \rightarrow B + CDE$
C (Incursion)	0.72	0.08	-60.06	$C \rightarrow C + BDE$
D (Surface)	0.18	-0.10	13.91	$D \rightarrow D + BCE$
E (Spraying)	0.45	-0.04	8.51	$E \rightarrow E + BCD$
BC	-0.70	-0.06	-12.19	$BC \rightarrow BC + DE$
BD	0.14	0.04	18.10	$BD \rightarrow BD + CE$
BE	-0.59	-0.04	16.44	$BE \rightarrow BE + CD$

* Values acquired by fitting a linear model to the data and treatment combinations of Table 5.3. The 'lm' R function is used for this.

Fig. 5.23 Half-normal (A) and Lenth's plot (B) for normal force. Red has been used to represents negative values and blue for positive.

Fig. 5.24 Half-normal (*A*) and Lenth's plot (*B*) for tangential force. Red has been used to represents negative values and blue for positive.
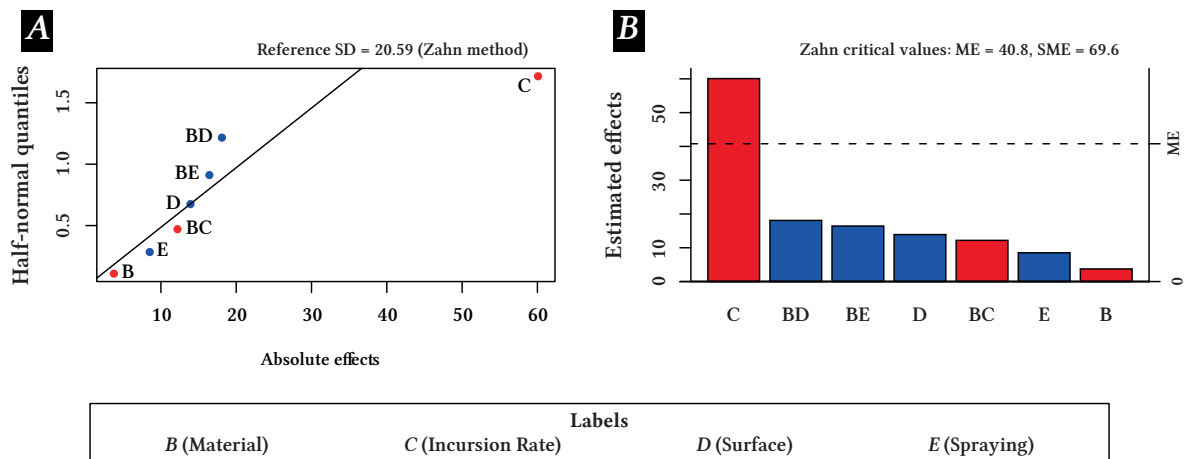
Fig. 5.25 Half-normal (*A*) and Lenth's plot (*B*) for apparent temperature. Red has been used to represents negative values and blue for positive.

The statistical results show that incursion rate (*C*) has a notable influence on all three metrics, with the most evident impact on temperature. The picture is then mixed for the other variables, with them showing a less consistent effect on the measured outputs. It is interesting to observe that, whilst material (*B*) dominates on normal forces, its influence on tangential forces and temperature is minimal and comparable to the effect of spraying (*E*). On the other hand, surface (*D*) has an almost negligible effect on normal forces yet outweighs the rest of the variables' effects on tangential forces and has a small but notable impact on temperature.

These results differ from those seen previously for material loss and provide a deeper understanding of the stator-blade/rotor system. A relation between normal force and material loss is apparent, with material (*B*), spraying (*E*), and their interaction (*BE*) having the largest

effects. Conversely, the influence of these factors is almost insignificant on tangential forces and temperature, and it is the effect of incursion rate (*C*), exclusively or with surface (*D*), that dominates instead. Normal forces commonly indicate grain penetration (sharpness and size of grain), whereas tangential forces usually denote material removal. The results thus suggest that metrics explain different aspects of the contact and emphasise the importance of certain factors for strengthening particular behaviours and is an area that will be explored further in the discussion. A summary of these relationships is presented in Table 5.7, once again showing the magnitude, direction, and relative importance of effects and interactions. Therein, surface (*D*) has been the pooled variable for normal forces, and material (*B*) for the calculation of temperature and tangential force. The results of the ANOVA calculations are provided in Appendix F, albeit as commented before, it would be unrealistic to expect accurate predictions from these models, and the results have no further implications.

Table 5.7 Summary of estimated effects, sum of squares and percentage contribution of each factor for normal forces, tangential forces, and apparent temperature.

Factor	Normal F.			Tangential F.			Temperature		
	Effect	*SS*	*% Con.**	*Effect*	*SS*	*% Con.**	*Effect*	*SS*	*% Con.**
B (Material)	1.01	8.18	38.76	–	–	–	–	–	–
C (Incursion)	0.72	4.19	19.85	0.08	0.05	21.98	-60.08	28878.05	77.86
D (Surface)	–	–	–	-0.10	0.08	38.76	13.91	1547.63	4.17
E (Spraying)	0.45	1.63	7.72	-0.04	0.01	6.43	8.51	579.87	1.56
BC	-0.70	3.91	18.51	–	–	–	–	–	–
BD	–	–	–	–	–	–	–	–	–
BE	-0.59	2.80	13.25	–	–	–	–	–	–
DE	–	–	–	-0.06	0.02	7.24	-12.19	2162.52	5.83
CE	0.14	0.15	0.70	0.04	0.01	4.97	18.10	2621.24	7.07
CD	–	–	–	-0.04	0.03	14.18	16.44	1189.50	3.21

Abreviations: *F.* Force; *SS* Sum of Squares; *Con.* Contributions. * % Con. = factor's SS/Total SS.

Force Ratio and SGE

Force ratio and SGE are measures of the process efficiency and are thus jointly considered herein. Fig. 5.26 corresponds to the data previously included in the results table (Table 5.3) and is presented in the same way as in the previous two cases: grouped by material and colour coded to distinguish between surfaces and incursion rates. The character '*' identifies those samples that show a double contact instead of a single one.

Fig. 5.26 shows that force ratios are broadly similar for all conditions, suggesting a consistent material removal regime with one exception, which may or may not be an outlier given

the construction of the experimental matrix. SGE values, in contrast, show a steep decrease when increasing the incursion rate from 0.31 um/pass to 1.71 um/pass. It is also apparent that alumina presents lower SGE values and slightly higher force ratios than zirconia, and changing surface leads to different outcomes depending on the incursion rate. At 0.31 um/pass, as-sprayed samples exhibit higher SGE values than trued samples, and the reverse happens at 1.71 um/pass. Given the structure of the DoE, caution must be applied, as a shift in spraying conditions could equally explain the latter observation and be the dominant factor instead. This relationship will now be further examined statistically.
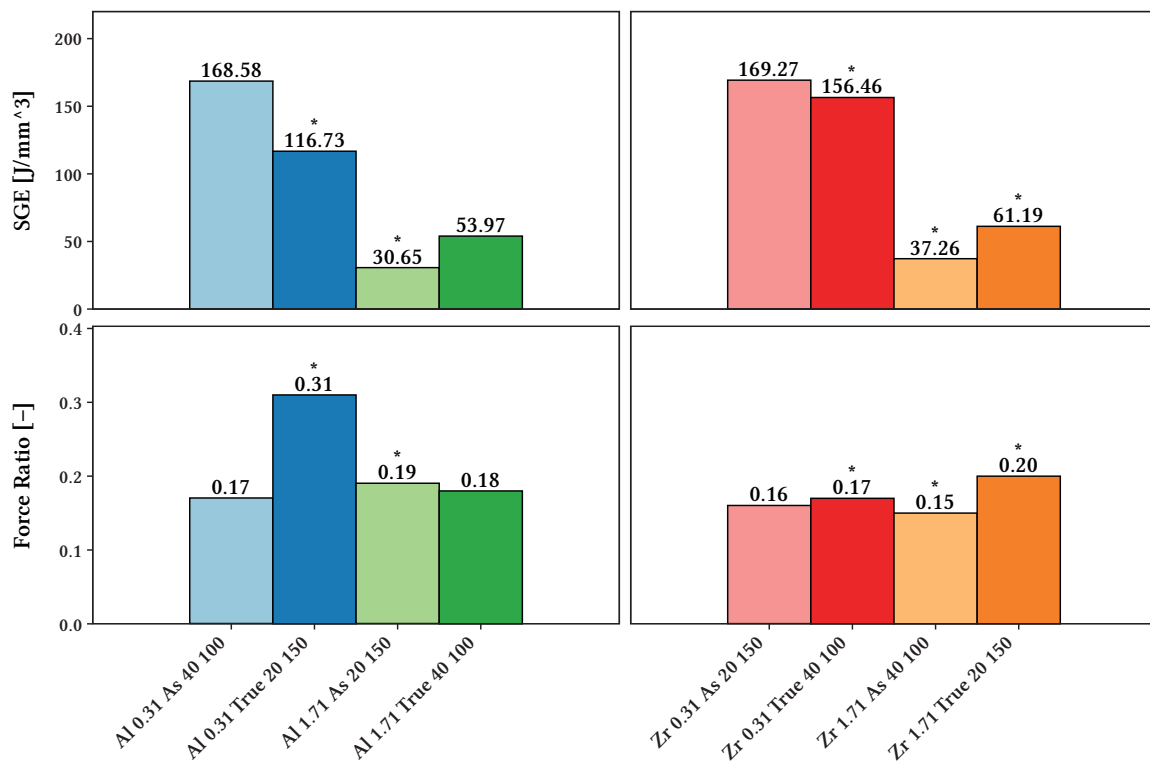
Fig. 5.26 Bar chart of force ratio and SGE. (*) Denotes double contact.

Once again, a linear model has been fitted to the data, and the effects are visualised through Lenth's and half-normal plots; the results are included in Table 5.8 and the plots in Fig. 5.27, and 5.28. It can be seen from these figures that the results are completely opposed, with incursion rate (*C*) being by far the most significant effect on SGE but barely affecting force ratios. These differences all come down to SGE considering the length of a test and the material removed, whereas force ratio does not. This finding is interesting because it shows that mechanisms are broadly similar, but material does not release as well at lower incursion rates. Further, it had been reported with regards to SGE values that spraying (*E*) and surface (*D*) could be equally important variables. However, given the strong influence of incursion rates and the

aliasing of the DoE, surface (*D*) is most likely the cause. The results thus show that surfaces' behaviour depends on the incursion rate; as-sprayed surfaces improve the performance at high incursion rates, whereas trued ones perform better at low incursion rates.

Table 5.8 Estimate of effects and aliase structure for SGE and force ratio.

Factor	Estimated effect*		Aliasing structure
	SGE	**F-rat.**	
B (Material)	6.78	-0.0213	$B \rightarrow B + CDE$
C (Incursion)	-53.50	-0.0113	$C \rightarrow C + BDE$
D (Surface)	2.18	-0.0238	$D \rightarrow D + BCE$
E (Spraying)	4.80	-0.0238	$E \rightarrow E + BCD$
BC	-3.32	0.0163	$BC \rightarrow BC + DE$
BD	-4.96	0.0988	$BD \rightarrow BD + CE$
BE	-13.99	-0.0138	$BE \rightarrow BE + CD$

* Values acquired by fitting a linear model to the data and treatment
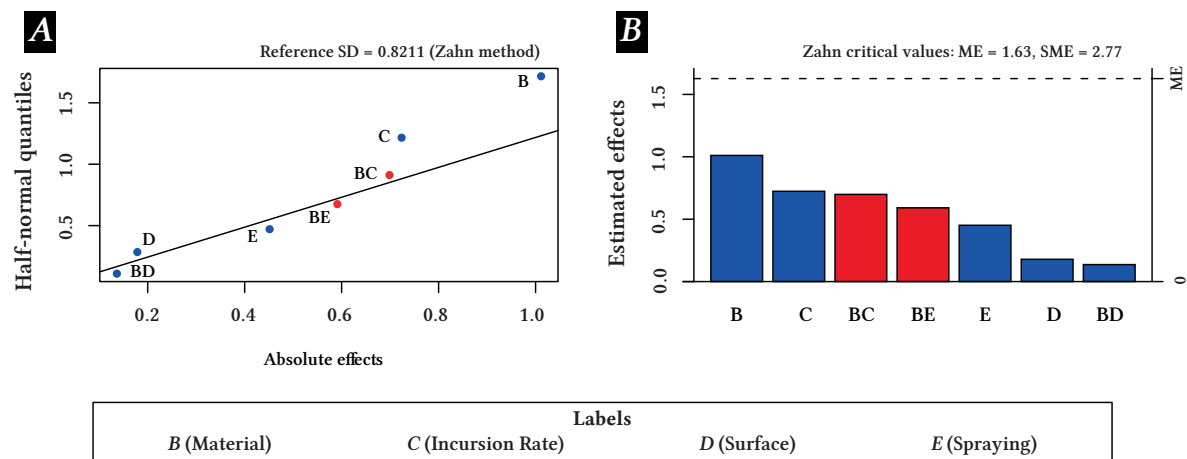combinations of Table 5.3. The 'lm' R function is used for this.
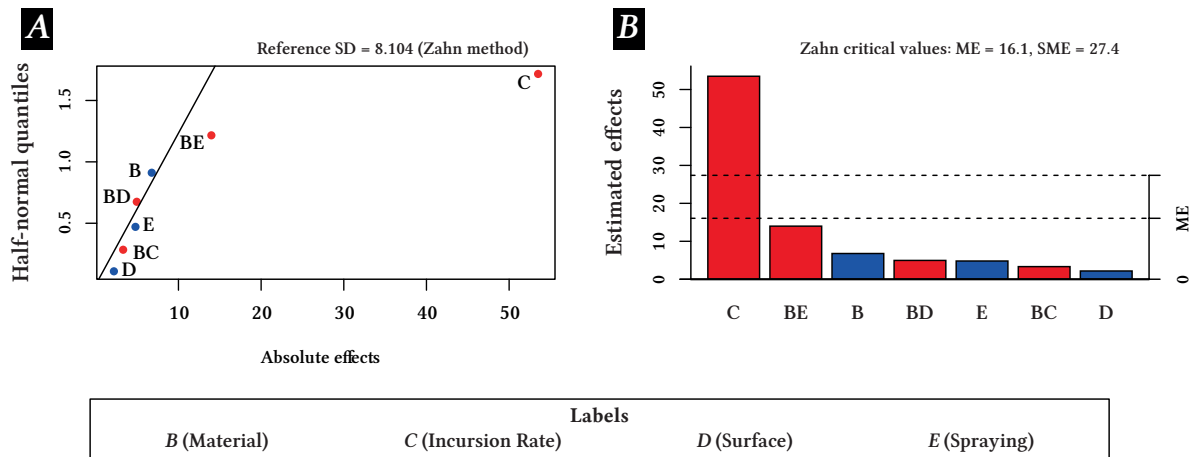
Fig. 5.27 Half-normal (*A*) and Lenth's plot (*B*) for SGE. Red has been used to represents negative values and blue for positive.
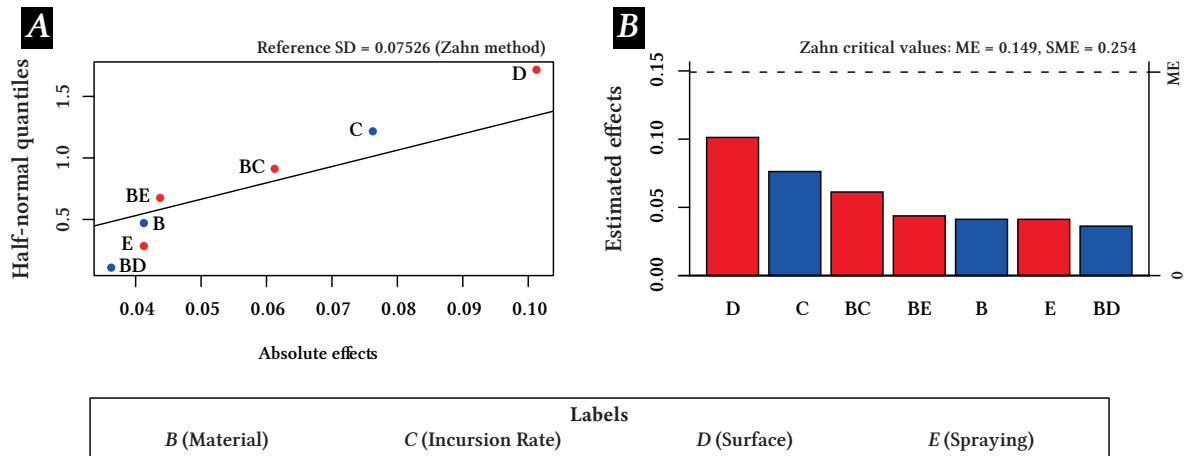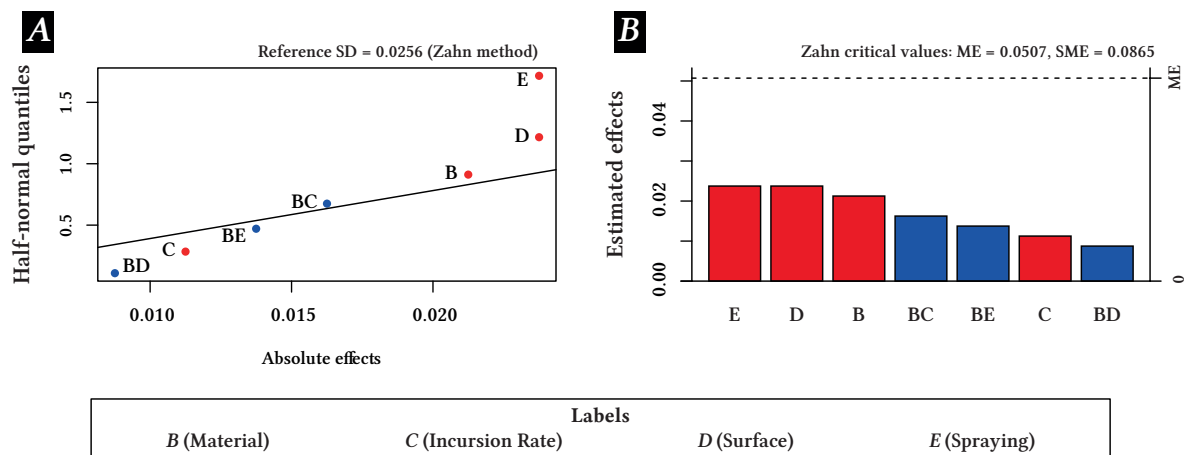
Fig. 5.28 Half-normal (*A*) and Lenth's plot (*B*) for force ratio. Red has been used to represents negative values and blue for positive.

A summary of the latter relationships is included in Table 5.9, and the ANOVA analysis is provided in Appendix F. For the SGE values, spraying (*E*) has been dropped from consideration and for force ratio, incursion rate (*C*). It is essential to note that particularly these results must be taken with care, given that they come from secondary measurements and the effects of outliers may be further evidenced. It would also be unrealistic to expect an accurate estimate of the metrics, given the DoE.

Table 5.9 Summary of estimated effects, sum of squares and percentage contribution of each factor for SGE and force ratio.

Factor	SGE			F-rat.		
	Effect	*SS*	*% Con.**	*Effect*	*SS*	*% Con.**
B (Material)	6.78	367.88	1.45	-0.021	0.0036	20.20
C (Incursion)	-53.40	22894.79	90.37	–	–	–
D (Surface)	2.18	37.89	0.15	-0.024	0.0045	25.23
E (Spraying)	–	–	–	-0.024	0.0045	25.23
BC	-3.32	88.38	0.35	–	–	–
BD	-4.96	196.52	0.78	0.01	0.0006	3.42
BE	–	–	–	0.01	0.0015	8.46
DE	–	–	–	0.02	0.0021	11.81
CE	–	–	–	–	–	–
CD	-13.99	1565.48	6.18	–	–	–

Abbreviations: *F.* Force; *SS* Sum of Squares; *Con.* Contributions. * % Con. = factor's SS/Total SS.

5.3 Discussion

The preceding results section showed with a series of metrics the response of the tribological process. In order to bring these descriptors together and view the process holistically, a PCA (Principal Component Analysis) can be applied. This technique has been computed with the function 'prcomp' from R [195], using the six variables and values presented in the results table (Table 5.3) and basing it on a correlation matrix. In addition, only the first two components are considered since their eigenvalues are above one and together explain more than 75% of the total variance (Fig. 5.29a and 5.29b). Their loadings are shown in Table 5.10, where values over 0.408 are emphasised to show that a variable's contribution is more than average; thus, taken as important.
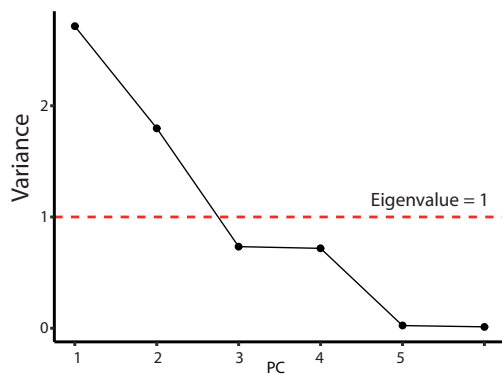
(a) Scree plot (explained variance vs number of components)
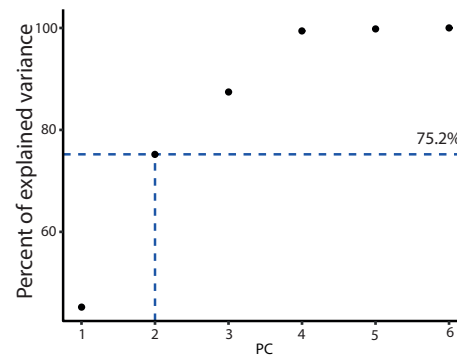
(b) Cumulative variance.

Table 5.10 Loading of the first two principal components.

Variable	PC1	PC2
Normal Force	**0.521**	-0.251
Temperature	**-0.472**	-0.349
Force ratio	-0.377	**0.498**
Material loss	0.337	**-0.420**
SGE	-0.325	**-0.538**
Tangential Force	0.379	0.318
Cut off: |PC| > 0.408*		

* Given six variables, 0.408 results from $(1/6)^{0.5}$ (sum of squares equals one).

A biplot of the principal components (Fig. 5.30) allows the investigation of the process as a whole as it combines the experimental variables and the outputs. This figure confirms the importance of incursion rate (previously seen in the results), with higher incursion rates leading to efficiency improvements, reduction in temperatures, and/or increase in tangential forces. Furthermore, minor differences appear within these groups, verifying that the rest of the variables have a smaller effect. Prior studies in the field of abradables [156] and grinding [194, p. 110] have already noted the importance of the speed at which material is fed, namely incursion rate as is know herein. Thus, these results are in line with what has already been reported.
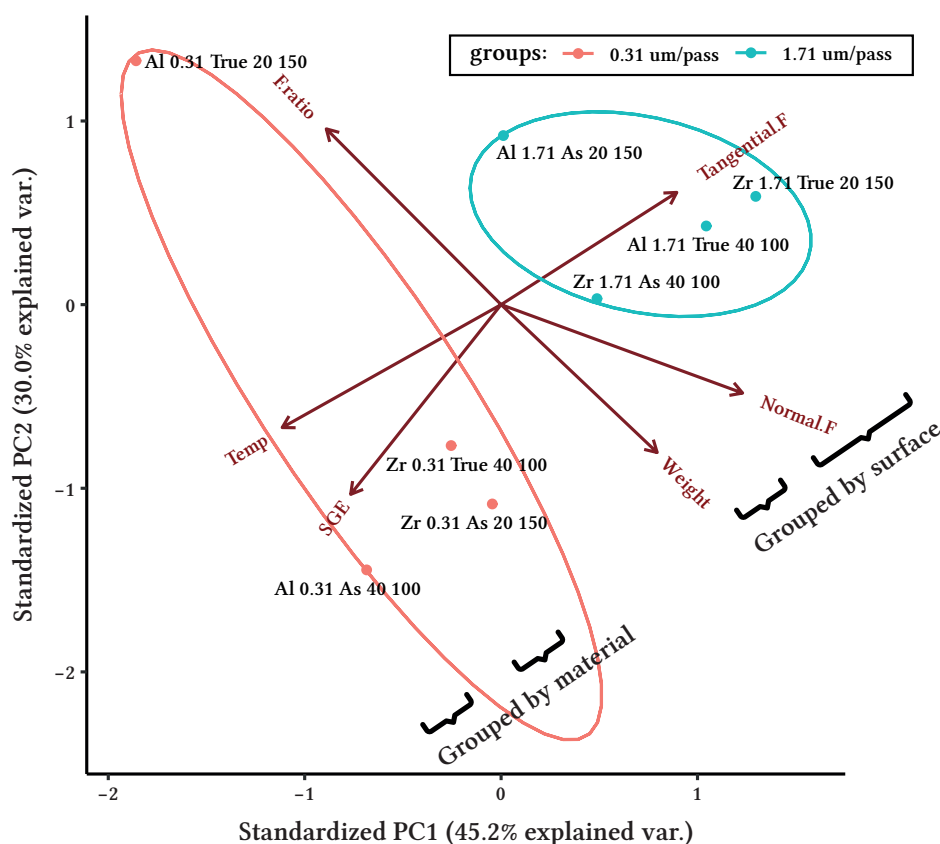
Fig. 5.30 PCA biplot showing clusters of samples tested at 0.31 um/pass and 1.71um/pass. Created with the R function 'ggbiplot' [197]

It stands out, however, that along the axis of temperatures, tangential forces, and SGE values, results are grouped by surface at 1.71 um/pass and by material at 0.31 um/pass (Fig. 5.30). In addition, in light of the two upmost samples of the PCA, it appears that at both incursion rates only surface is the variable that moves samples in the axis of material removal, normal forces, and force ratios. The influence of material or spraying conditions cannot be discarded

which may be due to the DoE or the strength of the surface variable; however, studies on abrasive machining [194] have highlighted the importance of the size effect, indicating that grain penetration (sharpness and the size of grains itself) become more critical as higher removal rates are intended. Hence, it is a possible explanation that thermal effects are more important at 0.31 um/pass, whereas surface effects are more important at 1.71 um/pass. It follows that materials may exhibit differences because of their conductivities (one dissipating more heat than the other, see Table 2.5) and surfaces because of their roughness, and that the effects of the latter will be reduced as the wheel congests, explaining why at low incursion rates mainly material effects are seen. This idea will be further explored in the next paragraphs.

The results section showed a degree of correlation amongst variables, which is further highlighted by the PCA's loadings. The correlation between tangential forces and temperatures is a well-known relation happening in grinding [130] and with abradable linings [156], which indicates that tangential forces increase with the cutting behaviour of the process, and heat in the contact is reduced because of there being less frictional heating and material being removed [156, 194]. In this case, however, no chip formation is observed, so instead it could be that material adheres to the ceramic's surface and heat is removed in an more inefficient manner through atmospheric convection. In contrast to the chip formation process, the removal of heat through adhered material would support the previous idea; the effect of material conductivities would be observed in the heat partition between wheel and blade, and a larger heat flow will result in the more conductive ceramic. Thereby, alumina would outperform zirconia because of its highest conductivity, exhibiting a better removal mechanism with lower contact temperatures and levels of adhesion, which is in line with observations.

What is surprising is the relationship between force ratio, material removal, and normal forces. The stress state changes with a change in incursion rate; thus, some of these variables would have been expected to align with the incursion rate axis. Normal forces indeed show a slight influence but minimal, whilst it can be seen that force ratio (an indicator of the efficiency of the cutting process) is completely at 90 degrees from the incursion rate axis and coincides in position and direction with material removal. Recalling that material loss is taken as a negative value, this relation between metrics shows that even with a change in incursion rate (i.e., the most influential variable) does not translate into a higher amount of material removal, improve the cutting efficiency, or even a change in mechanism.

The previous behaviour is rather unexpected, although the size effect and the adhesion of the wheels offers an explanation. Grains in the wheels are small and rapidly congest, resulting in a metal-to-metal contact, heating, and a rather viscous contact with low friction coefficients. Thereby, explaining why force ratio and material removal remain virtually the same despite a change in incursion rate. The slight influence of normal forces with incursion rate might

indicate a slightly higher indentation of the grains, and thus a slight improvement in the removal mechanisms with incursion rate. This seems unlikely given the level of adhesion that rapidly covers the surface and the force ratio values below 0.2, commonly related to well lubricated blunt abrasive grains and very little penetration [194, p. 148, 163]. What instead seems to be happening is a less ideal process, where there is push back of material because the wheel is not able to remove it, causing the normal forces to increase disproportionately [156] [130, p. 127]. This observation would also explain why zirconia's samples at low incursion rate appear to outperform alumina's, whilst what is happening is that all samples at 0.31um/pass yield similar temperatures but zirconia's result in higher tangential and normal forces, resulting from the extremely poor removal mechanism, high thermal effects, and melt layer on the surface. Further supporting the idea that thermal effects are more important at low incursion rates. This will be further explored in the next chapter by considering the time histories looking at how the contact progresses.

Considering the SGE values one could conclude that there is a significant improvement in mechanism with incursion rate. Contextualising, SGE values of $\sim$30 J/mm^3 are close to those of a highly efficient grinding process $\sim$10 J/mm^3 [194, p. 124]; however, none of the characteristics seen therein are observed in this process. SGE results seem to be highly biased (or influenced), by how is mathematically calculated, which does take into account the incursion rate and material removal, and thus there is a visible change with these in the PCA. It would be worth considering if the metric's values are comparable to those achieved in grinding processes or if instead another metric like wear rate (done in material's science research Section 2.7.1), could be a more interesting alternative. It is not possible to calculate the latter with the current experimental method as the real arc of contact is extremely difficult to estimate.

All results appear similar; however, two samples depart from the general trend. Initially, the trued alumina sample at a low incursion rate ("Al-0.31-True-20-150") was thought an outlier. Instead, it seems to highlight an alternative: extending the contact so that work and adhesion are more evenly spread along the ceramic's surface. The as-sprayed alumina sample at a high incursion rate (i.e., "Al-1.71-AS-20-150") is the other sample that departs from the general trend, in this case showing what is expected: the benefits of higher roughness, heat dissipation, and shorter contacts that lead to higher removal rates, efficiencies, and lower temperatures. Therefore, the PCA suggests the best outcome, a combination of a rougher surface and a more extended contact area. It is worth noting that these results might change if the ceramic's surface is renewed or the ceramic contains sharp grits.

5.4   Conclusion

This chapter set out to determine which variables had a more significant impact in the aero-engine abrasive drum–stator-blade system. Preliminary analysis revealed that the influence of speed could not be investigated because of the design of the disc, and the research proceeded with the exploration of materials, incursion rate, surface, and spraying condition.

The results suggest that the tribological process is governed by the inefficient mechanism in which heat is dissipated from the contact. Albeit all wear mechanisms have been found to be broadly similar, and sit in the undesirable side of adhesive wear, several treatments showed a degree of improvement. For instance, incursion rate established a clear difference in sample behavior, finding benefits at high incursion rates where contacts are shorter in time and rub length (less heat) than at low incursion rates. In addition, results suggest that advantages are provided by rougher surface, longer arcs of contacts, and higher conductive materials; the importance of which would vary depending on the incursion rate, on the basis that sample's surface does not renew and adhesion rapidly grows and congests the wheel. A clear example is that at low incursion rates (that yield the worst performance), truing compacts the surface and probably makes cutting worse; however, it spreads out the contact, slowing loading and actually making it better. Conversely, there is marginally more cutting at high incursion rates, and it is best to preserve the rough as-sprayed surface.

In general, it seems that the stator-blade/rotor abrasive system can be studied in the context of abradables and abrasive machining processes. However, these findings are limited to a single contact speed, which was unfortunate that the study could not finally include as a variable due to the experimental design; further studying the effect of contact speed would substantiate the previous findings. A further study could compare the impact of different geometries in the blades (e.g. introduction of angles), or alternatively investigate the impact of slightly renewing the ceramic's surface to prevent or delay the adhesion levels and extend the sharpness of the wheel. Design work has been undertaken that allows for achieving a broader speed range, and extends the capabilities of the rig to investigate a number of different variables. This has been included in Appendix G.

Chapter 6

Wear mechanisms of stator-blade/rotor abrasive system

The previous chapter has established the statistical relationships between variables, and a convenient way to now give them a practical interpretation is through a wear map. Such an approach relates wear behaviour with operational conditions, giving guidance for a designer for selecting appropriate or more benign settings for a tribological system. Given the benefits, it is not surprising that wear maps have been used extensively in many fields, and especially in the context of this thesis, to classify wear responses of abradable materials. Borel *et al.* [138], for instance, classifies the different wear regimes contextualising them in terms of speed and incursion rate for an engine (Fig. 6.1). By doing so, guiding the design of abradable material to provide enhanced performance in aero-engines.
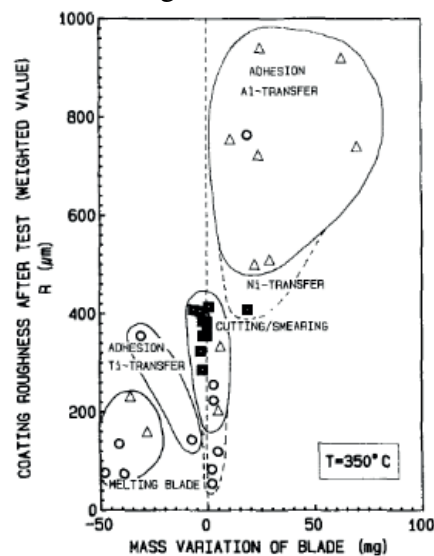
Fig. 6.1 Exemplar wear map obtained for abradable research. Extracted from Borel *et al.* [138]

Although this such mapping cannot yet be done for abrasive liners in the context of engine parameters because it is less advanced, the equivalent procedure is still applicable within the context of these tests and serves to start comprehending the response of the contact. Focusing on the contact's transient nature becomes pertinent after a wear map as it leads to a deeper understanding of the undergoing mechanisms and allows determining favourable events that can be exploited within the limited contact time.

The aim of this chapter is, first of all, to translate the statistical relationships into a wear map. Then, to understand how the wear mechanisms have developed, and consider 'if' and 'how' the contact can be influenced. The first section of this chapter will thus examine the samples to identify the wear mechanism occurring in the stator-blade/rotor abrasive system. After that, a more formal definition of the wear mechanisms will be reached, and knowledge will be extended relying on closely related research (e.g., the grinding process and abradable linings). Additionally, to recognise the degree of severity of their occurrence, these will also be evaluated in an aero-engine context. The remaining part of the chapter will investigate the time-domain data, which will assist in differentiating between wear mechanisms and distinguishing advantageous operation regimes. Exemplar case studies will be used for the latter purpose.

6.1   Methodology

Before proceeding, it is necessary to note that the data presented in this chapter is the same as the previous one, now being concerned with its time-domain variant, which has not been studied earlier. The reader is thus referred to Section 5.1 for the methodology used for acquiring and processing the data.

It is also noteworthy that time is used for the X-axis of the plots instead of rub length, which use is generalised in abradable research. Time is best suited as a comparative metric for the type of contact studied herein, given that the continuous (or quasi-continuous) nature of the contact makes the real contact area (essentially the rub length) very difficult to estimate.

6.2   Wear mechanisms

In the previous chapter, metrics were treated as descriptors of the tribological system and were then considered holistically through a PCA. Such work is relevant as if the selected metrics are indeed the response to a specific wear mechanism, then the PCA, which organises samples based on an average response, is much like a wear map, and samples exhibiting similar behaviours are clustered together. From examining the wear scars in combination with the PCA (Fig. 6.2), some common behaviours become clear, highlighting that the PCA and a wear map are certainly alike (both reflect the outcome of different mechanisms) and can therefore be used in a similar fashion.
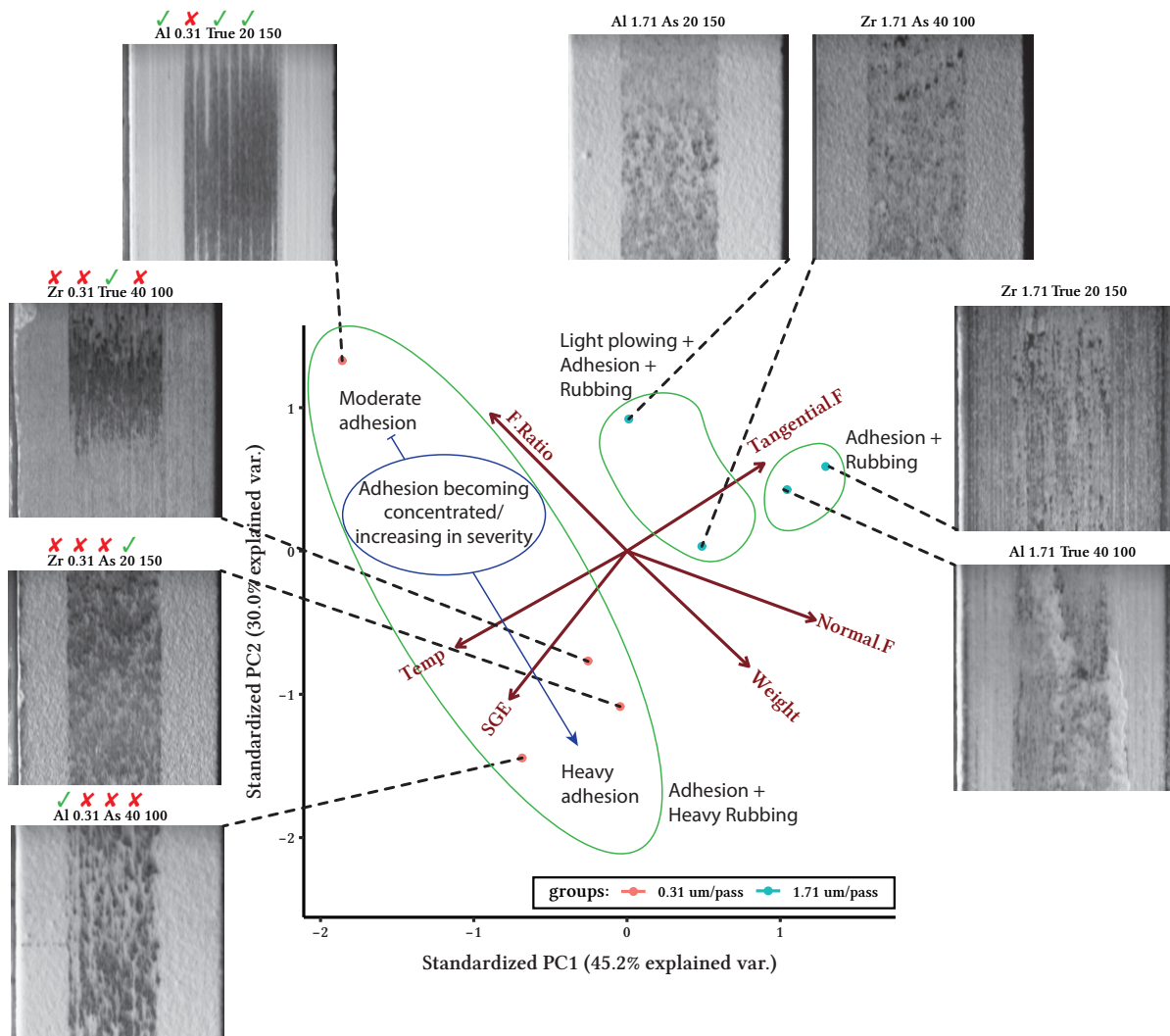
Fig. 6.2 PCA of the tested samples. Regions exhibiting similar mechanism have been identified. Check mark symbol (✓) indicates favorable treatment; cross (×), unfavorable treatment at the lower incursion rate condition.

An example can be seen from those tests clustered at the left of the PCA (Fig. 6.2), which are tested at the low incursion rate of 0.31 um/pass. The previous chapter showed that trued surfaces outperformed as-sprayed ones at this condition because of the increase in arc of contact; material and then spraying followed in strength, and selected appropriately could also influence performance. In this latter case, alumina showed better wear behaviour than zirconia because of its increased conductivity, and 20 g/min over 40 g/min because of the higher density and/or conductivity. It thus becomes significant that this trend, which was attained statistically, is also seen from the wear scars of Fig. 6.2. Although all these samples fall within the group of heavy rubbing of the PCA, a clear order is visible depending on which variables are in the worse condition and indeed their combination. The top-left sample

(Al-0.31-True-20-150) possessing 3 out of 4 favourable treatments and shows mild adhesion with rubbing. In contrast, the remaining three samples have 1 out of 4 favourable treatments and show heavy adhesion with very similar behaviours, but are ordered as per the relative strength of the variables as identified in the previous chapter. In essence, as-sprayed samples show more localised adhesions than trued ones, and of there trued samples, material represents a stronger variable than spray conditions, meaning that zirconia samples sprayed at 20 g/min has the highest adhesion.

Moving now to capture the different regions of the PCA, three different underlying mechanisms can be identified. Going from left to right of Fig. 6.2, these are:

- *Adhesion + heavy rubbing (AHR):* this is the mechanism previously described on the left side of the PCA and predominantly occurs at a low incursion rate. Due to the incursion condition, very little grain penetration occurs, rubbing arises, and material adheres to the coating's surface. Given the low incursion rate and level of adhesion, coatings of different surfaces result in similar outcomes despite their topology, and rubbing occurs for a more extended period, which leads to counterparts showing more thermal damage than with sorter tests (Fig. 6.3). Severe adhesion forms (e.g. commencing of galling) are observed, but mainly where stresses have concentrated, i.e., on the tip of asperities of as-sprayed. Likewise, these forms of galling are lighter than those happening at a higher incursion rate, given that the coatings are subjected to lower stresses.
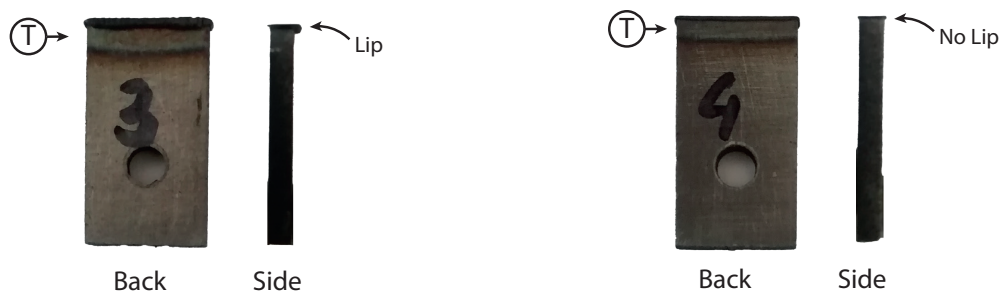
(a) Typical blade sample tested at 0.31 um/pass   (b) Typical blade sample tested at 1.71 um/pass

Fig. 6.3 Back and side views of typical blade samples tested at different incursion rates, correlating with a period of extended rub vs short rub. Label: (T) area with thermal decoloration.

- *Light ploughing + adhesion + rubbing (PAR):* this mechanism lies towards the right of the previous and has predominantly occurred with as-sprayed samples at a high incursion rate. It falls within a region where surfaces do differ, in this case, exhibiting a short initial period of ploughing before rubbing starts. Adhesion is also present; however, given that tests are shorter than at low incursion rates, the thermal damage on the counterpart is lower (Fig. 6.3). Herein, localised galling has also been identified.

- *Adhesion + rubbing (AR):* this mechanism is located at the far right corner of the PCA, close to the previous. It has been found to predominate at a high incursion rate, but instead, among trued surfaces. The mechanism is characterised by samples directly rubbing upon contact and material adhesion. The counterparts show similar thermal decolouration to the previous (given the short contact); however, infill levels are lighter but not as localised. Samples also show more severe wear mechanisms like galling (generalised in this case), which may develop into material rupture.

It can be appreciated from the above group of underlying mechanisms that all develop adhesion and progress into more severe adhesive transfer such as galling, depending on the treatment combinations. In effect, it is apparent that the abrasive coatings are not effectively removing material, and given enough time, samples will eventually reach the same point. As tests are of a set length in this study, the combination of variables thus dictate how far samples get along the journey. For example, samples tested at low incursion rate have longer rub lengths and greater infill levels than those tested at high incursion rate; yet, they resemble each other at the same rub distance. The specific wear progression in this process will be described below, where the aim is also to assess their significance in an aero-engine context. The terms used herein to identify the progressive severity in adhesive wear (i.e., adhesion, galling, spalling) are not strictly defined in literature. To give some clarification on how these terms are used in the context of these samples and contact (and prevent a loose use), a more detailed description will be given in the following subsections when a wear mechanism is identified.

6.2.1   Adhesive transfer

The most generalised wear mechanism that has been found is adhesive transfer, which has been the predominant mechanism occurring where contact has happened for all the samples, and represents the start of the wear process. From a macroscopic standpoint it has been identified with two different morphologies (Fig. 6.4). Surfaces initially exhibit isolated points of adhered material that either remain separate with contact time (Fig. 6.4B) or grow to affect a more extensive area of the wheel (Fig. 6.4A). From a microscopic standpoint, however, the structure of both forms of adhesion are comparable (Fig. 6.5).
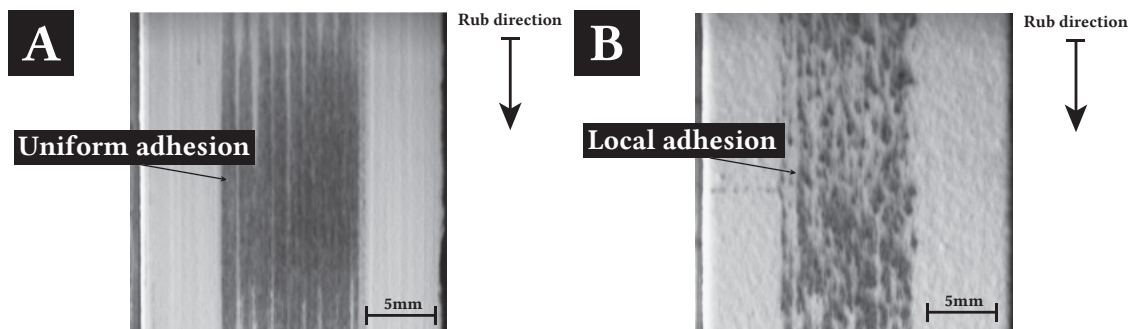
Fig. 6.4 Images from the high-speed camera distinguishing between a uniform (A) and a local (B) forms of adhesion. Samples correspond to: (A) Al-1.71-True-40, and (B) Al-0.31-As-40.
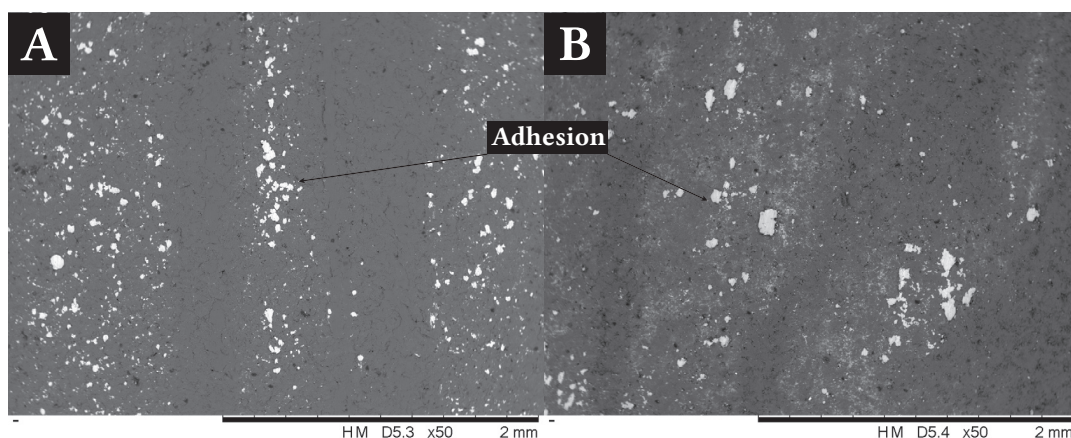
Fig. 6.5 Backscattered electron images of uniform (A) and local (B) forms of adhesion. Samples correspond to: (A) Al-1.71-True-40, and (B) Al-0.31-As-40. Images are top view, scar section.

Such process of adhesion may be illustrated by a blunt asperity contact (adhesive friction) [194, p. 148] where grains show a very low penetration and the material of lower hardness is sheard. If the process is not working as intended, metal will completely cover the wheel, and a metal-to-metal contact results [198]. Forces then become almost entirely the consequence of this new contact [199]; essentially, making the wheel topology irrelevant. High adhesion levels on grinding wheels translate into high wheel wear either because of the high coefficient of friction or local welding at the tips creating large scale fracture. On abradable linings, adhesive transfer has also been related to high frictional heat levels, leading in this case to thermal cracking and densification [138]. All the tests show this process.

In the stator-blade/rotor abrasive system, adhesive transfer would thus be highly undesirable, not only deteriorating the material removal process and introducing thermal damage into the blades, but also increase the risk of spalling or large scale delamination, which can lead to a catastrophic event in aero-engines or the more benign but still highly undesirable aerodynamic losses because of the gap opening between stator-blade and rotor.

6.2.2   Commencing of galling

Multiple samples progress into galling (Fig. 6.6), a more severe form of adhesion. This degree of adhesion has been found to predominate on samples tested at the high incursion rate and also where localised adhesion has occurred with extended rubbing. Such a mechanism may appear with sufficient forces and temperatures and happens when metal-to-metal junctions weld and tear to a greater extent than with the previous adhesion condition. In this scenario, links grow in strength and break along the weakest sections, leading to higher interface forces and making extreme wear types like seizure or delamination more possible [194, 200].
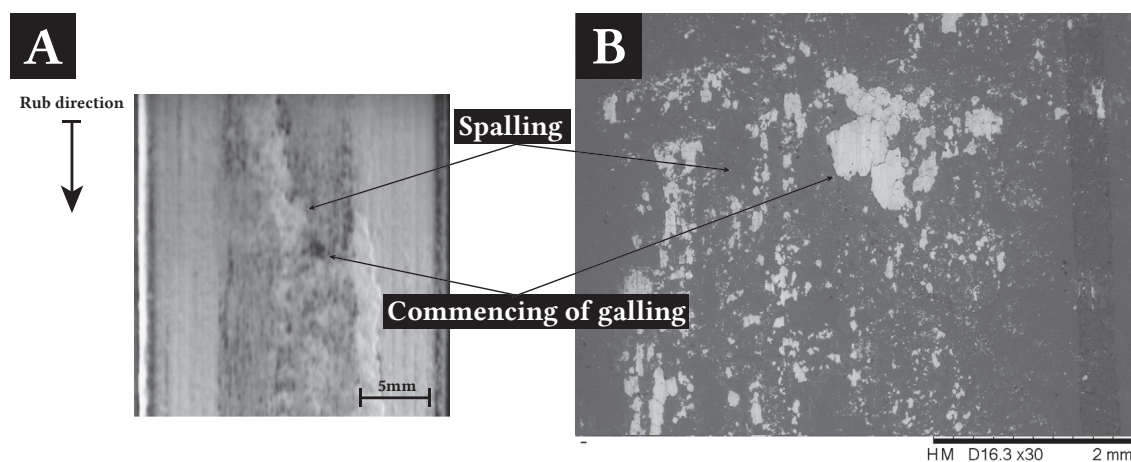
Fig. 6.6 Top view images showing commencing of galling and spalling of the coating. (A) Backscattered electron image, (B) High-speed camera image. Images correspond to sample: Al-1.71-True-40.

Galling in aero-engines would lead to the same catastrophic events listed previously for adhesion but in an aggravated form. It would thus be a mechanism that should be avoided.

6.2.3   Spalling

Spalling is related to the previous process of adhesion and galling, when the weaker link occurs within the coating instead of the counterpart, tearing apart the coating. In general terms, spalling is associated with a process of initiation and propagation of cracks, which commonly happens at the bond coat level for thermal barrier coatings such as these. This event leads to their final failure [59], which has been previously described in more detail in Section 2.3.

Adhesion and galling are, however, not the only causes of spalling; the level of imperfections in the coatings and how coatings operate will influence the specific mechanisms that lead to this failure phenomenon [59]. In fact, this study has identified spalling in places where contact has not even happened (Fig. 6.7B). It is also true, however, that more severe forms have been
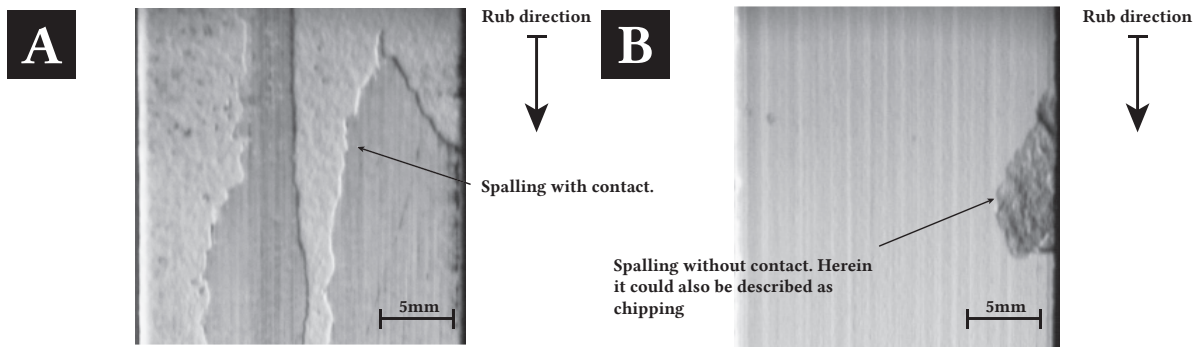
Fig. 6.7 High-speed camera images showing (A) spalling where contact has happened, and (B) spalling or chipping where contact has not happened. Samples: (A) Al-1.71-True-40, (B) Al-0.31-True-20.

identified on those tests located at the far right of the PCA (Fig. 6.2), which are trued samples tested at high stresses, and where galling is observed (Fig. 6.7A). Although spalling has not been seen with the high-speed camera at low incursion rates, a backscattered image of the cross-section along the contact has revealed longitudinal cracks parallel to the surface (Fig. 6.8). It can thus be seen that damage (particularly on trued surfaces) is still present even at low incursion rates, and that due to the testing conditions (e.g., limited contact time or the stresses), it has not been externalised in this case.
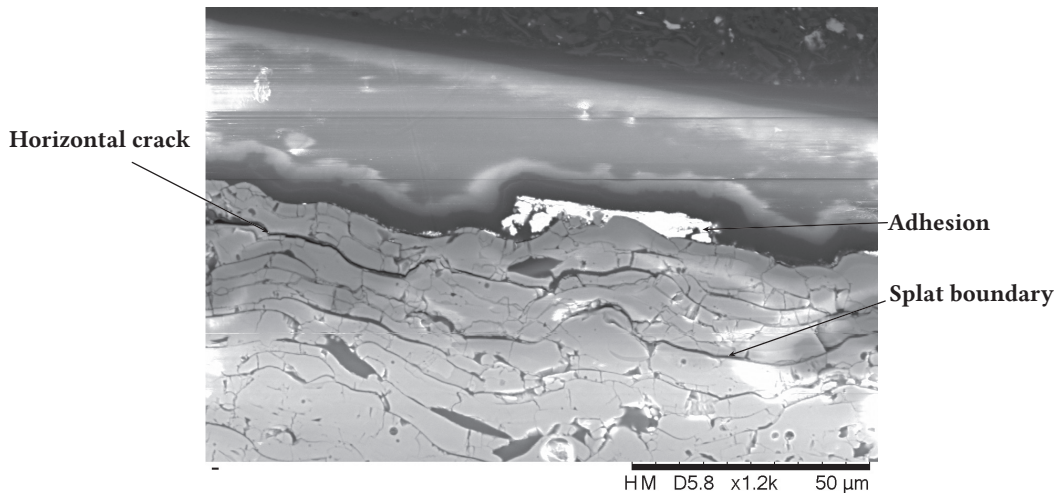
Fig. 6.8 Backscattered image of the cross section of sample "Al-0.31-True-20" showing longitudinal cracking parallel to the surface on a sample tested at low incursion rate.

When these coatings spall, thermal effects are not a primary concern in the abrasive rotor/stator system, given that they are not intended for thermal insulation. However, the coatings do provide thermal benefits, and spalling will avoid their primary purpose, which is to be abrasive to the stator blades for sealing purposes. Furthermore, spalling might become

a major concern as cracks could propagate into more critical elements in aero-engines, for instance, in cases where coatings are applied over welded joints in the rotor. In fact, vertical cracks have been identified in some coatings (Fig. 6.9), and whilst it coincides with trued samples, it is worth noting that it may not be exclusive for samples with such treatment. However, the high stresses introduced during the truing process might indeed promote the occurrence of vertical cracks. Spalling should thus be avoided in aero-engines.
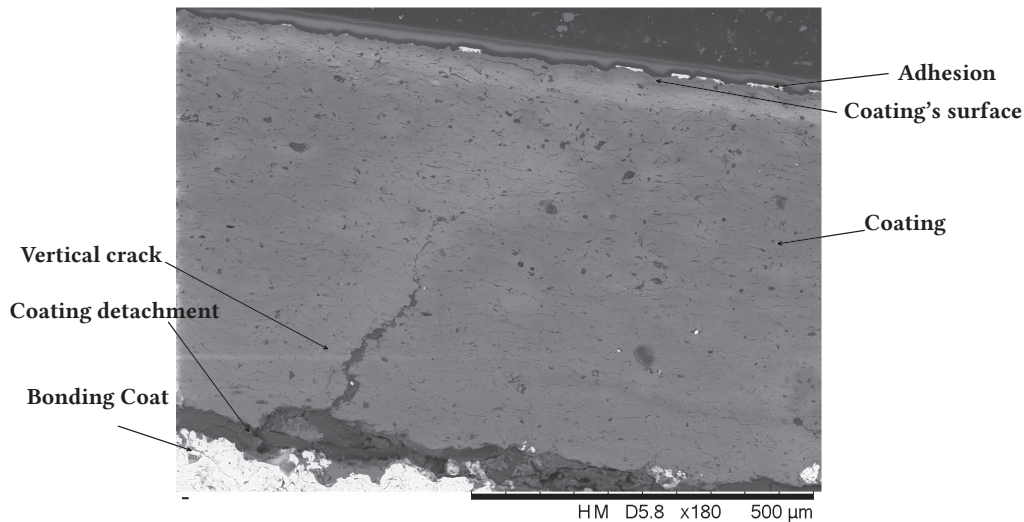
Fig. 6.9 Backscattered image of the cross-section of sample "Al-0.31-True-20" evidencing the development of vertical cracks in the coating despite being tested at the low incursion rate.

6.2.4 Large scale delamination

Delamination is a large scale loss of material and can occur at the end of the aforementioned adhesion progression should forces become high enough. Whilst it has not been identified as a wear mechanism in the PCA, SEM images of alumina samples already show a complete coating detachment from the bond coat (Fig. 6.10). Hence, demonstrating that large-scale delamination is indeed the ultimate and extreme failure mechanism for these coatings, as previously highlighted in the literature (Section 2.3). The fact that coatings "Al-1.71-True-40" and "Al-0.31-As-40" completely detached from the substrate during preparation for SEM is further evidence in support. This outcome indicates that large-scale delamination has just been avoided as an experimental outcome, this not being the case for aero-engines, where adhesion is severe and can occur within the engine for extended periods (Section 1.5).
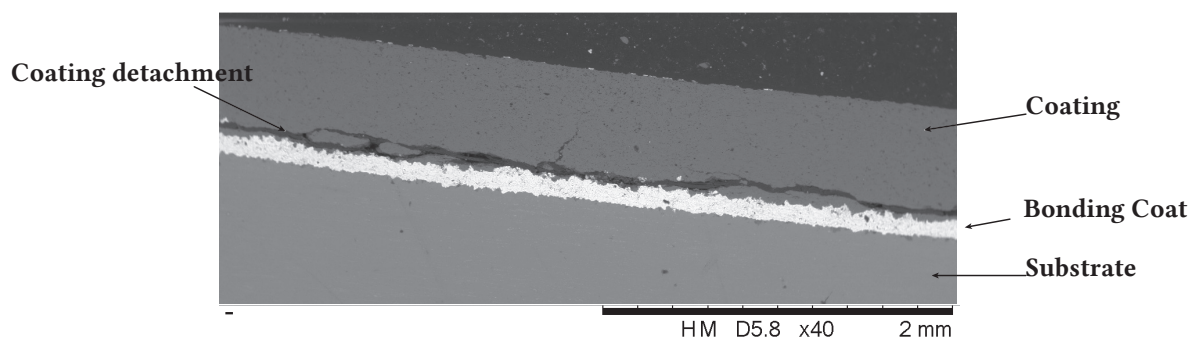
Fig. 6.10 Backscattered image of the cross-section of sample "Al-0.31-True-20" evidencing large scale delamination.

For the remaining two alumina samples, it coincides that SEM images show a clear transition "substrate–bond coat–top coat" (Fig. 6.10), whereas zirconia coatings do not (Fig. 6.11). Whilst an SEM observation is not evidence for believing that the strong transition in elastic modulus is the cause for alumina delaminating at the bond coat level, it does provide some insight as it is in line with literature (Section 2.3).
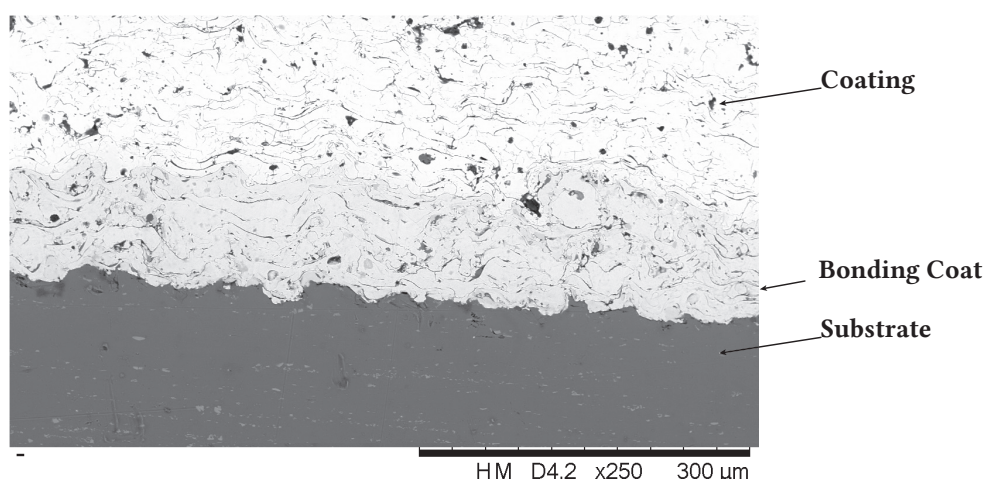
Fig. 6.11 Backscattered image of the cross-section of a zirconia samples evidencing a well bonded coating

It is worth noting that delamination does not necessarily need to be related to a contact event, as operational stresses may already suffice to make the coatings fail (Section 1.5). Either because of an inappropriate selection of the coating, a defective manufacturing process, contact scenario, or an inadequate substrate design, in essence, it all comes down to the coating being subjected to stresses that are not designed for (Section 2.3).

Delamination causes an aero-engine to be removed earlier from service for repair and is thus not desirable.

6.2.5 Summary

The preceding section has looked into the wear mechanisms occurring in the tested samples. The results range from mild adhesive transfer into more severe forms of wear like galling and spalling. Clearly, these mechanisms represent a progressive wear process that falls along the same spectrum of adhesion, and the study of the time domain data will give a deeper understanding of such progression, in which the selected variables (i.e., material, surface finish, incursion rate, and spraying) might have indeed defined the outcome.

6.3 Results

As mentioned earlier, eight different samples have been tested, and the data consists of in situ measurements of forces, temperature, and surfaces changes taken throughout the test. Upon evaluation of these, it can be seen that although samples eventually exhibit different wear outcomes along the spectrum previously discussed, their time histories show many similarities. Fig. 6.12 presents two exemplar tests.
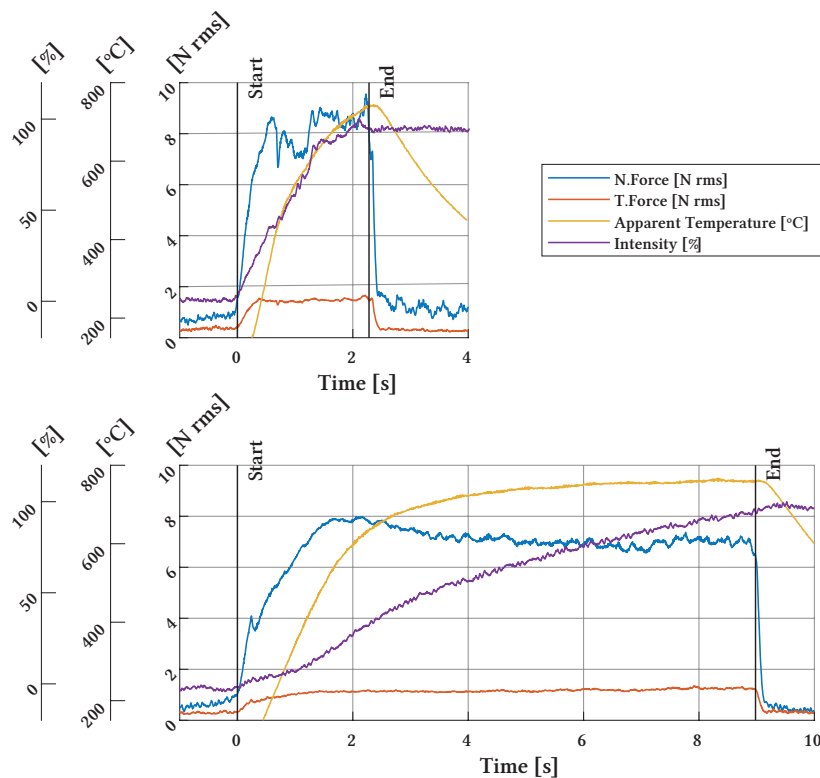
Fig. 6.12 Time histories of samples "Al-1.71-AS-20-150" (top) and "Al-0.31-AS-40-100" (bottom). Plots generated with 'plotNy' [201]

The above time-domain data corresponds to samples "Al-1.71-AS-20-150" and "Al-0.31-AS-40-100" and is an exemplar of tests at different incursion rates. The previous chapter established such a variable as that introducing the most significant variation, and it can be seen from Fig. 6.12 that it also results in the most distinctive characteristic in the time domain: a difference in contact time or rub length (marked with 'Start' and 'End'). It turns out that tests at different incursion rates also show distinct wear mechanisms. Those at a low incursion rate exhibit heavy rubbing compared to those at higher incursion rates, which show lighter forms of rubbing. For this case, the selected samples fall respectively in these distinct groups, herein named PAR and AHR. Aside from this difference, Fig. 6.12 shows that all metrics have a similar tendency with a steep initial increase and relatively stable values until the test finishes. Tests at higher incursion rates seem to evolve faster than those at low incursion rates and thus show a difference in average; however, it is appreciable that forces and temperatures eventually reach similar values. This highlights the inability of the grit to efficiently remove material at any condition.

The time domain data of all samples is presented in Fig. 6.13 and Fig. 6.14. In these, the aforementioned patterns and differences are also visible, further emphasizing that rub length (or contact time) is the most distinctive characteristic and happens when shifting incursion rates. It can also be appreciated that variations remain minor within the same incursion rate, with similarities being particularly close for temperatures at 0.31um/pass and all tangential forces.
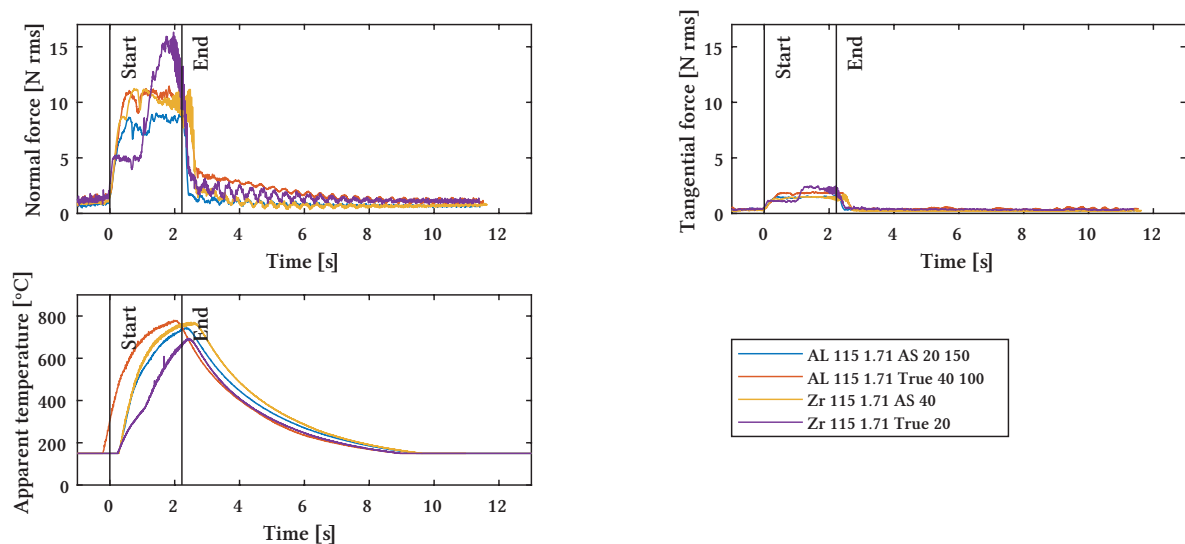
Fig. 6.13 Time domain data (forces and temperature) of samples at 1.71um/pass
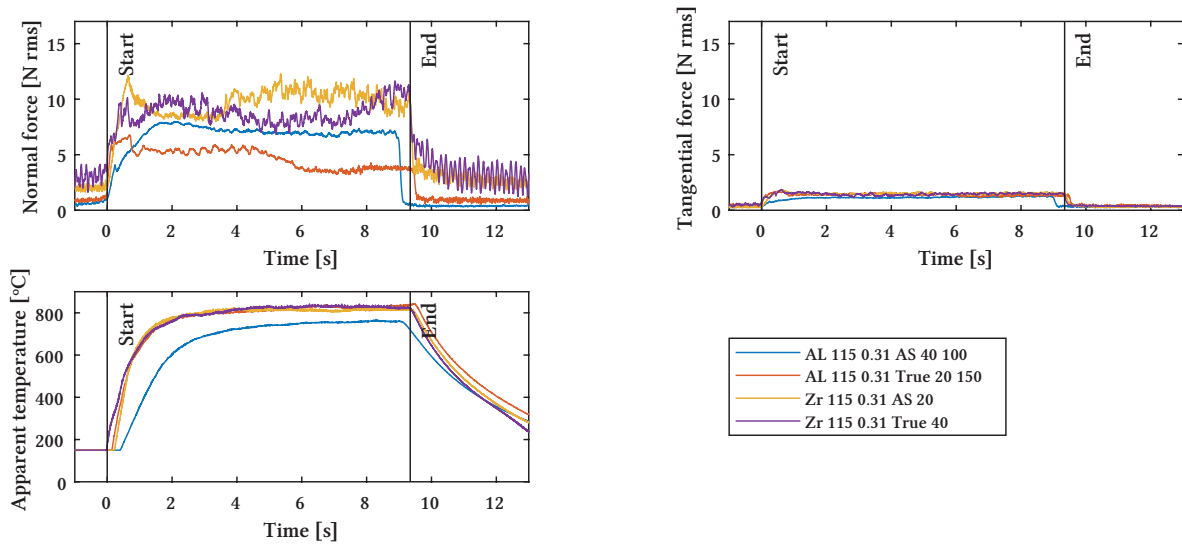
Fig. 6.14 Time domain data (forces and temperature) of samples at 0.31um/pass.

The time-domain data will now be considered for each of the wear regions identified to explore any differences that occurs. The samples considered are exemplar for each wear mechanism identified previously on the PCA and are summarised in Table 6.1. Two samples from the AHR regime are included to illustrate the variability within the group.

Table 6.1 Summary table presenting the three identified wear mechanism and the exemplar samples chosen to illustrate them.

Wear regime	Test Name
"Adhesion + Rubbing" (AR)	Zr-115-1.71-True-20
"Ploughing + Adhesion + Rubbing" (PAR)	Al-115-1.71-AS-20-150
"Adhesion + Heavy Rubbing" (AHR)	Al-115-0.31-True-20-150
Spectrum from moderate to heavy adhesion	Al-115-0.31-AS-40-100

6.3.1 Adhesion + Rubbing (AR)

The trued zirconia sample tested at the high incursion rate (1.71um/pass) is located at the top right-hand corner of the PCA (Fig. 6.2) and is an exemplar test for AR. Fig. 6.15 shows the time-domain of this test, where labels A-F are used to highlight events on the coating's surface. These are captured with a high-speed camera and are shown in Fig. 6.16. In the paragraph that follows, references will be made to these two figures.
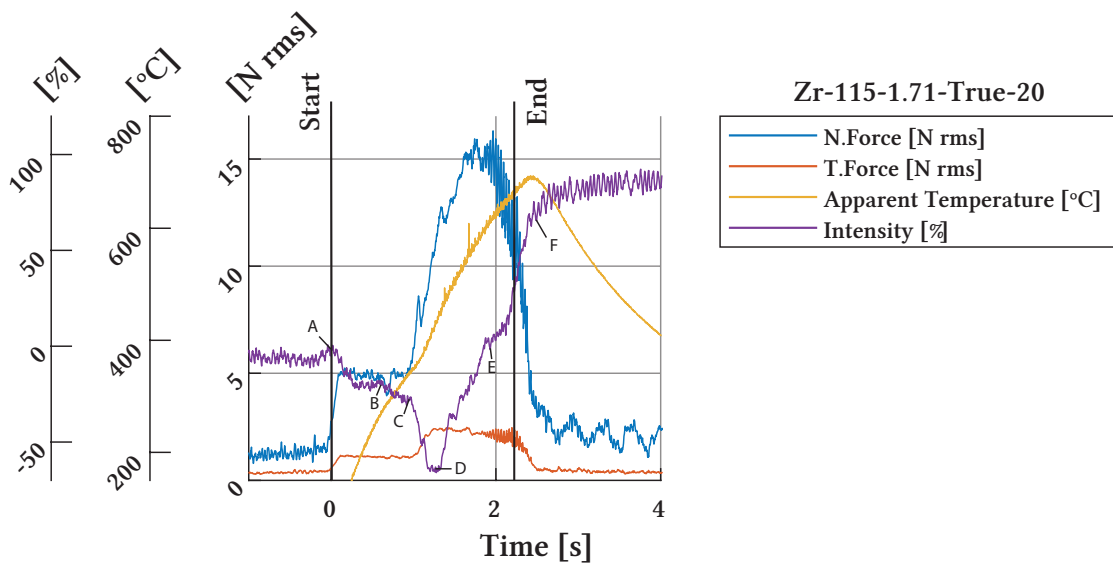
Fig. 6.15 Time domain data of Zr-115-1.71-True-20. The labels A-F are used to indicate significant transitions in the test.
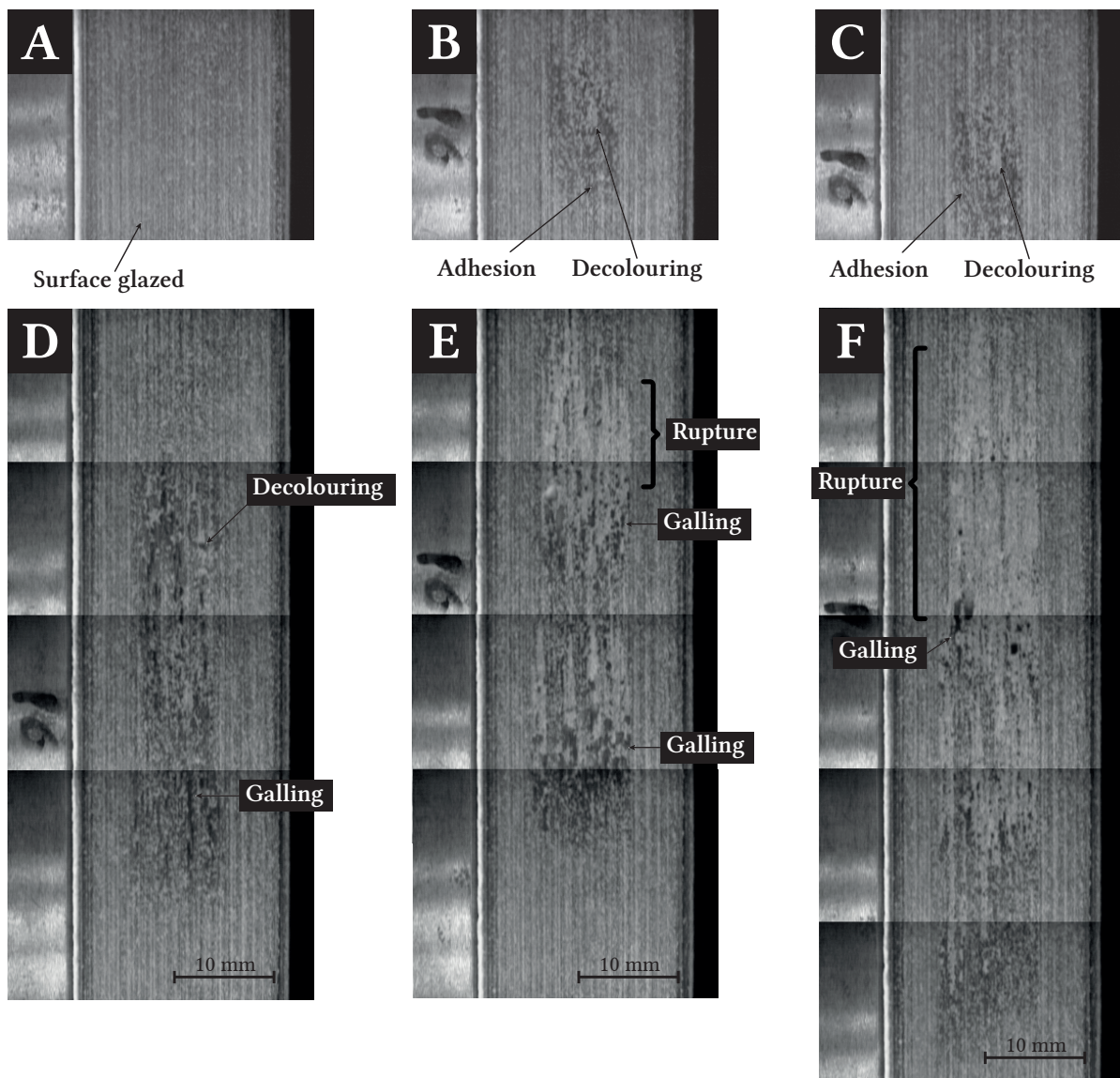
Fig. 6.16 Images collected during the Zr-115-1.71-True-20 test with the high-speed camera. Images correspond to times: (A) 0.00s; (B) 0.57s; (C) 0.93s; (D) 1.21s; (E) 2.51s; (F) 2.51s

The surface of this sample initially shows damage in the form of glazing (Fig. 6.16A). Upon start of the contact (marked with "Start"), the high-speed camera records a slight change in tone and images show slight adhesion in some areas and decoloration in others Fig. 6.16B. After this initial period, which is also characterised by rapid growth in normal and tangential forces, the system stabilises. The surface appearance is maintained at this point (Fig. 6.16 shortly after A up to C), and the system shows almost constant forces and heat addition (temperature increase at ~233 ºC/s). This stable position is not sustained for long, as the surface slightly ruptures shortly after and reaches an inflexion point (Fig. 6.16D). This shows as a decolouration on the

high speed camera images as new material is exposed (the truing process left a dull residue on the surface), but also an extension of arc of contact, that immediately transitions into a material adhesion process. It can be seen that material adhesion grows steeply after that with some galling too, and there is a surge in forces (from ~ 0 to 12.56 N$_{rms}$/s) and temperatures (from roughly 233 ℃/s to 356 ℃/s before and after D). Towards the end of the test (Fig. 6.16E), the coating shows signs of more severe galling, and forces contain high-frequency vibrations not previously present in the signals. Upon termination of the test (Fig. 6.16F), the sample shows severe forms of galling and also material rupture. A summary of the above events is presented in Table 6.2.

Table 6.2 Timeline summary of the Zr-115-1.71-True-20 test, exemplar for AR

Identifier	t (s)	Event
A	0.00	*Start*. Wheel is glazed
B	0.57	Slight change in tone with areas colouring and others decolouring. Forces rapidly grow and temperature starts rising.
C	0.93	The process has been stable but surface slightly ruptures. Rub length increases and forces and temperatures start a steep increase.
D	1.21	Inflexion point: adhesion starts increasing, there is evidence of galling.
E	1.88	There is rupture in the surface galling is more severe, temperatures keep rising, and forces now show vibrations.
F	2.51	*End*. Arc of contact slightly increases and galling is severe.

Post mortem analysis evidences the presence of subsurface damage in the form of cracks (Fig. 6.17), and it also shows surface renewing with adhesion blocks detaching from the surface.
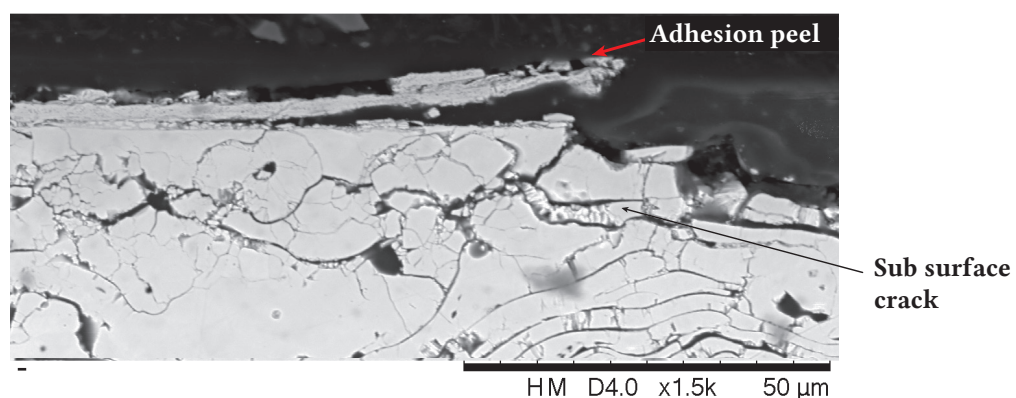
Fig. 6.17 Backscattered image of the cross section of Zr-115-1.71-True-20, showing sub surface cracks and adhesion peel.

6.3.2   Ploughing + Adhesion + Rubbing (PAR)

The time-domain data of sample "Al-115-1.71-AS-20-150" is presented in Fig. 6.18 as an example of PAR. This sample is placed in the PCA close to the previous but shows slight differences.
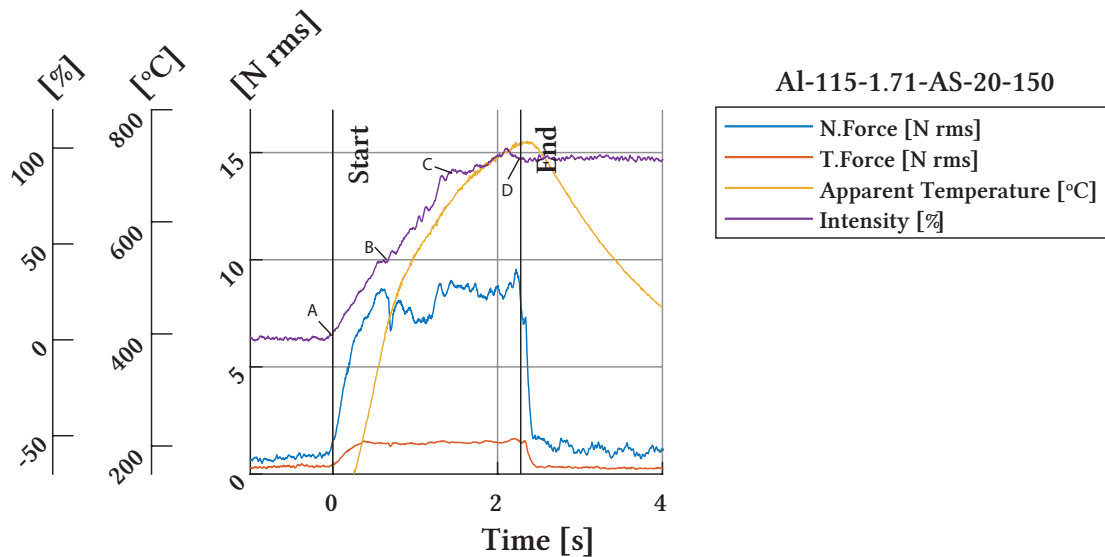
Fig. 6.18 Time domain data of Al-115-1.71-AS-20-150. The labels A-D are used to indicate significant transitions in the test.

From Fig. 6.18 and Fig. 6.19, it can be seen that the coating's surface is as-sprayed, white, and with no glaze (Fig. 6.19A). Upon contact, the high-speed camera shows that material immediately adheres to the wheel. Forces and temperatures behave similarly to those observed in the previous case; the former sharply rise before reaching a steady state, while the latter increases at a constant rate (roughly at 610 ºC/s). In the early stages of this period, the high-speed camera shows that the wheel engages in a second contact (Fig. 6.19B), increasing the arc of contact and showing a continuation in adhesion rate. This event coincides with a dip in the forces (which soon recover without influencing the overall forces' steady-state trend) and a deceleration in the temperature rate of increase (from roughly 610 ºC/s to 334.90 ºC/s before and after B). This state lasts until forces jump from 7.23 Nrms to 8.78 Nrms (Fig. 6.19C), matching the point where adhesion has no apparent increase in size but instead darkens in tone, indicating galling initiation. Conversely to in the previous case, galling appears localised instead of generalised, and forces do not show any vibrations. A new steady state is established at this point that lasts until the test terminates, wherein adhesion does not increase in size but in darkness, forces are stable, and temperatures keep rising. Thus, it is a period where

galling becomes more severe but still localised at the tip of asperities (Fig. 6.19D), Table 6.3 summarises the above events.
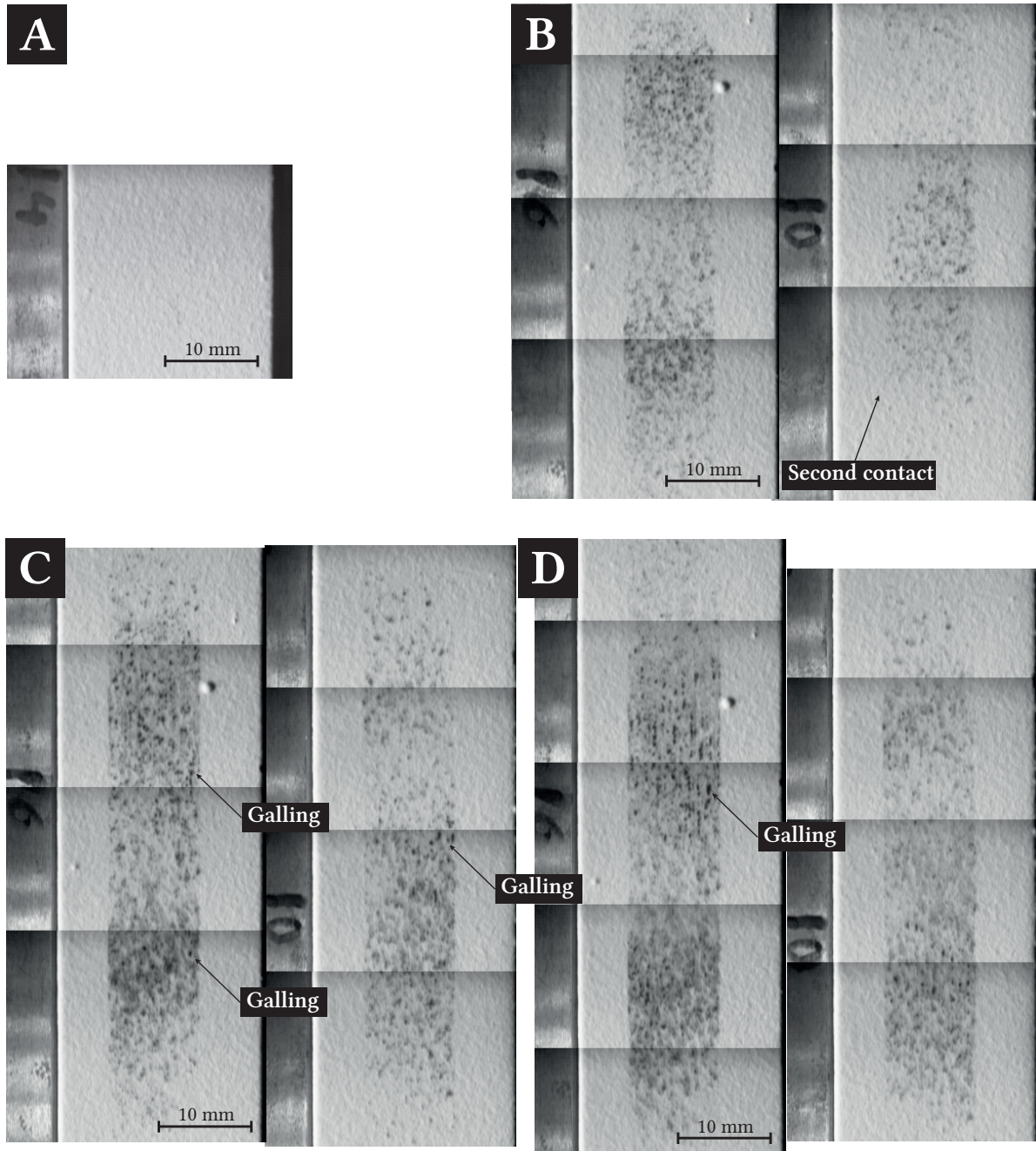
Fig. 6.19 Images collected during the Al-115-1.71-AS-20-150 test with the high-speed camera. Images correspond to times: (A) 0.00s; (B) 0.7s; (C) 1.31s; (D) 2.13s

Table 6.3 Timeline summary of the Al-115-1.71-As-20-150 test, exemplar for PAR

Identifier	t (s)	Event
A	0.00	*Start*. Wheel is as-sprayed, white, no glaze.
B	0.70	Adhesion has grown at a constant rate and a second contact is established. Forces are in steady state but dip, then recover; temperature decelerates.
C	1.31	Adhesion on wheel stops increasing in size and starts darkening (commencing of galling). Forces escalate and reach a new stable position. Temperatures show no change.
D	2.13	*End*. Contact length has not increased and galling appears extended through the surface.

It is of interest to consider the difference in mechanism between the two regions, as whilst wear is similar, indicated by their proximity on the wear map, truing has had an influence. The difference in mechanisms between the previous two cases are further highlighted by comparing the time domain of the high-speed camera, now plotted together in Fig. 6.20.
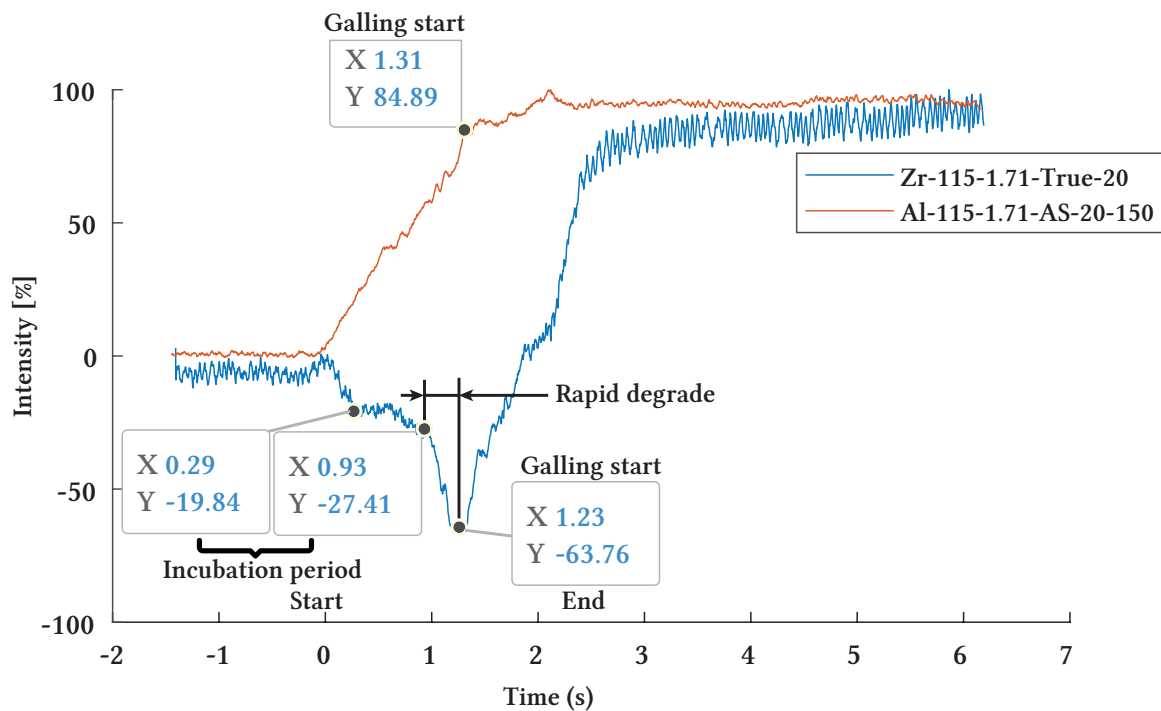
Fig. 6.20 Graphs of intensity change for samples Zr-115-1.71-True-20 and Al-115-1.71-As-20-150; exemplar of AR and PAR regions.

From the latter figure it can be seen that there is an incubation period of about 0.64s for the AR mechanism, whereas the adhesion in the PAR region is progressive from the start. During this period the surface slightly renews and based on the normal force (8.66Nrms vs 5.00Nrms from Fig. 6.21 at "*"), this translates into an improvement in the material removal process over the PAR mechanism. Despite the initial delay in adhesion, however, the wheel condition of the AR mechanism soon shows an accelerated degradation with a detrimental effect on the removal mechanism, and showing galling and rupture of the surface prior to that seen with the PAR mechanism. Not only initiated earlier but also in a more generalised and aggressive form. In other words, whilst the AR region shows an initial delay in adhesion with benefits in terms of removal mechanism, it also reaches a critical state faster, and leads to more severe forms of adhesion than what are seen with the PAR region. The latter being more progressive and not reaching the more severe forms.
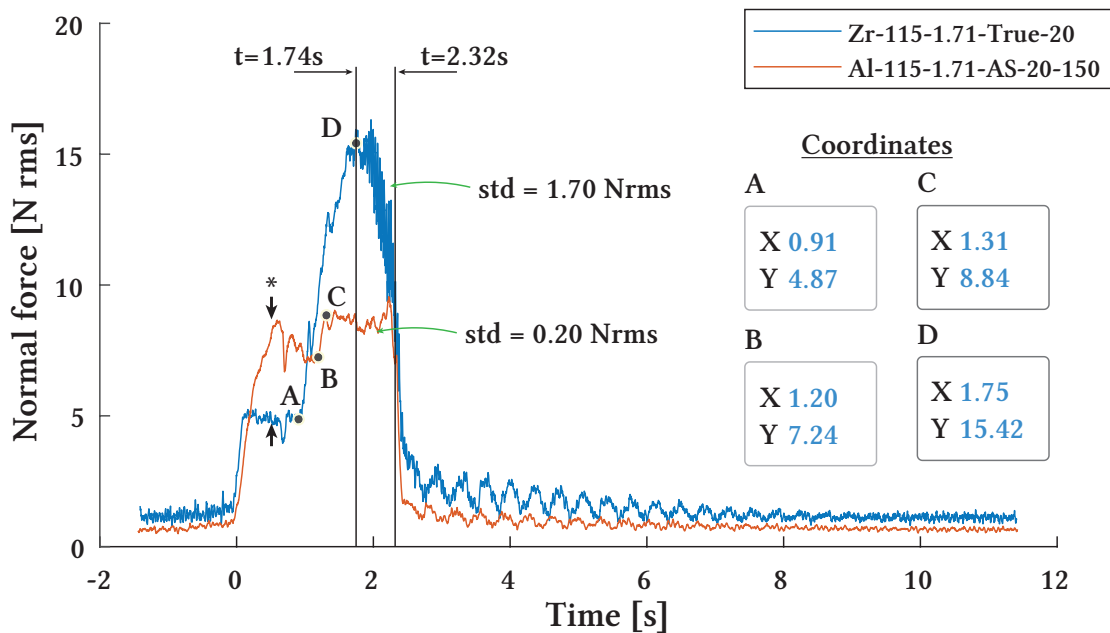
Fig. 6.21 Graphs of normal force for samples Zr-115-1.71-True-20 and Al-115-1.71-As-20-150; exemplar of AR and PAR regions.

It is noteworthy that whilst the camera metric increasing indicates a progressive mechanism, it is imperfect because of the difference in the tonality of samples and non-uniform lighting, and gradients of the metric cannot be directly compared. However, a progressive mechanism should also be captured very closely by the temperatures and forces. Therefore, the changes in these can be used instead to reflect and compare the respective processes. Examining, for instance, the standard deviation of the force data at the end of each test results in values of $0.89N_{rms}$ and $0.19N_{rms}$ respectively (time interval from 1.75s to 2.32s from Fig. 6.21 after

applying "detrend" [202]). Such results highlight that oscillations in the signal showing severe galling are much higher than those with localised galling. It can also be seen from comparing gradients at the rapid change in forces (respectively points A/D and B/C from Fig. 6.21) that the AR mechanism has a similar gradient but lasts for a prolonged period (12.56 Nrms/s and 0.84s, compared to 14.54 Nrms/s and 0.11s). This latter results emphasise the aggressiveness of the transition seen for the AR mechanism and also that for a gradual infill, such that observed on the PAR region, there is not a particular change in gradient, more like a discontinuity in the time-domain. It is therefore clear that truing has influenced the mechanism by both delaying it as well as accelerating severity when it initiates. The reasons for this will be considered further in the discussion.

6.3.3   Adhesion + Heavy Rubbing (AHR)

The adhesion and heavy rubbing mechanism is much like those previously presented but more progressive. This mechanism will be illustrated with two examples, given the spread of the results that, in spite of being essentially equivalent, contain slight variations. The exemplar tests are those pertaining to "Al-115-0.31-AS-40-100" and "Al-115-0.31-True-20-150", which are located at the extremes of the AHR region. Their figures are presented in the same form as before, by first showing the comparison of the time-domain data (Fig. 6.22).
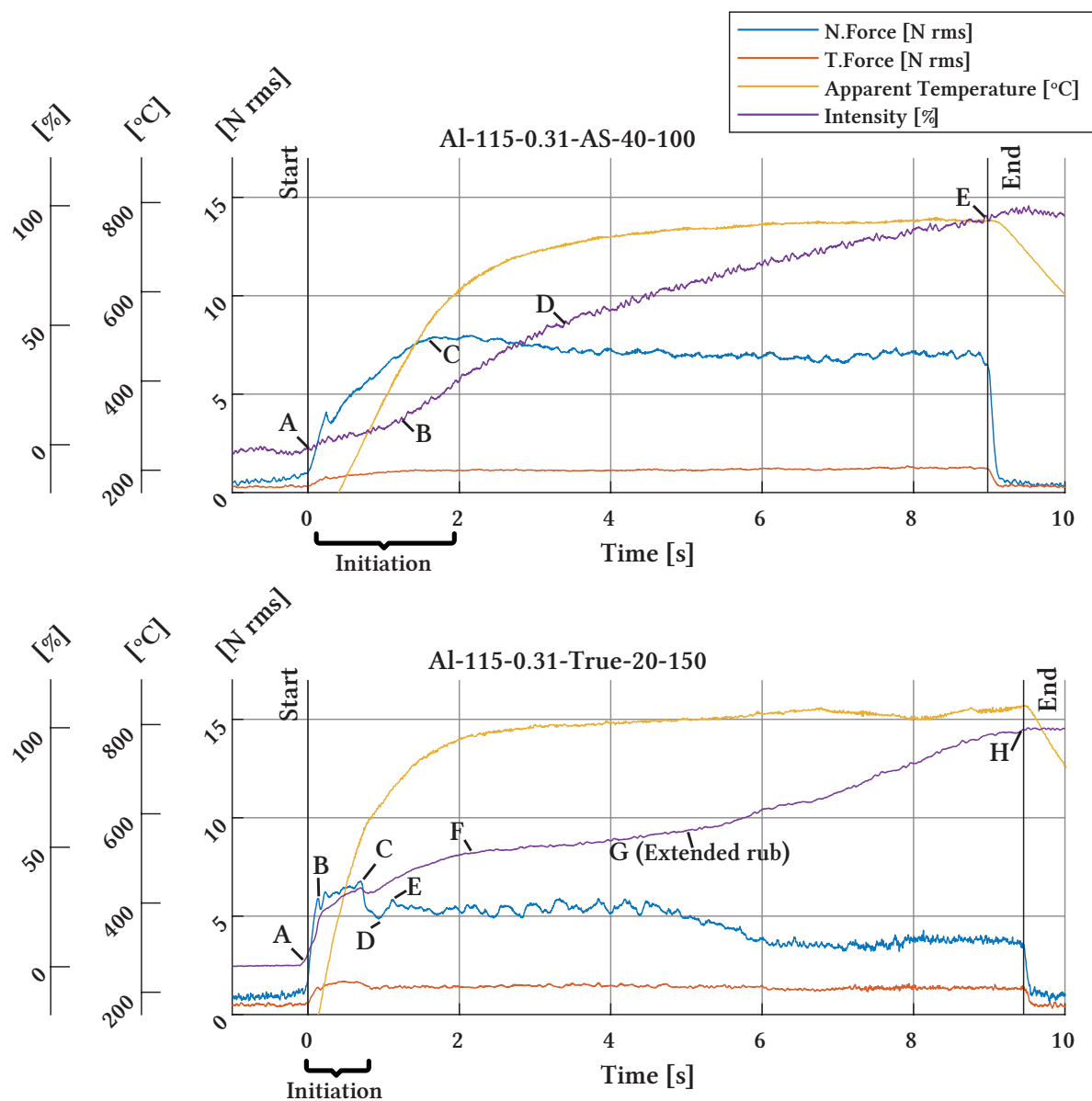
Fig. 6.22 Time domain data of Al-115-0.31-AS-40-100 (top) and Al-115-0.31-True-20-150 (bottom) as examples of the AHR region. The labels A-E (top) and A-H (bottom) are used to indicate significant transitions in the test.

In addition, images have been taken and processed. These are sequentially shown for comparison in the coming pages (Fig. 6.23, Fig. 6.24, Fig. 6.25). It is worth noting that Fig. 6.25 is a continuation of Fig. 6.24, not placed together due to the limited space.
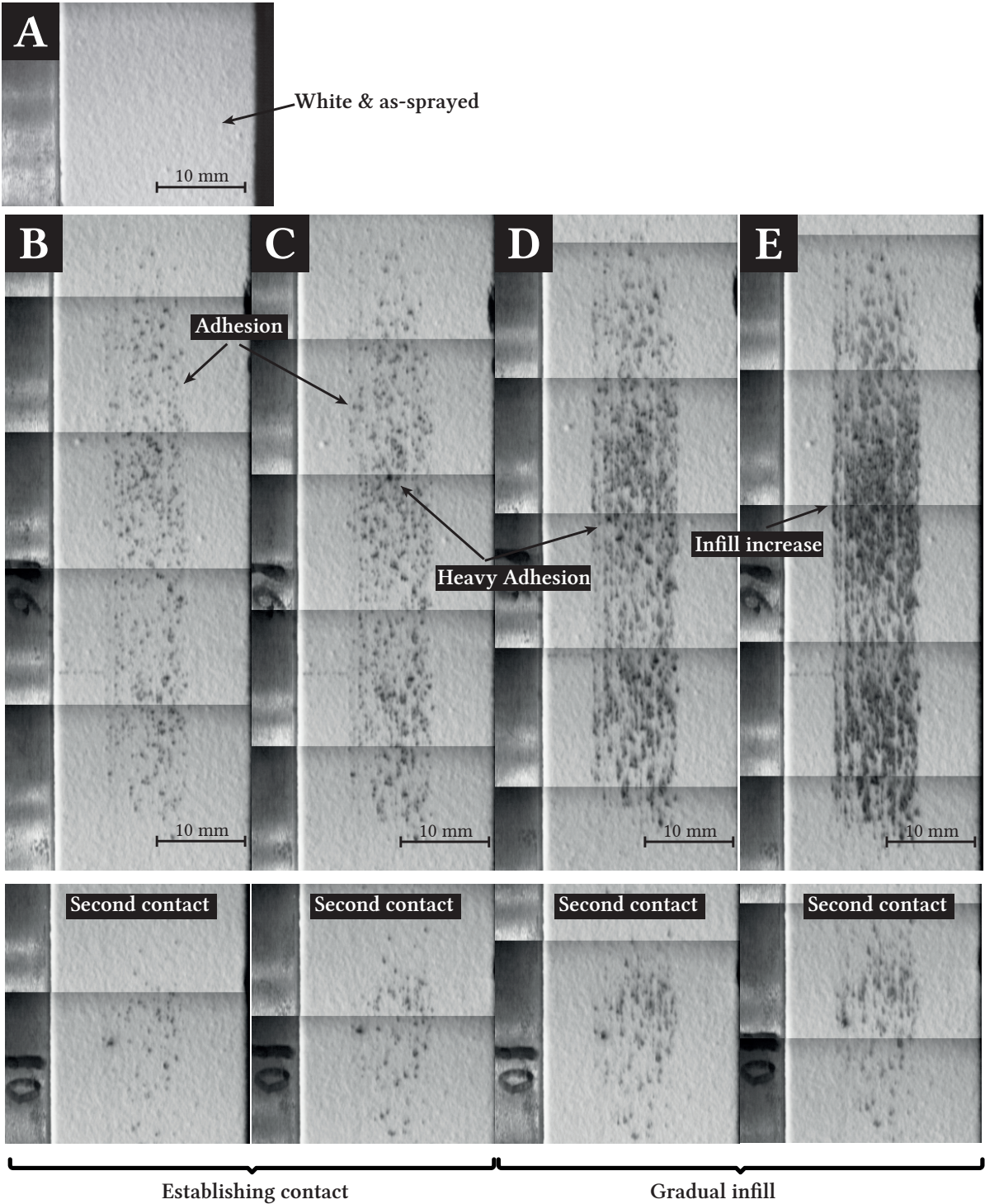
Fig. 6.23 Images collected during the Al-115-0.31-AS-40-100 test with the high-speed camera. These correspond to times: (A) 0.00s; (B) 1.28s; (C) 1.82s; (D) 3.54s; (E) 8.83s
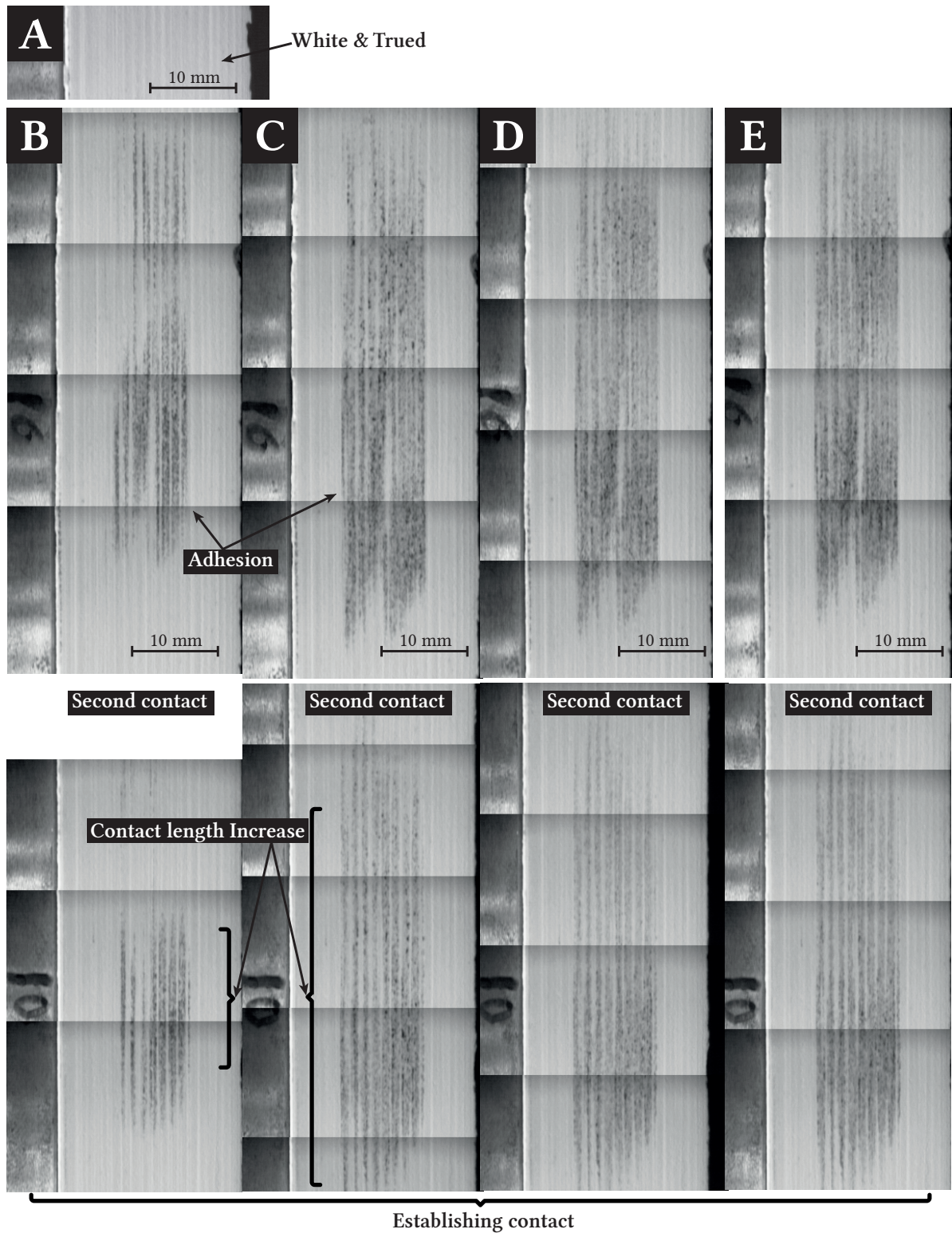
Fig. 6.24 Images collected during the Al-115-0.31-True-20-150 test with the high-speed camera. Collection times: (A) 0.00s; (B) 0.12s; (C) 0.68s; (D) 0.90s; (E) 1.11s ... Continue in Fig. 6.25
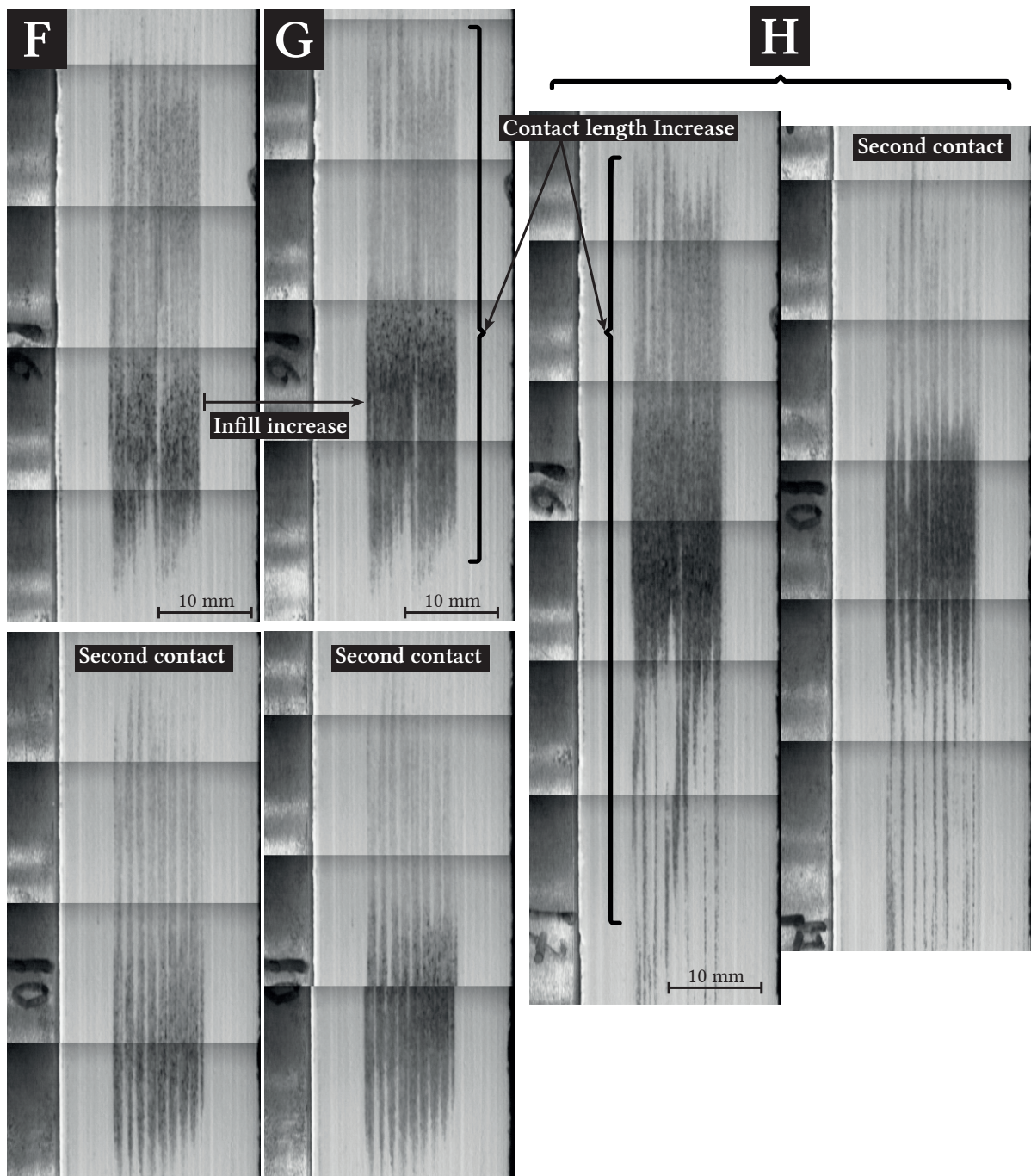
Fig. 6.25 Continuation from Fig. 6.24. Images collected during the Al-115-0.31-True-20-150 test with the high-speed camera. Collection times: (F) 2.28s; (G) 4.95s; (H) 9.31s

It can be seen from Fig. 6.23A-C and Fig. 6.24A-E that both tests undergo an initiation period where the contact increases in length, and forces and temperatures grow (Fig. 6.22). It can also be seen from Fig. 6.22 that this period is longer for the as-sprayed sample than for the trued one (C = 1.82s vs E = 1.11s), and that entails a further delay in temperatures that grow

at a rate of $\sim$303 ºC/s compared to $\sim$687 ºC/s of the trued sample. Thereafter the contact is established and metrics plateau. Meaning that from this point on, the contact length remains fairly stable and instead infill levels grow in the contact area, forces are almost constant, and temperatures start stabilising (these have a delay with respect to the forces). Whilst it can be seen that the as-sprayed sample infills progressively until the test terminates, contact length extends one more time for the trued sample (point G). Infill levels are allowed to extend and normal forces plateau on a lower level, indicating an improvement in the removal mechanism.

Comparing the above images (Fig. 6.23, Fig. 6.24, Fig. 6.25), it is clear that for the trued wheel, lighter adhesion occurs on a larger area (either contact length is extended). In contrast, for the as-sprayed wheel, adhesion is more localised and intense. These similarities and differences are further emphasised by comparing the high-speed camera metric in Fig. 6.26, this time used in absolute values as a proxy for adhesion coverage of the coatings, given that the coating's initial tone is almost equivalent.
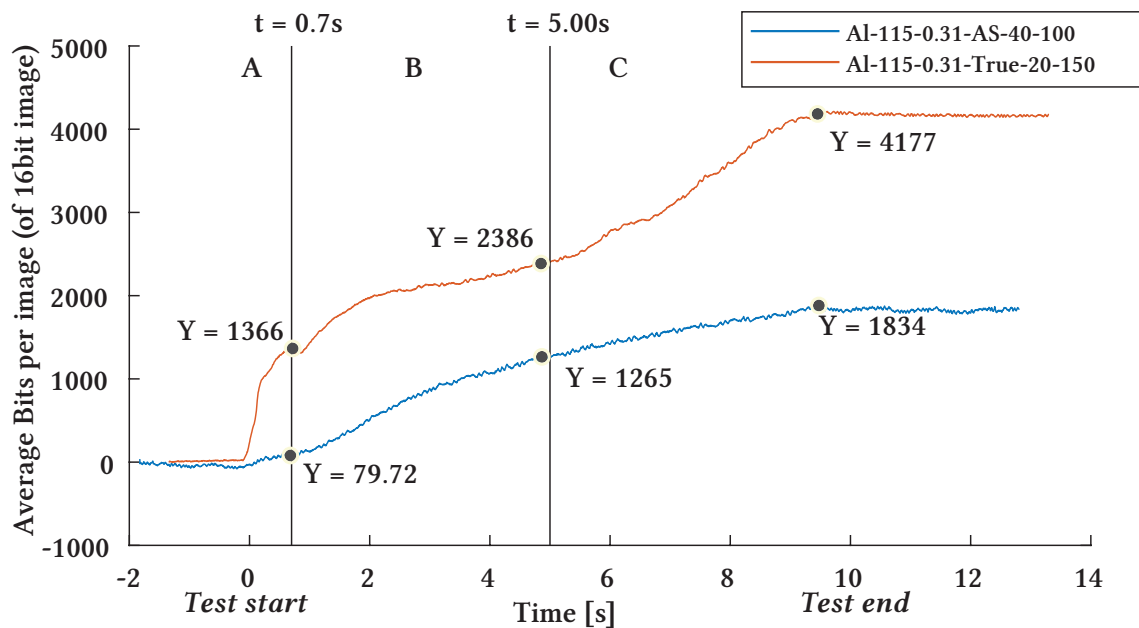
Fig. 6.26 Graph comparing tone change (in absolute value) of wheels as a proxy for adhesion level. Wheels : Al-115-0.31-AS-40-100 and Al-115-0.31-True-20-150

What is shown in the above figure is that there is an initial period (section A) where gradients are significantly different (rate of 1951 bits/s vs 114 bits/s), highlighting that the available areas for infill are distinct. For the as-sprayed sample, infill is limited to a short segment as that is the fragment that can geometrically contact. Conversely, the trued coating shows a higher gradient because more area is initially exposed and cover.

Additionally, Fig. 6.26 shows that once the available initial topography is filled, both samples reach a very similar steady-state (section B). During this period, the adhesion in both samples progresses at a very similar rate (respectively 237 bits/s for trued and 275 bits/s for as-sprayed), intensifying and moving towards a state of heavier adhesion. Both samples become once again distinguishable when the regions of light infill are exhausted (section C). For the as-sprayed sample, adhesion has been relatively progressive (Fig. 6.23D-E), and small pockets of adhesion can be seen, indicating that there has been no significant adhesion growth and instead these have mainly intensified/darkened. On the other hand, it can be seen that the trued sample exhibits a further rise in gradient at approximately 405 bits/s, and Fig. 6.25H shows that adhesion breaks out into newly available areas, given that the wheel is broadly round. It coincides that this trued sample showed far more material removal than the rest and was thus initially thought an outlier (Section 5.2). However, this improved behaviour is because new areas of the wheel with unadhered material enter the tribosystem. Although, in doing so, it also exhibits extreme contact temperatures, indicating that in spite of material being removed from the blade, this adheres to a greater extent to the coating's surface, and the system is incapable of evacuating heat.

6.4   Discussion

The above results present strong evidence that the primary wear mechanism is adhesive wear, and as for classic adhered materials, it is depicted as a progressive surface degradation (Fig. 6.27). The AR, PAR, and AHR regions are captured in Fig. 6.27, where the figure shows that they all fall on a classical wear spectrum. More precisely, the figure illustrates that material transfer occurs first, then grows and coalesces before forming more significant areas of large-scale material transfer such as galling. In the case of the AR samples, this process does ultimately lead to failure. As it is also noted in the figure, the combination of the variables present in the different regions also either accelerate or slow down the process.
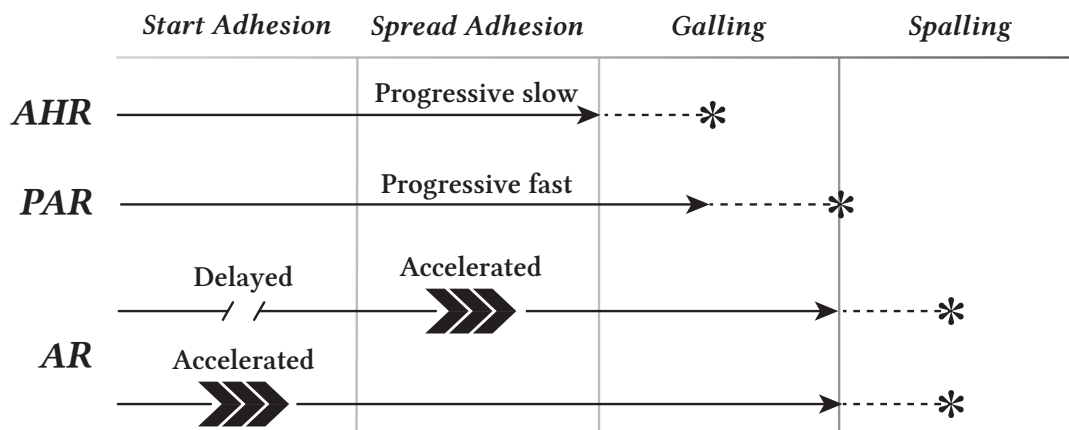
Fig. 6.27 Schematic diagram illustrating the progression of the different wear mechanisms.

This results are consistent with the "asperity junction growth" theory established for adhesive wear [183, p. 583-584], wherein for a sliding contact, stresses are high enough to deform adhesion junctions and cause their rupture. When material adheres to the surface, a loop with positive feedback is created and eventually may become unstable [183, p. 583-584]. The outcome is a rapid change in forces, an increase in force ratio, and a progression to more severe forms of adhesion. It can clearly be seen that the above theory correlates with the experimental behaviours observed in this research (Fig. 6.27). Thus, the general knowledge on adhesive wear is relevant and can essentially be used to enhance the contact conditions.

As noted, variables such as material, surface, spraying, and incursion rate have been investigated, and relationships have been established to highlight how these have either enhanced or diminished the tribological process. However, what is ultimately more of interest is how these variables affect the underlying process. For instance, changing material has a direct impact on thermal capabilities. Similarly, truing the coatings spreads the contact and introduces damage to the surface layer. For the case of spraying, the conditions used affects both of the above, influencing the material's thermal properties and the defect structure of the coatings, but this was found to be a less strong variable than the previous two. Finally, the adhesion rate is very much linked to the grit penetration into the material and also the contacts' duration, in essence, linking it to the incursion rate.

Studying the time domain revealed that extending the contact length or slightly renewing the coating's surface were the most effective processes for improving material removal. Extending the contact length has a significant tribological implication [130]. Amongst many key factors, a longer contact entails work being divided around the coating, reducing normal stresses and allowing to sustain larger tangential ones for a longer period [183, p. 584]. Adhesion is also spread more uniformly around the coating, which further extends the coating's effective life. The effects of surface renewal are much like the above, delaying the effects of adhesion.

However, with added benefits: that as the transferred material can now detach from the coating's surface when forces grow above a threshold, it advocates for sharper surface, and it also serves as a heat removal mechanism [203].

Based on the above, one would favour a trued surface over an as-sprayed one, given that it presents both a longer contact and superficial damage that promotes surface renewal. This is particularly pertinent at the high incursion rate as the process can benefit from this superficial damage. However, the defect structure is not inherently of the wheel (it is introduced by truing), and the results evidence that the system destabilises when these are no longer present (Fig. 6.27AR). After that, forces and temperatures surge, and surface degradation is accelerated, which eventually has manifested as the most catastrophic failures experimentally seen. What is more, preparing the samples through truing might already be detrimental because of the high stresses. In fact, vertical cracks and delamination has been seen particularly in trued alumina coatings (Section 6.2.3, and Section 6.2.4). These findings thus emphasise that superficial defects are beneficial, but truing might not be the most appropriate process to introduce them.

Regarding the aforementioned rapid change in forces, further research would be needed to clarify. However, it is likely due to a high percentage of wear flat areas left on the wheel after the exhaustion of the surface renewing and the start of workpiece burn. Such an event is established in grinding literature [194, p. 139]. It would thus be interesting to investigate if such an event correlates with the blade's burn or the lip formation observed in the tests (Section 6.2) and also if the truing process has introduced compaction in the samples that favour this outcome.

The behaviours of as-sprayed coatings (Fig. 6.27PAR) contrast with those above as material transfer is observed to be more progressive, and none of the severe adhesive effects are seen for the test duration. What these results show is that when surfaces are not preconditioned, their deterioration is more gradual, and the coating's life is extended. On the one hand, this would be desirable given the extended life of the coating. However, the effectiveness of delaying adhesion and heat then relies on how the coating is manufactured (i.e., material and spraying parameters), and in this research, no significant evidence has been found to believe that the defect structure alone is sufficient to promote surface renewal (for the induced stress state).

Moving to low incursion rate, the only influence of truing is to extend the contact length, as stresses are not sufficient to actuate the dislocations and damage in the coating. Contact times are long, and thermal effects are therefore a primary drives in this scenario. Extending the contact area benefits significantly the system in comparison to a shorter contact [194, p. 91], as spreading adhesion and work more uniformly around the wheel means that the rate of progression from low to high adhesion is slower and material removal is increased. This provides a further interesting perspective as it highlights that lower adhesion levels are beneficial,

and whilst this can be achieved by spreading the contact, it is worth noting that contact time is also increased and it translates into heavier thermal damage of the workpiece [194, p. 91]. Overall, truing is clearly beneficial at the lower rate, but given the lack of control in closure rate of the engines, this is not acceptable due to the catastrophic failures seen at higher rates.

The preceding discussion highlights the role of heat creation and dissipation within the contact, and this is influenced by the duration of the contact and the coating's ability to refresh (i.e., either by mechanical fracture or better conductivity). In a dry contact like this one, heat is divided between the wheel and the workpiece, and if surface renewal happens, also between the debris or chips [203]. As incursion rate increases and surface renewal is promoted, the contact moves from a thermal dominated, to a thermal-mechanical, to a mechanical contact [199]. Low incursion rate for instance is exemplar of a thermal driven condition given that surfaces rub regardless of their finish, surfaces do not renew, and adhesion constantly grows (Fig. 6.27AHR). In this scenario heat is solely divided between the wheel and the Inconel blade [203], and any change that reduces heat in the contact is beneficial. A more conductive material for instance (alumina over zirconia), or interrupting the contact would show as a reduction in temperatures and an improvement.

An example of a thermal-mechanical contact happens at the high incursion rate, where trued and as-sprayed surfaces are seen to differ (Fig. 6.27PAR and AR). At this condition, stresses are higher than at lower incursions, and grit sharpness plays a more significant role since they can penetrate deeper into the material [194, p. 130]. However, surfaces do not renew, and adhesion is seen to cover the wheel eventually. A metal-to-metal contact is established at this point, and the contact that was first thermo-mechanical transitions into one that is solely thermally dominated (e.g., materials with different conductivities will once again show a difference). As surface renewal is triggered, heat is more efficiently removed from the contact, and the material's heat properties become less important. The trued zirconia sample tested at the high incursion rate exhibits this behaviour (Fig. 6.27AR), highlighting that when stresses are sufficient to trigger the defects in the structure, adhesion and heat are delayed. In essence, evidencing that contacts that delay adhesion and manage the thermal load more effectively, either by reduced heat creation or better dissipation, perform better.

Incursion rate therefore plays an essential role as previously found statistically, and the time domain study further supports. Incursion rate (as it is used herein) tackles two subjects at the same time. It defines the stresses in the contact and also the overall contact time. These are both key issues as stresses would be the ones responsible of triggering specific mechanism in the coating (depending on the defect structure), and the contact time would be the one responsible for heat input and the eventual severity of the process. The trued samples are evidence of this process as at low incursion rate they are no different to as-sprayed samples (Fig. 6.27AHR),

but at high incursion rates they progress to the most severe forms of adhesion (Fig. 6.27AR). Such outcomes highlight the ability of stresses to promote pre-existent damage in the coatings, and its difference with contact time.

Finally, it could be inferred from these results that an as-sprayed microstructure is desirable, and a post-spraying process could supplement it if (and only if) it were able to introduce defects in a controlled manner, increase concentricity, or both thereof. In this way, being able to tune the coatings' defects for inducing a particular behaviour at the desired stress states, and also dividing the work around the wheel. It is interesting to note the link between renewing the surface and extending the contact length, and it is encouraging to compare this results with those found by Yossifon and Rubenstein [204], who suggested changing the wheel's grade to encourage grit pull out and surface renewal when forces go beyond a threshold. This suggestion is in line with the previous idea of introducing defects to prevent or shift the wear mechanism to more benign forms. Changing the coatings' hardness may be a way of accomplish such behaviour as done in grinding [204] and also seen in the wear properties of these coatings (see Fig. 2.15 in the literature review). Further study focusing on how to achieve these beneficial features via alternative mechanism, given the fact many of the variables studied in this work move outcomes in multiple directions, is recommended.

6.5 Conclusion

The previous chapter established the statistical relationships between varaibles and a PCA was plotted. In this chapter the PCA was interpreted as a wear map and the different regions in the map have been explored. As could be expected from the PCA, depending if a variable has a positive or a negative influence on the material removal process the outcome is moved around the PCA. For example in the heavy adhesion region, depending on the combination of variables either moderate to severe adhesion could be achieved.

The time-domain study has provided strong evidence that these coatings do not effectively remove material and instead all sit in the adhesion's hierarchy, ranging in severity from mild adhesion to extreme cases like galling, spalling, and delamination. In general, the results are explained in terms of how surfaces cope with infill and heat, and the discussion may thus be moved to a higher ground, where the treatments studied herein are mere examples of ways to delay adhesion and thermal effects.

On the above basis, and given that increasing contact length and renewing surface have been seen to have the most significant impact, it would be interesting to reach a further understanding on the defect structure and how this relates to the threshold stresses required to promote surface renewal. Possible options could be those patented, namely, increasing porosity, or introducing

hard particles in the coatings, as well as techniques used for abradable linings like introducing blade angles.

Chapter 7

Investigation of porosity for abrasive ceramics

The previous chapter showed that using alumina for this contact is advantageous as it delays the progression of adhesion. Applying alumina would allow engine manufacturers to decrease tolerances in the cantilever-vane/rotor arrangement, decreasing the pressure losses and improving engine efficiency. Despite the many benefits, engine manufacturers have grown reluctant to use alumina because it ultimately delaminates and is not compliant with engine requirements (Section 2.6.2). The results in the previous chapter reinforced this view as all alumina coatings were found to detach from the bond coat. Conversely, zirconia prevents such an event to a greater extent. Thus its use is favoured. The issue is that zirconia does not manage heat as effectively (Section 6.4), and adhesion progresses faster. Hence, improving zirconia's performance is the major objective of this chapter.

Earlier, this research revealed that thermal properties are less critical when a coating has a mechanical response. An option would be to introduce hard particles, turning the coatings into ceramic matrix composite materials, much like how grinding wheels are designed. Despite the benefits of sharp/hard grits and heat dissipation through surface renewal, the thermal effects in aero-engines joined with differences in thermal expansion coefficients between constituents can lead to the coating's fatigue and eventual delamination (Section 2.3). What is more, entities that may act as crack initiators would not be something desirable on the surface of a highly stressed rotor. Hence, whilst the grinding process is probably the abrasive system to look up to, introducing hard grits is not an ideal architecture to implement.

Another alternative is to change the defect structure through porosity control. In grinding, the grade of wheels is chosen based on the stresses generated in the contact [204] and a similar process is undertaken with abradable coatings, where friability is changed through porosity [205] or hardness control. For the latter case, a filler like polyester is introduced [134],

which can be burned out post-deposition through thermal treatment. The benefit is that the ceramic matrix is left free of extraneous particles after that; hence, resolving the issues of having different constituents in the coating and delaying material fatigue.

Clearly, introducing porosity is preferable over hard grits, and it is thus the option that will be studied through this chapter. Herein, zirconia with different levels of polyester will be tested to investigate if and how material removal is influenced when porosity/friability/defect structure is changed. The hypothesis to be tested is that whilst a porosity increase causes a thermal conductivity decrease (which is detrimental for this contact), it also promotes surface renewal, which makes the material's thermal properties less relevant. The side benefits of taking such an approach are noteworthy. The literature (Section 2.4) has reported that increasing porosity makes coatings more compliant against uneven stresses and increases thermal shock resistance and thermal cycling life.

7.1   Methodology

7.1.1   Materials

In this experiment, zirconia (Zr) is studied alone and with two increasing levels of polyester (PE). That is, three different coatings have been manufactured: Zr sprayed at 40 g/min, Zr sprayed at 30 g/min with PE at 2.2 g/min, and Zr sprayed at 30 g/min with PE at 4.5 g/min. Whilst deposition rate was previously shown to have a weak influence on the contact, with material and truing stronger variables, it still showed an influence. The reason is that the degree of splat melting is changed, essentially altering the inter-splat contact and the defect structure in the coatings. As such, spray rate and PE content are investigated here to both fully understand their benefit and to determine if the inclusion of PE is a stronger variable than material structure. Further details about the spraying parameters are provided in Table 7.1.

Table 7.1 Spraying parameters used to manufacture the zirconia and zirconia+polyester coatings

Parameters	Bond coat	Top coat	
Powder / run	M450	M204	M600
Powder port	1.5@90	1.8@90	2.0@105
Carrier/1st Gas (Ar)	2.3/40	2.5/35	4.0
2nd gas (H)	10	12	
Volts (V)/Power(kW)	68.7/41.2	67.5/40.5	
Powder flow (g/min)	50	40	4.5
Hopper setting	16	26	7.5
Spray distance [mm]	140	120	
Surface speed (m/min)	6	60	

Traverse speed: 6.7 mm/sec
Thickness: 500 um
Gun: PT-F4 (Oerlikon Metco)
Nozzle: 6 mm

Run 1: M204B-NS@40 g/min

Run 2: M204B-NS@30 g/min + PE@2.2 g/min

Run 3: M204B-NS@30 g/min + PE@4.5 g/min

Notation: *M* Metco; *PE* Polyester.

It can be seen from the backscattered images of the coatings (Fig. 7.1) that adding polyester has increased the level of defects in the microstructures, which is in line with the literature ([206]) and as intended. Upon comparison of the microstructures, it can also be seen that the increase in defect structure is slight when PE is introduced at 2.2 g/min (Fig. 7.1A-B), whilst the difference is visibly more significant when PE is sprayed at 4.5 g/min (Fig. 7.1B-C).
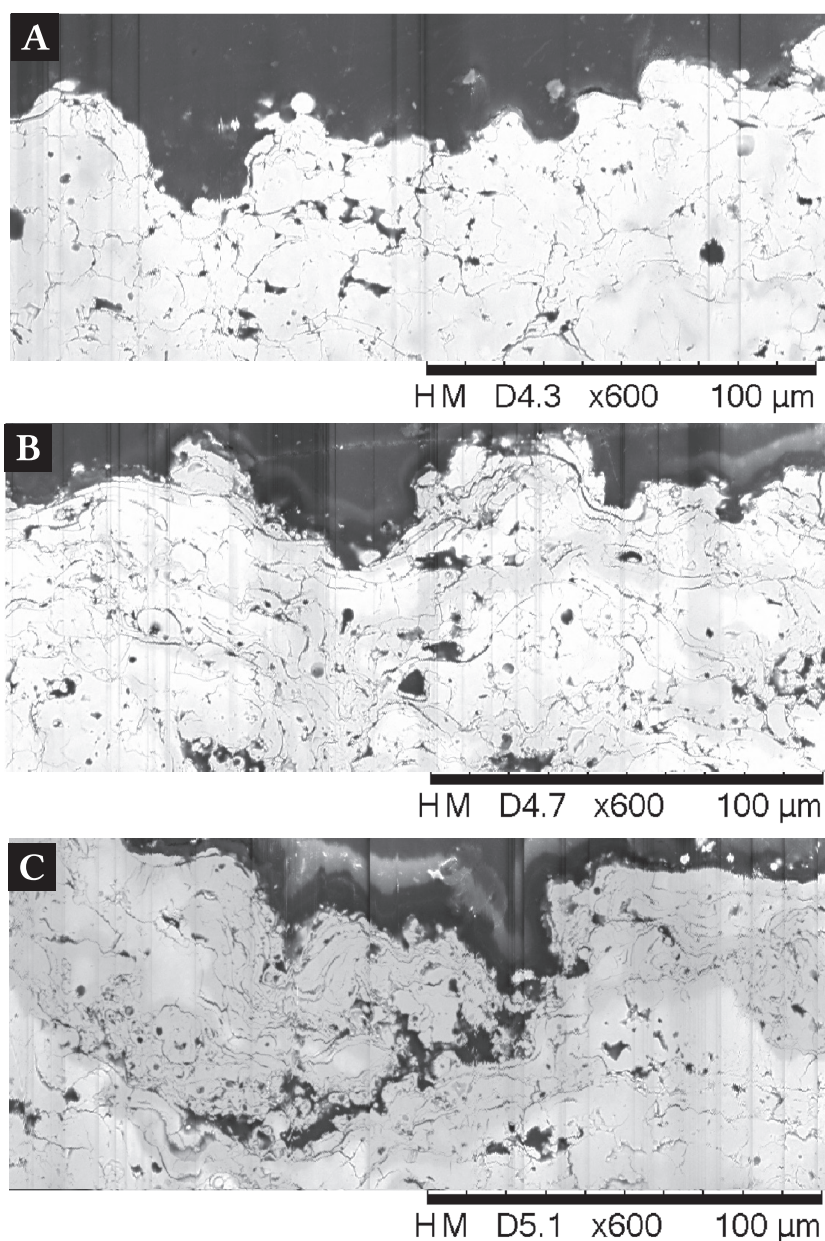
Fig. 7.1 Backscattered image of the cross section of (A) Zirconia at 40 g/min; (B) Zirconia at 30 g/min with PE at 2.2 g/min; (C) Zirconia at 30 g/min with PE at 4.5 g/min.

It is worth discussing the impact on material properties of the amount of polyester used for this experiment. Based on Fig. 7.1, an increase in PE deposition rate means an increase in porosity, which according to literature ([64]), entails a decrease in thermal conductivity and elastic modulus (amongst many other factors). Porosity is thus a limiting factor for these coatings, given that they operate on a highly stressed rotor and are required to maintain their structural integrity. Although the actual level of polyester to be integrated into the coatings is still to be determined, the ratio polyester/zirconia is respectively ∼7 and 15 total wt%, placing them in the mid and top-level range of total filler weight reported for abradable linings prior deposition (0.3-15 total wt%) [206]. Therein, a degree of abradability is conferred; however, given they are ceramics, they remain abrasive to a great extent, and engine manufacturers tend to tip the blades with harder materials to prevent them from wearing (Section 2.7.2). Other aspects that have previously been noted to affect the homogeneity or properties of the coatings, e.g., the mixing rate of polyester in the feedstock (Section 2.6), have not been controlled — representing how it is applied to engines at the current state. In this way, variabilities in the experimental results may highlight a lever that may need further investigation.

Besides of a porosity increase, the increase in PE deposition rate also causes a surface roughness increase (Table 7.2); as shown by measurements taken with the Alicona.

Table 7.2 Roughness measurements of zirconia coatings with range of polyester. Measurements taken with Alicona from exemplar samples.

Material	Roughness [R_a/R_q]
Zr40	5.93 /7.36 μm
Zr30+PE2.2	8.51 /10.90 μm
Zr30+PE4.5	14.35/17.87μm

The change in zirconia's deposition rate from 40 g/min to 30 g/min may also have an effect on the coatings strength as lower particle velocities lead to lower porosity and an improved inter-splat contact ([48]); thus an improvement in mechanical properties. To allow for batch comparison, zirconia sprayed at 20 g/min from the batch of tests performed earlier in Chapter 5 is also added to the testing matrix, joined with another at 40 g/min to verify repeatability between batches. All the samples used with their spraying processes are summarised in Table 7.3.

Table 7.3 Table presenting all the samples used for this experiment, and how manufactured.

	Material	**Condition**	**Manufacturing**
New batch	Zr40	As-sprayed	Table 7.1
	Zr30+PE2.2	As-sprayed	
	Zr30+PE4.5	As-sprayed	
Old batch	Zr40Rep	As-sprayed	Table 5.1
	Zr20Rep	As-sprayed	

7.1.2   Experimental method

To investigate the effect of porosity, the test rig and instrumentation described earlier in Chapters 3 and 4 are used in the same way as previously done. The methodology followed can thus be found in Section 5.1.3.

Table 7.4 summarises the experimental matrix and testing conditions. As before, these tests are carried out at a single speed (115 m/s) since samples do not uniformly deform when changing speeds. Additionally, 115 m/s is chosen for testing as samples sprayed with different conditions do not show evident deformation differences at this speed. The incursion rates are equivalent to those used earlier (0.31 um/pass and 1.71 um/pass), allowing to compare results. However, in this case, each condition has three repeats per incursion to increase the statistical significance and evaluate the variability of the process. The two zirconia samples of the previous experiment are exceptions, which are tested only once per incursion. As also previously done, the coatings are tested against an Inconel 718 blade.

Table 7.4 Experimental matrix showing the materials tested and the number of repeats

n° Samples	**Material**	**Counterpart**	**Incursion Rate [um/pass]**	**Test speed [m/s]**
2	Zr40Rep	Inconel 718	0.31/1.71	115
6	Zr40	Inconel 718	0.31/1.71	115
6	Zr30+PE2.2	Inconel 718	0.31/1.71	115
6	Zr30+PE4.5	Inconel 718	0.31/1.71	115
2	Zr20Rep	Inconel 718	0.31/1.71	115

7.2   Results

The proceeding section will present the experimental results. The order will be the same used previously in Chapter 5, where images were first presented to provide a visual description of the tests. Since there are repeats, the selected images will exemplify the typical appearance post-test of the coatings. However, it is worth noting that there is some variability within the tests, mainly due to the random nature of the samples' manufacturing process and the experimental procedure. Throughout this first section, time-domain data will also be used as needed to support observations.

The second half of this section is reserved for comparing the results numerically. In this section and equivalently to what was done in Chapter 5, primary descriptors of the contact will be presented first. These are material removal, normal and tangential force, and the apparent temperature of the blade. Secondary level descriptors will then be evaluated next, i.e., force ratio and specific grinding energy. Since this time the DoE includes repeats, there is no need to compare samples or results through their time domains. Behavioural changes and trends will thus be mainly evaluated through the mean response of the above descriptors. Nonetheless, to further investigate behavioural changes in the coatings' abrasive function, the time-domain data will still be shown when a significant trend is observed.

Fig. 7.2 is a typical example of Zr40 tested at both incursion rates. Comparing the appearance of the adhesion with that happening on the old batch (named "Zr40rep" for clarity in Fig. 7.3), both seem very similar. These figures show that adhesion at the low incursion rate is concentrated in a single contact. In contrast, there are two contacts at the higher incursion rate, where adhesion also spreads and lightens. These figures evidence what was learned in the previous chapters; namely, going from low to high incursion rate spreads adhesion and divides work around the coatings' surface, reducing the severity of adhesion. The contact for Zr40 (Fig. 7.2) does appear less uniform than the one on Zr40rep (Fig. 7.3), and it is something that will be further explored in the next section when evaluating the contact numerically.
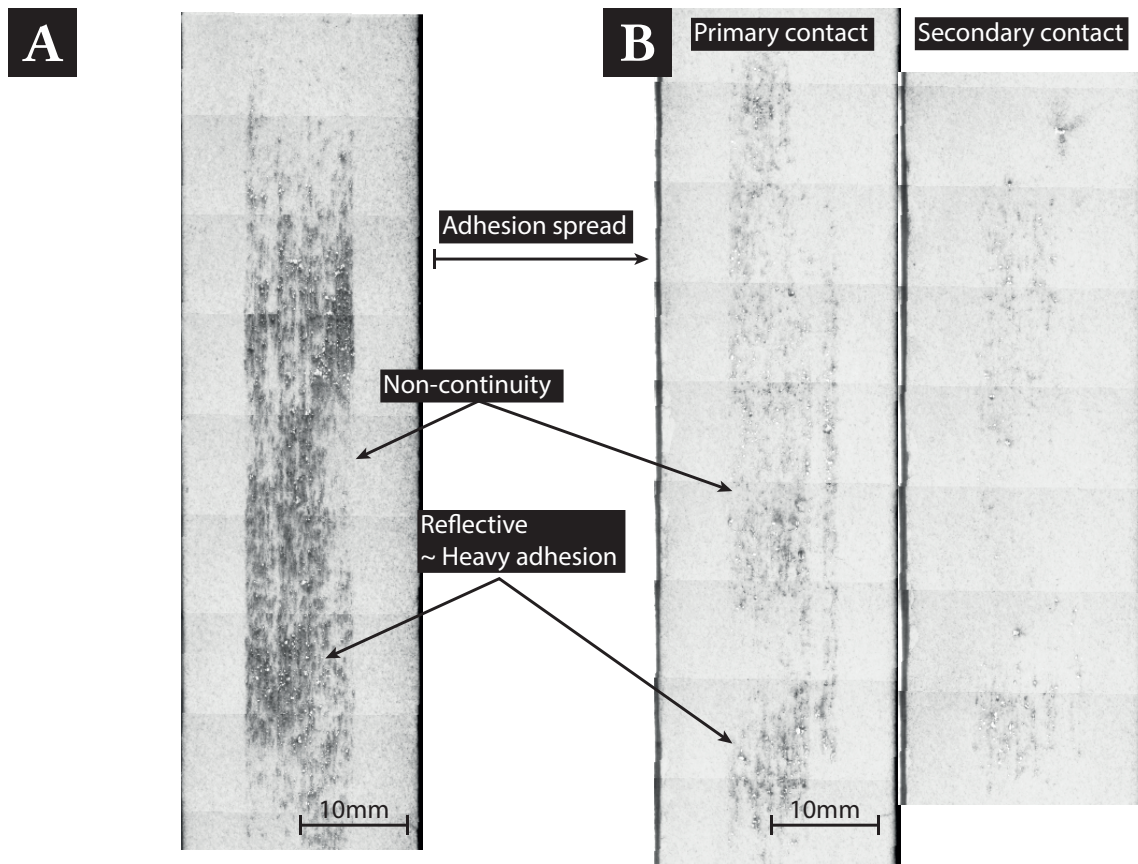
Fig. 7.2 Post-test stitched images of Zr40 at 0.31 um/pass (A) and 1.71 um/pass (B).

Whilst the severity of the adhesion appears equivalent for both Zr40 and Zr40rep, it slightly contrasts with the results presented earlier in Section 5.2.1 (Fig. 5.16). For instance, the Zr40 coating in this section appears brighter than those shown previously in Section 5.2.1. In addition, Zr40 at the high incursion rate showed signs of galling, whereas such a severe form of adhesion cannot be distinguished in these images. However, from physically evaluating the samples, the reality is that the samples' tone is alike, and high levels of adhesion do happen and broadly correlate with where reflective points are seen in the images. These results are thus in line with those presented earlier in Section 5.2.1, and the observed changes are due to the variation in lighting conditions between experimental set-ups. This latter point will be further considered in the discussion section, given that it also further highlights that the high-speed camera is not objective/consistent. The issue is that there is a misreading for these samples when a dark point becomes reflective, and whilst previously it could be used for evaluating the adhesion's progression on a single sample, this drastic tone shift entails that readings no longer serve their purpose.
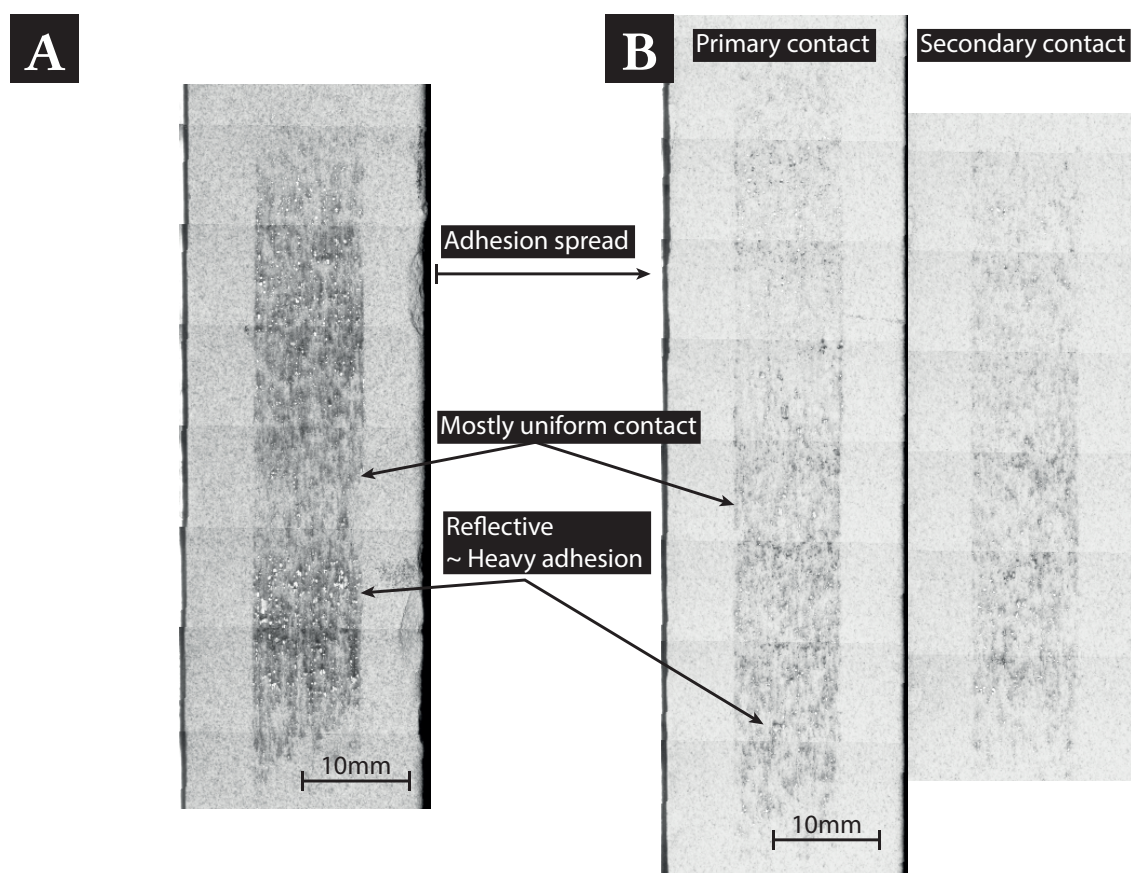
Fig. 7.3 Post-test stitched images of Zr40rep at 0.31 um/pass (A) and 1.71 um/pass (B).

Samples manufactured from Zr30+2.2PE are shown in Fig. 7.4. These are darker in tone than the Zr40 samples previously described, which makes adhesion challenging to distinguish given the low contrast. This tone change is particularly evident at the high incursion rate as adhesion is not apparent, but the images do show localised reflections and examining the normal and tangential forces (Fig. 7.5) show signs of pull and pushing; evidence micro-welding/galling. This indicates that the surface has suffered minor damage and primarily on a local level at the tip of asperities. The severity of adhesion is hardly comparable between the wear scars of Zr40 (above) with those of Zr30+2.2PE (Fig. 7.4); yet, it is apparent that the arc of contact has increased at both incursion rates when adding polyester (Fig. 7.4). Furthermore, the equivalent behaviour previously mentioned when going from low to high incursion rate can also be seen: two contacts appear, and adhesion and work are spread around the coating.
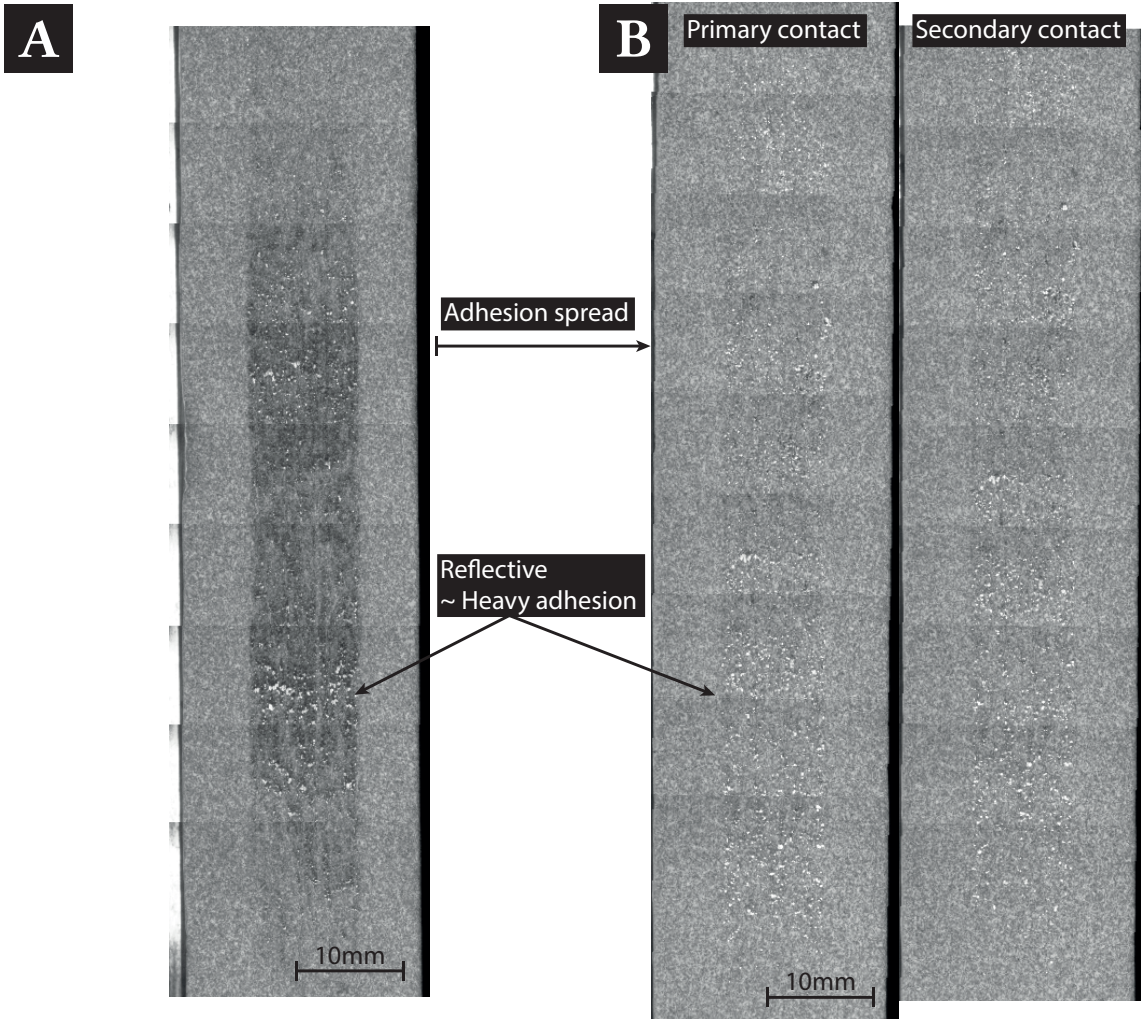
Fig. 7.4 Post-test stitched images of Zr30+2.2PE at 0.31 um/pass (A) and 1.71 um/pass (B).
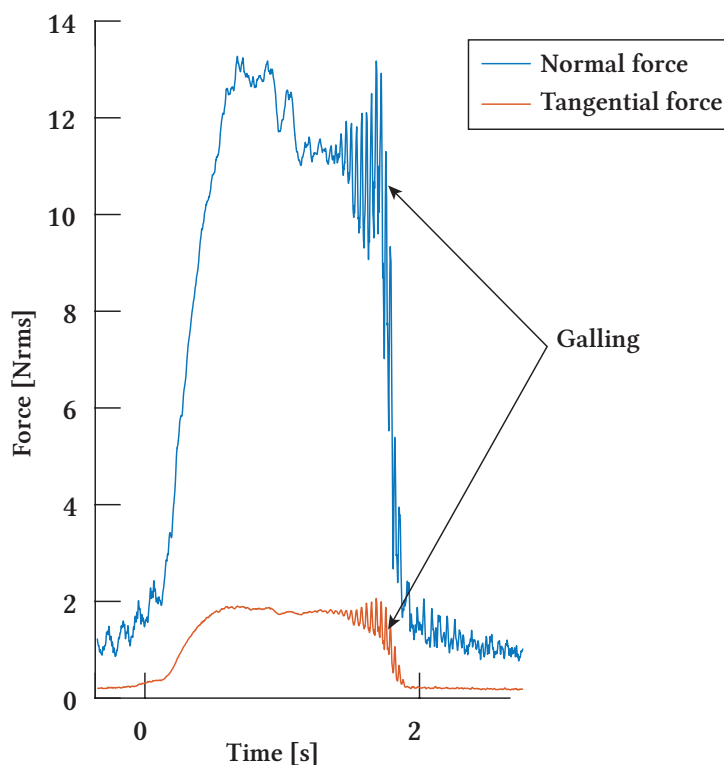
Fig. 7.5 Normal and tangential force (time-domain) of Zr30+2.2PE at 1.71um/pass evidencing the appearance of high vibrations towards the end of the test, corresponding to galling effects.

Fig. 7.6 shows the rub scars of Zr30+PE4.5. The coating has a similar tone to that shown previously (Zr30+PE2.2), once again, meaning that adhesion does not contrast with the coating and thus, it is more difficult to distinguish than when Zr40 and Zr40rep were evaluated. Nevertheless, it can be appreciated that there is a double contact at the low incursion rate and the arc of contact is consequently considerably longer than in the previous cases (i.e., Zr40 and Zr30+PE2.2). In contrast, the arc of contact at the higher incursion rate appears to have reached a maximum as it does not show a significant increase compared to that seen on Zr30+PE2.2. Despite the significantly longer arc of contact at the low incursion rate, a slight increment can still be appreciated when shifting from a low to a high incursion rate, but this is not as obvious as that shown for Zr40 and Zr30+PE2.2 coatings.

Furthermore, considerably more adhesion can be seen at both incursion rates compared to Zr30+PE2.2 (Fig. 7.6 vs Fig. 7.4); however, it is difficult to distinguish if severity has also changed from the images. These do have high spots much alike, but this time denser and showing a slight trail of adhesion after the heavy spot, suggesting that as with Zr30+PE2.2, heavy adhesion is localised at the tip of asperities. In this case, however, then transitioning and spreading to a greater extent to show a thin trail of adhesion after the localised point.

The aforementioned progression can be seen from the forces (Fig. 7.7), also evidencing that introducing polyester at 4.5 g/min in some cases leads to the most severe galling, as it happens from the start of the test. It is worth noting, however, that these coatings show particularly high variability, and this is an extreme event within the spread of the contact response, with the variation in severity probabilistic in nature, based on the material structure. Nevertheless, recalling that Zr30+PE4.5 has the highest roughness, these results indicate that sharp tips lead to fast galling when they congest.
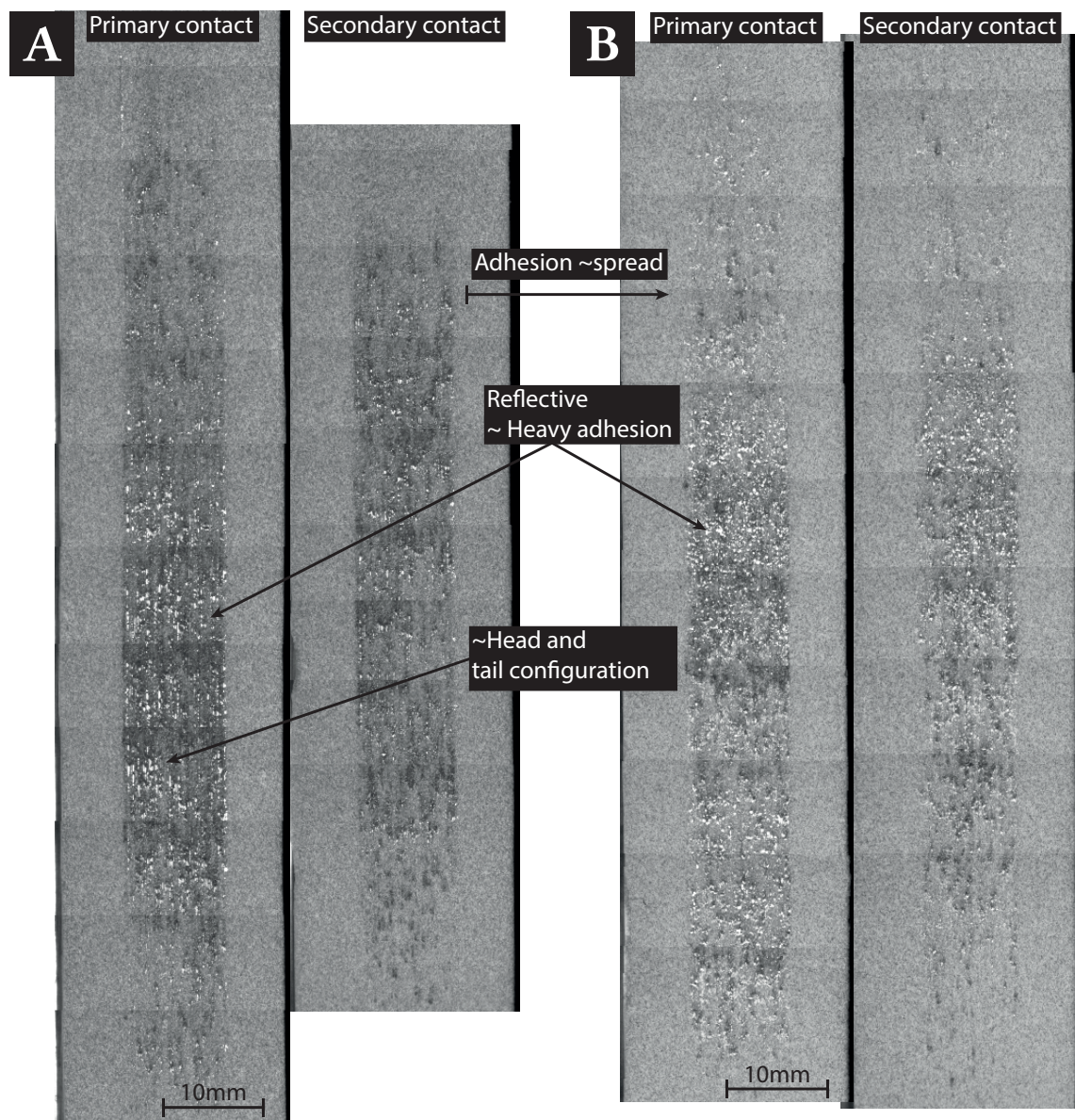
Fig. 7.6 Post-test stitched images of Zr30+4.5PE at 0.31 um/pass (A) and 1.71 um/pass (B).
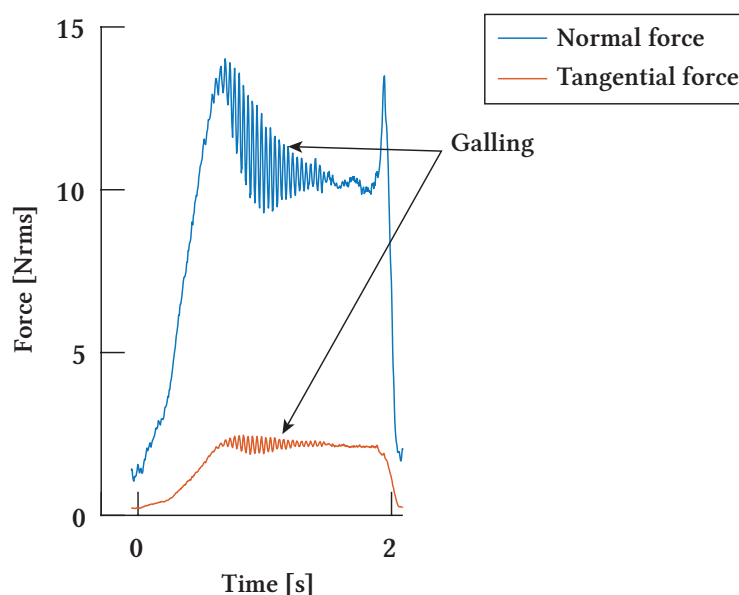
Fig. 7.7 Normal and tangential force (time-domain) of Zr30+4.5PE at 1.71 um/pass evidencing the appearance of high vibrations from the start of the test, corresponding to galling effects.

The wear scars of Zr20 are presented in Fig. 7.8. The figure shows a similar pattern to that observed on Zr40 and PE coatings, with adhesion once again spreading and lightening around the coating's surface when moving from low to high incursion rates. The arc of contact for these samples lies between those of Zr40 (the shortest) and PE samples (the longest), and in contrast to all the other samples, only shows a marginal increase when shifting to a higher incursion rate. The adhesion's appearance, however, is localised at the tip of asperities, similar to that seen on PE coatings but slightly more prominent in size in this case.

When comparing the adhesion happening on Zr20 with that of Zr40 coatings (Fig. 7.9), it can be seen that they are different. On Zr20, adhesion is localised on a more significant number of points than on Zr40, which in contrast shows a small number of large protuberances that are highly congested and a smooth adhesion elsewhere. This change in adhesion's appearance highlights that the interaction coating/blade has been different when decreasing the spraying deposition rate and has provided Zr20 with smaller asperities but in a greater number where adhesion can accumulate. This change in appearance when moving from Zr40 to Zr20 is similar to that seen when moving from Zr40 to Zr30+PE, as adhesion can also be seen accumulating on asperities when PE is introduced into the coatings. However, adding PE also confers a much longer arc of contact.
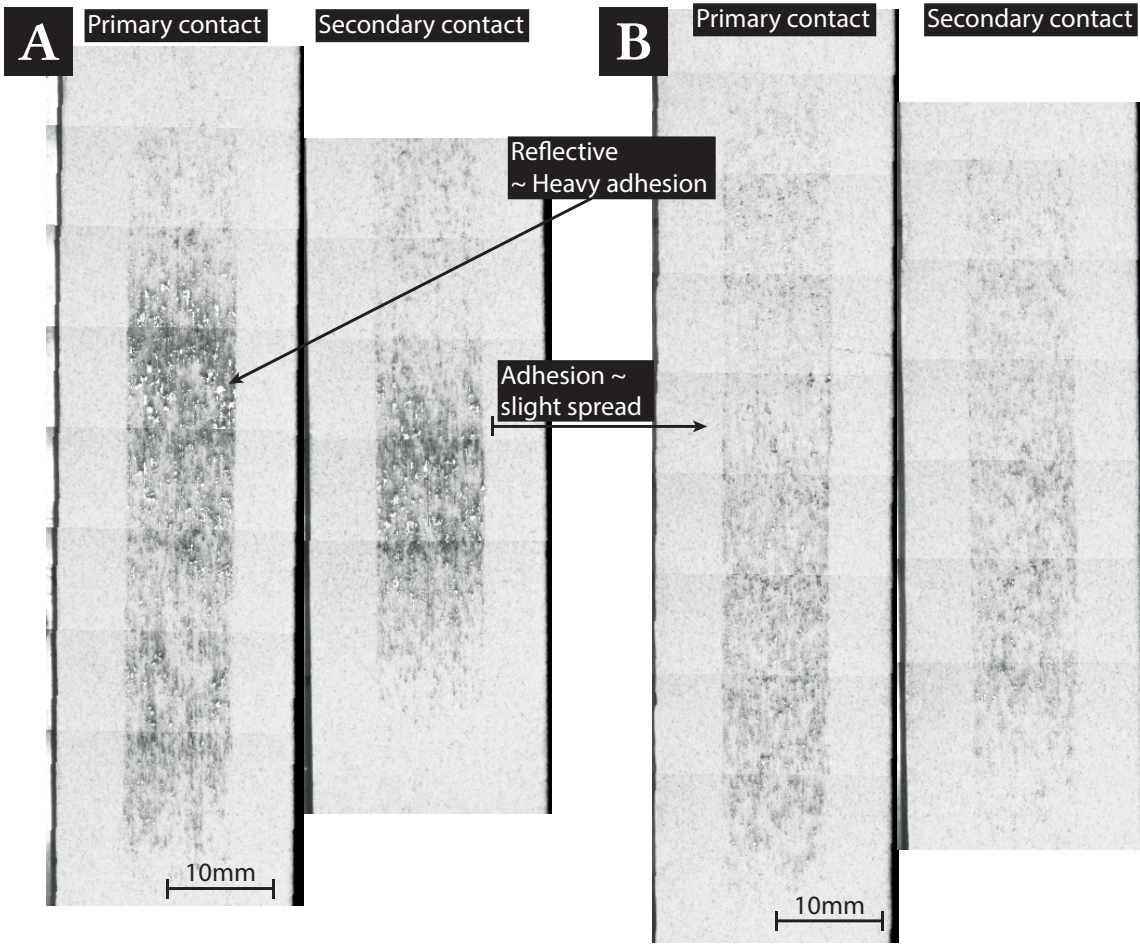
Fig. 7.8 Post-test stitched images of Zr20 at 0.31 um/pass (A) and 1.71 um/pass (B).
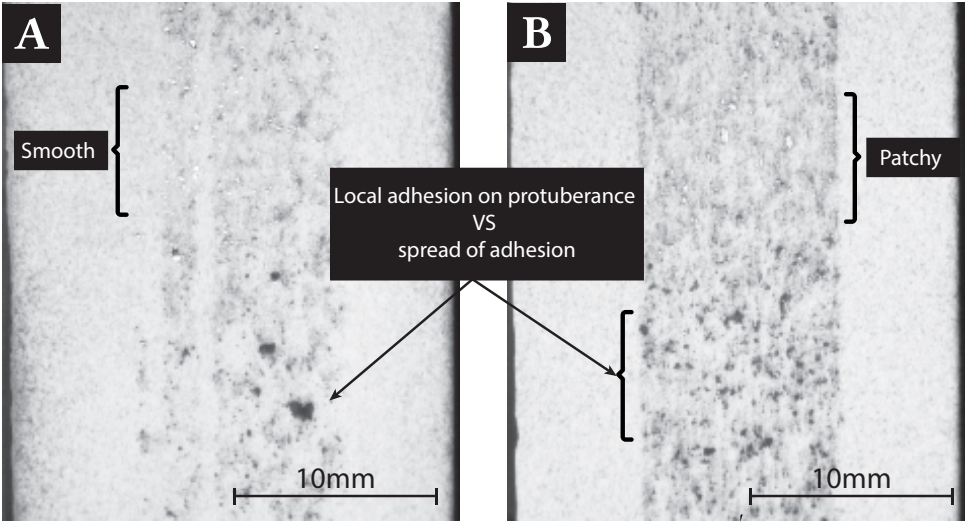
Fig. 7.9 Images showing adhesion on Zr40 (A) and Zr20 (B) tested at 1.71um/pass.

The numerical descriptors of the contact will now be examined to provide further insight into the performance of the different materials. Given the experimental design, direct comparison between time domains is unnecessary to detect trends in the data, and as previously mentioned, averages of the time domain will be evaluated instead. The results are presented in Table 7.5, and plots will follow to facilitate comparisons. This procedure is equivalent to that followed in Chapter 5, and the metrics will be examined in the same order. It should also be noted that given the limited variables under consideration, direct comparison between sample is possible.

Table 7.5 Table presenting time-domain averages.

Sample	Material	I.R.	M	NF	TF	T	F.ratio	SGE
S1	Zr40	0.31	-0.0656	7.10	0.97	662.10	0.14	146.40
S2	Zr40	0.31	-0.0509	9.84	1.05	588.04	0.11	172.74
S3	Zr40	0.31	-0.0610	6.89	1.01	630.70	0.15	182.45
S13	Zr40	1.71	-0.0455	8.56	1.39	328.63	0.17	43.51
S14	Zr40	1.71	-0.0357	14.84	1.73	477.46	0.12	64.32
S15	Zr40	1.71	-0.0293	20.46	1.78	445.54	0.09	73.02
S26	Zr40Rep	0.31	-0.0607	8.04	1.19	638.30	0.16	186.03
S28	Zr40Rep	1.71	-0.0594	14.11	1.92	516.92	0.14	47.71
S25	Zr20Rep	0.31	-0.0816	6.31	1.04	721.31	0.17	134.88
S27	Zr20Rep	1.71	-0.0732	8.26	1.43	573.12	0.18	35.77
S4	Zr30+PE2.2	0.31	-0.0794	6.42	1.09	635.42	0.17	134.29
S5	Zr30+PE2.2	0.31	-0.0689	8.48	1.13	677.29	0.13	159.19
S6	Zr30+PE2.2	0.31	-0.0755	7.19	1.07	674.23	0.16	137.10
S16	Zr30+PE2.2	1.71	-0.0661	11.16	1.60	441.59	0.15	44.42
S17	Zr30+PE2.2	1.71	-0.0594	10.68	1.63	622.17	0.15	40.52
S18	Zr30+PE2.2	1.71	-0.0660	10.83	1.66	515.97	0.16	45.79
S7	Zr30+PE4.5	0.31	-0.0760	4.64	0.92	692.67	0.21	122.86
S8	Zr30+PE4.5	0.31	-0.0757	5.90	1.09	665.02	0.19	135.86
S9	Zr30+PE4.5	0.31	-0.0653	5.09	1.01	652.56	0.20	115.91
S19	Zr30+PE4.5	1.71	-0.0773	9.55	1.78	484.00	0.18	40.88
S20	Zr30+PE4.5	1.71	-0.0553	8.92	1.50	455.99	0.16	34.45
S21	Zr30+PE4.5	1.71	-0.0513	6.37	1.13	455.84	0.17	37.39

Table 5.3 abbreviations:*I.R.* Incursion Rate [um/pass]; *M* Matrial loss [g]; *NF* Normal force [N rms]; *TF* Tangential force [N rms]; *T* Apparent temperature [ºC]; *F.ratio* Force ratio [-]; *SGE* Specific grinding energy [J/mm^3]

7.2.1 Material loss

Fig. 7.10 shows a similar trend in material removal at low and high incursion rates. These results indicate that coatings behave similarly at both incursions, and a change in the variable translates into a similar shift in material removal for all coatings, i.e., more material is removed at the low rate.

Fig. 7.10 Chart showing the material removal of the blade. Mean and standard deviation has been calculated and plotted from the measurements shown in Table 7.5.

The figure shows that material loss is limited at a deposition rate of 40 g/min. When the deposition rate is decreased to 20 g/min for a Zr only sample, the material removal is increased. This trend suggests that the material removed is increased by reducing the deposition rate. Moving to the samples that have a deposition rate of 30 g/min with PE2.2, as might be expected given the deposition rate of 30g/min, the material removed is between that of 40g/min and 20 g/min. Given that it falls nearly at the middle, this suggests that the inclusion of PE at 2.2 g/min has had a limited impact, and the effect of deposition rate has dominated instead. However, comparing the samples with PE2.2 and PE4.5, it is apparent that the material removed has increased, which suggests that PE has a degree of influence. Comparing these two PE results suggest that increasing PE contents reduces material removal.

7.2.2 Forces and apparent temperature

The data of normal and tangential force is plotted below, joined with the apparent temperature. For normal force (Fig. 7.11), there is once again a clear difference between incursion rates where higher normal forces at each condition result at the higher incursion rate. When comparing

forces, the force drops when the deposition rate is reduced from 40 g/min to 20 g/min. This suggests again that there is a trend in reduction in force with a reduced deposition rate. As discussed previously for material removal, it is interesting to notice that Zr30+PE2.2 falls in the middle between Zr40 and Zr20, again suggesting that the addition of PE2.2 has limited impact. However, when moving to PE4.5, it is now interesting to note that force does not only decrease further but now reduces to a lower value than Zr20, highlighting that PE has had a significant impact on normal forces.

Fig. 7.11 Chart showing the RMS values of normal force. Mean and standard deviation has been calculated and plotted from the measurements shown in Table 7.5.

Moving to tangential forces (Fig. 7.12), the same trends are apparent. However, it should be noted that where before normal forces significantly reduced for PE2.2 samples, this effect is now more limited, and for PE4.5 samples, forces are now similar to Zr20 samples. One of the most interesting impacts seen in the tangential force is the increased scatter of the results, particularly for Zr40 and Zr30+PE4.5 samples at the higher incursion rate. It coincides that repeats of these samples show the most significant differences in the arc of contact. Results thus suggest at the high incursion rate it is more likely to have an increase in arc of contact and consequently in tangential forces. Whilst increasing tangential forces may imply an improvement in the removal mechanism, measurements of material loss show that this is not the case for the Zr40 coatings. The results for Zr40 suggest that tangential forces increase with the arc of contact, but further material is not removed with this change. Additionally, the increased scatter also indicates inconsistencies in the manufacturing or testing procedure for Zr40 and Zr30+PE4.5 coatings. These will be further addressed in the discussion.

Fig. 7.12 Chart showing the RMS values of tangential force. Mean and standard deviation has been calculated and plotted from the measurements shown in Table 7.5.

Temperature results (Fig. 7.13) follow the inverse of the force results except for the case of Zr30+PE4.5 at the high incursion rate. Given the relationship mentioned earlier, the temperature would have been expected to rise where, in fact, drops. This event will be investigated further in the discussion. Fig. 7.13 further shows that temperatures fall for the higher incursion rate, indicating that shorter contact times reduce temperatures.
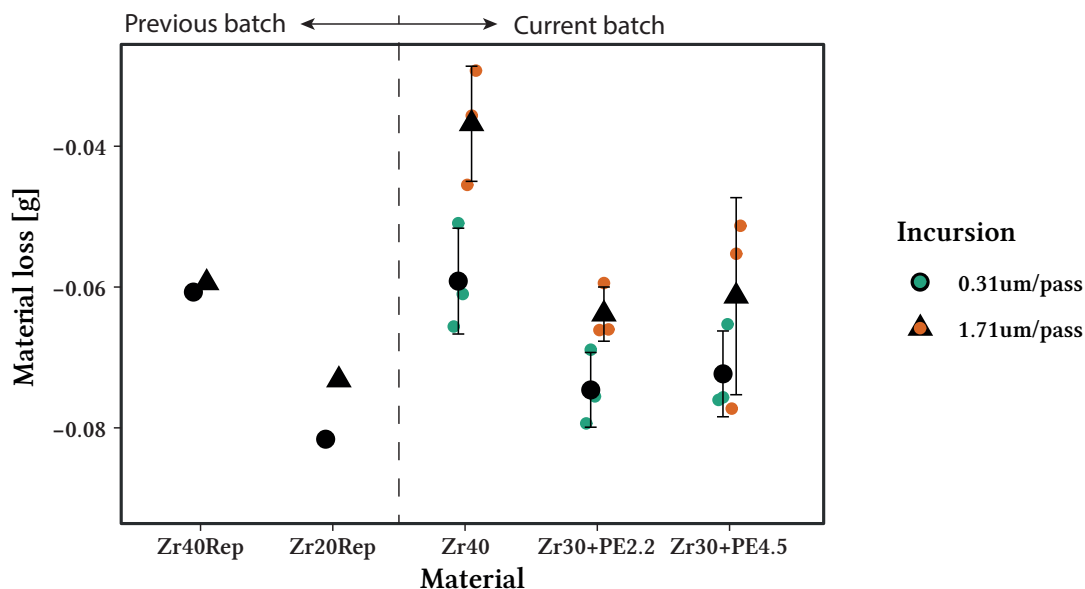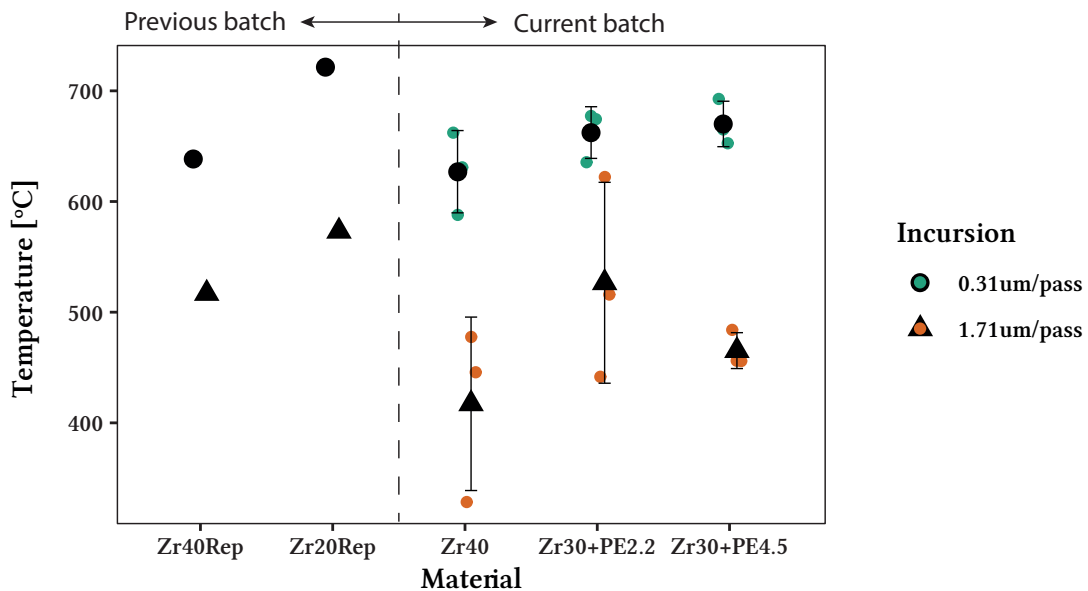

Fig. 7.13 Chart showing the apparent temperature of the blade. Mean and standard deviation has been calculated and plotted from the measurements shown in Table 7.5.

7.2.3 Force ratio and SGE

Comparing forces through the force ration (Fig. 7.14) evidences that decreasing deposition rate and/or increasing polyester improves the efficiency in which material is removed as this is show with an increase in force ratio values. Additionally, it can be seen that the efficiency of the contact is unchanged regardless of shifting incursion rate given that samples tested at different conditions yield broadly equivalent force ratio values. What this indicates is that the contact has not fundamentally changed despite of an increase in rub length or change of stresses.
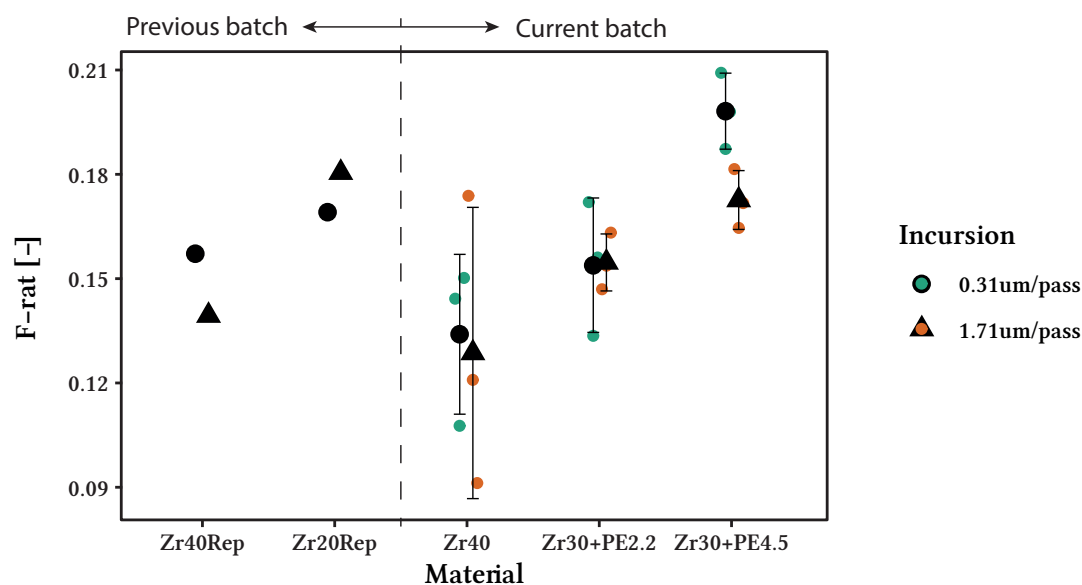
Fig. 7.14 Chart showing the force ratio. Mean and standard deviation has been calculated and plotted from the measurements shown in Table 7.5.

The SGE results (Fig. 7.15) show that there is inherently more energy at the low incursion rate due to the longer contact time. Differences in SGE values are notable and correlate with the contact temperatures presented earlier, where higher temperatures occurred at the higher incursion rate. Fig. 7.15 also shows that the contact's efficiency increases with deposition rate, which agrees with the force ratio values. It is worth noting that both force ratio and SGE reflect the process efficiency. However, SGE considers the length of the procedure and the material removal, whilst the force ratio is a global average of the process. The figure further shows that standard deviations are much larger where contact times (or rub lengths) are longer (i.e., at the low incursion rates), which shows that behavioural changes are evidenced when contact times are longer.
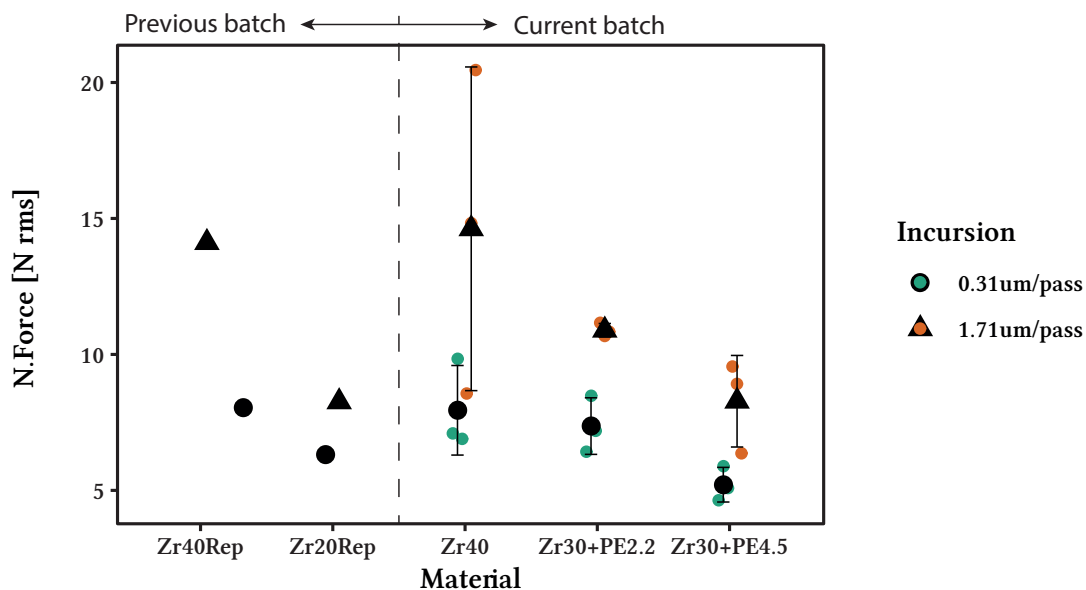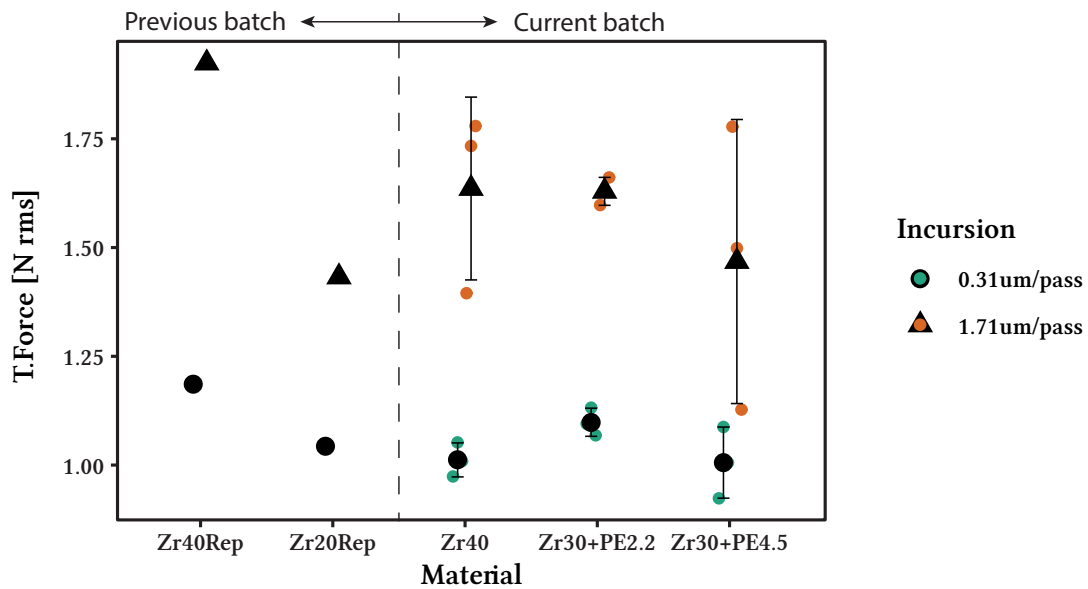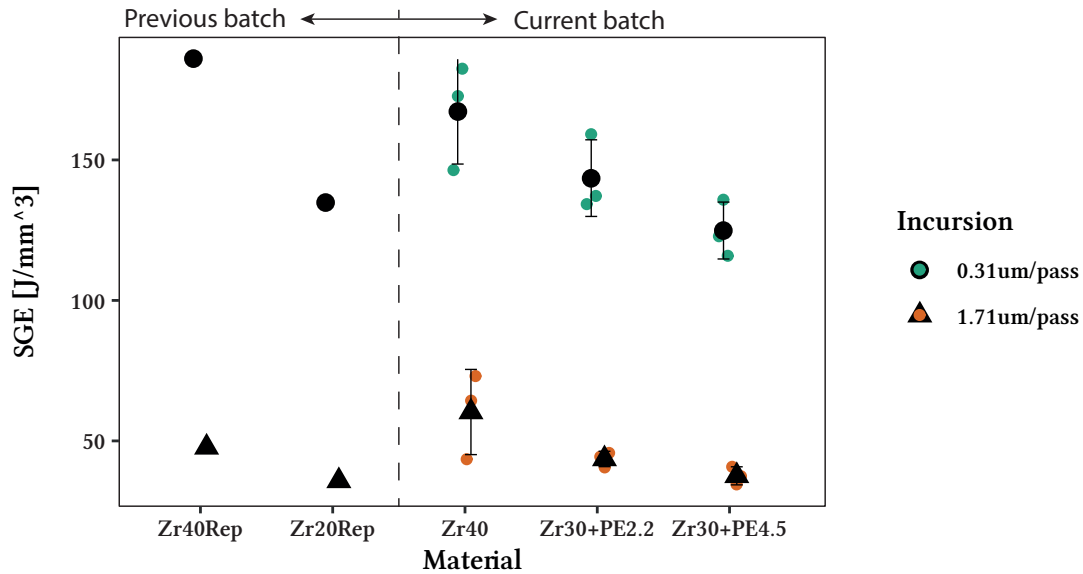
Fig. 7.15 Chart showing the SGE. Mean and standard deviation has been calculated and plotted from the measurements shown in Table 7.5.

7.3 Discussion

Earlier, Chapter 5 presented statistical evidence of improved material removal performance with a decrease in deposition rate. The statistical models in Section 5.2.1 showed that a rate change from 40 g/min to 20 g/min increased material removal and tangential forces whilst decreasing normal forces and temperatures in the contact. Essentially, the analysis showed that a reduction in deposition rate would produce a more effective abrasive process, one that not simply removes more material but also at lower contact temperature. Despite the consistency of the previous results, the effect of deposition rate was relatively subtle compared to changing material or truing, and due to the limited resolution of the screening DoE, the actual effect of deposition rate could not fully be understood. In this chapter, in contrast, the sole emphasis is on the spraying process, and the impact of such a variable can be further explored.

From the literature, it is known that particles spend longer periods in the plasma jet at low deposition rates than when faster ones are employed, and thus they melt to a higher degree (Section 2.2). The consequence is that splat connectivity is improved, and fewer defects are present in the coatings' structure (Section 2.2). Metrics such as the elastic modulus [48, 64], thermal cycling life, or thermal shock resistance have been reported in the literature to improve with these microstructural changes (Section 2.3). In turn, changes in microstructure and surface topography have been previously linked to the measured outputs, where for example, the force and temperature response give insight into the removal mechanics. This relationship was true

in the proceeding chapter and is more widely considered in grinding research [130]. More specifically, for instance, the normal force can be related to grit penetration, and tangential force to remove material and the force to overtake friction.

Viewing the results in this context, decreasing deposition rate from 40 g/min to 20 g/min does lead to an overall improvement in the removal mechanism, much as the results in Chapter 5 highlighted when statistically analysed. The results show that Zr40 coatings remove minimal material at either incursion rate (Section 7.2.1) and with relatively high forces (Section 7.2.2). These characteristics resemble those of a polishing process [130, p. 106] and evidence the ineffectiveness of the Zr40 coating at removing material. Images of the coating (Fig. 7.9) provide a possible explanation as adhesion appears smooth, suggesting that asperities are either not present (highly unlikely) or that they are not sufficiently strong to engage and remove material. The latter is significant as it correlates with the aforementioned likely decrease in elastic modulus of the Zr40 coatings.

Images of coatings at 20 g/min (Fig. 7.9) in contrast show localised adhesion at the tip of asperities, and the metrics show that significantly more material is removed at this condition. These results are relevant as they evidence that asperities have been able to indent the surface at the 20 g/min condition, improving the contact mechanics, but have also congested. These results correlate with the increase in elastic modulus for the 20 g/min condition and suggest that it is now excessive for the stress state generated at the studied incursion rates. Images of these coatings (Fig. 7.8) further support this idea as they show that the arc of contact does not significantly increase with incursion rate, evidencing that the elastic modulus is high at the 20 g/min condition and that neither of the incursion rates have managed to trigger fracture of the defects in the coatings and hence surface renewal. In other words, asperities are not released, and instead blunt and result in the congestion mentioned above. The process is essentially similar to what the literature on grinding has reported when sharp grits get blunt and do not renew [204]. That is, temperatures are high and localised at the tips of asperities, adhesion coalesces to a greater extent, and eventually, a metal-to-metal contact occurs, which results in high frictional heating. This progression in behaviours is analogous to what is seen on the Zr20 coatings, and gives an explanation for why material is removed yet contact temperatures are high.

Comparing how the asperities actuate in both Zr20 and Zr40 coatings makes it clear why Zr20 removes more material than Zr40 coatings and yet results in higher temperatures. On the Zr20 coatings, work is concentrated in a small area and localised at the asperities' tips, resulting in high concentrated heat. Conversely, the lower elastic modulus of the Zr40 coatings has allowed the contact to spread when stresses are high, dividing the work more evenly around the coating and thus causing a temperature decrease. It is worth noting that this trend in

temperatures contrasts with those presented by the models of Chapter 5, where they suggested a slight trend in the other direction but with a higher uncertainty due to the DoE. Now that the relationship between spraying parameters and temperatures has been examined more closely, the uncertainty has been resolved. The above effects on Zr20 and Zr40 coatings are summarised in Table 7.6.

Table 7.6 Table comparing the effects of Zr20 and Zr40 coatings

Coating	Surface Aspect	Results based hypothesis	Consequence
Zr40	Smooth adhesion	Elastic modulus too low and grits do not engage in a material removal process.	Low material is removed but contact is spread and low temperatures
Zr20	Localised adhesion at tip of asperities	Elastic modulus too high and grits do not renew, and eventually congest.	Material is removed but contact is localised, giving high temperatures.

From the behavioural comparison of Zr20 and Zr40 coatings, it appears that removing material goes against attaining low contact temperatures (Fig. 7.16). Essentially, a compromise has to be reached when considering zirconia only coatings. More precisely, either removing more material at the cost of introducing thermal damage or removing little material and not introducing thermal damage. Neither option is of industrial interest as, ideally, low contact temperatures are desirable to avoid the onset of blade burn, and material removal is required to minimise clearances between the stator-blade and rotor. This comparison however does highlight that stiff asperities are beneficial for removing material, and spreading the contact decreases temperatures.
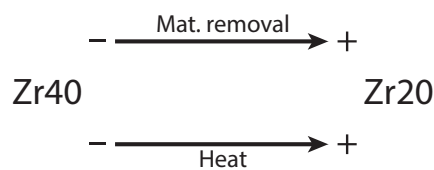
Fig. 7.16 Illustration depicting the trends observed in material removal an heat when changing deposition rate of zirconia from 40g/min to 20g/min.

A solution is offered from evaluating force ratios and SGE values. The results show that force ratios (Section 7.2.3) for the above coatings do not change with the incursion rate. In contrast, SGE values (Section 7.2.3) show very distinct energy inputs between incursion rates. It is interesting to observe that whilst both metrics reflect the efficiency of the process, they are also particularly different. The force ratio is an overall average and, in this case, explains that there is no real change in mechanism for either of the above coatings when the incursion rate is changed, showing that the induced stresses at either incursion essentially trigger an

equivalent response in the coating. SGE values, on the other hand, consider the duration of the tests and shows that at the high incursion rate, there is significantly less energy in the system because of the shorter duration of the contact. The above correlates with the temperature readings (Section 7.2.2) and evidence that for coatings that do not effectively evacuate heat, a continuous contact entails a heat buildup, given that heat is not dissipated fast enough from the system. Accordingly, one could easily improve the system by, for instance, finding a way of decreasing heat input. One way of doing this would be to interrupt the contact or, as done in grinding, promote surface renewal so that grits remove heat as they detach from the coatings' surface [194, p. 348]. It is worth noting that the incursion rate would indeed affect this latter option since these will influence the induced stresses. As an example, applying such an approach on Zr20 coatings would both lead to the best material removal and decrease the risk of blade burn, resolving the caveat depicted in Fig. 7.16.

When introducing polyester into the coatings, samples with low PE contents broadly reflect what would be expected based on zirconia's spray rate. That is, given that for this experiment the spray rate of zirconia is reduced to 30 g/min when polyester is added, forces and temperatures are between those shown by Zr20 and Zr40 coatings (Section 7.2.2). In contrast, when higher levels of polyester are used (4.5 g/min), there is a clear impact on forces and temperatures evident from polyester (Section 7.2.2), resulting in broadly the equivalent material removal (Section 7.2.1) than at the 2.2 g/min condition (slight decrease), but now exhibiting a drop in forces and a stable temperature (or drop in the case of the high incursion rate). An outlier was of note for the high polyester level at the high incursion rate where, as mentioned, both forces and temperatures dropped (Section 7.2.2). This latter outcome outperforms the results of both Zr20 and Zr40 coatings and has important implications as it implies a mechanism with no trade-off between material removal and temperatures.

Considering the effects of adding polyester to the coatings, there is an increase in surface roughness with polyester content (Table 7.2), and porosity also increases (Fig. 7.1). It is worth noting that this leads the coatings with polyester to have a fundamentally different microstructure to that seen in both Zr20 and Zr40 coatings. The images of these coatings (Fig. 7.6 and Fig. 7.4) show that the above changes translate into adhesion once again happening at asperity level much as it is seen on the Zr20 coatings. Additionally, coatings containing PE show an increase in the arc of contact with respect to zirconia only coatings, evidencing that the increase in porosity has now also allowed the coating to slightly collapse when forces are high like the Zr40 coatings, in this case however, extending the contact and leaving new asperities to engage in a removal process. This is analogus to introducing porosity and bond strength in grinding wheels where the requirement is that when grits blunt or compact and no longer effectively cut, they brake away and refresh [194, p. 348]. In this scenario, for instance, if the

depth of cut is too low (herein incursion rate), the surface is not renewed and instead congests and collapses. Compared to the results presented in this chapter, this is the equivalent process seen at the low incursion rate and low PE levels (2.2 g/min), given the fact that the results do not show a big change from what might be expect of a zirconia only coating at 30g/min, the induced stresses are low given the incursion and the surface does not renew and instead congests (Fig. 7.17A). The likelihood of a renewing mechanism happening is increased with polyester level and incursion rate (Fig. 7.17D), since there are higher forces able to activate the mechanism and porosity is the highest. Thus, the high polyester level at the high incursion rate (i.e., Zr30+PE4.5) is the test with highest potential for a surface break down. As might be expected the beginning of this type of behavior can be seen and this point is the aforementioned outlier result, not only exhibiting low forces, but now also a drop in temperatures. At the other conditions either the activation forces are too low (Fig. 7.17B) or the structure too strong (Fig. 7.17C) to trigger such a mechanism and the results follow the trend expected given the deposition rate of zirconia, with a marginal performance improvement seen where surface roughness is increased.
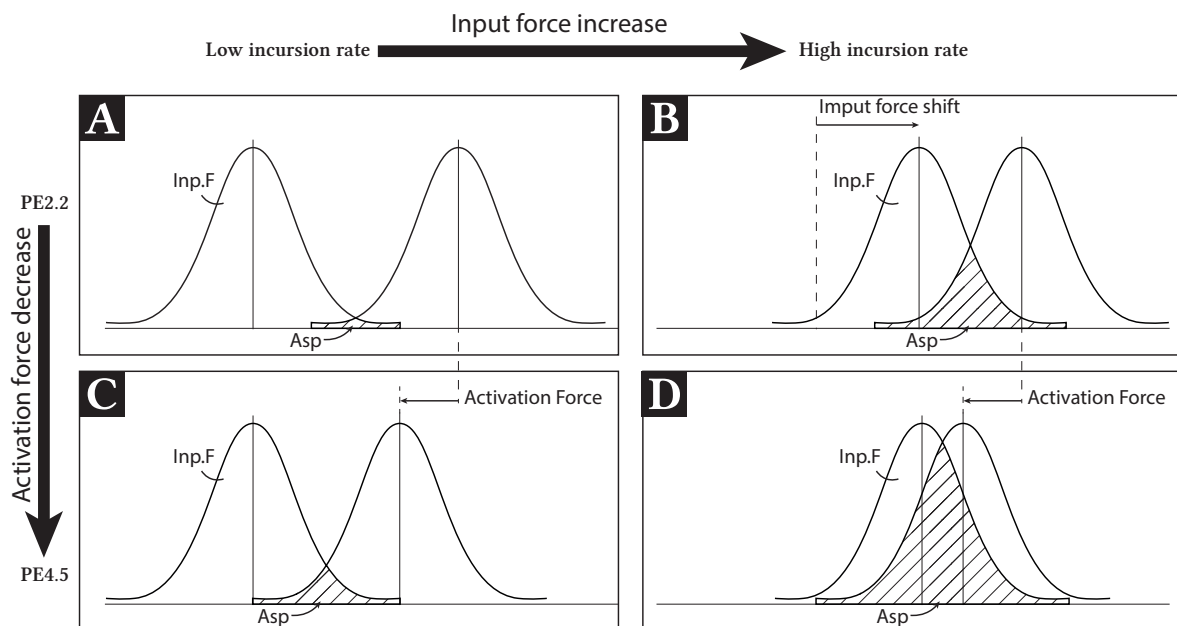
Fig. 7.17 Illustration depicting the behavioural changes of polyester coatings in terms of probability density functions. The illustration shows a decrease in activation energy with an increase in polyester, and an increase in input force (Inp.F) with increased incursion rate. The illustrations are: (A) Zr30-PE2.2 at 0.31 um/pass; (B) Zr30-PE2.2 at 1.71 um/pass; (C) Zr30-PE4.5 at 0.31 um/pass; (D) Zr30-PE4.5 at 1.71 um/pass. These reflect the amount of active asperities (Asp) in the contact based on the spraying and stresses.

Up until now, the relationship between incursion rate and the arc of contact has not been addressed. In Chapter 5 it was show that increasing rub length, for instance through truing, entailed a significant improvement for the contact. Accordingly, it may be easy to say that samples cannot be compared, since changing incursion rate changes the arc of contact in these coatings, and essentially the rub length. However, given that mechanisms are fundamentally different, with asperities being present or not, engaging or collapsing, or the contact being localised or extended, even if the samples were perfectly balanced and concentric, the samples will still result in different rub lengths and the outcomes would be different. In other words, even if the apparent area of contact was fixed from the start, the real area would be different [194, pp. 103-106]. Hence, samples can indeed be compared as the arc of contact is a response of the material properties to the process by which they are tested.

Nevertheless, for experimental purposes it might be interesting to fix the apparent area of contact in order to get further insight into the fundamental differences between materials. That is, it could be interesting to detach material properties from the process by which they are tested. An option could be to restrain the apparent area of contact and a system has been accordingly designed where samples can be more consistently tested and evaluated based on their material properties. This is presented in Appendix G, where the design has also addressed the issue of not being capable of reaching higher speeds.

7.3.1   Evaluating the improvement of samples with polyester

In the previous chapter, the coating's material was shown to be a strong driver, and alumina proved advantageous over zirconia given the lower temperatures and higher material removals. However, alumina is not popular with engine manufacturers because it is not compliant with the spraying process and delaminates in most cases. Therefore, zirconia is likely to remain the material of choice. In this chapter, the ability to affect the microstructure by changing spraying parameters or the polyester contents has been explored, with the proceeding section considering up to what level these changes can improve performance in the contact. The question now is whether the improvements with the addition of polyester are comparable to those seen when simply moving from zirconia to alumina.

To compare alumina samples with zirconia ones, and to get a holistic view of the results, alumina coatings at the 20g/min condition from the previous batch have been tested, and a PCA has been calculated and plotted following the same procedure as in Section 5.3. More precisely, as before the first two components are sufficient given they explained more than 85% of the total variation within the results and eigenvalues are above one. The summary of the alumina results are included in Table 7.7, and the resulting bi-plot in Fig. 7.18.

Table 7.7 Table presenting time-domain averages of alumina samples.

Sample	Material	I.R.	M	NF	TF	T	F.ratio	SGE
S10	Al20	0.31	-0.0905	7.43	1.17	710.99	0.17	124.25
S11	Al20	0.31	-0.0812	7.24	1.20	627.27	0.18	138.32
S12	Al20	0.31	-0.0797	7.89	1.26	653.83	0.16	128.68
S22	Al20	1.71	-0.0763	9.75	1.71	457.43	0.18	39.56
S23	Al20	1.71	-0.0776	10.56	1.92	560.36	0.19	41.15
S24	Al20	1.71	-0.0813	10.25	1.82	541.25	0.18	40.59

Table 5.3 abbreviations:*I.R.* Incursion Rate [um/pass]; *M* Matrial loss [g]; *NF* Normal force [N rms]; *TF* Tangential force [N rms]; *T* Apparent temperature [ºC]; *F.ratio* Force ratio [-]; *SGE* Specific grinding energy [J/mm^3]
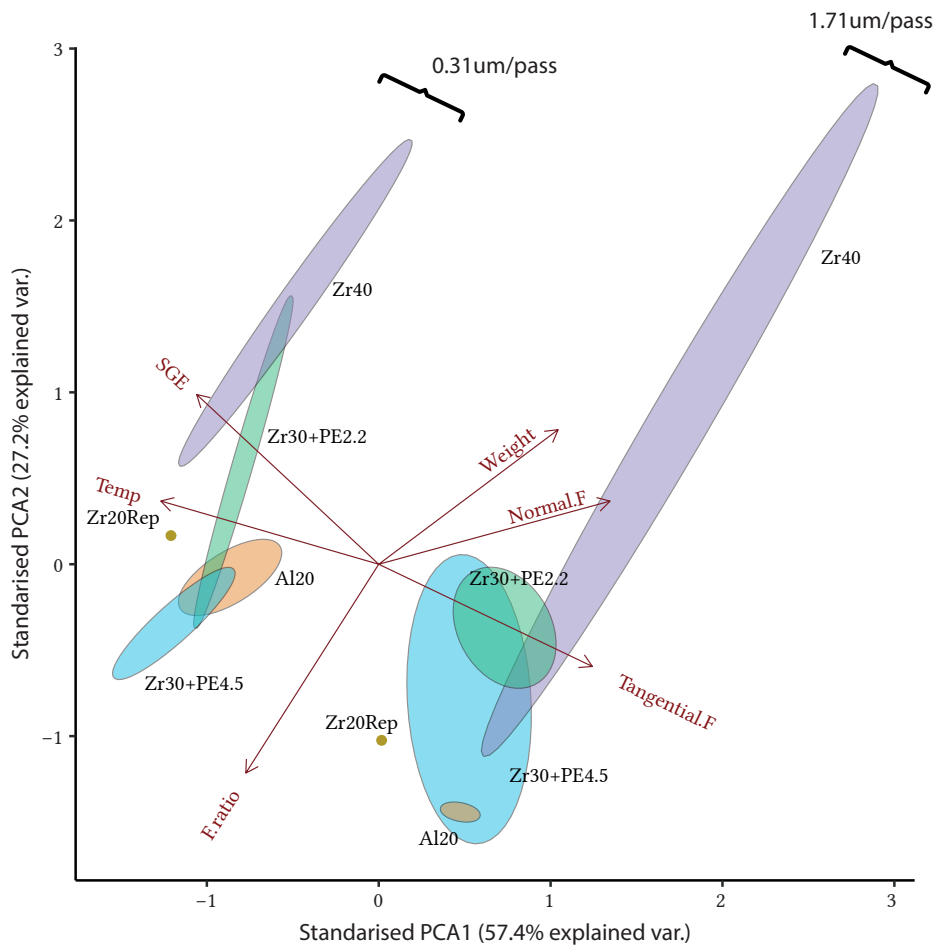

Fig. 7.18 PCA bi-plot collecting the tests of zirconia and alumina samples. Note: "•" corresponding to Zr20Red represents a single repeat in comparison to the rest of the groups that are conformed by three repeats.

The PCA in Fig. 7.18 further emphasises that shifting incursion rate does not generally entail a change in mechanism; it merely alters the temperatures in the system due to the contact time shortening, given that in most cases stresses are not sufficient to trigger the defects in the coatings. This can be seen as coatings generally follow the same trend in material removal at low and high incursion rates, with Zr40 resulting in the worst performance, Zr30+PE4.5 the best, and Zr30+PE2.2 sitting in between. However, the behaviour is most different for PE coatings when considering temperatures and tangential forces, evidencing a degree of influence with incursion rate, i.e., the mechanism slightly changes when shifting the incursion rate. When compared to the performance of Al20 coatings, it is encouraging to observe that introducing PE has improved the removal mechanism, placing it at the same level as Al20 or even outperforming it in some cases. This is in contrast to Zr20 coatings which whilst sitting side by side with Al20 coatings in terms of material removal have higher temperatures. This evidences that coatings of similar topographies result in similar material removals, but if they do not renew, their conductivities influence the contact and result in higher temperatures for those with worse heat dissipation (zirconia in this case). This is no different to what is currently documented for grinding processes [194], and gives an explanation for the results.

Based on the above one sits in a difficult position when using zirconia only coatings. Moving from 40g/min to 20g/min means trading an increase in metal removal with a more concentrated contact and heating. It is true that as discussed using 20g/min and interrupting the contact would resolve the issue; however, this approach is not always applicable in an engine given that closure rates cannot be particularly controlled during the engine's entire life. Hence, a dense coating without the ability to renew and refresh would accumulate adhesion, and most certainly fatally fail eventually. What this work has shown, is that higher material removals at lower temperatures are achievable by introducing polyester. In this sense, polyester is useful, but this result are not specifically the panacea of what is to do next since the coatings have not been engineered satisfactory enough that it actuates over the whole spectrum of engine closure rates. What these results have really highlighted is a lever with significant strength and merit, and now further work is needed to optimise the mechanisms so that it actuates over the engine rates. Not necessarily being restricted to the use of polyester to do so.

7.4   Conclusion

The aim of this chapter was to study ways of improving the performance of zirconia coatings. Changing deposition rate and introducing polyester were investigated, as based on the literature, these are approaches that target the coatings' microstructure and are applicable methods within aero-engines.

The most significant finding to emerge from this study is that if a material does not fracture and renew like a grinding wheel, any improvement in cutting performance by creating sharper asperities, in effect, concentrates the contact and comes at the expense of heating. The only opportunity to both improve the cutting performance without other measures becoming worse is to add an extra element to the microstructure to promote friability of the wheel. This study partially achieved the above by introducing polyester into zirconia, where the impact of such a lever was substantial, and the zirconia's performance was enhanced due to the polyester up to levels shown by the alumina coatings.

The empirical findings in this study thus provide a new understanding of the contact mechanics happening in the abrasive-rotor/stator blade system and extend the knowledge about the important factors driving the removal mechanism. Essentially, materials are not a limiting factor if the system effectively dissipates heat, and spraying parameters alone do not help as shifting them always come with a price. Therefore, there is a need to look in a third direction to improve the process, one that can introduce asperities and friability in the coatings as required depending on the operational conditions they will be exposed to.

Chapter 8

Discussion

The introduction and literature review highlighted a number of critical questions. Given that these materials have not been used as abrasives before, there were key questions with regards to what tribological mechanism they operated in and how this connected to the broader body of research. Furthermore, the relevance of this tribological understanding to how they operate in an engine and also, given the novel nature of the test rig, how much this study could gain insight into the contact and address the aforementioned research questions are also key points to explore. This discussion will cover these high-level points, bringing the work together against the overall research question.

8.1   The contact

This section's purpose is to discuss the findings of this research concerning the contact. More precisely, it will cover what has been learnt about how these coatings work, what variables have been seen to be effective (and which ones are not), and possible development opportunities. The findings will be supported by literature, which also serves a secondary purpose, i.e., to highlight where these coatings sit in the wider body of research.

Investigating the rub specimens showed adhered material on all coatings, i.e., an adhesive wear mechanism. This is significantly different to what might be seen in a standard abrasive process such as grinding, where instead the grits would be expected to micro-machine and remove material without immediately clogging up [194, p. 46]. As such, it was established that a conventional abrasive machining process was not taking place. From the evaluation of the high-speed camera images, this adhesion showed a progressive nature. Additionally, the force ratio values were generally low for an abrasive removal process (below 0.2) and did not change with the incursion rate. These observations show that wear mechanisms are progressive and have no real change with incursion rate but are instead affected by the duration

of the contact, which defines the heat input. In other words, the mechanism is not defined by the stresses (which can be high or low without changing the outcome), but is thermally driven. This type of contact is highly ineffective and correlates with what literature refers to as rubbing [194, p. 135]; else, increasing stresses would have increased asperity indentation (Fig. 8.1), translating in an improvement (which was not seen). Whilst this contact may be thought of as an abrasive grinding style contact, the absence of grits and the small scale of asperity penetration entails that it is always rubbing no matter the incursion (Fig. 8.1). Thus, the contact is rather a subset of grinding akin to when the depth of cut is not high enough, or much like what would be expected from a polishing process, where high forces can exist during prolonged periods without material actually being removed.
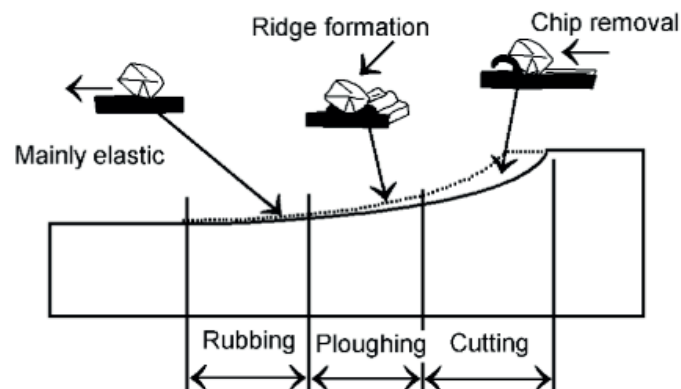
Fig. 8.1 Transition in regimes with grit penetration for abrasive machining. Figure extracted from Marinescu *et. al.* [194, p. 136]

Whilst this contact was identified as not a classical grinding process, the screening experiment found that material, surface finish, and incursion rate affected the removal process, which are similar drivers to those found in a grinding process [194, p. 9]. However, these variables had a limited effect on the overall outcome given that this is a rubbing contact, which contrasts with what would be expected from a grinding process, where changing one of these variables might result in a significant enhancement in material removal. It should be noted, however, that some of these variables did have a positive effect, but not akin to the level that might be seen in grinding. Given the rubbing nature of the contact, truing was the most significant variable as it allowed to spread the contact around the wheel, in essence, prolonging the life of the failing process. The importance of surface roughness was also acknowledged (particularly at the higher incursion rate), evidencing that asperities are needed in the coating to remove material similar to what would be expected from a grinding process [194, pp. 130-131]. The results thus suggest that the combined effect of high roughness and a long arc of contact would yield the best outcome. Hence, revealing two ways to improve the contact conditions.

Despite the strong impact of truing, which is unsurprising since it is also a fundamental element in grinding operations [194, pp. 457-463], further examination of the samples through SEM analysis revealed that it had caused the coatings to detach from the bond coat (Fig. 8.2). This outcome is reiterated in the literature on thermal barrier coatings as it highlights the end of a coatings life (Section 2.3). As such, the results emphasise a weakness of the truing process as the stresses introduced had been sufficient to cause the coatings to fail. These coatings are different to a grinding wheel in the sense that they are only 500 um thick, and whilst truing may be a method to introduce defects in the coatings (desirable as this enhances friability), it can also concentrate stresses at the bond coat, causing a significant reduction in their life. The results reveal that truing is not an immediate option for changing surface properties as the process does not allow to control stresses accurately; hence, not being able to regulate the coatings' contact arc and defects as may be desired. Other courses of action would need to be explored if this approach (i.e. a post-deposition process) was to be taken. Examples could be sandblasting, crush grinding or laser engraving, as shown in the patents (Section 1.5). However, given that this adds an extra operation in the manufacturing process of the coatings (an extra level of difficulty), which needs to be optimised and may instead introduce damage from the start (as SEM has shown), it is not the most desirable course of action. Nevertheless, post-deposition operations are an option if necessary for further improving the coatings. These can be applied independently of the selected parameters and are thus not a limiting factor, but results show that their impact is high, and the process should be optimised when applied.
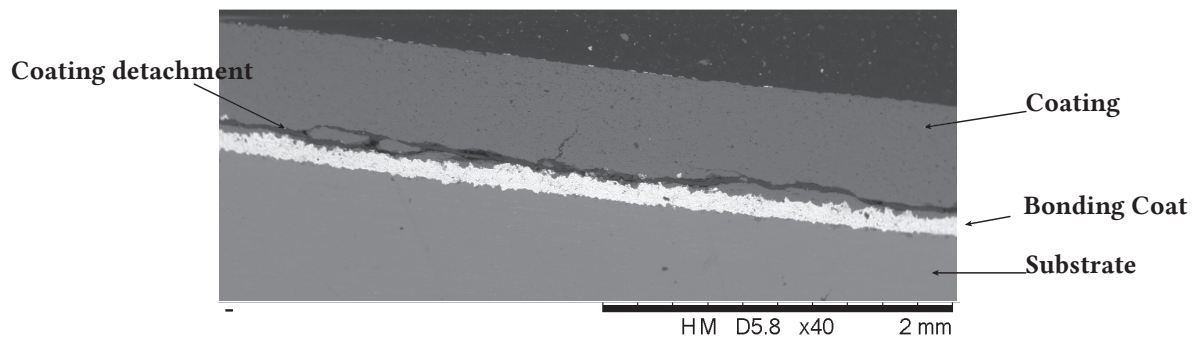
Fig. 8.2 Backscattered image presented earlier in Section 6.2.4. The image is a cross-section of a trued sample, evidencing large scale delamination.

The coating's material was highlighted as a key variable as it is linked to the ability to channel heat away from the contact. These results are akin to that of classical abrasive machining processes, where the choice of grinding media in relation to the material and the cutting conditions are important to avoid overheating and surface burn [194, p. 27]; it is why lubrication is often used [194, p. 533], which is obviously not available inside an engine. On

the question of which material to use, the screening experiment found that alumina and zirconia mainly differ on the temperature input. In view of the literature on grinding and thermal barrier coatings, such an outcome was related to the difference in thermal conductivity between materials, where zirconia's performance is dragged down by its lower conductivity (Table 2.5). There are, however, other possible explanations. This effect could, for instance, be due to materials behaving differently in the plasma jet (e.g. because of different conductivities, particle size, or flowability), leading to the coating being built differently [49]. Nonetheless, further experimentation with a DoE of higher accuracy would later reinforce this view showing that materials remove the same material but have a different thermal performance (Section 7.3.1). Therefore, the evidence supports the idea that the thermal properties have had an effect and are the cause of the temperature variations. This is in line with what is expected from the nature of the contact. Meaning, given that the coatings rub, thermal effects are high, and the effect of the coatings' conductivities is visible given that it plays a meaningful role in removing heat from the contact.

What the above results really indicate is that the contact can be improved by effectively dissipating heat from the contact; thus decreasing the importance of the coatings' conductivity on the wear mechanic. Literature on grinding highlights that thermal effects become of lesser importance when the contact transitions into a mechanical contact [199]; a process that is achieved by carefully choosing the topography and the wheels' bond strength so that a surface renewal process is triggered with the operational stresses [199]. The consequence is that adhesion is delayed, heat is remove more effectively, and the removal process is improved as there is a grit resharpening effect [194, pp. 347-349]. Clearly such a scenario is desirable, and evidence of it has already been seen in one of the trued zirconia samples where SEM analysis of the specimen revealed that the post-deposition process had introduced superficial defects in the coating, allowing adhesion to detach from the surface. Additionally, investigation of the time-domain data showed both an initial delay in adhesion buildup and in temperature rise. These results suggest that heat is carried away when material detaches from the surface, which is an equivalent explanation to the behaviours highlighted by the aforementioned research on grinding. As the presence of defects entails a delay in adhesion progression and temperatures, the results show that defects are desirable for the microstructure of coatings. However, it is also interesting to observe from the time-domain of this trued zirconia sample that after the initial delay in metrics, measurements rapidly change, escalating to a severe final outcome. This observation indicates that the defect structure present in the sample is superficial, and when exhausted, leads to a runaway event. These results reaffirm that truing is not an option for introducing defects in the structure, and suggest that the defect structure, whilst moving the contact in the desired direction, should be sufficient for the duration of the contact.

These results add to the previous knowledge, evidencing that with the appropriate microstructure and stresses, surface renewal can be triggered. As a result, delaying adhesion and heat, and allowing to use materials for coatings without being limited by their conductivities. These findings have important implications for development as other requirements could decide which material to use. For instance, from the investigation of cross section through SEM, it was shown that alumina samples had delaminated, which is in line with historical evidence of the coatings and is a reason why manufacturers dislike its use today [98–100]. The coating selection is thus limited to zirconia given that the use of alumina is limited. The above findings in summation have considerable implications as for the first time:

- Define a set of tools to engineer coatings (Table 8.1).

- Set preferred outcomes and at the same time limitation of the current coatings (Table 8.1)

- Establish the aim and risk of post-deposition operations if these were to be employed.

Table 8.1 Summary showing the desired outcomes as set by the results of this study with some applicable tools and alternatives that can be applied to achieve them.

Tools	Alternative
Triggering surface renewal sufficient for the contact's duration	Limiting the contact time
Introducing sharp asperities	
Increasing arc of contact	
Using a more conductive material	
Desired outcome	
Remove material	
Delay adhesion	
Delay heat	

The question then becomes: *how to engineer a better zirconia coating given that alumina is not applicable and the contact time needs extending?* As shown in the results, the main drawback of zirconia is that it does not effectively evacuate heat. Hence, addressing this issue would result in an improvement. Amongst the different levers identified (Table 8.1), triggering surface renewal is the single option that essentially makes materials' thermal properties irrelevant. Furthermore, the results already evidenced the benefit, showing that heat effects become of lesser importance when it moves the contact to a mechanically driven one. With this approach of triggering surface renewal, it is interesting to note that the arc of contact would also be affected (Fig. 8.3), meaning that benefits of both levers being actuated simultaneously

would be seen. The literature reports many methods to achieve surface renewal, but as shown previously in this research, it all comes down to stresses in the contact going beyond a threshold over which the defects in the microstructure are actuated. Highlighting the new focus of the research, i.e., to optimise the microstructure of the coatings.
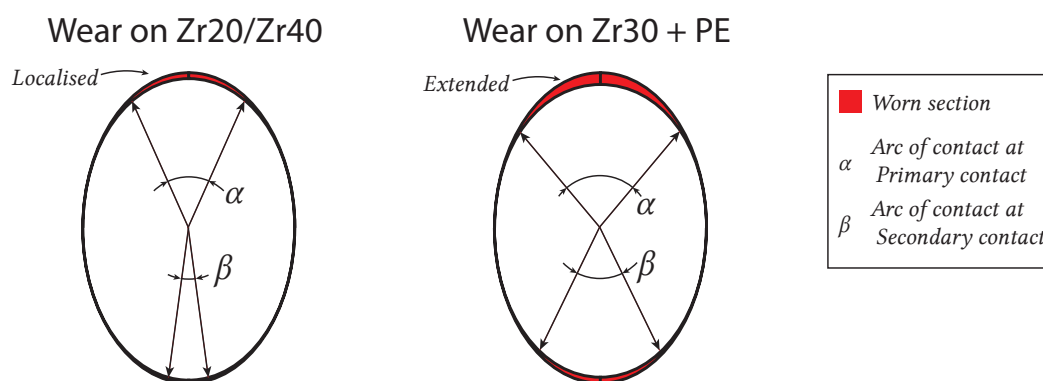

Fig. 8.3 Figure illustrating that the arc of contact is increased when more wear/compaction is produced in the coatings.

Whilst a post-deposition operation (e.g. truing) can be used to introduce microstructural changes mentioned above, and indeed this is akin to dressing a grinding wheel where before use, the wheel is sharpened to try and ensure good cutting performance around the entire circumference [194, pp. 457-463], its application is limited. It is notable that even after dressing, regions will still exist where either grits are blunt and clogged or not orientated well for cutting [194, p. 422]. As such, issues still persist. In trying to overcome these limitations, it is worth noting that Rolls-Royce developed VIPER grinding [207], which was a continuous dress/truing process for the grinding wheel. Whilst effective, such a process would clearly not be applicable for this case as it is not possible to continually refresh the engines' rotor. An alternative way to do this is to create aspects of the material microstructure that allow it to self-refresh or self-generate, in other words, a friable structure. This has been a long-time area of application in vitreous bonded wheels whereupon blunting, forces grow, causing grits or bonds to break down and expose new surfaces [194, p. 348]. This approach was explored by looking at two spray rates (20 g/min and 40 g/min) where the coatings' cohesion strength changed and including polyester to drive through increased porosity. In line with findings for grinding wheels where porosity is introduced and/or the bond strength is changed, it was found that tough asperities congest; these remove material but lead to high heat. In contrast, weak structures fail upon contact; these do not remove material, but temperatures are lower give the contact and work is spread more evenly around the surface (Fig. 8.4).
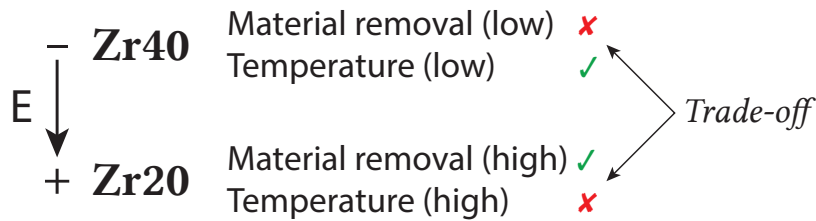
Fig. 8.4 Illustration depicting the trends happening on elastic modulus, material removal, and temperatures when changing depositions rate of the coatings. Also, showing the trade-off in properties with '✓' signifying desirable and '×' undesirable.

The significance of the above findings is noteworthy given that the results show that changing the coatings' cohesion through the spraying parameters influences how asperities work, which correlates to what would be expected from the grinding literature [194, p. 348]. Nevertheless, these also show that high material removals and low temperatures cannot be achieved through spraying, which highlights a dead-end (Fig. 8.4). The screening experiment had already shown that the strength of spraying parameters is smaller than that of a material change (at least in terms of temperatures), reinforcing that spraying alone is not sufficiently strong to counteract the alumina to zirconia change. Hence, the results stress that the only possible route is to add an extra element to impact the microstructure further.

As already proposed, the approach taken in this research has been to introduce PE to create porosity and friability in the abrasive. As mentioned earlier, this is analogous to the process undertaken in a vitreous bonded wheel, whereby introducing porosity or reducing adhesion strength between grits allows the wheel to fracture upon loading, as high forces are introduced and self-refresh [194, p. 348]. Given the nature of the process that was taking place, mixed results were observed with polyester. At the lower polyester level, evidence of increased surface roughness and arc of contact was observed, but in terms of measured outcomes (i.e., forces, material removal, temperatures, force ratios, SGE) it had a minor influence with respect to what would have been expected from not adding polyester. In contrast, differences were more significant at the higher polyester levels, with the most interesting point occurring when a high incursion rate was also used. Wherein it appeared forces were reaching a level that could actuate and cause the wheel to refresh, causing a drop in temperature values. In many ways, this is analogous to the design issues that manufacturers of grinding wheels face as if the forces resulting from the grinding process are insufficient to fracture the wheel (which is a product of porosity and bond strength), the wheel congests, loading occurs, and burn happens [194, pp. 422-427]. These events coincide with those happening in all these samples, and even at the high polyester coating at the low incursion. Hence, it highlights how the same design

parameters as considered in grinding are applicable here. However, it is imperative from a design perspective to ensure that the conditions are appropriate to actuate the friability of the wheel.

An important finding comes from comparing the strength of introducing polyester with that of material change. A PCA was used for this purpose, where it was seen that the impact of PE is high at both incursion rates and has improved the performance of zirconia coatings to the same level of alumina or even outperforming it. Such a finding implies that a coating can be tuned for stresses, or equivalently, stresses for a specific coating without being limited by the thermal properties of the bulk material. These findings open the field to a broader range of options, e.g., the investigation of angles in the blades that can create localised high stresses, or radiac fan style grooves like in grinding, or the implementation of nano-powders that literature has already reported improvements in wear performance and capabilities for tuning the properties and consistency of the outcomes (Section 2.5).

Another important finding is exposed from comparing coatings with increasing PE levels. Measurements of material removal are between those of Zr20 and Z40 coatings regardless of the PE content. In fact, adding PE leads to a slight decrease in material removal. These results are explained by the competing events that drive the contact. On the one hand, adding PE weakens the structure, whilst on the other hand, it increases roughness and allows the arc of contact to grow (Fig. 8.3). The results thus show that increasing PE has a slightly detrimental effect on material removal (due to the effect of the weaker structure), but overall, the effects balance out. There is, however, another possible explanation for these results. It is interesting to notice from the high-speed camera images that increasing incursion rate entails an increase in the arc of contact for the low PE level, whilst for the higher PE level, the arc of contact is similar at both incursion rates. These results indicate that the structure at the low PE contents is still sufficiently strong at both incursion rates, whilst with added PE, the structure yields with not much difference between incursions. The results thus suggest that the arc of contact is important and that it has reached a limit. Clearly, this limit is equivalent to the dimension of the rotor: once the arc of contact reaches the full length of the circumference, further wear or compaction of the coatings would not lead to additional improvements. This effect was not previously seen with coatings manufactured fully from zirconia (given the high elastic modulus and localised contact) and is only now visible because the arc of contact significantly changes. In essence, the results highlight that the effect of the arc of contact would plateau as coatings allow for longer arcs of contact, the limit being the circumference of the rotor.

The above becomes of particular interest in aero-engines given that the larger size of the rotor means that a smaller change in wear or compaction results in a significantly longer arc of contact (Fig. 8.3). Hence, the results indicate that the arc of contact is an important topic

for further research. A way for proceeding has already been suggested, i.e., limiting the arc of contact for all samples. Taking such approach means studying material response separately from the effects of arc of contact, the effect of which could be factored in separately, e.g., through compaction and/or wear measurements. In this way, for instance, a correlation between the outputs and arc of contact could be established to then translate the results to the engine. A system for doing such study is presented in Appendix G, where the design of the disc has been changed for a discrete contact.

Based on the above results it is recommended to study stresses and duration of the contact as separate instances, instead of fixing the maximum material removed (here 500 micrometers) and these being enclosed under the name 'incursion rate'. The benefit would be, for instance, that materials could be compared through time to failure or material removed to failure, which could be interesting if the design criterion is not to design the coatings for ad infinitum life.

8.2   Appropriateness of a scaled test setup

This project aimed to investigate abrasive materials used in rotor-stator contact in an engine appropriate test context. Broadly, this objective has been achieved with an abradables' rig reconfigured and instrumentation added. This method has allowed a variety of variables with respect to both the abrasive materials and test conditions to be investigated and some meaningful conclusions to be drawn. However, such conclusions are in the context of the test rig that has been created, and as discussed throughout this thesis, the results of this study are subject to certain limitations.

In terms of the mechanics of the contact, a major drawback is that the mandrel introduces uneven stresses into the samples. Unfortunately, not allowing to study the effect of speed and also making the samples lose their roundness, which means that the contact is not completely continuous. Further, the study is forced to investigate material properties and the arc of contact together, which adds ambiguity when both factors are important. In terms of instrumentation, the study also suffers from using the high-speed camera as a tool for evaluating the severity of adhesion. Taking such action made it particularly difficult to compare between samples, not being possible when the background tone was changed.

One question that needs to be asked, however, is whether the above are truly limitations. In regards to the samples not being round and the contact not being continuous, the rotor of an aero-engine also loses its roundness tolerances when it sits on its own weight, which makes the contact not completely continuous. Further, the rotor is not perfectly balanced and there are vibrations (e.g., natural frequencies of the shaft), which have the equivalent outcome [16]. With respect to not being able to study the impact of speed, the research on

grinding has highlighted improvements in cutting efficiency, but only because workspeed can also be changed, else efficiency actually decreases due to the reduction of depth of cut per revolution that accompanies the increase in speed [194, pp. 172-175]. This process is thus very similar to what happens when the incursion rate decreases, the process takes longer, and more heat is introduced. Given that the matter depends on how asperities interact with the surface, that they need to indent sufficiently instead of rub, the relevance of speed is arguable. A main concern could be the contact temperatures; however, given that contact happens at asperity tips, these are already well beyond the melting temperatures of the material [194, p. 138]. Hence, the importance of speed (within a range) is still questionable.

In view of the forgoing, there seems to be no reason to doubt about the representativity of the rig or the contact itself. In fact, what seems to be the case is that limitations come from achieving it to a certain degree. The implications are important as industrially there is always a drive to build more representative rigs, and this research shows that taking such action would entail setting more limitations, restraining the depth of the research and even leading to doubtful research paths. The fact that with a continuous contact the arc of contact and material properties cannot be studied independently, if anything highlights that further simplicity is needed for providing scientific knowledge.

A more representative rig can still be used to provide confirmatory results, but to explore contact variables, simplicity is key. In this research this has translated into a degree of confidence, for instance leading to suspicion when speed was firstly seen as the most important factor. Another example is when samples were seen to severely delaminate. If it was not because of this simplicity, a failure analysis would not have been done, and stresses would have not been understood. In the first case leading to a misleading conclusion (i.e., that speed is the most important factor), and in the second case to attributing the failure to the unsuitability of the coatings and this research would have been long concluded.

It is true that the current rig, even with some limitations, has allowed to place the coatings in terms of a wider research topic, contextualising in terms of grinding literature, friability of the wheels and how these impact the outcome. There has been a clear progression from earlier in the literature, where it was highlighted that these coatings had never been used as abrasives before. At the time, it was speculated that it was similar to grinding, but in truth, it was uncertain. Now that the contact is placed in context, a wider understanding has been unlocked. However, part of the success of this rig resides on the fact that the coatings are not optimised. The rig, for instance would not be able to detect if different materials have different chemical affinities and adhesion progresses to a different severity. That is, visual interpretation is not sufficient for this and clearly the high-speed camera is not suited for the purpose. Along the same lines, there is a need to improve the repeatability of the results. Statistical significance

has been critical in this research, without it, the influence of spraying parameters would not have been detected; consequently, not allowing to have a debate of whether zirconia's microstructure can be enhanced sufficiently to overcome the effect of a material change. In this case, the effects were relatively large and effects were visible, but with further optimisation of the coatings there is no certainty that the consistency of the rig is sufficient.

What has been learned so far can be used to move the engine forward, but as mentioned earlier, it would be recommended to take some actions for improving the consistency of the tests and to increase the accuracy of the process monitoring. On this note, learning can be done from the research on grinding, where process monitoring is a major topic [208, 209]. The implementation of process monitoring though Acoustic Emissions could be one approach. Its use is not much different to what is currently done with forces in this research, using *rms* values as a descriptor of the energy in the system. Aside from allowing to evaluate the severity of the contact, it would add to the research for instance, allowing to calculate the length of the contact. In doing so, enabling to calculate the full rub length, which is another metric to evaluate the severity of the contact. A change to a design like that proposed in Appendix G is still advised for adding consistency in the tests.

8.3 Industrial context

Going back to the beginning of this research, the motivation for studying abrasive linings was the benefits shown, as the current interstage sealing arrangement (Fig. 8.5) requires a sub-assembly with an abradable, and removing it will reduce engine weight and size, effectively improving the efficiency. Placed into context, at present, abrasive linings are clearly not at the same position as the best abradable linings (e.g., not getting the levels of burning, congestion, smearing). Equally, abrasive lining cannot be ignored as a research topic for the obvious benefits they bring. Besides, this research has also shown that there is a potential to improve them and overcome the limitation with a more clever design of the coatings.

This research has proposed to introduce friable coatings. However, they might not be applicable in engines as these are hard ceramics and particles breaking off and flying down the engine might have undesirable outcomes,as they could lead to erosive wear or blockages of cooling holes. This issue could be resolved with smaller particles (e.g. investigating nanostructured powders) or limiting the amount of wear. However, there is an interesting question to ask, are the coatings required to refresh ad infinitum, or instead is it sufficient to have a coating that delays deleterious effects enough so that the rub is within an acceptable regime until the end. In this regard, engines have a limiting amount of rub they ever do, so it might be worth investigating options that merely delay deleterious processes. The use of
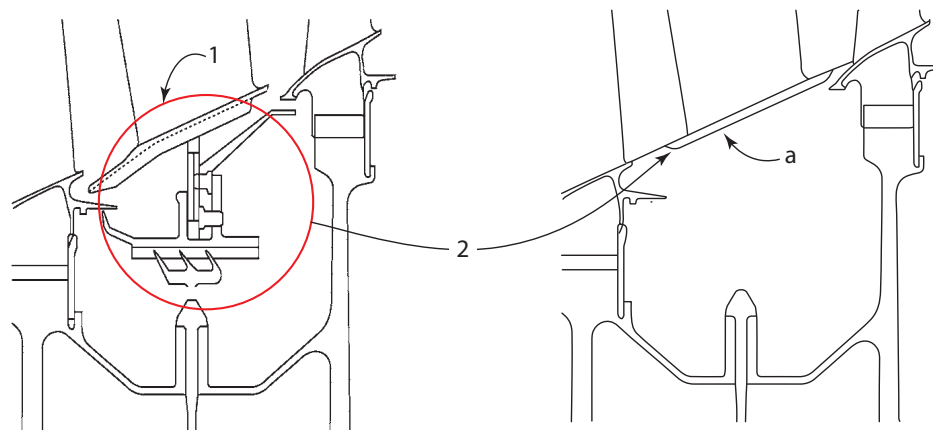
Fig. 8.5 Figure presented earlier in Section 1.4, which shows how the current interstage sealing arrangement (1) can be simplified with the introduction of an abrasive coating (2) directly applied on the rotor and immediately beneath stator vanes. Figure extracted from Piggott *et al.* [15] and adapted to show the abrasive lining.

polyester fits in this description, with such an element conferring the coating with the ability to collapse and spread the contact, introducing a slight delay and ultimately also a degree of friability that stops the outcomes from maxing out. Additional friability would make the coating work as a grinding wheel and ad infinitum, but at that point, there would be particles flying down the engine, and it is strictly not needed because the coatings would not require to work forever. Nevertheless, if such a coating was required, this research provides sufficient knowledge to implement the required changes.

Another point of view to consider is that friable coatings are only desirable because they congest, and there is a need to remove heat. If as highlighted in the previous discussion there is an alternative method to channel the heat away, then there would not be that need for such a friable coating; or a combination of both approaches could be applied. Considering that engines' rotors are significantly larger than the one used for this research, and thus the effect of an increased arc of contact with added porosity is stronger, this would entail that a large change in the coatings is not really needed. Overall, significant opportunities for the abrasive/stator contacts exist, although further work is also clearly needed. In summary, with the research presented and the rig developed, there is now a clear route to continue this research, where the rig could be further enhanced with the relevant outcomes.

Chapter 9

Conclusions

This study set out to determine the wear mechanisms resulting from the abrasive rotor/stator-blade contact and whether the abrasive performance can be improved. With the goal of answering these questions, a review of literature has been performed, a representative test rig has been developed and instrumented, metrics have been established, and statistically planned experiments have been executed. Overall, a number of outcomes have emerged from this study, and the proceeding section will now cover them in more detail.

- A scaled test rig has been developed and instrumented, reproducing the contact happening in aero-engines between the stator blade and the rotor, and allowing to monitor it in-situ. This experimental method has provided the means to investigate the tribological behaviours of the aforementioned abrasive contact.

- A number of meaningful metrics have been established to characterise and classify the contact. These metrics are forces in *rms*, the apparent temperature of the blade, force ratio, and specific grinding energy. Adhesion has also been monitored in-situ, but its suitability is arguable. Further work or alternatives for assessing the severity of the wear would be required.

- The wear mechanism has been identified as adhesive wear, with adhesion happening progressively and thermal effects having an important implication. The contact is akin to grinding when depth of cut is not sufficiently high to remove material, or grits are blunt. That is, rubbing happens, material is not removed effectively, and the outcomes are essentially thermally driven.

- The contact has been placed into the context of the relevant literature, which is primarily the literature on grinding and that on thermal barrier coatings. However, whilst valuable, this literature is not directly applicable. Concerning grinding, the coatings are built

fundamentally different from how a grinding wheel is built and works on a different scale from grinding processes. A similar challenge occurs when considering research on TBCs; these coatings function differently to what is commonly investigated, now requiring them to be abrasive, whilst usually, it is desirable of them to be abrasion resistant. Consequently, they are also tested in non-representative conditions,i.e., smaller scale test platforms.

- The contact is currently thermally driven, which means that variables that affect the heat in the system have the biggest effects. Incursion rate in this way affects the contact because it defines the overall time of the test (i.e, the total energy input into the contact) not because of the stresses introduced. A high incursion rate translates into shorter contacts, thus less energy and less temperatures than when a lower incursion rate is used. Material is also very important given that conductivities influence the behaviours; alumina showing benefits but its use is impractical because it delaminates. Other variables (spraying condition, surface finish) do impact but not significantly in this sense.

- An increase in the arc of contact divides work around the wheel more evenly, and consequently delays the progressive wear mechanism. However, thermal effects are still pertinent in this condition. Surface renewal on the other hand remove heat from the contact more effectively, and also delays adhesion and extends the arc of contact. In this latter condition thermal effects are less important and materials behave similarly despite their different conductivities.

- Changing microstructure can have the same effect as a material change, but not when just produced through spraying parameters. Additional changes are required to trigger the surfaced defects. Possible options could be the increase of the stresses in the contact or further changing the microstructure to weaken the coatings' structure.

- Post-deposition operations are a development opportunity for coatings. They have a high impact on the coatings and thus on their performance. However, this also means that care should be taken not to provoke early failure of the coatings. Whenever used, post-deposition operations should thus be optimised for the specific operating conditions the coatings will be subjected to. A key aspect is that the process allows rigorous control over the defects introduced and avoids concentrating stresses at the bond coat, which will prevent delamination.

- Introducing polyester into the coatings' micostructure or changing spray rate varies the cohesion strength of the splats in the coatings. This is similar to impacting friability in

grinding, changing how asperities work in the contact and how defects are activated with the contact stresses.

- This research has highlighted various tools to enhance the coatings' performance. A further understanding of aero-engine requirements is now needed to define a development route. More precisely, if the coatings need to perform ad infinitum or a delay in the failure process is sufficient.

- The current rig has shown that experimental repeatability is critical; achieving statistical significance allows identifying and discriminating meaningful variables. Given the dynamics of the rig, it is unlikely that a more representative rig gives further insight, which would instead be better suited as confirmatory of the findings.

- Albeit the current rig has fulfilled the aims of this research, with further development of the coatings, the rig would require improvements to add sensitivity. Particularly in characterisation of the severity of the wear, where the strength of the high-speed camera has been limited. Along the same lines, repeatability of the tests is also critical, and a more stable system can be designed as that proposed in Appendix G. Furthermore, separating the arc of contact and material properties can broaden the area of research, and this can be done through a discontinuous contact

- This research has established a procedure, a hierarchy of testing, that can now be used to study this abrasive contact.

Chapter 10

Further work

The findings mentioned in the previous Chapter 9 are subjected to certain limitations, which in turn translate into paths that may be interesting to explore in future work. The aim of this section is to gather these aspects as well as others that may not have been explicitly revealed throughout the course of this study but still may be of interest for further investigation. Further work will be shown related to three areas, namely the development of the test, fundamental understanding, and practical application of the technology.

Further work on developing the test

- The effect of speed could be further investigate as Rolls-Royce's engines run at different speeds and understanding this relationship is important. To include such an effect in the current study was not possible due to the design of the expandable mandrel and the samples, and further investigating this variable would allow to verify whether these ceramics sit in the broader research of grinding processes. If speed is disregarded as an important variable, the hypothesis established in this thesis would be verified and the existing knowledge on grinding would be applicable for the development of the coatings. For undertaking such action however, the design of the samples and mandrel would require changing such as those suggested in Appendix G.

- To further understand the effect of arc of contact. Whilst from the point of view of an aero-engine it is clear this is a factor that cannot be controlled, from a scientific point of view it is interesting to isolate the arc length so that the effects of it can be truly understood.

- It could be interesting to develop other forms of characterising and/or measuring the amount of adhesion. Currently this has been done through the high speed camera but

such metric depends on the tone of the substrate and lighting used during the test; thus not being a metric that can be used for comparing between different materials or even between test setups. Besides, measuring tonal changes is not a tangible measure of the adhesion present on the ceramics. Further investigating this issue could be valuable if samples are improved to the point where surface renewal happens or to define a level of adhesion that is considered detrimental and beyond which the adhesion process should not continue.

- To increase the precision of the instrumentation and of the metrics used. A suggestion is to introduce the use of Acoustic emissions for monitoring, which is a tool that has been valuable for characterising the contact during grinding processes and can serve to assist in quantifying the severity of the wear, something that has not been able to achieve in this study to a satisfactory level.

- To provide a method to investigate the defects in the coatings prior testing, with particular interest on identifying interlamelar defects. This could be for instance through ultrasounds much like its done for thin film lubrication and would confirm if the coating has been manufactured correctly. Thus if failure happens being able to attribute it to the operation conditions and not to the manufacturing process.

Further work on fundamental understanding

- To study the impact of textures on the ceramics and/or geometries in the blade sample. This could be achieved in combination with the use of a filler like it has been used in this thesis with the introduction of polyester. It could be interesting how textures like grooves affect the removal mechanism and polyester or geometries in the blades (e.g., angles) may change the stresses required for activating the defect structure in the coatings, and whether this truly leads to an improvement because of surface renewal. The aim of such an experiment would be to identify if the stress state generated can be tuned to produce the desired outcomes by changing the internal structure of the coatings, surface topography, and/or blade profile.

- From an industrial point of view it may be interesting to investigate the degree of thermal damage introduced into the rotor. In other words, if the high temperatures generated during the contact have managed to damage the rotor.

- Similarly, the material flow in vane element could be charcteised , i.e., to identify the transition between mass rooming (lip formation) and cutting. The characterisantion

could be done, for instance, by chopping the blade and taking progressive hardness measurements along it, identifying in this way transitions in loading regimes. Failure would be identified differently to military, but it might lead to consider length of vanes, the stiffness, and the loading regimes itself.

Further work on practical application of the technology

- To investigate if there is a system to channel heat away from the contact, as these ceramics are thermal barrier coatings and heat builds up, favoring adhesion. This is equivalent to how it is done in grinding where cooling is used for a reason, and if this is taken away, heat builds up and adhesion starts. The results suggested that reducing the thermal input would improve the mechanism and it may be interesting to put some thought on whether there is a mechanism to channel heat away better (alternative to that of triggering surface renewal/fracture).

- If designing a system that cannot work ad infinitum as proposed, another option to explore is to become more precise on how long the contact is going to work for. This research has shown that if heat cannot be managed the onset of adhesion can be delayed and a safe working envelope created. Roll-Royce would thus need to design around that and not transgress.

References

[1] J. K. Whalen, E. E. Alvarez, and L. P. Palliser, "Thermoplastic labyrinth seals for centrifugal compressors," in *Proc. of the 33rd Turbomachinery Symposium*, Texas A&M University, Turbomachinery Laboratories, 2004, pp. 113–126. DOI: 10.21423/R19651.

[2] C. Raper, "Shaft seal crack obviation," U.S. Patent 10400618B2, Sep. 3, 2019.

[3] J. Denecke, V. Schramm, S. Kim, and S. Wittig, "Influence of rub-grooves on labyrinth seal leakage," *Journal of Turbomachinery*, vol. 125, no. 2, p. 387, Apr. 2003. DOI: 10.1115/1.1539516.

[4] R. E. Chupp, R. C. Hendricks, and B. M. Steinetz, "Gas turbine engines: Seals," in *Encyclopedia of Aerospace Engineering*. 2010. DOI: 10.1002/9780470686652.eae095.

[5] J. R. Webster, G. Franceschini, J. R. Aubry, D. R. H. Gillespie, and A. K. Owen, "Sealing arrangements," U.S. Patent Application 20170051834A1, Feb. 23, 2017.

[6] J. M. Becker, M. C. Margetts, B. N. Hodgson, D. E. McAdams, and R. M. Johnson, "Vane assembly," U.S. Patent Application 20160017731A1, Jan. 21, 2016.

[7] C. Borgnakke and R. E. Sonntag, *Fundamentals of Thermodynamics*, Eigth, L. Ratts, Ed. Don Fowley, 2012, p. 877.

[8] N. Hall, Ed., *Ideal Brayton Cycle*, NASA Glenn Research Cente, 2015. [Online]. Available: https://www.grc.nasa.gov/WWW/K-12/airplane/brayton.html (visited on 03/06/2020).

[9] J. R. S. Cruz, J. M. L. Martínez, J. Arrégle, J. A. B. Jacobi, J. V. P. Soriano, J. G. Lucas, and R. P. Marín, *Procesos y tecnología de máquinas y motores térmicos*. Ed. Univ. Politéc. Valencia, 2002.

[10] N. Hall, Ed., *Isentropic Compression (or Expansion)*, NASA Glenn Research Cente, 2021. [Online]. Available: https://www.grc.nasa.gov/WWW/K-12/airplane/compexp.html (visited on 03/05/2022).

[11] B. Gunston, *Jane's Aero-engines*. Jane's Information Group, 1998.

[12] S. Wilson, "Thermally sprayed abradable coating technology for sealing in gas turbines," in *6th Int. Conf. on the Future of Gas Turbine Technology*, (Brussels, Belgium), Oct. 2012.

[13] K. J. Melcher and J. A. Kypuros, "Toward a fast-response active turbine tip clearance control," in *16th Int. Symp. on Airbreathing Engines*, Cleveland, Ohio, 2003.

[14] M. P. Keenan, "Circumferential seal," U.S. Patent Application 20190234226A1, Aug. 1, 2019.

[15] K. S. Piggott, P. A. Davis, and M. J. Simms, "Interstage seal," U.S. Patent 8864451B2, Oct. 21, 2014.

[16] G. Jacquet-Richardet, M. Torkhani, P. Cartraud, F. Thouverez, T. N. Baranger, M. Herran, C. Gibert, S. Baguet, P. Almeida, and L. Peletan, "Rotor to stator contacts in turbomachines. review and application," *Mechanical Systems and Signal Processing*, vol. 40, no. 2, pp. 401–420, Nov. 2013. DOI: 10.1016/j.ymssp.2013.05.010.

[17] S. B. Lattime and B. M. Steinetz, "Turbine engine clearance control systems: Current practices and future direction," in *38th AIAA/ASME/SAE/ASEE Joint Propulsion Conf. & Exhibit*, Indianapolis, Indiana, Jul. 2002.

[18] T. J. Freeman, J. A. Walston, J. Shi, and T. G. Schetzel, "Vane assemblies for gas turbine engines," U.S. Patent Application 20160230576A1, Aug. 11, 2016.

[19] L. V. Lewis, "Cantilevered stator stage," U.S. Patent 7241108B2, Jun. 10, 2007.

[20] I. Alvanos, "Pretrenched rotor for gas turbine engine," U.S. Patent 10550699B2, Feb. 4, 2020.

[21] J. A. Storer and N. A. Cumpsty, "Tip leakage flow in axial compressors," *Journal of Turbomachinery*, vol. 113, no. 2, pp. 252–259, Apr. 1991. DOI: 10.1115/1.2929095.

[22] D. K. Hall, E. M. Greitzer, and C. S. Tan, "Performance limits of axial compressor stages," Jun. 2012. DOI: 10.1115/GT2012-69709.

[23] C. W. Strock and P. H. Zajchowski, "Friable ceramic rotor shaft abrasive coating," U.S. Patent 9169740B2, Oct. 27, 2015.

[24] P. H. Zajchowski, C. W. Strock, and M. E. Bintz, "Abrasive rotor shaft ceramin coating," U.S. Patent 8790078B2, Jul. 29, 2014.

[25] C. W. Strock and P. W. Baumann, "Spall resistant abradable turbine air seal," U.S. Patent 8876470B2, Nov. 4, 2014.

[26] C. W. Strock and C. Guo, "Abrasive cutter formed by thermal spray and post treatment," U.S. Patent 8770927B2, Jun. 8, 2014.

[27] C. W. Strock, K. Lagueux, M. E. Bintz, T. W. Stowe, and P. H. Zajchowski, "Abrasive rotor coating for forming a seal in a gas turbine engine," U.S. Patent Application 20120099992A1, Apr. 26, 2012.

[28] M. E. Bintz and C. W. Strock, "Self dressing, mildly abrasive coating for clearance control," U.S. Patent Application 20120099971A1, Apr. 26, 2012.

[29] C. Guo, C. W. Strock, and P. W. Baumann, "Rough dense ceramic sealing surface in turbomachines," U.S. Patent 8770926B2, Jul. 8, 2014.

[30] D. Sporer, M. Dorfman, L. Xie, A. Refke, I. Giovannetti, and M. Giannozzi, "Processing and properties of advanced ceramic abradable coatings," in *Global Coating Solutions, Proc. from the Int. Thermal Spray Conf.*, Beijing, China: ASME International, May 2007.

[31] *Thermal spraying–Terminology, classification*, ISO 14917:2017, 2017.

[32] O. Metco, *Material product data sheet pure aluminum oxide powders*, DSM-0237.0– Aluminum Oxide Powders, 2019. [Online]. Available: https://bit.ly/2wbSrAz (visited on 03/19/2020).

[33] ——, *Material product data sheet Alumina 3% Titania thermal spray powders*, DSM-0236.0–Alumina 3% Titania Thermal Spray Powders, 2019. [Online]. Available: https://bit.ly/2R5v4Q7 (visited on 03/19/2020).

[34] ——, *Material Product Data Sheet 8% Yttria Stabilized Zirconia Agglomerated and HOSP Powders*, DSM-0242.0–HOSP 8% YsZ Powders, 2019. [Online]. Available: https://bit.ly/3e1FxGq (visited on 03/19/2020).

[35] H. Herman, S. Sampath, and R. McCune, "Thermal Spray: Current Status and Future Trends," *MRS Bulletin*, vol. 25, no. 7, pp. 17–25, 2000. DOI: 10.1557/mrs2000.119.

[36] O. Metco, *Thermal spray equipment guide*, BRO-0002.13–Thermal Spray Equipment Guide, 2017. [Online]. Available: https://bit.ly/2JyfIzJ (visited on 03/19/2020).

[37] L. Pawlowski, *The science and engineering of thermal spray coatings*, Second. John Wiley & Sons, 2008, p. 596.

[38] H. Herman, "Plasma-sprayed coatings," *Scientific American*, vol. 259, no. 3, pp. 112–117, 1988. [Online]. Available: http://www.jstor.org/stable/24989234.

[39] O. Metco, *An introduction to thermal spray*, BRO-0005.6–An Introduction to Thermal Spray, 2016. [Online]. Available: https://bit.ly/3bOV22p (visited on 03/19/2020).

[40] P. Fauchais, A. Vardelle, M. Vardelle, and M. Fukumoto, "Knowledge concerning splat formation: An invited review," *Journal of Thermal Spray Technology*, vol. 13, no. 3, pp. 337–360, 2004. DOI: 10.1361/10599630419670.

[41] S. Kuroda and T. W. Clyne, "The quenching stress in thermally sprayed coatings," *Thin Solid Films*, vol. 200, no. 1, pp. 49–66, 1991. DOI: 10.1016/0040-6090(91)90029-W.

[42] R. McPherson, "Formation of metastable phases in flame and plasma-prepared alumina," *Journal of Materials Science*, vol. 8, no. 6, pp. 851–858, Jun. 1973. DOI: 10.1007/BF02397914.

[43] ——, "On the formation of thermally sprayed alumina coatings," *Journal of Materials Science*, vol. 15, no. 12, pp. 3141–3149, Dec. 1980. DOI: 10.1007/BF00550387.

[44] ——, "A review of microstructure and properties of plasma sprayed ceramic coatings," *Surface and Coatings Technology*, vol. 39-40, no. C, pp. 173–181, 1989. DOI: 10.1016/0257-8972(89)90052-2.

[45] S. Sampath and H. Herman, "Rapid solidification and microstructure development during plasma spray deposition," *Journal of Thermal Spray Technology*, vol. 5, no. 4, pp. 445–456, 1996. DOI: 10.1007/BF02645275.

[46] S. Sampath, X. Y. Jiang, J. Matejicek, A. C. Leger, and A. Vardelle, "Substrate temperature effects on splat formation, microstructure development and properties of plasma sprayed coatings Part I: Case study for partially stabilized zirconia," *Materials Science and Engineering: A*, vol. 272, no. 1, pp. 181–188, 1999. DOI: 10.1016/S0921-5093(99)00459-1.

[47] R. Dykhuizen, "Review of impact and solidification of molten thermal spray droplets," *Journal of Thermal Spray Technology*, vol. 3, no. 4, pp. 351–361, Dec. 1994. DOI: 10.1007/BF02658980.

[48] A. Kulkarni, A. Vaidya, A. Goland, S. Sampath, and H. Herman, "Processing effects on porosity-property correlations in plasma sprayed yttria-stabilized zirconia coatings," *Materials Science and Engineering: A*, vol. 359, no. 1, pp. 100–111, 2003. DOI: 10.1016/S0921-5093(03)00342-3.

[49] P. Fauchais, G. Montavon, and G. Bertrand, "From powders to thermally sprayed coatings," *Journal of thermal spray technology*, vol. 19, no. 1-2, pp. 56–80, 2010. DOI: 10.1007/s11666-009-9435-x.

[50] P. Fauchais, "2–Current status and future directions of thermal spray coatings and techniques," in *Future Development of Thermal Spray Coatings*, Woodhead Publishing, 2015, pp. 17–49. DOI: 10.1016/B978-0-85709-769-9.00002-6.

[51] P. Fauchais and M. Vardelle, "Plasma spraying: Present and future," *Pure and Applied Chemistry*, vol. 66, no. 6, pp. 1247–1258, 1994. DOI: 10.1351/pac199466061247.

[52] R. S. Lima and B. R. Marple, "Thermal spray coatings engineered from nanostructured ceramic agglomerated powders for structural, thermal barrier and biomedical applications: A review," *Journal of Thermal Spray Technology*, vol. 16, no. 1, pp. 40–63, 2007. DOI: 10.1007/s11666-006-9010-7.

[53] P. Fauchais and M. Vardelle, "Sensors in spray processes," *Journal of Thermal Spray Technology*, vol. 19, no. 4, pp. 668–694, 2010. DOI: 10.1007/s11666-010-9485-0.

[54] S. Sampath, V. Srinivasan, A. Valarezo, A. Vaidya, and T. Streibl, "Sensing, control, and in situ measurement of coating properties: An integrated approach toward establishing process-property correlations," *Journal of Thermal Spray Technology*, vol. 18, no. 2, pp. 243–255, 2009. DOI: 10.1007/s11666-009-9314-5.

[55] T. Steinke, G. Mauer, R. Vaßen, D. Stöver, D. Roth-Fagaraseanu, and M. Hancock, "Process design and monitoring for plasma sprayed abradable coatings," *Journal of thermal spray technology*, vol. 19, no. 4, pp. 756–764, 2010. DOI: 10.1007/s11666-010-9468-1.

[56] D. Aussavy, R. Bolot, G. Montavon, F. Peyraut, G. Szyndelman, J. Gurt-Santanach, and S. Selezneff, "YSZ-Polyester abradable coatings manufactured by APS," *Journal of Thermal Spray Technology*, vol. 25, no. 1-2, pp. 252–263, 2016. DOI: 10.1007/s11666-015-0358-4.

[57] M. Karger, R. Vaßen, and D. Stöver, "Atmospheric plasma sprayed thermal barrier coatings with high segmentation crack densities: Spraying process, microstructure and thermal cycling behavior," *Surface and Coatings Technology*, vol. 206, no. 1, pp. 16–23, 2011. DOI: 10.1016/j.surfcoat.2011.06.032.

[58] G. Qian, T. Nakamura, and C. C. Berndt, "Effects of thermal gradient and residual stresses on thermal barrier coating fracture," *Mechanics of Materials*, vol. 27, no. 2, pp. 91–110, Feb. 1998, ISSN: 0167-6636. DOI: 10.1016/S0167-6636(97)00042-2.

[59] A. G. Evans, D. R. Mumm, J. W. Hutchinson, G. H. Meier, and F. S. Pettit, "Mechanisms controlling the durability of thermal barrier coatings," *Progress in Materials Science*, vol. 46, no. 5, pp. 505–553, 2001. DOI: 10.1016/S0079-6425(00)00020-7.

[60] A. Rabiei and A. G. Evans, "Failure mechanisms associated with the thermally grown oxide in plasma-sprayed thermal barrier coatings," *Acta Materialia*, vol. 48, no. 15, pp. 3963–3976, 2000. DOI: 10.1016/S1359-6454(00)00171-3.

[61] D. R. Clarke, M. Oechsner, and N. P. Padture, "Thermal-barrier coatings for more efficient gas-turbine engines," *MRS Bulletin*, vol. 37, no. 10, pp. 891–898, 2012. DOI: 10.1557/mrs.2012.232.

[62] N. P. Padture, M. Gell, and E. H. Jordan, "Thermal Barrier Coatings for Gas-Turbine Engine Applications," *Science*, vol. 296, no. 5566, pp. 280–284, 2002. DOI: 10.1126/science.1068609.

[63] B. Bernard, A. Quet, L. Bianchi, A. Joulia, A. Malié, V. Schick, and B. Rémy, "Thermal insulation properties of YSZ coatings: Suspension Plasma Spraying (SPS) versus Electron BeamPhysical Vapor Deposition (EB-PVD) and Atmospheric Plasma Spraying (APS)," *Surface & Coatings Technology*, vol. 318, pp. 122–128, 2017, ISSN: 0257-8972. DOI: 10.1016/j.surfcoat.2016.06.010.

[64] J. G. Odhiambo, W. Li, Y. Zhao, and C. Li, "Porosity and its significance in plasma-sprayed coatings," *Coatings*, vol. 9, no. 7, p. 460, Jul. 2019, ISSN: 2079-6412. DOI: 10.3390/coatings9070460.

[65] K. A. Khor and Y. W. Gu, "Thermal properties of plasma-sprayed functionally graded thermal barrier coatings," *Thin Solid Films*, vol. 372, no. 1, pp. 104–113, 2000. DOI: 10.1016/S0040-6090(00)01024-5.

[66] M. Tamura, M. Takahashi, J. Ishii, K. Suzuki, M. Sato, and K. Shimomura, "Multilay-ered thermal barrier coating for land-based gas turbines," *Journal of Thermal Spray Technology*, vol. 8, no. 1, pp. 68–72, 1999. DOI: 10.1361/105996399770350584.

[67] K. Kokini, A. Banerjee, and T. A. Taylor, "Thermal fracture of interfaces in precracked thermal barrier coatings," *Materials Science and Engineering: A*, vol. 323, no. 1, pp. 70–82, 2002. DOI: 10.1016/S0921-5093(01)01361-2.

[68] E. Bakan and R. Vaßen, "Ceramic top coats of plasma-sprayed thermal barrier coatings: Materials, processes, and properties," *Journal of Thermal Spray Technology*, vol. 26, no. 6, pp. 992–1010, 2017. DOI: 10.1007/s11666-017-0597-7.

[69] T. A. Taylor, "Thermal properties and microstructure of two thermal barrier coatings," *Surface and Coatings Technology*, vol. 54-55, pp. 53–57, 1992. DOI: 10.1016/S0257-8972(09)90027-5.

[70] Z. Lu, S.-W. Myoung, H.-S. Kim, M.-S. Kim, J.-H. Lee, Y.-G. Jung, J.-C. Jang, and U. Paik, "Microstructure evolution and interface stability of thermal barrier coatings with vertical type cracks in cyclic thermal exposure," *Journal of thermal spray technology*, vol. 22, no. 5, pp. 671–679, 2013. DOI: 10.1007/s11666-013-9886-y.

[71] T. A. Taylor, "Thermal barrier coating for substrates and process for producing it," U.S. Patent 5 073 433, Dec. 17, 1991.

[72] C. U. Hardwicke and Y.-C. Lau, "Advances in thermal spray coatings for gas turbines and energy generation: A review," *Journal of Thermal Spray Technology*, vol. 22, no. 5, pp. 564–576, 2013. DOI: 10.1007/s11666-013-9904-0.

[73] U. Schulz, B. Saruhan, K. Fritscher, and C. Leyens, "Review on advanced EB-PVD ceramic topcoats for TBC applications," *International Journal of Applied Ceramic Technology*, vol. 1, no. 4, pp. 302–315, 2004. DOI: 10.1111/j.1744-7402.2004.tb00182.x.

[74] L. Pawlowski, "Suspension and solution thermal spray coatings," *Surface and Coatings Technology*, vol. 203, no. 19, pp. 2807–2829, 2009. DOI: 10.1016/j.surfcoat.2009.03.005.

[75]   L. Gao, H. Guo, L. Wei, C. Li, and H. Xu, "Microstructure, thermal conductivity and thermal cycling behavior of thermal barrier coatings prepared by plasma spray physical vapor deposition," *Surface and Coatings Technology*, vol. 276, pp. 424–430, 2015. DOI: 10.1016/j.surfcoat.2015.06.033.

[76]   C. Wang, Y. Wang, S. Fan, Y. You, L. Wang, C. Yang, X. Sun, and X. Li, "Optimized functionally graded La2Zr2O7/8YSZ thermal barrier coatings fabricated by suspension plasma spraying," *Journal of Alloys and Compounds*, vol. 649, pp. 1182–1190, 2015. DOI: 10.1016/j.jallcom.2015.05.290.

[77]   S. R. Choi, J. W. Hutchinson, and A. G. Evans, "Delamination of multilayer thermal barrier coatings," *Mechanics of Materials*, vol. 31, no. 7, pp. 431–447, 1999. DOI: 10.1016/S0167-6636(99)00016-2.

[78]   H. Jamali, R. Mozafarinia, R. S. Razavi, and R. Ahmadi-Pidani, "Comparison of thermal shock resistances of plasma-sprayed nanostructured and conventional yttria stabilized zirconia thermal barrier coatings," *Ceramics International*, vol. 38, no. 8, pp. 6705–6712, 2012. DOI: 10.1016/j.ceramint.2012.05.060.

[79]   M. Gell, E. H. Jordan, Y. H. Sohn, D. Goberman, L. Shaw, and T. D. Xiao, "Development and implementation of plasma sprayed nanostructured ceramic coatings," *Surface and Coatings Technology*, vol. 146-147, pp. 48–54, 2001. DOI: 10.1016/S0257-8972(01)01470-0.

[80]   A. Keyvani, M. Saremi, and M. H. Sohi, "An investigation on oxidation, hot corrosion and mechanical properties of plasma-sprayed conventional and nanostructured YSZ coatings," *Surface and Coatings Technology*, vol. 206, no. 2, pp. 208–216, 2011. DOI: 10.1016/j.surfcoat.2011.06.036.

[81]   R. S. Lima and B. R. Marple, "Superior performance of high-velocity oxyfuel-sprayed nanostructured TiO2 in comparison to air plasma-sprayed conventional Al2O3-13TiO2," *Journal of Thermal Spray Technology*, vol. 14, no. 3, pp. 397–404, Sep. 2005. DOI: 10.1361/105996305X59413.

[82]   R. S. Lima, A. Kucuk, and C. C. Berndt, "Bimodal distribution of mechanical properties on plasma sprayed nanostructured partially stabilized zirconia," *Materials Science and Engineering: A*, vol. 327, no. 2, pp. 224–232, 2002. DOI: 10.1016/S0921-5093(01)01530-1.

[83]   X. Lin, Y. Zeng, S. W. Lee, and C. Ding, "Characterization of alumina–3 wt.% titania coating prepared by plasma spraying of nanostructured powders," *Journal of the European Ceramic Society*, vol. 24, no. 4, pp. 627–634, 2004. DOI: 10.1016/S0955-2219(03)00254-1.

[84]   G. Di Girolamo, A. Brentari, C. Blasi, and E. Serra, "Microstructure and mechanical properties of plasma sprayed alumina-based coatings," *Ceramics International*, vol. 40, no. 8, Part B, pp. 12 861–12 867, 2014. DOI: 10.1016/j.ceramint.2014.04.143.

[85]   S. I. Bae and S. Baik, "Sintering and grain growth of ultrapure alumina," *Journal of Materials Science*, vol. 28, no. 15, pp. 4197–4204, Jan. 1993. DOI: 10.1007/BF00351254.

[86]   I.-J. Bae and S. Baik, "Abnormal grain growth of alumina," *Journal of the American Ceramic Society*, vol. 80, no. 5, pp. 1149–1156, 1997. DOI: 10.1111/j.1151-2916.1997.tb02957.x.

[87] S. I. Bae and S. Baik, "Determination of critical concentrations of silica and/or calcia for abnormal grain growth in alumina," *Journal of the American Ceramic Society*, vol. 76, no. 4, pp. 1065–1067, 1993. DOI: 10.1111/j.1151-2916.1993.tb05338.x.

[88] X. Q. Cao, R. Vassen, and D. Stoever, "Ceramic materials for thermal barrier coatings," *Journal of the European Ceramic Society*, vol. 24, no. 1, pp. 1–10, 2004. DOI: 10.1016/S0955-2219(03)00129-8.

[89] T. Tsuchida, R. Furuichi, T. Ishii, and K. Itoh, "The effect of Cr3+ and Fe3+ ions on the transformation of different aluminum hydroxides to α-Al2O3," *Thermochimica Acta*, vol. 64, no. 3, pp. 337–353, 1983. DOI: 10.1016/0040-6031(83)85009-6.

[90] J. Ilavsky, C. C. Berndt, H. Herman, P. Chraska, and J. Dubsky, "Alumina-base plasma-sprayed materials-Part II: Phase transformations in aluminas," *Journal of thermal spray technology*, vol. 6, no. 4, pp. 439–444, 1997. DOI: 10.1007/s11666-997-0028-2.

[91] R. Yılmaz, A. O. Kurt, A. Demir, and Z. Tatlı, "Effects of TiO2 on the mechanical properties of the al2o3–TiO2 plasma sprayed coating," *Journal of the European Ceramic Society*, vol. 27, no. 2-3, pp. 1319–1323, Jan. 2007. DOI: 10.1016/j.jeurceramsoc.2006.04.099.

[92] V. Fervel, B. Normand, and C. Coddet, "Tribological behavior of plasma sprayed Al2O3-based cermet coatings," *Wear*, vol. 230, no. 1, pp. 70–77, 1999. DOI: 10.1016/S0043-1648(99)00096-4.

[93] K. Ramachandran, V. Selvarajan, P. V. Ananthapadmanabhan, and K. P. Sreekumar, "Microstructure, adhesion, microhardness, abrasive wear resistance and electrical resistivity of the plasma sprayed alumina and alumina–titania coatings," *Thin Solid Films*, vol. 315, no. 1, pp. 144–152, 1998. DOI: 10.1016/S0040-6090(97)00738-4.

[94] A. R. M. Sahab, N. H. Saad, S. Kasolang, and J. Saedon, "Impact of plasma spray variables parameters on mechanical and wear behaviour of plasma sprayed Al2O3 3%wt TiO2 coating in abrasion and erosion application," *Procedia Engineering*, vol. 41, pp. 1689–1695, 2012. DOI: 10.1016/j.proeng.2012.07.369.

[95] M. Bounazef, S. Guessasma, G. Montavon, and C. Coddet, "Effect of APS process parameters on wear behaviour of alumina–titania coatings," *Materials Letters*, vol. 58, no. 20, pp. 2451–2455, 2004. DOI: 10.1016/j.matlet.2004.02.026.

[96] M. Wang and L. L. Shaw, "Effects of the powder manufacturing method on microstructure and wear performance of plasma sprayed alumina–titania coatings," *Surface and Coatings Technology*, vol. 202, no. 1, pp. 34–44, 2007. DOI: 10.1016/j.surfcoat.2007.04.057.

[97] B. H. Kear, Z. Kalman, R. K. Sadangi, G. Skandan, J. Colaizzi, and W. E. Mayo, "Plasma-sprayed nanostructured Al2O3/TiO2 powders and coatings," *Journal of Thermal Spray Technology*, vol. 9, no. 4, pp. 483–487, Dec. 1, 2000. DOI: 10.1007/BF02608550.

[98] R. A. Miller, "Thermal barrier coatings for aircraft engines: History and directions," *Journal of Thermal Spray Technology*, vol. 6, no. 1, p. 35, Mar. 1997. DOI: 10.1007/BF02646310.

[99] R. A. Miller, "History of thermal barrier coatings for gas turbine engines: Emphasizing nasa's role from 1942 to 1990," Tech. Rep., 2009.

[100] S. J. Grisaffe, "Analysis of shear bond strength of plasma-sprayed alumina coatings on stainless steel," NASA, Cleveland, Oh, Lewis Research Center, Tech. Rep., 1965, 19 pp. [Online]. Available: https://bit.ly/2KmUHbI (visited on 04/20/2020).

[101] A. C. Karaoglanli, E. Altuncu, I. Ozdemir, A. Turk, and F. Ustel, "Structure and durability evaluation of YSZ Al2O3 composite TBCs with APS and HVOF bond coats under thermal cycling conditions," *Surface and Coatings Technology*, vol. 205, S369–S373, Jul. 2011. DOI: 10.1016/j.surfcoat.2011.04.081.

[102] S. Lakiza, O. Fabrichnaya, M. Zinkevich, and F. Aldinger, "On the phase relations in the ZrO2–YO1.5–AlO1.5 system," *Journal of Alloys and Compounds*, vol. 420, no. 1-2, pp. 237–245, Aug. 2006. DOI: 10.1016/j.jallcom.2005.09.079.

[103] K. He, J. Chen, W. Weng, C. Li, and Q. Li, "Microstructure and mechanical properties of plasma sprayed al 2 o 3 -YSZ composite coatings," *Vacuum*, vol. 151, pp. 209–220, May 2018. DOI: 10.1016/j.vacuum.2018.01.038.

[104] A. Aygun, A. L. Vasiliev, N. P. Padture, and X. Ma, "Novel thermal barrier coatings that are resistant to high-temperature attack by glassy deposits," *Acta Materialia*, vol. 55, no. 20, pp. 6734–6745, Dec. 2007. DOI: 10.1016/j.actamat.2007.08.028.

[105] F. Lu, W. Huang, and H. Liu, "Thermal shock resistance and failure analysis of plasma-sprayed thick 8ysz-al2o3 composite coatings," *Surface and Coatings Technology*, vol. 384, p. 125 290, Feb. 2020. DOI: 10.1016/j.surfcoat.2019.125290.

[106] S. A. Tsipas, "Effect of dopants on the phase stability of zirconia-based plasma sprayed thermal barrier coatings," *Journal of the European Ceramic Society*, vol. 30, no. 1, pp. 61–72, 2010. DOI: 10.1016/j.jeurceramsoc.2009.08.008.

[107] P. A. Langjahr, R. Oberacker, and M. J. Hoffmann, "Long-term behavior and application limits of plasma-sprayed zirconia thermal barrier coatings," *Journal of the American Ceramic Society*, vol. 84, no. 6, pp. 1301–1308, Dec. 2004. DOI: 10.1111/j.1151-2916.2001.tb00833.x.

[108] G. V. Srinivasan, J.-F. Jue, S.-Y. Kuo, and A. V. Virkar, "Ferroelastic domain switching in polydomain tetragonal zirconia single crystals," *Journal of the American Ceramic Society*, vol. 72, no. 11, pp. 2098–2103, Nov. 1989. DOI: 10.1111/j.1151-2916.1989.tb06038.x.

[109] L. Xie, M. R. Dorfman, A. Cipitria, S. Paul, I. O. Golosnoy, and T. W. Clyne, "Properties and performance of high-purity thermal barrier coatings," *Journal of Thermal Spray Technology*, vol. 16, no. 5-6, pp. 804–808, Nov. 2007. DOI: 10.1007/s11666-007-9079-7.

[110] N. Curry, N. Markocsan, X.-H. Li, A. Tricoire, and M. Dorfman, "Next generation thermal barrier coatings for the gas turbine industry," *Journal of Thermal Spray Technology*, vol. 20, no. 1-2, pp. 108–115, Nov. 2010. DOI: 10.1007/s11666-010-9593-x.

[111] F. Guo and P. Xiao, "Effect of Fe2O3 doping on sintering of yttria-stabilized zirconia," *Journal of the European Ceramic Society*, vol. 32, no. 16, pp. 4157–4164, Dec. 2012. DOI: 10.1016/j.jeurceramsoc.2012.07.035.

[112] Y. D. Wei, Y. G. Yu, X. J. Ji, and H. R. Peng, "Influence of impurities on the microstructure and thermal shock resistance of YSZ coatings," *Materials Science Forum*, vol. 898, pp. 1414–1423, Jun. 2017. DOI: 10.4028/www.scientific.net/MSF.898.1414.

[113] N. Curry, W. Janikowski, Z. Pala, M. Vilémová, and N. Markocsan, "Impact of impurity content on the sintering resistance and phase stability of dysprosia- and yttria-stabilized zirconia thermal barrier coatings," *Journal of Thermal Spray Technology*, vol. 23, no. 1-2, pp. 160–169, Oct. 2013. DOI: 10.1007/s11666-013-0014-9.

[114] A. J. Allen, G. G. Long, H. Boukari, J. Ilavsky, A. Kulkarni, S. Sampath, H. Herman, and A. N. Goland, "Microstructural characterization studies to relate the properties of thermal-spray coatings to feedstock and spray conditions," *Surface and Coatings Technology*, vol. 146-147, pp. 544–552, Sep. 2001. DOI: 10.1016/S0257-8972(01) 01433-5.

[115] Z. Wang, A. Kulkarni, S. Deshpande, T. Nakamura, and H. Herman, "Effects of pores and interfaces on effective properties of plasma sprayed zirconia coatings," *Acta Materialia*, vol. 51, no. 18, pp. 5319–5334, Oct. 2003. DOI: 10.1016/S1359-6454(03) 00390-2.

[116] J. F. Li, H. Liao, X. Y. Wang, B. Normand, V. Ji, C. X. Ding, and C. Coddet, "Improvement in wear resistance of plasma sprayed yttria stabilized zirconia coating using nanostructured powder," *Tribology International*, vol. 37, no. 1, pp. 77–84, 2004. DOI: 10.1016/S0301-679X(03)00138-5.

[117] J. F. Li, H. Liao, X. Y. Wang, C. Coddet, H. Chen, and C. X. Ding, "Plasma spraying of nanostructured partially yttria stabilized zirconia powders," *Thin Solid Films*, vol. 460, no. 1-2, pp. 101–115, 2004. DOI: 10.1016/j.tsf.2004.01.078.

[118] S. Tao, B. Liang, C. Ding, H. Liao, and C. Coddet, "Wear characteristics of plasma-sprayed nanostructured yttria partially stabilized zirconia coatings," *Journal of Thermal Spray Technology*, pp. 518–523, 2005. DOI: 10.1361/105996305X76540.

[119] H. Chen, S. Lee, X. Zheng, and C. Ding, "Evaluation of unlubricated wear properties of plasma-sprayed nanostructured and conventional zirconia coatings by SRV tester," *Wear*, vol. 260, no. 9-10, pp. 1053–1060, May 2006. DOI: 10.1016/j.wear.2005.07.004.

[120] Y. Wang, Y. Jin, and S. Wen, "The friction and wear performance of plasma-sprayed ceramic coatings at high temperature," *Wear*, vol. 129, no. 2, pp. 223–234, Feb. 1989. DOI: 10.1016/0043-1648(89)90260-3.

[121] H. Chen, Y. Zhang, and C. Ding, "Tribological properties of nanostructured zirconia coatings deposited by plasma spraying," *Wear*, vol. 253, no. 7-8, pp. 885–893, Oct. 2002. DOI: 10.1016/S0043-1648(02)00221-1.

[122] E. P. Song, J. Ahn, S. Lee, and N. J. Kim, "Microstructure and wear resistance of nanostructured al2o3–8wt.%TiO2 coatings plasma-sprayed with nanopowders," *Surface and Coatings Technology*, vol. 201, no. 3-4, pp. 1309–1315, Oct. 2006. DOI: 10.1016/j. surfcoat.2006.01.052.

[123] ——, "Effects of critical plasma spray parameter and spray distance on wear resistance of al2o3–8 wt.%TiO2 coatings plasma-sprayed with nanopowders," *Surface and Coatings Technology*, vol. 202, no. 15, pp. 3625–3632, Apr. 2008. DOI: 10.1016/j.surfcoat. 2008.01.002.

[124] A. Rico, J. Rodriguez, E. Otero, P. Zeng, and W. M. Rainforth, "Wear behaviour of nanostructured alumina–titania coatings deposited by atmospheric plasma spray," *Wear*, vol. 267, no. 5-8, pp. 1191–1197, Jun. 2009. DOI: 10.1016/j.wear.2009.01.022.

[125] S. T. Aruna, N. Balaji, and K. S. Rajam, "Phase transformation and wear studies of plasma sprayed yttria stabilized zirconia coatings containing various mol% of yttria," *Materials Characterization*, vol. 62, no. 7, pp. 697–705, Jul. 2011. DOI: 10.1016/j. matchar.2011.04.018.

[126] V. P. Singh, A. Sil, and R. Jayaganthan, "A study on sliding and erosive wear behaviour of atmospheric plasma sprayed conventional and nanostructured alumina coatings," *Materials & Design*, vol. 32, no. 2, pp. 584–591, Feb. 2011. DOI: 10.1016/j.matdes. 2010.08.019.

[127] J. Stringer and M. B. Marshall, "High speed wear testing of an abradable coating," *Wear*, vol. 294-295, pp. 257–263, Jul. 2012. DOI: 10.1016/j.wear.2012.07.009.

[128] T. E. Fischer, Z. Zhu, H. Kim, and D. S. Shin, "Genesis and role of wear debris in sliding wear of ceramics," *Wear*, vol. 245, no. 1-2, pp. 53–60, Oct. 2000. DOI: 10.1016/S0043-1648(00)00465-8.

[129] M. Ghazali, S. Forghani, N. Hassanuddin, A. Muchtar, and A. Daud, "Comparative wear study of plasma sprayed TiO2 and al2o3–TiO2 on mild steels," *Tribology International*, vol. 93, pp. 681–686, Jan. 2016, 41st Leeds-Lyon Symposium on Tribology - Integrated Tribology, ISSN: 0301-679X. DOI: 10.1016/j.triboint.2015.05.001.

[130] I. D. Marinescu, W. B. Rowe, B. Dimitrov, and H. Ohmori, "Forces, friction, and energy," pp. 95–136, 2013. DOI: 10.1016/B978-1-4377-3467-6.00005-7.

[131] R. Rajendran, "Gas turbine coatings - An overview," *Engineering Failure Analysis*, vol. 26, pp. 355–369, 2012. DOI: 10.1016/j.engfailanal.2012.07.007.

[132] R. E. Chupp, R. C. Hendricks, S. B. Lattime, and B. M. Steinetz, "Sealing in turbomachinery," *Journal of Propulsion and Power*, vol. 22, no. 2, pp. 313–349, 2006. DOI: 10.2514/1.17778.

[133] Y. Huang, N. Hu, Y. Zeng, X. Song, C. Lin, Z. Liu, and J. Zhang, "Effect of different types of pores on thermal conductivity of YSZ thermal barrier coatings," *Coatings*, vol. 9, no. 2, p. 138, Feb. 2019. DOI: 10.3390/coatings9020138.

[134] D. Sporer, S. Wilson, I. Giovannetti, A. Refke, and M. Giannozzi, "On the potential of metal and ceramic based abradables in turbine seal applications," in *Proc. of the 36th turbomachinery symp.*, Texas A&M University, College Station, TX, Sep. 2007, pp. 79–86. DOI: 10.21423/R1336H.

[135] W. F. Laverty, "Rub energetics of compressor blade tip seals," *Wear*, vol. 75, no. 1, pp. 1–20, 1982. DOI: 10.1016/0043-1648(82)90137-5.

[136] B. Berthoul, A. Batailly, M. Legrand, L. Stainier, and P. Cartraud, "Abradable coating removal in turbomachines: a macroscopic approach accounting for various wear mechanisms," in *ASME Turbo Expo 2015: Turbine Technical Conf. and Expo.*, ASME, Jun. 2015. DOI: 10.1115/GT2015-42500.

[137] N. Fois, M. Watson, and M. B. Marshall, "The influence of material properties on the wear of abradable materials," *Proceedings of the Institution of Mechanical Engineers, Part J: Journal of Engineering Tribology*, vol. 231, no. 2, pp. 240–253, Aug. 2017. DOI: 10.1177/1350650116649528.

[138] M. O. Borel, A. R. Nicoll, H. W. Schläpfer, and R. K. Schmid, "The wear mechanisms occurring in abradable seals of gas turbines," *Surface and Coatings Technology*, vol. 39-40, no. C, pp. 117–126, Dec. 1989. DOI: 10.1016/0257-8972(89)90046-7.

[139] N. Fois, J. Stringer, and M. B. Marshall, "Adhesive transfer in aero-engine abradable linings contact," *Wear*, vol. 304, no. 1, pp. 202–210, 2013. DOI: 10.1016/j.wear.2013.04.033.

[140] M. Watson, N. Fois, and M. B. Marshall, "Effects of blade surface treatments in tip-shroud abradable contacts," *Wear*, vol. 338-339, pp. 268–281, 2015. DOI: 10.1016/j.wear.2015.06.018.

[141] E. R. Novinski, "The selection and performance of thermal sprayed abradable seal coatings for gas turbine engines," *SAE Aerospace/Turbine Plating and Metal Finishing Forum and Exposition*, pp. 60–63, 1989.

[142] M. Bounazef, S. Guessasma, and B. A. Saadi, "The wear, deterioration and transformation phenomena of abradable coating BN-SiAl-bounding organic element, caused by the friction between the blades and the turbine casing," *Materials Letters*, vol. 58, no. 27, pp. 3375–3380, Nov. 2004. DOI: 10.1016/j.matlet.2004.02.049.

[143] S. Y. Gao, Y. Liu, D. L. Duan, F. Yi, P. Wang, S. H. Hou, and S. Li, "A rubbing type of friction and wear tester simulating working condition of seal coatings," *Zhingguo Biaomian Gongcheng(China Surface Engineering)*, vol. 25, no. 4, pp. 100–106, 2012.

[144] W. H. Xue, S. Y. Gao, D. L. Duan, Y. Liu, and S. Li, "Material transfer behaviour between a Ti6Al4V blade and an aluminium hexagonal boron nitride abradable coating during high-speed rubbing," *Wear*, vol. 322-323, pp. 76–90, Jan. 2015. DOI: 10.1016/j.wear.2014.10.001.

[145] T. A. Taylor, B. W. Thompson, and W. Aton, "High speed rub wear mechanism in IN-718 vs. NiCrAl-Bentonite," *Surface and Coatings Technology*, vol. 202, no. 4-7, pp. 698–703, 2007. DOI: 10.1016/j.surfcoat.2007.05.054.

[146] I. Hutchings and P. Shipway, *Triblology: Friction and wear of engineering materials*, Second. Butterworth-Heinemann, 2017, p. 412.

[147] A. F. Emery, J. Wolak, S. Etemad, and S. R. Choi, "An experimental investigation of temperatures due to rubbing at the blade-seal interface in an aircraft compressor," *Wear*, vol. 91, no. 2, pp. 117–130, 1983. DOI: 10.1016/0043-1648(83)90248-X.

[148] C. Padova, J. Barton, M. G. Dunn, S. Manwaring, G. Young, J. Adams Maurice, and M. Adams, "Development of an Experimental Capability to Produce Controlled Blade Tip/Shroud Rubs at Engine Speed," *Journal of Turbomachinery*, vol. 127, no. 4, pp. 726–735, Mar. 2004. DOI: 10.1115/1.1934429.

[149] C. Padova, J. Barton, M. G. Dunn, and S. Manwaring, "Experimental Results From Controlled Blade Tip/Shroud Rubs at Engine Speed," *Journal of Turbomachinery*, vol. 129, no. 4, pp. 713–723, Aug. 2006. DOI: 10.1115/1.2720869.

[150] C. Padova, M. G. Dunn, J. Barton, K. Turner, A. Turner, and D. DiTommaso, "Casing Treatment and Blade-Tip Configuration Effects on Controlled Gas Turbine Blade Tip/Shroud Rubs at Engine Conditions," *Journal of Turbomachinery*, vol. 133, no. 1, Sep. 2010. DOI: 10.1115/1.4000539.

[151] A. Dadouche, M. J. Conlon, W. Dmochowski, B. Liko, and J.-P. Bedard, "Experimental evaluation of abradable seal performance at high temperature," in *ASME Turbo Expo 2008: Power for Land, Sea, and Air*, ASME, vol. 5, Jun. 2008, pp. 143–150. DOI: 10.1115/GT2008-51228.

[152] E. Irissou, A. Dadouche, and R. S. Lima, "Tribological characterization of plasma-sprayed CoNiCrAlY-BN abradable coatings," *Journal of thermal spray technology*, vol. 23, no. 1-2, pp. 252–261, 2014. DOI: 10.1007/s11666-013-9998-4.

[153] S. Gao, W. Xue, D. Duan, and S. Li, "Tribological behaviors of turbofan seal couples from friction heat perspective under high-speed rubbing condition," *Friction*, vol. 4, no. 2, pp. 176–190, 2016. DOI: 10.1007/s40544-016-0114-x.

[154] W. Xue, S. Gao, D. Duan, H. Zheng, and S. Li, "Investigation and simulation of the shear lip phenomenon observed in a high-speed abradable seal for use in aero-engines," *Wear*, vol. 386-387, pp. 195–203, 2017. DOI: 10.1016/j.wear.2017.06.019.

[155] S. Gao, W. Xue, D. Duan, S. Li, and H. Zheng, "Effect of thermal-physical properties on the abradability of seal coating under high-speed rubbing condition," *Wear*, vol. 394-395, pp. 20–29, 2018. DOI: 10.1016/j.wear.2017.09.006.

[156] N. Fois, M. Watson, J. Stringer, and M. Marshall, "An investigation of the relationship between wear and contact force for abradable materials," *Proceedings of the Institution of Mechanical Engineers, Part J: Journal of Engineering Tribology*, vol. 229, no. 2, pp. 136–150, Jun. 2014. DOI: 10.1177/1350650114545139.

[157] S. Baïz, J. Fabis, X. Boidin, and Y. Desplanques, "Experimental investigation of the blade/seal interaction," *Proceedings of the Institution of Mechanical Engineers, Part J: Journal of Engineering Tribology*, vol. 227, no. 9, pp. 980–995, 2013. DOI: 10.1177/1350650112472853.

[158] A. Batailly, Q. Agrapart, A. Millecamps, and J.-F. Brunel, "Experimental and numerical simulation of a rotor/stator interaction event localized on a single blade within an industrial high-pressure compressor," *Journal of Sound and Vibration*, vol. 375, pp. 308–331, 2016. DOI: 10.1016/j.jsv.2016.03.016.

[159] N. Zhang, H.-j. Xuan, X.-j. Guo, C.-p. Guan, and W.-r. Hong, "Investigation of high-speed rubbing behavior of labyrinth-honeycomb seal for turbine engine application," *Journal of Zhejiang University-SCIENCE A*, vol. 17, no. 12, pp. 947–960, 2016. DOI: 10.1631/jzus.A1600367.

[160] X. Haijun, N. Zhang, L. Bin, L. Cheng, and H. Weirong, "Investigation of high-speed abrasion behavior of an abradable seal rubber in aero-engine fan application," *Chinese Journal of Aeronautics*, vol. 30, no. 4, pp. 1615–1623, 2017. DOI: 10.1016/j.cja.2017.02.019.

[161] T. Pychynski, C. Höfler, and H.-J. Bauer, "Experimental Study on the Friction Contact Between a Labyrinth Seal Fin and a Honeycomb Stator," *Journal of Engineering for Gas Turbines and Power*, vol. 138, no. 6, Nov. 2015. DOI: 10.1115/1.4031791.

[162] O. Munz, T. Pychynski, C. Schwitzke, and H.-J. Bauer, "Continued experimental study on the friction contact between a labyrinth seal fin and a honeycomb stator: slanted position," *Aerospace*, vol. 5, no. 3, 2018. DOI: 10.3390/aerospace5030082.

[163] B. Zhang and M. Marshall, "Investigating the application of a honeycomb abradable lining in the turbine stage of an aero-engine," *Tribology International*, vol. 125, pp. 66–74, 2018. DOI: 10.1016/j.triboint.2018.04.013.

[164] J. E. Shigley and B. Nisbett, *Shigley's mechanical engineering design*, Eighth. New York: Tata McGraw-Hill Education, 2008.

[165] D. W. A. Rees, "Elastic-plastic stresses in rotating discs by von mises and tresca," *ZAMM*, vol. 79, no. 4, pp. 281–288, Apr. 1999. DOI: 10.1002/(SICI)1521-4001(199904) 79:4<281::AID-ZAMM281>3.0.CO;2-V.

[166] S. Miyazawa and Y. Usui, "Measurement of transient cutting force by means of a fourier analyser," *Precision Engineering*, vol. 7, no. 2, pp. 99–104, Apr. 1985, ISSN: 0141-6359. DOI: 10.1016/0141-6359(85)90099-6.

[167] *Tfestimate*, The Math Works, Inc. [Online]. Available: https://www.mathworks.com/help/signal/ref/tfestimate.html (visited on 01/11/2021).

[168] *Mscohere*, The Math Works, Inc. [Online]. Available: https://www.mathworks.com/help//signal/ref/mscohere.html (visited on 05/18/2021).

[169] *Movmean*, The Math Works, Inc. [Online]. Available: https://www.mathworks.com/help/matlab/ref/movmean.html (visited on 05/18/2021).

[170] M. P. Groover, *Fundamentals of modern manufacturing: materials, processes, and systems*. John Wiley & Sons, 2020.

[171] *Test method for calibration and accuracy verification of wideband infrared thermometers*, ASTM E2847-14, 2014. DOI: 10.1520/E2847-14.

[172] B. Lane, E. Whitenton, V. Madhavan, and A. Donmez, "Uncertainty of temperature measurements by infrared thermography for metal cutting applications," *Metrologia*, vol. 50, no. 6, pp. 637–653, Nov. 2013. DOI: 10.1088/0026-1394/50/6/637.

[173] P. A. Hooper, "Melt pool temperature and cooling rates in laser powder bed fusion," *Additive Manufacturing*, vol. 22, pp. 548–559, 2018, ISSN: 2214-8604. DOI: 10.1016/j.addma.2018.05.032.

[174] *Ratio Pyrometer Technology*, Williamson Corporation. [Online]. Available: https://www.williamsonir.com/ratio-pyrometers/ (visited on 11/04/2020).

[175] *Condition monitoring and diagnostics of machines – thermography – part 1: General procedures*, ISO 18434-1:2008, 2008.

[176] *Condition monitoring and diagnostics of machine systems – thermography – part 2: Image interpretation and diagnostics*, ISO 18434-2:2019, 2019.

[177] O. M. Alifanov, *Inverse heat transfer problems*. Springer Science & Business Media, 2012.

[178] J. V. Beck, B. Blackwell, and C. R. S. Clair Jr, *Inverse heat conduction: Ill-posed problems*. James Beck, 1985.

[179] H. R. B. Orlande, "Inverse problems in heat transfer: New trends on solution methodologies and applications," *Journal of Heat Transfer*, vol. 134, no. 3, p. 031 011, 2012. DOI: 10.1115/1.4005131.

[180] *Rangefilt*, The Math Works, Inc. [Online]. Available: https://www.mathworks.com/help/images/ref/rangefilt.html (visited on 06/10/2021).

[181] *Imfilter*, The Math Works, Inc. [Online]. Available: https://www.mathworks.com/help/images/ref/imfilter.html (visited on 06/10/2021).

[182] *Hough*, The Math Works, Inc. [Online]. Available: https://www.mathworks.com/help/images/ref/hough.html (visited on 06/10/2021).

[183] G. Stachowiak and A. W. Batchelor, *Engineering tribology*. Oxford: Butterworth-Heinemann, 2014, ISBN: 978-0-12-397047-3.

[184] *Mechanical vibration and shock – mechanical mounting of accelerometers*, ISO 5348:1998, 1998.

[185] *Mechanical vibration – measurement and evaluation of machine vibration – part 1: General guidelines*, ISO 20816-1:2016, 2016.

[186] *Condition monitoring and diagnostics of machines – vibration condition monitoring – part 1: General procedures*, ISO 13373-1:2002, 2002.

[187] *Condition monitoring and diagnostics of machines – vibration condition monitoring – part 2: Processing, analysis and presentation of vibration data*, ISO 13373-2:2016, 2016.

[188] *Condition monitoring and diagnostics of machines – vibration condition monitoring – part 3: Guidelines for vibration diagnosis*, ISO 13373-3:2015, 2015.

[189] *Condition monitoring and diagnostics of machines – vibration condition monitoring – part 9: Diagnostic techniques for electric motors*, ISO 13373-9:2017, 2017.

[190] *Mechanical vibration of rotating and reciprocating machinery – requirements for instruments for measuring vibration severity*, ISO 2954:2012, 2012.

[191] *Rotating shaft vibration measuring systems – part 1: Relative and absolute sensing of radial vibration*, ISO 10817-1:1998, 1998.

[192] *Field balancing equipment – description and evaluation*, ISO 2372:1974, 1974.

[193] D. Montgomery, *Design and analysis of experiments*. Hoboken, NJ: John Wiley & Sons, Inc, 2017, ISBN: 9781119320937.

[194] I. D. Marinescu, W. B. Rowe, B. Dimitrov, and I. Inaski, *Tribology of abrasive machining processes*. Elsevier, 2004.

[195] R Core Team, *R: A language and environment for statistical computing*, R Foundation for Statistical Computing, Vienna, Austria, 2020. [Online]. Available: https://www.R-project.org/.

[196] R. Lenth, *Unrepx: Analysis and graphics for unreplicated experiments*, R package version 1.0, 2017. [Online]. Available: https://CRAN.R-project.org/package=unrepx.

[197] V. Q. Vu, *Ggbiplot: A ggplot2 based biplot*, R package version 0.55, 2011. [Online]. Available: http://github.com/vqv/ggbiplot.

[198] S. Yossifon and C. Rubenstein, "The grinding of workpiece materials exhibiting high adhesion. part 2: Forces," *Journal of Engineering for Industry*, vol. 103, no. 2, pp. 156–164, May 1981. DOI: 10.1115/1.3184470.

[199] ——, "Wheel wear when grinding workpieces exhibiting high adhesion," *International Journal of Machine Tool Design and Research*, vol. 22, no. 3, pp. 159–176, Jan. 1982. DOI: 10.1016/0020-7357(82)90024-5.

[200] I. Choudhury and M. El-Baradie, "Machinability of nickel-base super alloys: A general review," *Journal of Materials Processing Technology*, vol. 77, no. 1-3, pp. 278–284, May 1998. DOI: 10.1016/S0924-0136(97)00429-9.

[201] T. R, *Plot with multiple y-axes*, MATLAB Central File Exchange. [Online]. Available: https://uk.mathworks.com/matlabcentral/fileexchange/67349-plot-with-multiple-y-axes (visited on 08/20/2021).

[202] *Detrend*, The Math Works, Inc. [Online]. Available: https://www.mathworks.com/help/matlab/ref/detrend.html (visited on 05/18/2021).

[203] W. Rowe, M. Morgan, A. Batako, and T. Jin, "Energy and temperature analysis in grinding," *WIT Transactions on Engineering Sciences*, vol. 44, 2003.

[204] S. Yossifon and C. Rubenstein, "The grinding of workpieces exhibiting high adhesion. part 1: Mechanisms," *Journal of Engineering for Industry*, vol. 103, no. 2, pp. 144–155, May 1981. DOI: 10.1115/1.3184469.

[205] O. Metco, *Material product data sheet zirconium oxide ceramic abradable powders*, DSMTS-0014.4 – Zirconium Oxide Ceramic Abradable Powders, 2017. [Online]. Available: https://bit.ly/3CjOaaE (visited on 09/16/2021).

[206] D. R. Sporer, T. Ulrike, M. R. Dorfman, A. R. Nicoll, G. Massimo, and G. Iacopo, "Dysprosia stabilized zirconia abradable," U.S. Patent 7981530B2, Jul. 19, 2011.

[207] C. Guo, M. Campomanes, D. Mcintosh, C. Becze, T. Green, and S. Malkin, "Optimization of continuous dress creep-feed form grinding process," *CIRP Annals*, vol. 52, no. 1, pp. 259–262, 2003. DOI: https://doi.org/10.1016/S0007-8506(07)60579-4.

[208] K. Wegener, H.-W. Hoffmeister, B. Karpuschewski, F. Kuster, W.-C. Hahmann, and M. Rabiey, "Conditioning and monitoring of grinding wheels," *CIRP Annals*, vol. 60, no. 2, pp. 757–777, 2011. DOI: 10.1016/j.cirp.2011.05.003.

[209] J. T. Roth, D. Djurdjanovic, X. Yang, L. Mears, and T. Kurfess, "Quality and inspection of machining operations: Tool condition monitoring," *Journal of Manufacturing Science and Engineering*, vol. 132, no. 4, Aug. 2010. DOI: 10.1115/1.4002022.

[210] D. C. Montgomery and G. C. Runger, *Applied statistics and probability for engineers*, 6th ed. John Wiley & Sons, 2010.

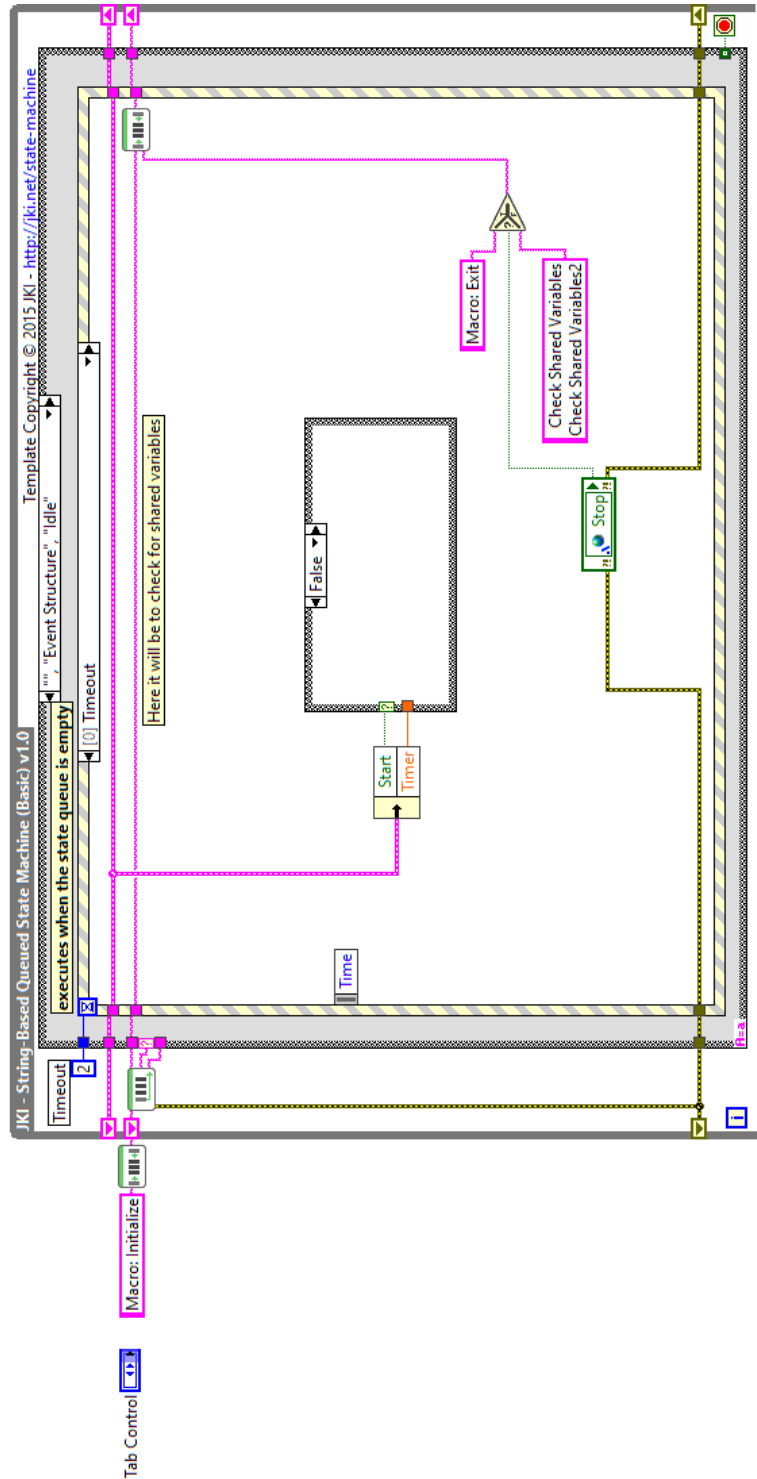# Appendix A

LabVIEW

A.1   MAIN VI

How to ADD a new device?

1. Place a LED button inside the cluster (on/Off bool), identify it with the name of the device you want to turn on
2. Go into "Check Devices" there you have to put code that tries to open the device port and then close it an error has to occur if the device can't be open create a new case with the name of the LED button and do as said
3. Go to "Reset Devices" and you should add a new case with the name of the LED you first created, create a property node as done befor ctrl+c -> right click-> link to ->select your LED button
4. Go to 'open devices' and add a case with the LED Button first created . Right click on the case structure->duplicate Case-> Change the name of case and the VI name to open (this will be the name of the device)
5. You will have to modify the VI of your device for this you will only need to add the **save structure**, **TDMS** file that you can see for examplein the Pyrometer VI. Then you should add the **recording structure** and the **shut down structure**. Reference to the Pyrometer VI to see how this is done.
6. Once finished remember to initialize the shared variables, go to "Data: Initialize Shared Variables" and initialize them to the corresponding value

** Shared variables are used for Record, Stop, Path; you will have to create another one called 'yourDeviceDataChange' and another one called 'yourDevice' place the name in the not bold letters. Open the project file-> rigth click on My Computer ->New-> Variable-> In varable type select single process->Select the data type of the variable-> click OK and the drag the variable under 'Shared Variables'-> delete the '.lvlib' created

JKI - String-Based Queued State Machine (Basic) v1.0

Template Copyright © 2015 JKI - http://jki.net/state-machine

"", "Event Structure", "Idle"

executes when the state queue is empty

[0] Timeout

Timeout

Here it will be to check for shared variables

Time

Start
Timer

False

Macro: Exit

Check Shared Variables
Check Shared Variables2

Stop

Macro: Initialize

Tab Control

Event Structure.   The interaction of the user with the front panel is detected by the event structure. During the initial period, where the user selects the devices and the properties, the main purpose of the event structure is to update the variables. In most cases the cluster is unbounded and bounded by name with the update.
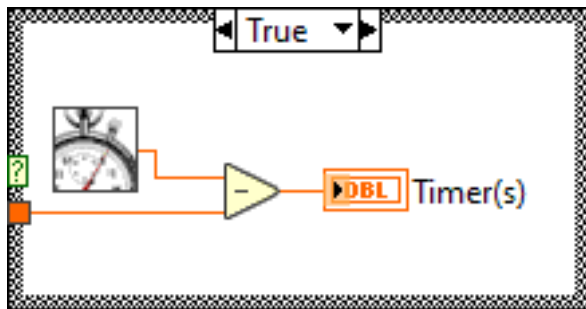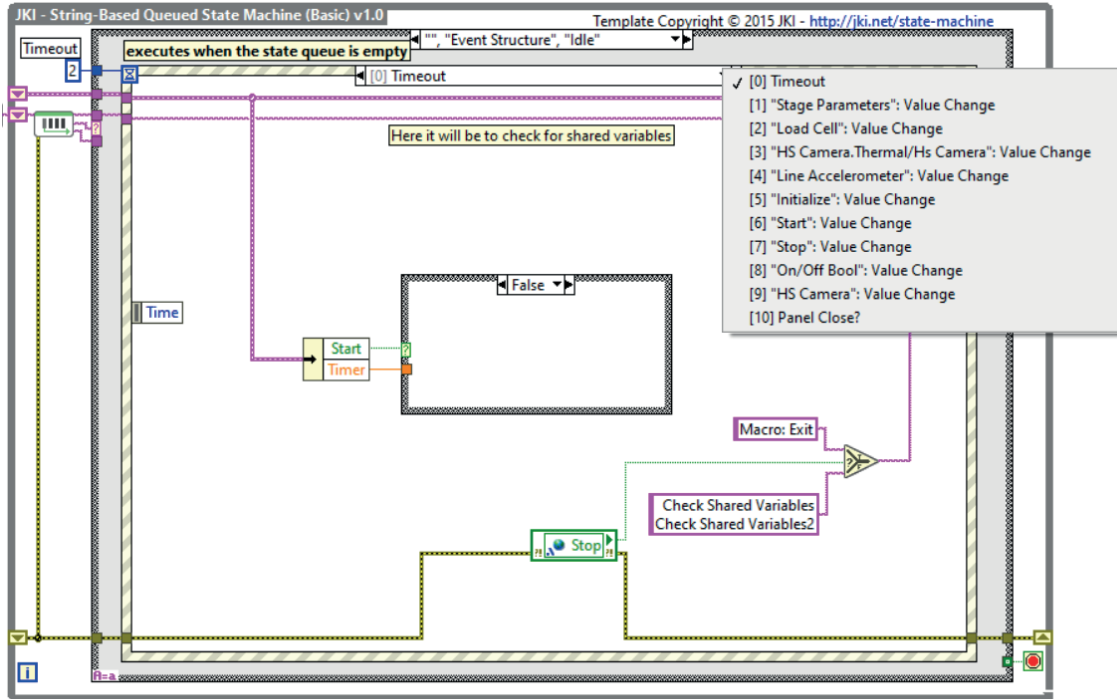
Timeout.   When there is no instruction there are two alternative tasks that are loaded to the queue. If the Stop button has been activated the macro terminates, else the shared variables that provide data from the sensors are updated and visualized in the front panel graphs. In this program these have been disabled for efficiency but can be switched on if needed. If the start button has been activated, the timer in the front panel starts displaying the test time.

Main wire The main wire contains all the values of the controls and indicators. It is created upon initialization and is the place where to put all the controls of the front panel so that all the values of the controls are updated on all time from the beginning of the program.
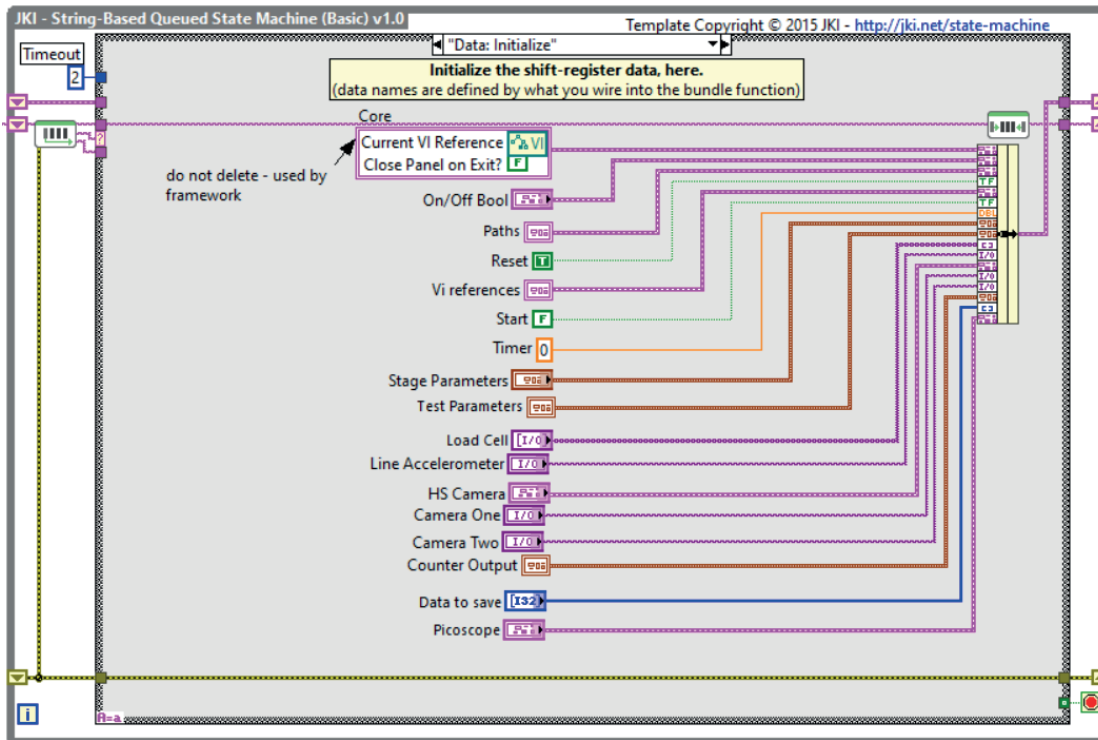
Example on how data is updated in the wire.   Most events in the event structure only trigger a simple operation, which is to update the information. The operation below is the same for the "Load Cell", the "High speed camera and Thermal camera", and the "Accelerometer". Some carry further actions like the stage controls or those of the high speed camera, which will calculate the stage's incursion rate and the full testing time.
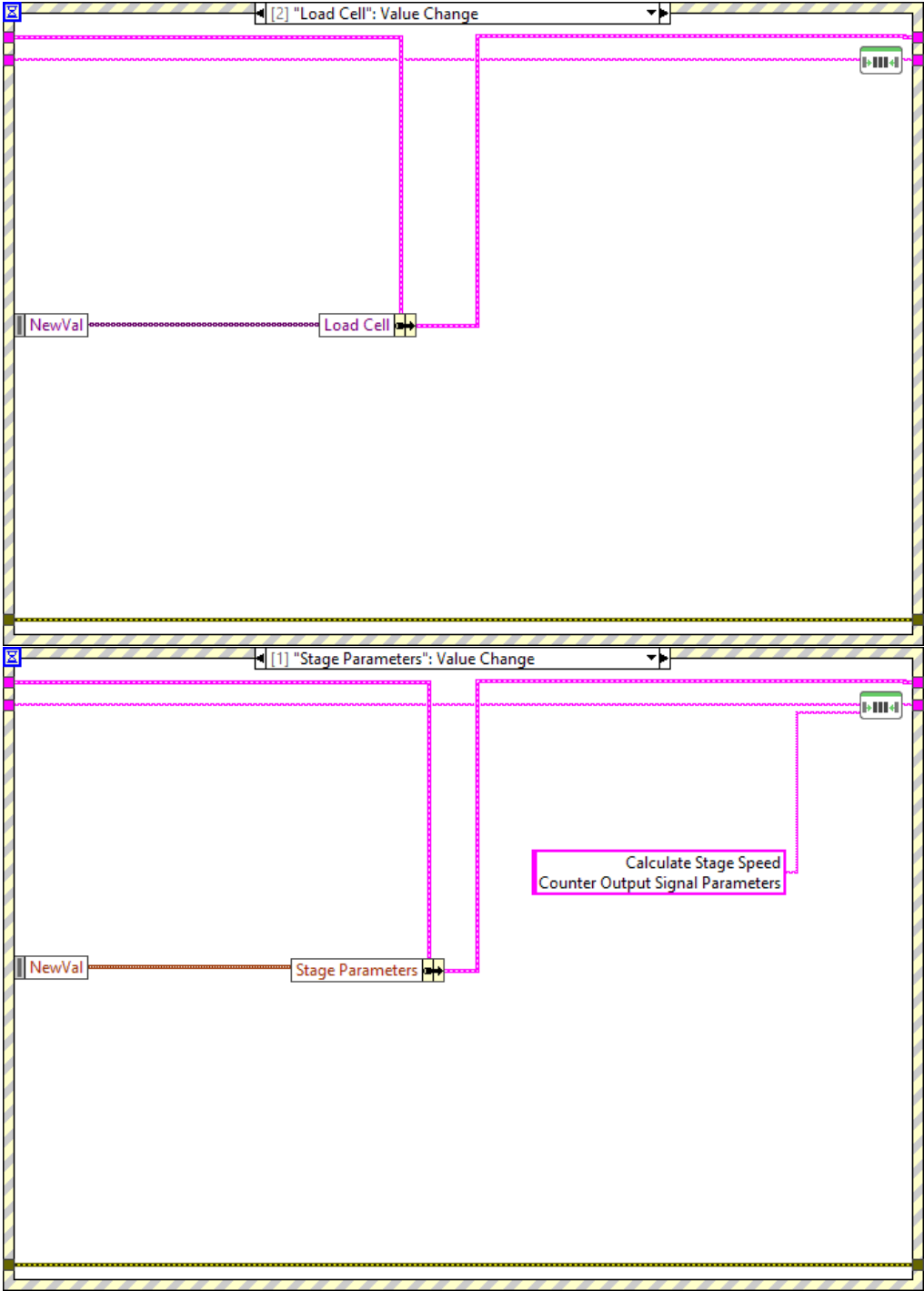
Start & Stop button.   On pressing the Start button the boolean shared variable Record is turned TRUE and all devices will proceed with their operations. On pressing the Stop button the "Stop" event is triggered which not only terminates the macro but also changes the "Stop" shared variable, which terminates all the programs that have been opened.
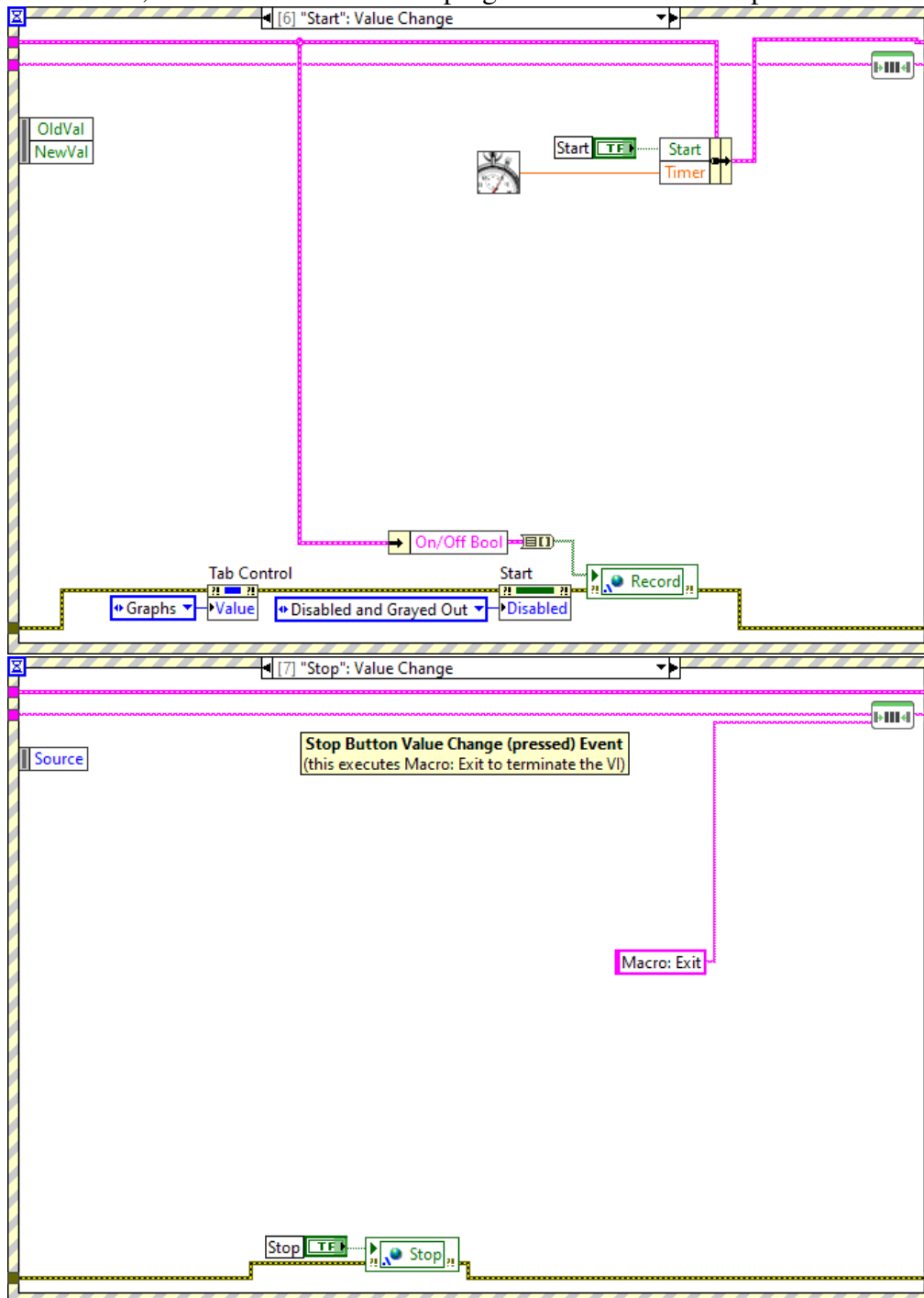
On/Off bool.   On pressing of a boolean control from the On/Off panel the boolean is checked and two instructions are sent into the queue: to check the device corresponding to the boolean, and to turn on or off depending if the device has been found connected plus a warning to the user. Each device is checked in different ways, as required by the device.
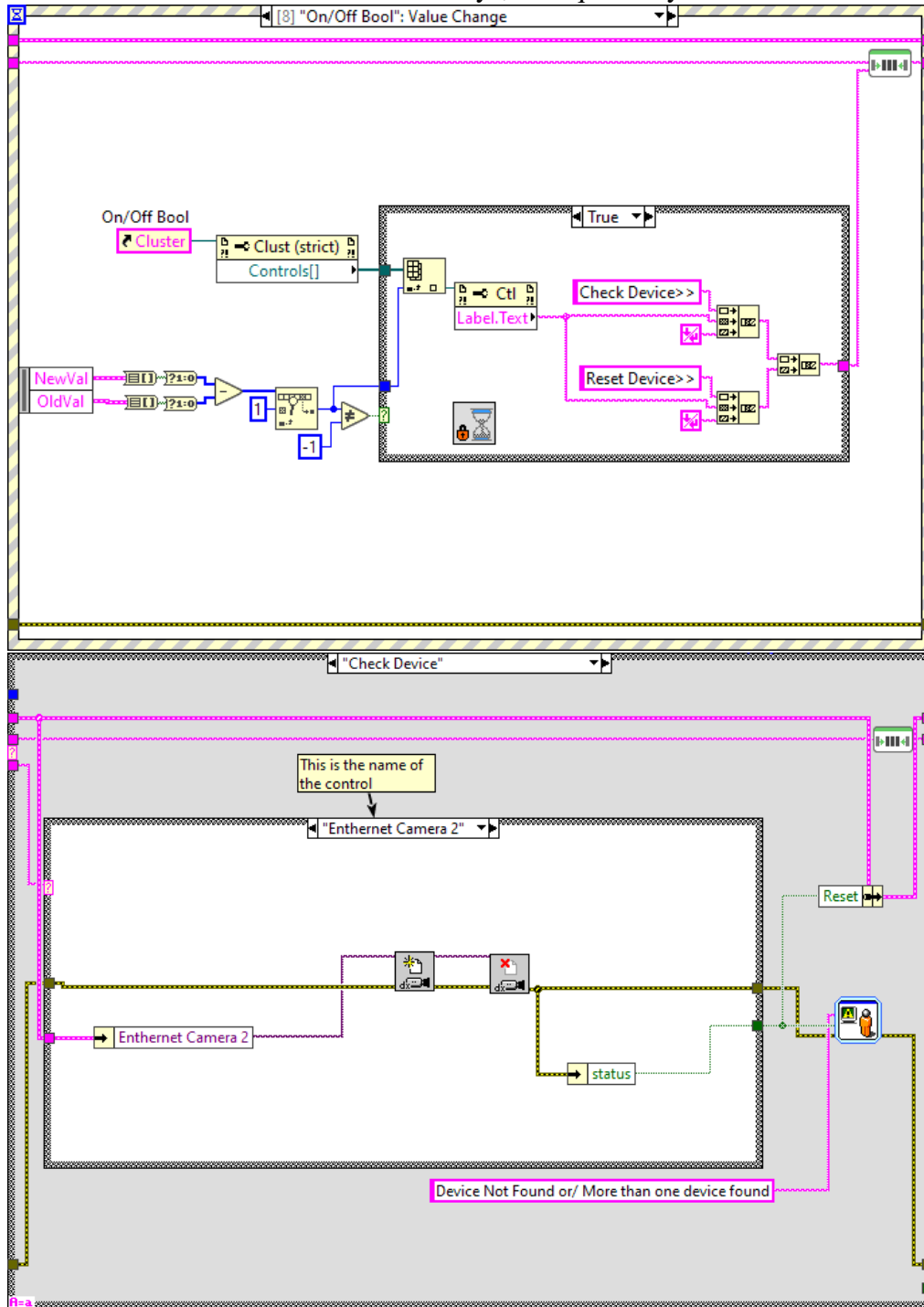
Initialization. When the initialization button is pressed the front panel is disabled and the VIs of those indicators that are on will be opened; conditions are accessed base on the names of these indicators so both need to match. The Open VI reference is used to open the VIs and the controls within are selected with the Invoke node - Control Value set.
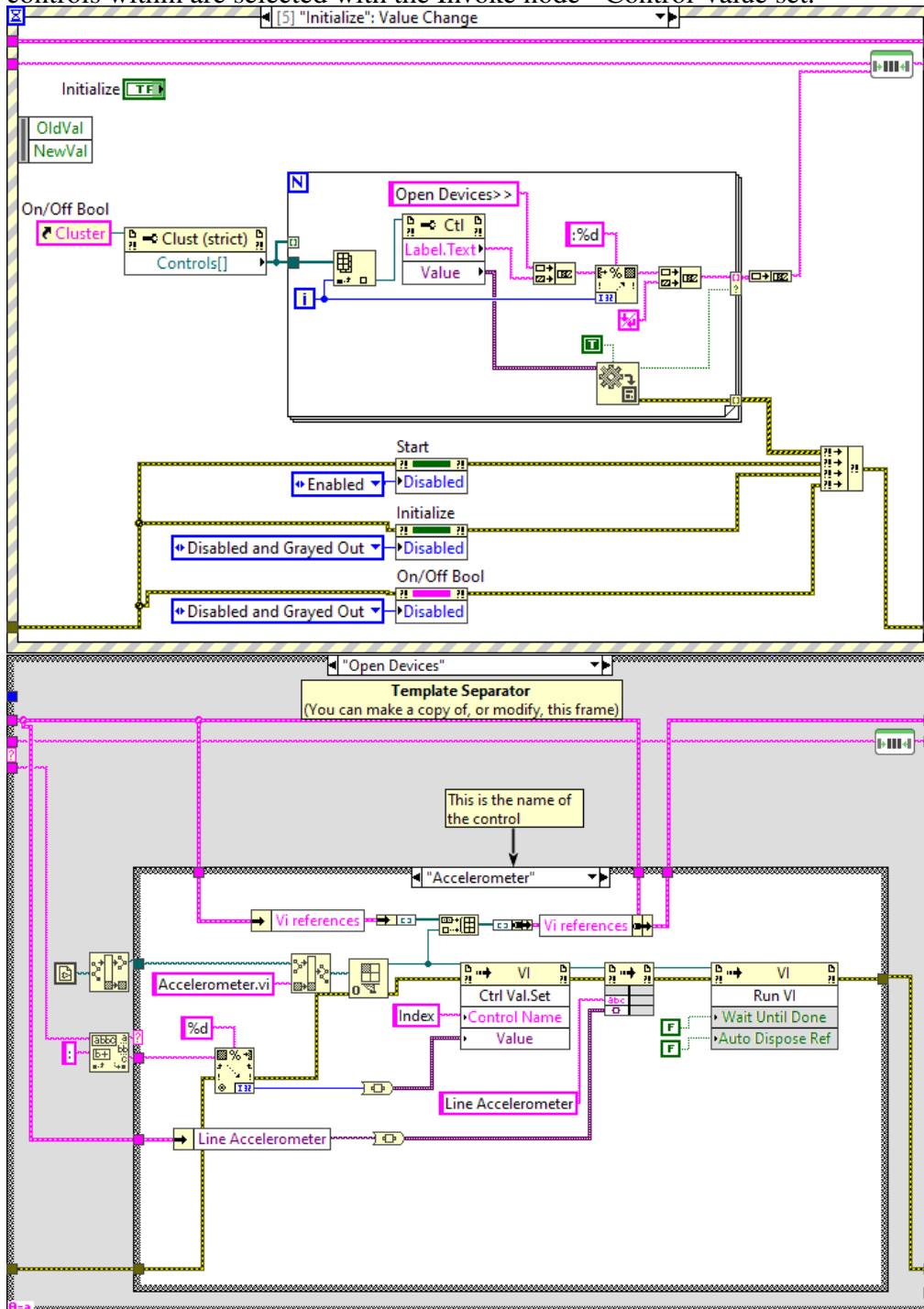
Plotting data in the main panel.   When the program has no tasks in the queue, two further tasks are added from the timeout, which is to check the shared variables. This checks with a boolean if there is new data to plot and if true it will plot it, reinitializing the same boolean to false to not re-enter until there is new data. If needed, these shared variables and indicators of the front panel (e.i. the graphs) would need to be initialized in the "UI: Initialize" task, as done for the "pyrometer" and "path" shared variable.
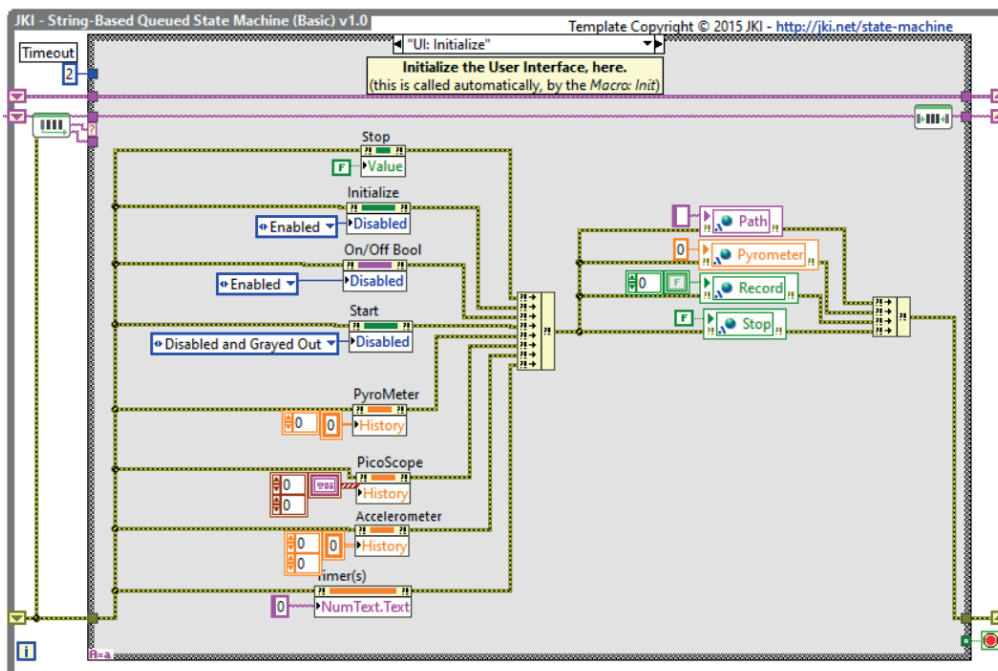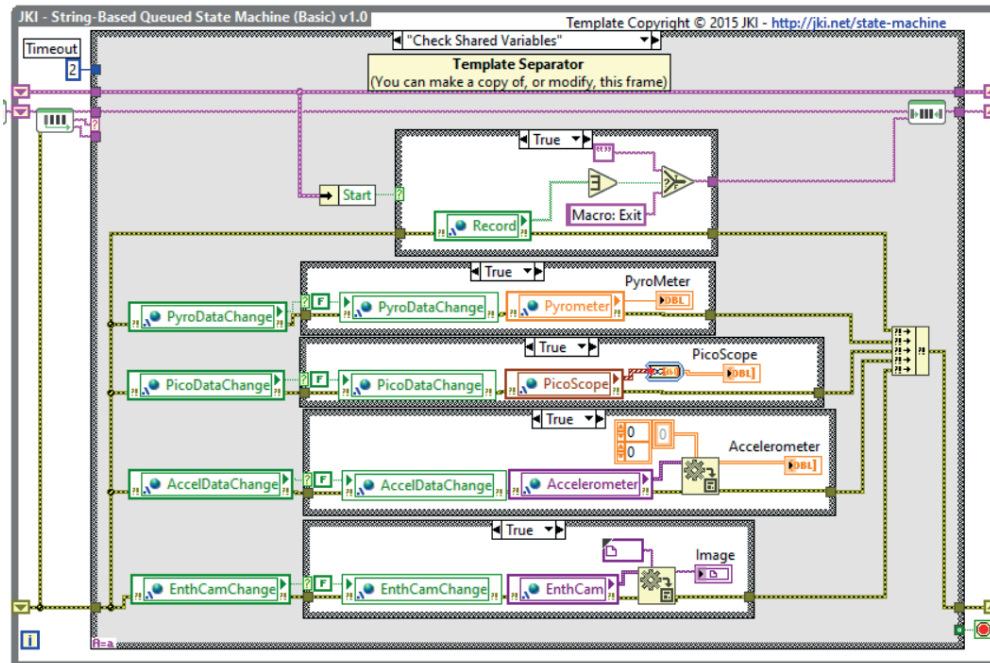
A.2   Main Structures to integrate VIs

As mentioned, VIs that generate data have been coded with a producer consumer loop architecture. To provide communication between the Main VI and the rest, three main structures are needed. These are discussed herein.

Start structure. On initialization of a VI the path where to save a file is provided through a shared variable "Path". To this, a string is added to identify the instrument, and then the desired file is opened (e.g. TDMS). The main panel of each VI contains a Stop and Record or Start which control the VI if opened alone. These are initialized to false at the start too.
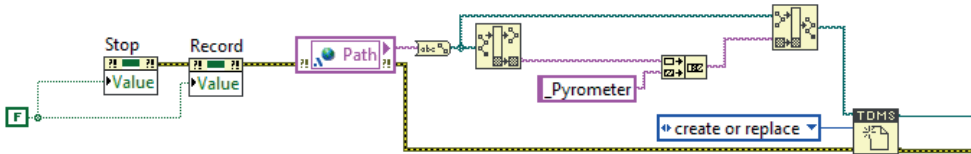
Initialize structure. Immediately after the Start structure the VI needs to remain in idle state. This mean that the VI would need to wait until the Record/Start button is pressed from the Main VI or the front panel of this individual VI. With this purpose the main instruction of the VI is placed inside a case structure awaiting for one of the Record controls are turned on. The alternative option is to do nothing. Beneath the main structure is to save the data, in others, to provide a signal, or to produce a movement.
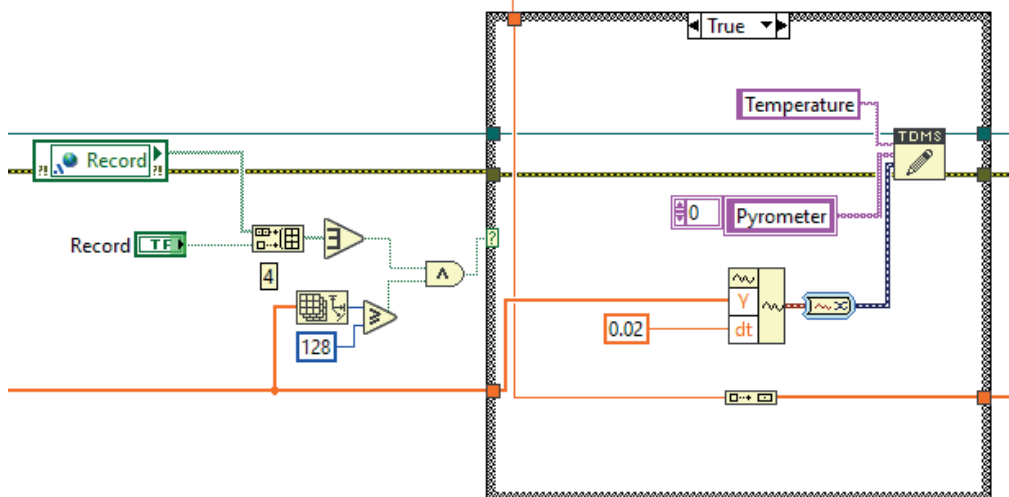
Stop structure. On termination of the Main VI, the particular VI, or on appearance of an error the loops must be ended. Consequently, a boolean array with these three conditions is provided to terminate main while loops.
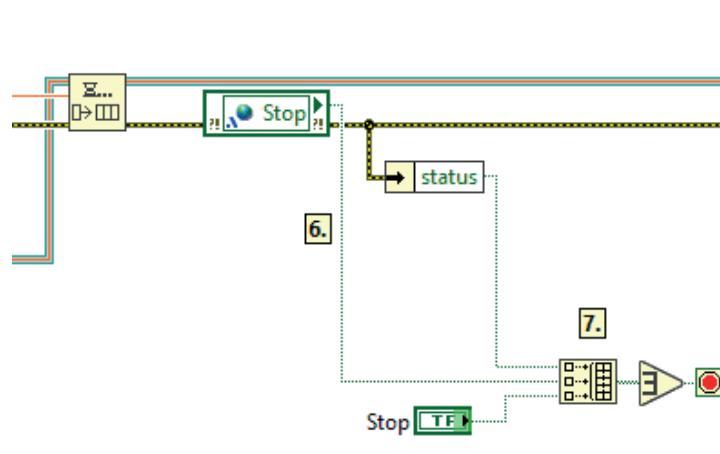
On termination, opened files must be closed too and this communicated to the Main VI if operated from it. When the particular VI finishes the Record button which is a boolean array is indexed and the particular entry of this array that corresponds to this VI is turned false. In this way if the particular VI is being run through the Main VI, this will terminate when all the entries of the Record array are false. This structure will not have any influence if the particular VI is run separately as the Record array is a shared variable and is placed only for communication purposes.
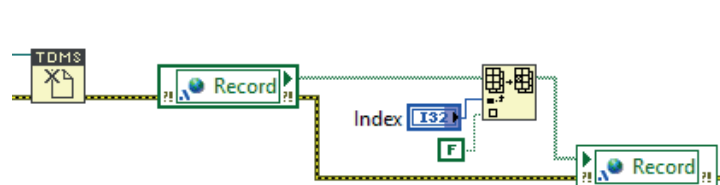
Appendix B

Active balancing with Hofmann's AB9000 system

The AB9000 system is composed of a ring that holds two internal spheres and a stator that controls the position of these spheres with a magnetic field (a non-contact process). Fig. B.1 shows how these components are mounted; the ring directly clamped to the shaft with the stator surrounding it (a small clearance separates both).
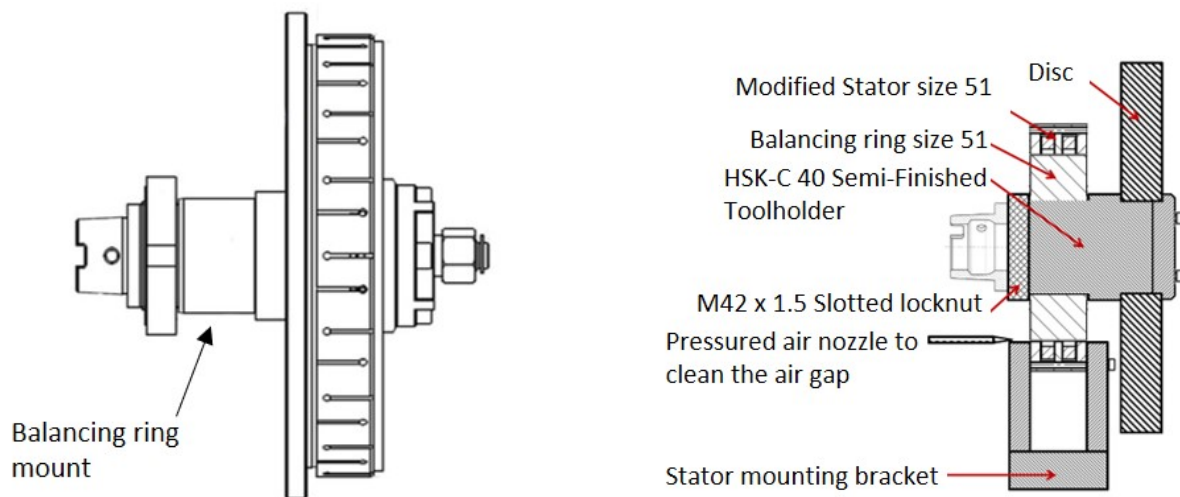
Fig. B.1 Active balancing system coupling. Schematic at the right provided by Hofmann.

When the system rotates, the stator monitors the unbalance and positions the spheres (located in the rotor) so that their force components counteract it. Fig. B.2 illustrates this with a cross-section of the system; the unbalance (green) has been pictured herein to assist with the explanation.
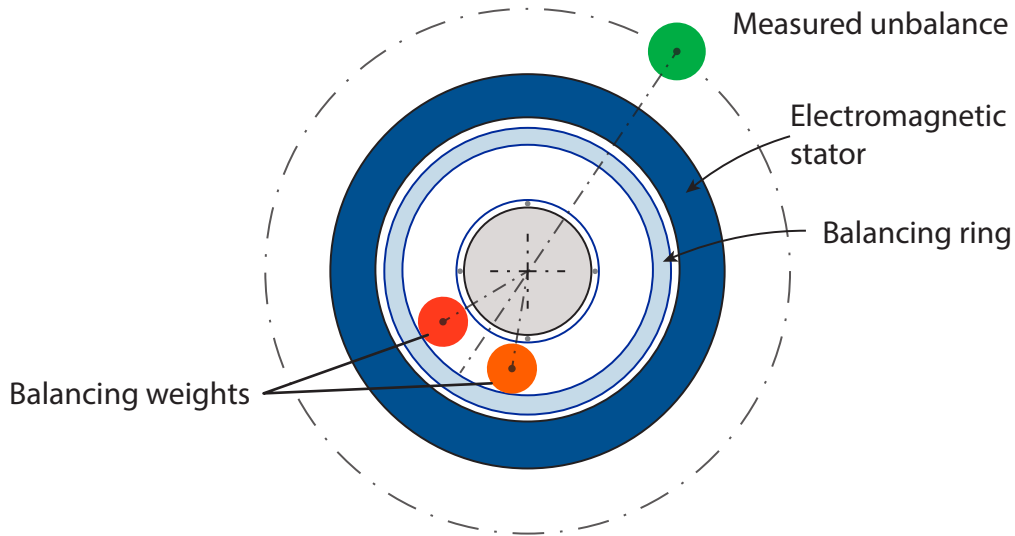
Fig. B.2 Hofmann's Balancing, sketch included in their manual

Ideally, the maximum unbalance of the rotating body has to be known because the weight of the balancing spheres is custom designed. Statistically, the parameter trying to be estimated is the highest unbalance that a sample could generate. One way of estimating this value could be from the initial experiments (Section 3.2.1) if unbalance was recorded and assumed to be normal distributed. The 6 samples of the desired substrate, in this case aluminium, could be though as a random sample of a normally distributed population with unknown variance, and the upper unbalance could be estimated (D. C. Montgomery and G. C. Runger [210, p. 284]). An illustration is provided in Fig. B.3.
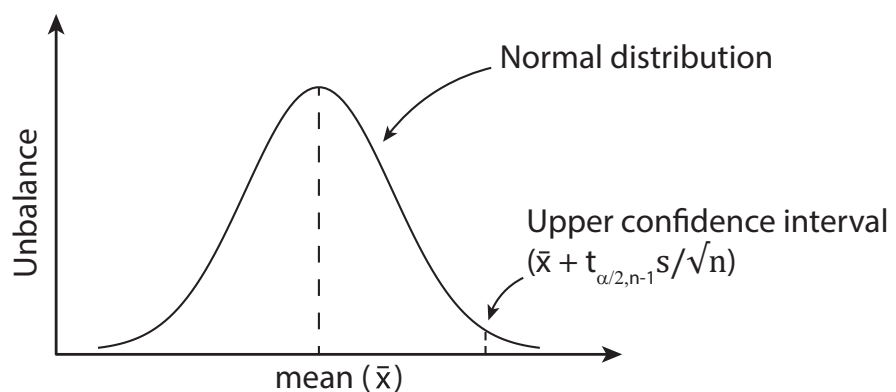
Fig. B.3 Estimation of upper unbalance limit given a sample mean, standard deviation and assuming a normal distribution

Given the mean ($\bar{x}$) and standard deviation (s) of the 6 aluminium samples, a $100(1\text{-}\alpha)\%$ confidence interval on the mean of the population could be estimated from a t distribution with $n-1$ degrees of freedom; the upper $100\alpha/2$ percentage point would be given by $t_{\alpha/2,n-1}$. The design point would be given by Equation (B.1):

$$\mu \leq \bar{x} + t_{\alpha/2,n-1}\frac{s}{\sqrt{n}} \tag{B.1}$$

$\bar{x}$ and $s \longrightarrow$ aample mean and standard deviation

$n \longrightarrow$ number of samples

$t_{\alpha/2,n-1} = t_{0.025,5} \longrightarrow$ For 95% confident interval and 6 samples

Appendix C

LabVIEW Program

Appendix D

Matlab Balancing

```matlab
clear all, close all, clc;

% Data of 3 runs: 1st at 0 deg, 2nd at 90deg, 3rd at 180deg
theta_ring = [0 90 180];  % Angle in which the ring has been placed
% Example vibration data in mm/s (other units can also be used)
vib = [0.527404 0.830312 0.513077];

theta_ring = theta_ring*pi()/180; % Converta deg to radians

% Fit a curve
[fitresult, gof] = createFit(theta_ring, vib);
fitresult, gof

% Results, angles are measured from my initial coordinate system
res = coeffvalues(fitresult);
a = res(1); % This is from the ring
b = res(2); % This is from the disc
c = res(3); % This is the angle of the unbalance of the disc

theta_plot = (0:0.5:360)*pi()/180; % Theta angle for plot
result = sqrt((a*cos(theta_plot)+b*cos(c)).^2 + ...
              (a*sin(theta_plot)+b*sin(c)).^2); %equation

%Plot
figure
plot(theta_plot*180/pi(),result);

% Find the minimum, which is the angle to rotate the sample.
minimum_u = result(result==min(result))
theta_plot(find(result == minimum_u))*180/pi()
```

```matlab
31
32  %%%%%%%%%% Function to fit from Matlab, other
33  %%%%%%%%%% methods can be used  Equation:
34  %%%%%%%%%% u(x) = sqrt((a*cos(x)+b*cos(c))^2+(a*sin(x)+b*sin(c))^2)
35  %%%%%%%%%% find a b and c given x and u(x),
36  %%%%%%%%%% the angle and the vibration respectively
37  function [fitresult, gof] = createFit(theta_ring, vib)
38  %CREATEFIT1(THETA_RING,VIB)
39  %  Create a fit.
40  %  Data for 'createFit':
41  %      X Input : theta_ring
42  %      Y Output: vib
43  %  Output:
44  %      fitresult : a fit object representing the fit.
45  %      gof : structure with goodness-of fit info.
46  %
47  %  See also FIT, CFIT, SFIT.
48  %  Auto-generated by MATLAB on 20-Jul-2020 11:48:46
49  %% Fit: 'createFit'.
50  [xData, yData] = prepareCurveData( theta_ring, vib );
51
52  % Set up fittype and options. - The function to fit is defined
53  ft = fittype( 'sqrt((a*cos(x)+b*cos(c))^2+(a*sin(x)+b*sin(c))^2)',...
54                'independent', 'x', 'dependent', 'y' );
55  opts = fitoptions( 'Method', 'NonlinearLeastSquares' );
56  opts.Display = 'Off';
57  opts.Lower = [-Inf -Inf 0];
58  opts.MaxIter = 1000;
59  opts.StartPoint = [0.0808664286235558 0.337678247516817
        0.952176332859615];
60  opts.Upper = [Inf Inf 2*pi()];
61
62  % Fit model to data.
63  [fitresult, gof] = fit( xData, yData, ft, opts );
64
65  % Plot fit with data.
66  figure( 'Name', 'untitled fit 1' );
67  h = plot( fitresult, xData, yData );
68  legend( h, 'vib vs. theta_ring', 'untitled fit 1', 'Location', '
        NorthEast');
69  % Label axes
70  xlabel theta_ring,ylabel vib, grid on
71  end
```

Appendix E

Further work on uncertainty estimation

Although with this approach the calibration curves are not needed, they are essential for exploring measurement uncertainty or for using third-party software. Given that manufacturers do not normally provide them, initial work has been conducted on this matter and two ways are proposed to obtain the camera's calibration curve. This is either by performing an in-house calibration or by reverse engineering Flir's; both very similar processes only that the latter uses the camera's temperature readings while the former uses those of a calibrated probe. The process that has been used to retrieve Flir's calibration curves (for the temperature ranges 55-350 ºC & 150-600 ºC) follows, further explanation can be attained from ASTME [171].

1. Expose the detector to a series of known temperatures ('blackbodies')

2. Record the temperature of the blackbody with a calibrated probe, the one sensed by the camera in radiance and in temperature units (Kelvin).

3. Plot a log-log scale of radiance-temperature

4. Fit the Sakuma-Hatori equation in Plankian form (E.1) to the collected data.

$$S(T) = \frac{C}{exp\left(\dfrac{c_2}{A\,T + B}\right) - 1}$$ (E.1)

From Equation (E.1): c_2 is the second radiation constant (0.014387752 mK), T is temperature in kelvin, C is a scalar coefficient, and A & B are coefficients used to attain the Planckian form; $\lambda_x = A + B/T$ will be the temperature dependent effective wavelength (in meters).

Notice that the signal perceived by the camera can be related with either of two temperatures, that pertaining to a calibrated probe that accurately measures the temperature of the black body, or the one provided by the camera after applying internal corrections (the ones not accessible
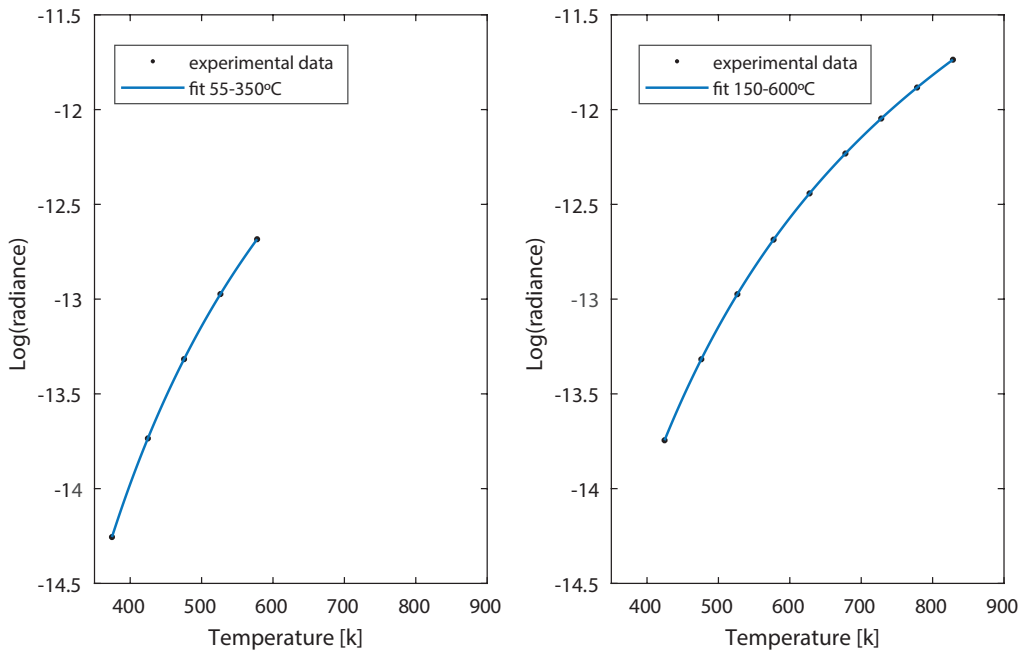
Fig. E.1 Sakuma-Hatori fitted curves to experimental data. Thermal camera calibration curves for camera options 55-350ºC (left) and 150-600ºC (right)

Table E.1 Curve fit results computed with Matlab's Curve Fitting Tool

Coefficients (with 95% confidence bounds)	
Curve 55-350ºC	**Curve 150-600ºC**
B = 2.339e-05 (1.160e-07, 4.667e-05)	1.191e-05 (2.133e-06, 2.168e-05)
A = 8.771e-06 (8.661e-06, 8.881e-06)	8.739e-06 (8.700e-06, 8.777e-06)
C = 4.924e-05 (4.805e-05, 5.043e-05)	5.015e-05 (4.978e-05, 5.052e-05)
Goodness of fit	**Goodness of fit**
SSE: 5.617e-08	SSE: 2.431e-07
R-square: 1	R-square: 1
RMSE: 0.0001676	RMSE: 0.0002013

for the user). Both give similar curves but only the first would be a calibration curve while the latter would be reverse-engineering the camera's calibration. The reverse-engineered curves can be seen in Fig. E.1 with their calibration coefficients and goodness of fit in Table E.1. From these, it must stands out the very small SSE (sum squared error) and the R^2 of 1, which is evidence for a curve that is mathematically calculated rather than one experimentally achieved.

It should also be noticed from the experimental data (Table E.2) how the camera and the probe's readings differ. This difference is a clear example of what has been previously

discussed, the inaccuracy of optical instruments for measuring temperature; it is also why it is imperative to think of the camera readings as "apparent temperature" rather than true absolute values. What's more, being more critical about the measurement accuracy, one should consider the radiometric data instead of the temperature data as the former does not include any assumptions about the observed system and hence, including less error. The main throwback is that the radiometric data is a measure for electromagnetic radiation and it is not as meaningful and self-explanatory as expressing the measurements in temperature units, which also allows for direct identification of physical changes that a material undergoes.

Table E.2 Experimental data collected from probe and from the thermal camera

Probe [K]	Cam. Setting 55-350 ºC		Cam. Setting 150-600 ºC	
	Radiometric [rad.]	Temp. [K]	Radiometric [rad.]	Temp. [K]
373.35	1.0838E-06	374.45	-	-
423.25	1.6467E-06	424.75	1.0732E-06	424.55
473.35	2.3213E-06	475.45	1.6458E-06	476.05
523.35	3.1003E-06	526.35	2.3199E-06	526.55
573.35	3.9696E-06	577.75	3.0937E-06	577.25
623.35	-	-	3.9487E-06	627.65
673.25	-	-	4.8732E-06	677.85
723.25	-	-	5.8616E-06	728.05
773.35	-	-	6.9030E-06	778.25
823.35	-	-	7.9945E-06	828.45

The size of source error (SSE), is said to be the second main source of uncertainty [171] after emissivity. For this reason, a conventional experiment has been performed to determine how the camera's uncertainty varies with the source's size. The camera looks at the temperature of a black body through an aperture, in this case a round aperture, that keeps decreasing in size. A diameter-of-spot vs signal-received graph is then plotted and the instance where the signal falls below 95% is identified. This point establishes the smallest possible area that the camera can measure accurately. With further work, the temperature error can be calculated back by placing the response into the calibration curve.

As shown in Fig. E.2, the SSE graph, an aperture of 2mm in diameter causes the signal to drop under 95%. This aperture equates to a radius of 11 pixels and is the minimum size of source that the camera can accurately measure. For verification, the experimental results were consulted with the manufacturer, and these almost matched their expectations. The minimum area that must be considered for taking measurements is therefore equivalent to a circular spot of 11 pixel radius. Measurements were taken with no extensions and for 13 different apertures of decreasing sizes (Table E.3). The experiment was then repeated by increasing and

decreasing in 5mm the distance to the source to identify the influence of focus in the SSE. The reference that sets the 100% signal was the 16mm aperture (the biggest one), at what it believed to be the focused position. Changes in setup like the use of extension tubes will influence this measurement.
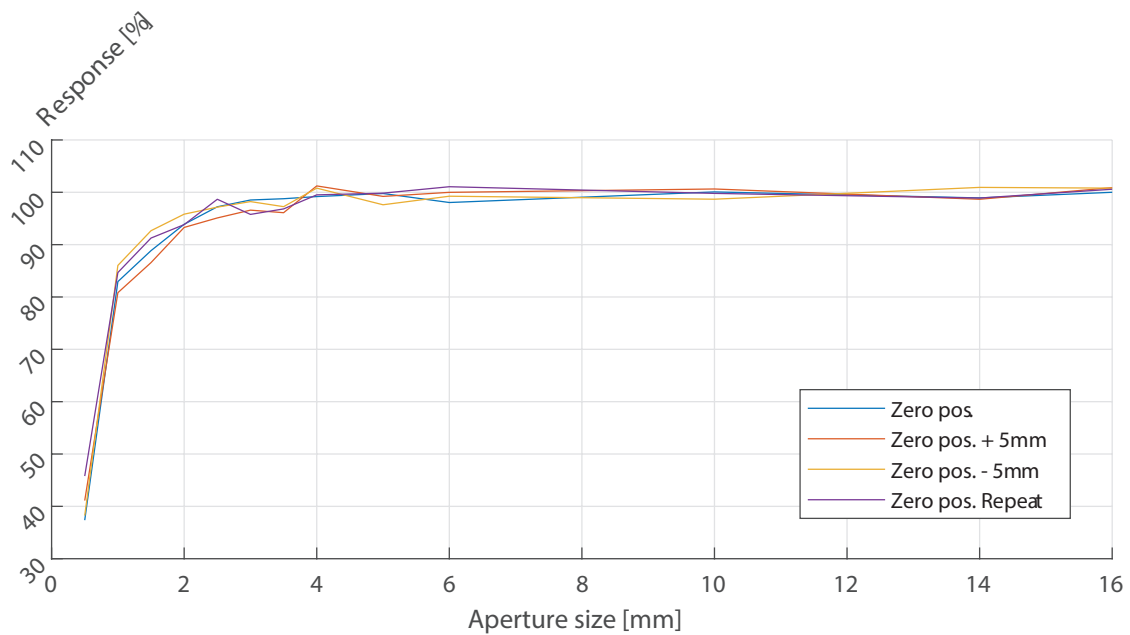
Fig. E.2 Size of source (SSE) graph: variation of the camera's signal with the size of source

Table E.3 SSE results table: aperture diameters and camera response with standard deviation

Aperture D [mm]	16	14	10	6	5	4	3.5
Response [%]	100.57 ±0.40	99.36 ±1.06	99.79 ±0.82	99.59 ±1.27	99.11 ±1.03	100.18 ±0.98	97.24 ±1.13
Aperture D [mm]	3	2.5	**2**	1.5	1	0.5	
Response [%]	97.28 ±1.31	97.04 ±1.47	**94.21** **±1.11**	89.84 ±2.69	83.61 ±2.25	40.62 ±3.80	

Appendix F

Analysis of variance for screening variables

Table F.1 ANOVA for material loss

Factor	Df	Sum Sq	Mean Sq	F value	Pr(>F)
B	1	0.000117	0.000117	936.36	0.02080 *
C	1	0.000013	0.000013	104.04	0.06221 .
E	1	0.000240	0.000240	1918.44	0.01453 *
BC	1	0.000067	0.000067	538.24	0.02742 *
BE	1	0.001480	0.001480	11837.44	0.00585 **
CE	1	0.000303	0.000303	2420.64	0.01294 *
Residuals	1	1.25E-07	1.25E-07		
Total	7	0.002220			
Multiple R-squared:	0.9999				
Adjusted R-squared:	0.9996				

Signif. codes: 0 '***' 0.001 '**' 0.01 '*' 0.05 '.' 0.1 ' ' 1

Table F.2 ANOVA for normal force

Factor	Df	Sum Sq	Mean Sq	F value	Pr(>F)	
B	1	8.18	8.18	32.01	0.11	.
C	1	4.19	4.19	16.39	0.15	
E	1	1.63	1.63	6.37	0.24	
BC	1	3.91	3.91	15.28	0.16	
BE	1	2.80	2.80	10.94	0.19	
CE	1	0.15	0.15	0.58	0.59	
Residuals	1	0.26	0.26			
Total	7	21.11				

Multiple R-squared:	0.9879
Adjusted R-squared:	0.9152

Signif. codes: 0 '***' 0.001 '**' 0.01 '*' 0.05 '.' 0.1 ' ' 1

Table F.3 ANOVA for tangential force

Factor	Df	Sum Sq	Mean Sq	F value	Pr(>F)
C	1	0.05	0.05	3.42	0.32
D	1	0.08	0.08	6.02	0.25
E	1	0.01	0.01	1.00	0.50
CD	1	0.02	0.02	1.12	0.48
CE	1	0.01	0.01	0.77	0.54
DE	1	0.03	0.03	2.20	0.38
Residuals	1	0.01	0.01		
Total	7	0.21			

Multiple R-squared:	0.9357
Adjusted R-squared:	0.5497

Signif. codes: 0 '***' 0.001 '**' 0.01 '*' 0.05 '.' 0.1 ' ' 1

Table F.4 ANOVA for apparent temperature

Factor	Df	Sum Sq	Mean Sq	F value	Pr(>F)
C	1	28878.05	28878.05	257.90	0.04
D	1	1547.63	1547.63	13.82	0.17
E	1	579.87	579.87	5.18	0.26
CD	1	2162.52	2162.52	19.31	0.14
CE	1	2621.24	2621.24	23.41	0.13
DE	1	1189.50	1189.50	10.62	0.19
Residuals	1	111.98	111.98		
Total	7	37090.79			

Multiple R-squared:	0.9970
Adjusted R-squared:	0.9789

Signif. codes: 0 '***' 0.001 '**' 0.01 '*' 0.05 '.' 0.1 ' ' 1

Table F.5 ANOVA for force ratio

Factor	Df	Sum Sq	Mean Sq	F value	Pr(>F)
B	1	0.0036	0.0036	3.5679	0.3100.
D	1	0.0045	0.0045	4.4568	0.2816.
E	1	0.0045	0.0045	4.4568	0.2816.
BD	1	0.0006	0.0006	0.6049	0.5792.
BE	1	0.0015	0.0015	1.4938	0.4365.
DE	1	0.0021	0.0021	2.0864	0.3855.
Residuals	1	0.0010	0.0010		
Total	7	0.0179			

Multiple R-squared:	0.9434
Adjusted R-squared:	0.6038

Signif. codes: 0 '***' 0.001 '**' 0.01 '*' 0.05 '.' 0.1 ' ' 1

Table F.6 ANOVA for SGE

Factor	Df	Sum Sq	Mean Sq	F value	Pr(>F)	
B	1	367.88	367.88	1.99	0.3924	
C	1	22894.79	22894.79	124.02	0.0570	.
D	1	37.89	37.89	0.21	0.7292	
BC	1	88.38	88.38	0.48	0.6147	
BD	1	196.51	196.52	1.06	0.4901	
CD	1	1565.48	1565.48	8.48	0.2106	
Residuals	1	184.61	184.61			
Total	7	25335.54				
Multiple R-squared:		0.9927				
Adjusted R-squared:		0.9490				

Signif. codes: 0 '***' 0.001 '**' 0.01 '*' 0.05 '.' 0.1 ' ' 1

Appendix G

New disc design for abrasive contact

The disc assembly is presented in Fig. G.1 and consists of 4 main components: the disc, the samples, the balancing system, and HSK-C40 shaft. The main difference of this disc is that samples are now a segment instead of a full ring. The motive for this is that now rub length will be fixed for all samples, independently of their materials' properties. As a consequence this will also mean that stresses are not introduced in the same way as before, and may preventing delamination as had been previously seen. Testing bond strength could be done separately,to supplemented this experiment. For instance, following the ASTM C633-13 procedure in relation to adhesion or cohesion strength of Thermal Spray Coatings.
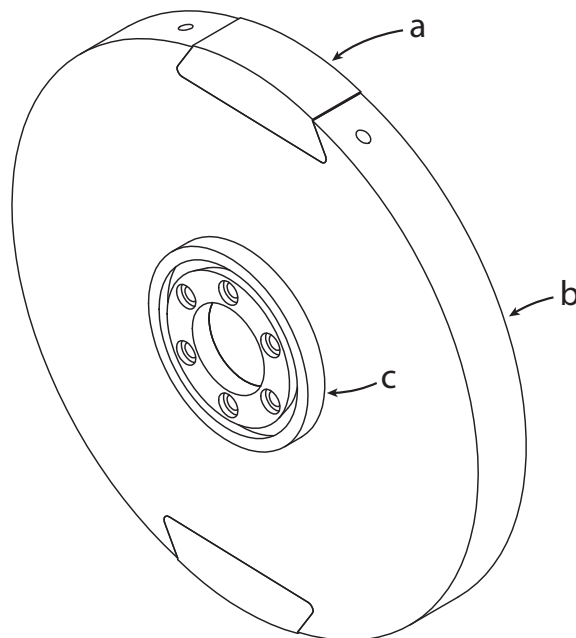

Fig. G.1 Disc assembly with main components: (a) Sample; (b) Disc; (c) Balancing system.

The design of the samples is presented in Fig. G.2. Sample thickness is 22mm to maintain the same thickness that is currently in use. The sample height is 13mm, and the region where the coating is applied is 50mm in length. The radius at the extremes coincides with that of the current disc i.e., 195mm, and the main body of the sample is retracted 1mm. The curvature of the samples is 195/2mm plus the thickness of the samples. This will give a slight oval shape to the disc and the intention is to avoid the edges of the sample to act as cutting tool. Samples can be manufactured through laser cutting or water jet and from aluminium, which will reduce costs. Geometries can be different, but it is suggested to keep in mind stresses and radial deformations with centrifugal loads. The geometry proposed (joined with that of the disc) allows the sample to deforms evenly along the full length of the coating.
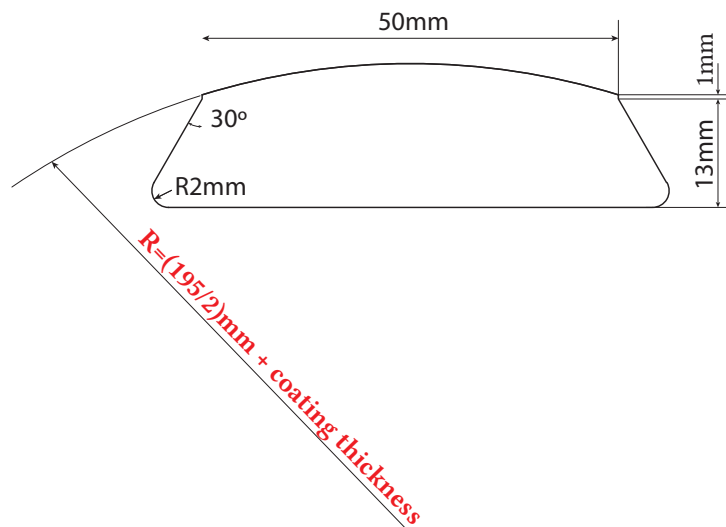

Fig. G.2 Design of samples

The disc is shown in Fig. G.3. It is 194mm diameter, 1mm short than the current one to avoid contact. The disc is connected to an HSK-C40 with 6 dowels and 6 screws; the Nord lock can also be used to avoid screws unfastening with vibrations (as its done with the current disc). An arrangement with dowels and screws is preferred over a more conventional shaft key, given it introduces more uniform stresses and deformations in the disc.
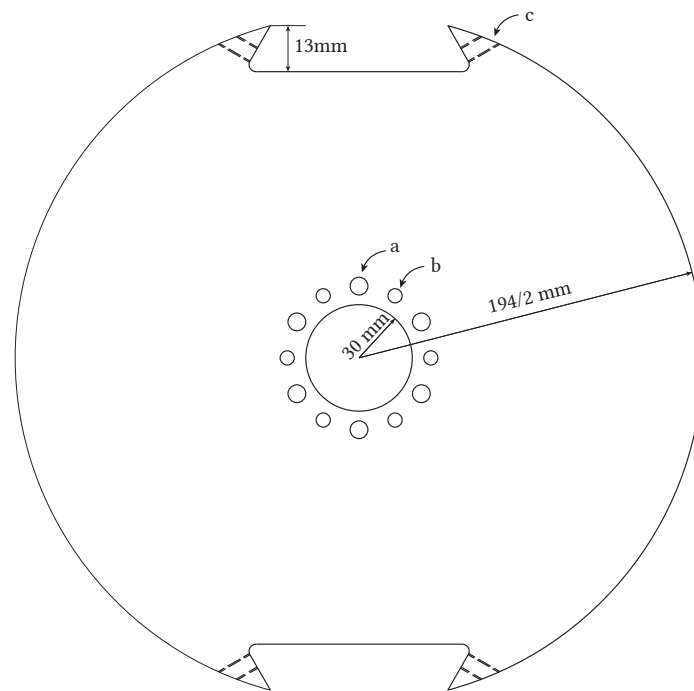
Fig. G.3 Design of disc. Labels: (a) High tensile M5 screws (b) 4mm diameter dowels (c) Grub screw to hold samples.

As there are two samples used, and one is used without coating to act as a counterbalance, there is a need to further balance the disc and the weight of the balances. A system such as this one allows the disc to be balanced without the need of an external company coming into the university or the need to drill holes into the disk, disturbing the stresses. The balancing approach that can be used is simple, and has been used in Section 5.1.3. The process will require only 3 acceleration measurements, as done in the aforementioned section this could be done moving all 3 weight (places together at the same point) 90° each time. This allows to locate the weight unbalance and its phase angle. Consequently the maths can be done in a similar way to what has been presented in Section 5.1.3 so that the position of the three weight counteract that of the measure unbalance. It should be noted that these weight need to be dimensioned appropriately, so that they can balance within a range the coatings that are going to be used. Similar systems are commercially available for grinding purposes (Fig. G.5).
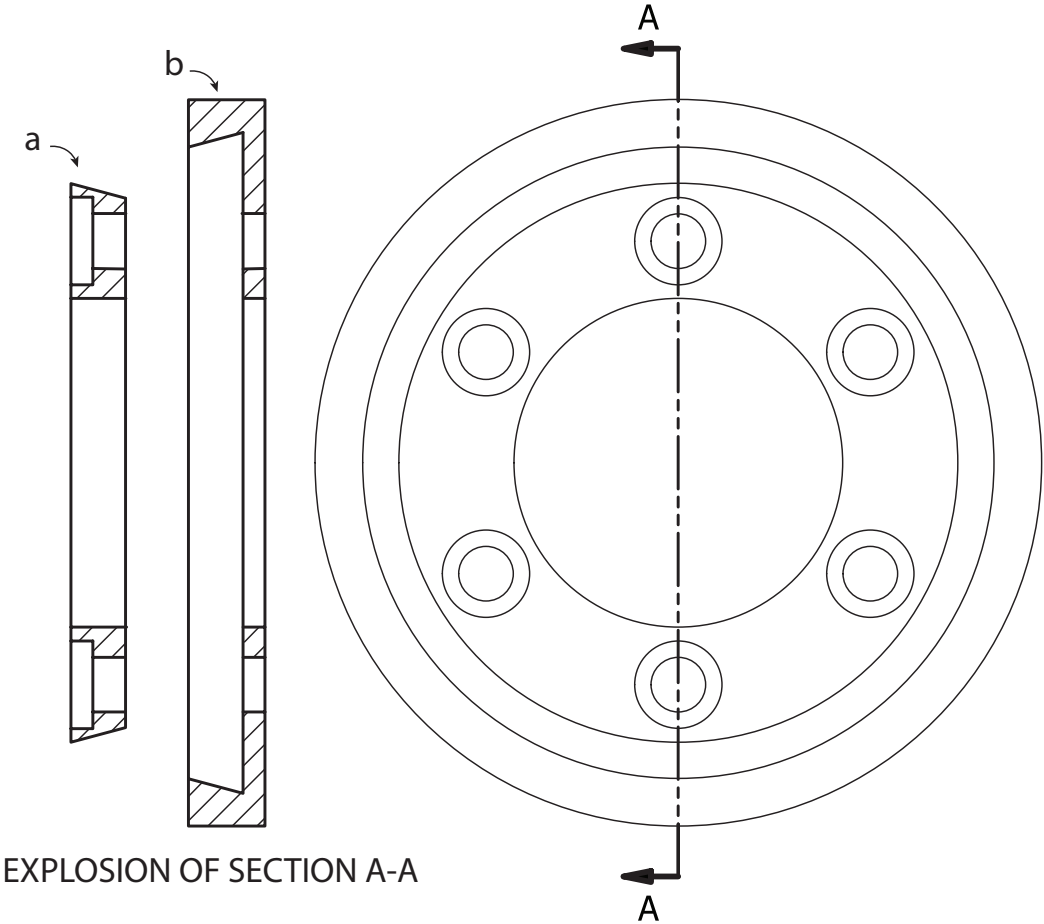
EXPLOSION OF SECTION A-A

x3 (use 3 weight)
Profile of balancing weight to fit in groove
Grub-screw in middle to hold

Fig. G.4 Design of balancing system. Labels: (a) A custom made washer with screws in the middle and a radially outwards taper (b) A custom design washer, flat in the middle and with a in taper in the outer segment

Fig. G.5 Commercial design for balancing grinding wheels, available from Sopko. Web: http://www.wmsopko.com/balancing.htm (accessed on 25/11/2021)